Nanostructured TM-Boron Based Hydrides for Solid State Hydrogen Storage (TM-transition metal)

by

Amirreza Shirani Bidabadi

A thesis
presented to the University of Waterloo
in fulfilment of the
thesis requirement for the degree of
Doctor of Philosophy
in
Mechanical Engineering

Waterloo, Ontario, Canada, 2016

Author declaration

I hereby declare that I am the sole author of this thesis. This is a true copy of the thesis, including any required final revisions, as accepted by my examiners.

I understand that my thesis may be made electronically available to the public.

Abstract

Several complex borohydride systems were investigated in this work as potential candidates for on-demand hydrogen generation and/or storage. All selected systems were synthesized by ball milling (BM) in expectation of inducing mechano-chemical activation synthesis (MCAS).

The ($LiBH_4$-$FeCl_2$) system with the molar ratio of 2:1 showed rapid hydrogen generation (mechanical dehydrogenation) at room temperature. Rapid mechanical dehydrogenation was also observed during milling of $LiBH_4$ with $TiCl_2$ and $TiCl_3$ with the molar ratio of 2:1 and 3:1, respectively. The Li-B-Fe/Ti-H systems are quite remarkable since their mechanical dehydrogenation rate at ambient temperature is much higher than their thermal dehydrogenation rate within the 100-250°C range. Mechanical dehydrogenation of the ($3LiBH_4$-TiF_3) system was rather slow without and with additives such as ultrafine filamentary Ni and graphene. Only minimal mechanical dehydrogenation was observed for the ($LiBH_4$-$MnCl_2$) system. Some additives such as ultrafine filamentary Ni and $LiNH_2$ accelerated the mechanical dehydrogenation rate of this system.

The $Mn(BH_4)_2$ and LiCl, which were identified as the MCAS products after ball milling of ($LiBH_4$-$MnCl_2$), are both nanocrystalline after synthesis. The $Mn(BH_4)_2$-LiCl nanocomposite was capable of desorbing up to ~ 4.5 wt.% at 100°C during isothermal dehydrogenation and was very stable and released no H_2 during long-term storage at room temperature for over 120 days. Mass spectrometry (MS) of the ball milled ($LiBH_4$-$MnCl_2$) showed the principal peaks of H_2 accompanied by a miniscule peak of B_2H_6 (diborane gas). Adding 5 wt.% of $LiNH_2$, graphene and Ni to the powder mixture during mechano-chemical synthesis increased the H_2/B_2H_6 peak ratio, consequently minimizing the release of B_2H_6 during isothermal dehydrogenation. $LiNH_2$ and Ni suppressed the release of B_2H_6 to a larger extent than graphene.

Isothermal desorption of ball milled ($3LiBH_4$-TiF_3) occurred at a very low temperature of 60°C resulting in desorption of 4.52 wt.% H_2 within 93 h. Interestingly, increasing milling energy from Q_{TR}=72.8 kJ/g (1 h BM) to Q_{TR}=364 kJ/g (5 h BM) led to a nearly complete disappearance of the MS B_2H_6 peak.

Acknowledgements

I would like to express my sincere gratitude to my Supervisor, Prof. Robert Varin, for the great support, trust, patience, assistance and guidance he has provided me over the past few years.

I hereby acknowledge my thesis examining committee members, Prof. Jacques Huot from Université du Québec à Trois-Rivières, Prof. Mostafa Yavuz, Prof. John Wen, and Prof. Mazda Biglari from the University of Waterloo, for the time spent reviewing my thesis.

My sincere thanks also goes to the technical team in the department of Mechanical and Mechatronic Engineering at the University of Waterloo, electronic technologist Andy Barber for helping us in setting up the electric box of Sieverts, Martha Morales for her IT support and Prof. Linda Nazar from the Department of Chemistry, University of Waterloo, for allowing access to the XRD equipment.

The research was financially supported by Natural Science and Engineering Research Council of Canada (NSERC), Hydrogen Canada (H2CAN) Strategic Research Network, and NSERC discovery grants, which are gratefully acknowledged. My special thanks also goes to Mary McPherson in the Writing Center of the University of Waterloo for helping me improve the writing of my thesis.

Last but not the least, I would like to thank my family and all my friends who supported me to be successful in my career.

Dedication

To my beloved parents and lovely wife--I am very proud to dedicate this work to all of you.

Table of Contents

List of figures

List of tables

1. *Introduction*

In the last two centuries, fossil-fuel resources have been the main sources of energy for the ongoing industrial revolution. However, fossil fuel resources are being depleted rapidly, and since they are not renewable, they are quite limited and might last only for a few more decades [1]. In addition, increasing CO_2 emission from fossil fuels has created such tremendous environmental problems as global warming and climate change, as well as poor urban air quality [2]. All of these necessitate searching for and developing new sustainable energy sources.

As an alternative energy carrier, hydrogen has received increasing attention, as it can facilitate transition from fossil fuels to clean energy for fuel-cell powered mobile and stationary applications. The Hydrogen Economy offers a potential solution to satisfying global energy requirements while reducing (and eventually eliminating) carbon dioxide and other greenhouse gas and pollutant emissions and improving energy security. Hydrogen is a very attractive alternative energy vector, being ubiquitous, clean, efficient, and also the most-plentiful element in the universe. However, despite its simplicity and abundance, hydrogen does not occur naturally as a gas on the Earth —it is always combined with other elements. Hydrogen is high in energy, yet an engine that burns pure hydrogen produces almost no pollution. NASA has used liquid hydrogen since the 1970s to propel the space shuttle and other rockets into orbit. Hydrogen fuel cells have been powering the shuttle's electrical systems, producing a clean by-product, pure water, which the crews drink [3].

As mentioned above, when hydrogen fuel burns by reacting with oxygen from air, whether in an external combustion engine or in a fuel cell, the oxidation product is nothing except water, according to the following reaction:

$$H_2 + \frac{1}{2} O_2 \rightarrow H_2O + \text{Heat} \qquad (1.1)$$

However, regarding the use of hydrogen as a fuel, one of the main problems is storage [1].

1.1 Hydrogen storage methods

For the transition from a fossil fuel to a hydrogen-based economy, hydrogen storage is a key issue. Transportation applications need a compact, light, safe and affordable containment to be used for on-board energy storage. Assuming that we have a modern car whose gasoline combustion rating is approximately 44 miles/gal (18.7 km/litre or 5.3 liters/100 km) in the city and 40 miles/gal (17 km/litre or 5.9 liters/100 km) on the highway (given by the Toyota Motor Corporation, 2013) [4] and further assuming that 42 miles/gal could be used in combined form, given that the combustion energy of gasoline is 46.9 (MJ/kg) and the density of gasoline is 0.74 (kg/L), we would need 16.6 kg of gasoline for a 400 km trip, by the following calculation:

$$\frac{1gallon}{42mile}\times\frac{3.8L}{1gallon}\times\frac{1mile}{1.61km}\times\frac{0.74kg}{L}\times 400km = 16.6kg$$

Since the combustion energy of hydrogen is 143 (MJ/kg), which is substantially more than that of gasoline (46.9 MJ/kg), to drive the same distance, about 5.5 kg of hydrogen would be needed for a fuel cell powered car. Since 5.5 kg of hydrogen has a volume of 61.6 m^3, at standard condition T = 0^0C and P = 1 atm, a tank with considerable storage space would be needed. This volume corresponds to a balloon 4.9 meter in diameter, which is hardly a practical solution for mobile applications.

In general, hydrogen storage can be categorized into (i) pressurized gas, (ii) cryogenic liquid, (iii) solid fuel such as from chemical or physical combinations with materials -- such as metal hydrides, complex hydrides and carbon materials -- or produced on-board the vehicle by reforming methanol (Table 1.1) [5].

Table. 1-1. Comparison of the major hydrogen storage methods [6].

Storage system	Volumetric density (kg H_2 m^{-3})	Drawbacks
Compressed hydrogen gas under 70 MPa pressure	~30-40	Safety problems (enormous pressures required); Pressurization cost
Liquid hydrogen at cryogenic tank at -252^{o}C (21K):	~71	Large thermal losses (open system), Liquefaction cost
Solid metal/intermetallic hydrides	~80-150	Neither of the above

Although with the newly developed light-weight composite cylinders, pressures up to 70 MPa can be supported, the hydrogen volumetric density can reach 30-40 kg m^{-3} , which is still too low [6]. However, the use of pressurized cylinders is a concern, especially in regions with high population [5]. The high cost of pressurization is also an issue; the other drawback is large pressure drops during use [7].

Even though the volumetric density of liquid hydrogen is ~71 kg m^{-3}, which is better than that of compressed hydrogen gas, it still has some drawbacks. Due to the low critical temperature of liquid hydrogen (-241^{o}C), above this temperature hydrogen is gaseous; thus, to prevent strong overpressure, liquid hydrogen can only be stored in open systems [6]. Cryogenic tanks can store liquid hydrogen at -252^{o}C and ambient pressure. The large thermal loss and cost of liquefaction are still a concern and could limit its application.

To date, the most attractive way of storing hydrogen has been the use of solid state hydrides. Solid state-light metal complex hydrides such as borohydrides (e.g., $NaBH_4$), amides (e.g. $LiNH_2$) and alanates (e.g. $LiAlH_4$) are deemed promising due to their high volumetric hydrogen capacity (~80-150 kg m^{-3} [6]) and the fact that they do not suffer such drawbacks as those experienced with compressed and liquid hydrogen. Because of the low pressures involved in metal hydride technologies, this method of hydrogen storage is the safest of all. Moreover, the hydrogen released from a metal hydride is of a very high purity and, therefore, can be used directly to feed a Proton Exchange Membrane (PEM) fuel cell [7].

1.2 Requirements for automotive on-board hydrogen storage materials

A number of long-term targets for on-board hydrogen storage systems have been introduced by the US Department of Energy (DOE) considering economic and environmental parameters for 2017. Some of these targets are listed in Table 1.2 [7].

Table. 1-2 DOE Hydrogen Storage System Targets (adopted from [7]).

Target	**2017 (new)**	**2010 (old)**	**Ultimate (new)**
Specific energy (MJ/kg)	10.8	7.2	10.8
Energy density (MJ/l)	9.72	5.4	9.72
System gravimetric density [wt%]	5.5	9	7.5
System volumetric density [g/l]	40	81	70
System fill time for 5-kg fill [min]	3.3	2.5	2.5
System cost [\$/kg H_2] (\$/kWh net)	TBD	67	TBD
Operating temperature range [°C]	Approx. -20°C to 100°C		

It should be taken into account that the 5.5 wt. % gravimetric density is for the system which includes auxiliary devices. The real H_2 storage materials capacity must be at least twice as much as for the system which means at least 11 wt. %. Thus, we must look for high hydrogen density storage materials.

The gravimetric and volumetric densities of hydrogen chemically stored using various methods are illustrated in Figure 1.1. It is clear that neither cryogenic nor high pressure hydrogen storage options can meet the mid-term DOE targets for transportation applications. It is worth noting that the only method that can satisfy the necessary gravimetric and volumetric target densities is solid state hydrogen storage in ionic-covalent hydrides of light elements, such as lithium, boron, sodium, magnesium and aluminum (or some combination of these elements).

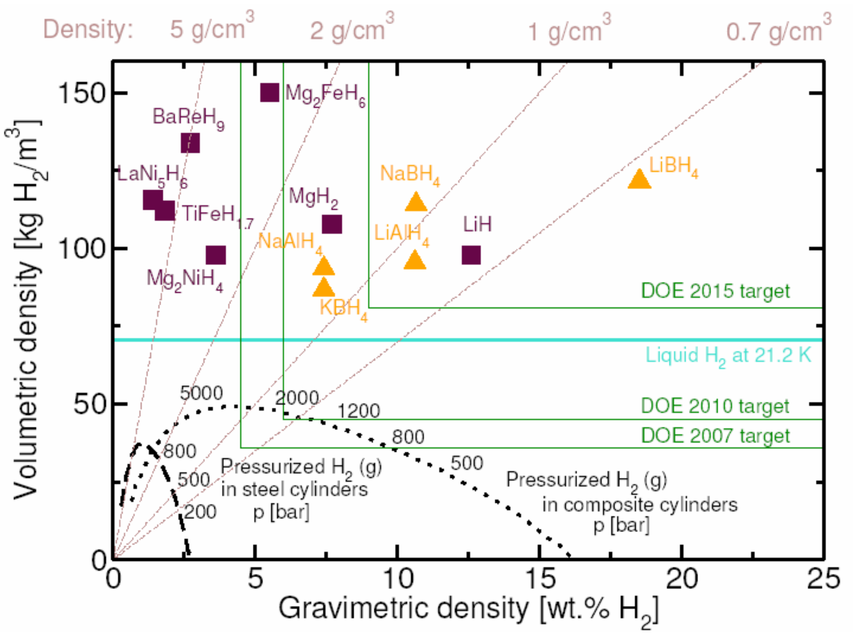

Fig. 1-1. Volumetric and gravimetric hydrogen storage densities of different hydrogen storage methods [8].

In spite of light metal hydrides satisfying the DOE requirements by providing good capacity, these materials are still subject to some thermodynamic and kinetic barriers [7]. One issue is their high thermodynamic stability due to the nature of their predominantly covalent and ionic bonds, which results in low dissociation to gaseous hydrogen. In covalent and ionic bonds, atoms bonds are highly directional, needing large activation energies to break the bonds, hence low hydrogen release kinetics [9].

1.3 Reversibility

Unlike many chemical reactions that are reversible, reactions involved in solid state hydrogen storage may not be practically reversible, often because they fail to reach a thermodynamically favorable temperature, composition or pressure. Thus, irreversibility may occur when reverse reactions become thermodynamically highly unfavorable, such as in the case for many highly exothermic forward reactions. The temperature or pressure needed to drive such a reaction in reverse may be unachievable because of experimental or practical limitations, or because high temperatures lead to decomposition of products or reactants [10]. Because of the high stability of metal hydrides, only a few have shown suitable properties for reversible hydrogen storage at moderately elevated temperatures [11].

Some stable metal hydrides such as LiH, TiH_2, CaH_2 or ZrH_2 can be rehydrogenated easily, and hydrogen absorption can be achieved even under low hydrogen pressures and at much lower temperatures than those needed for desorption [11]. At the other extreme, there are some hydrides, like $LiBH_4$, which have such a high pressure in equilibrium with the gas phase that they decompose at low temperature with relatively good kinetics. As a result, they cannot be practically formed from gaseous phase, and require chemical reactions for their formation [1, 2]. There are similar cases based on the Al-H and B-H complexes, such as $LiAlH_4$, $NaBH_4$, $NaAlH_4$, $Mg(AlH_4)_2$, which have very high gravimetric hydrogen and desorb hydrogen easily at temperatures between 100°C and 200°C, but normally cannot be rehydrogenated at hydrogen pressures lower than 100 atm [12, 13].

As described above, from a thermodynamic point of view, being endothermic is the prerequisite of reversibility in hydrogen-generation reactions. In other words, reverse H_2 absorption reactions in endothermic reactions is exothermic, and therefore the entropy loss can be compensated for by the released heat and consequent free energy gain that accompanies incorporation of H_2 into a condensed phase [11].

However, exothermic hydrogen-generating reactions are much more difficult to reverse [14]. Applying extreme hydrogen pressure, which reduces the H_2 gas entropy, can drive a reverse reaction in slightly exothermic reactions. For this reason, when hydrogen-generating reactions are exothermic and rehydrogenation is endothermic, one or more additional exothermic reaction(s) is needed to provide the energy for rehydrogenation [14]. The point that could be noted is that if reversibility is impractical, then we can overcome this problem by using a semi-disposable reservoir or cartridge--of course for predominantly non-automotive applications.

1.4 Thermodynamics

Solid state hydrogen storage has its own constraints imposed by the service parameters of high power density Proton Exchange Membrane fuel cells (PEM FCs) (sometimes also called Polymer Electrolyte Fuel Cells (PEFCs)). This type of a fuel cell is the most suitable for automotive as well as a number of other applications in portable electronic devices, stationary auxiliary power systems, off-road vehicles, lawn mowers, air transportation, coastal and international shipping, bulk hydrogen storage and many others [7, 15]. A PEM FC stack generates a quantity of waste heat, which is able to rise coolant temperatures to a range not exceeding 100°C, and operates at the H_2 fuel pressure slightly above 1 bar. Therefore, the hydride materials that are of potential interest for solid state hydrogen storage are only those that would desorb H_2 under at least 1 bar H_2 pressure (and higher) and temperatures not exceeding 100°C. In order to determine the thermodynamic properties of hydrogen storage materials, Pressure-Composition-Temperature (PCT) measurements must be understood. PCT measurements, which are also commonly referred to as Pressure-Composition-Isotherms (PCIs) since they are taken as isothermal conditions, are a collection of data points that represent the pressure, composition and temperature of a sample in equilibrium. Thus, they can be useful in determining the thermodynamic properties of hydrogen storage materials [10].

As shown in Figure 1.2, a PCT curve can be constructed by changing the hydrogen pressures and observing the corresponding changes in the hydrogen concentration in a metal at a given temperature.

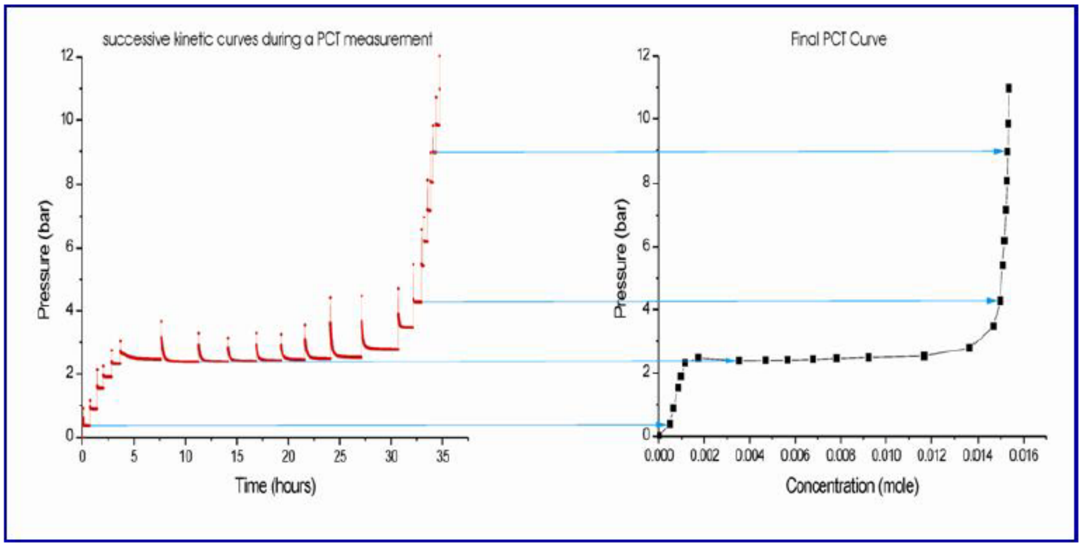

Fig. 1-2 Representative pressure/time measurement and resulting PCT plot of hydrogen absorption to form a metal hydride. The last point of each gas sorption provides concentration of hydrogen in the sample at the equilibrium pressure and temperature of each dose [10].

Figure 1.3 shows that the solid solution of hydrogen in a metal matrix phase (α) is formed by dissolving a small amount of hydrogen in the metal matrix. Afterwards, the interaction between metal atoms and hydrogen, and therefore the nucleation and growth of new metal hydride (β), is observed through the increasing hydrogen pressure and concentration. The amount of hydrogen that can be stored reversibly with a small pressure variation can be determined by the length of the plateau. As can be seen, raising the temperature will lead to increased pressure, and beyond the critical temperature (T_C), the plateau region disappears and the α phase converts to the β phase continuously [7].

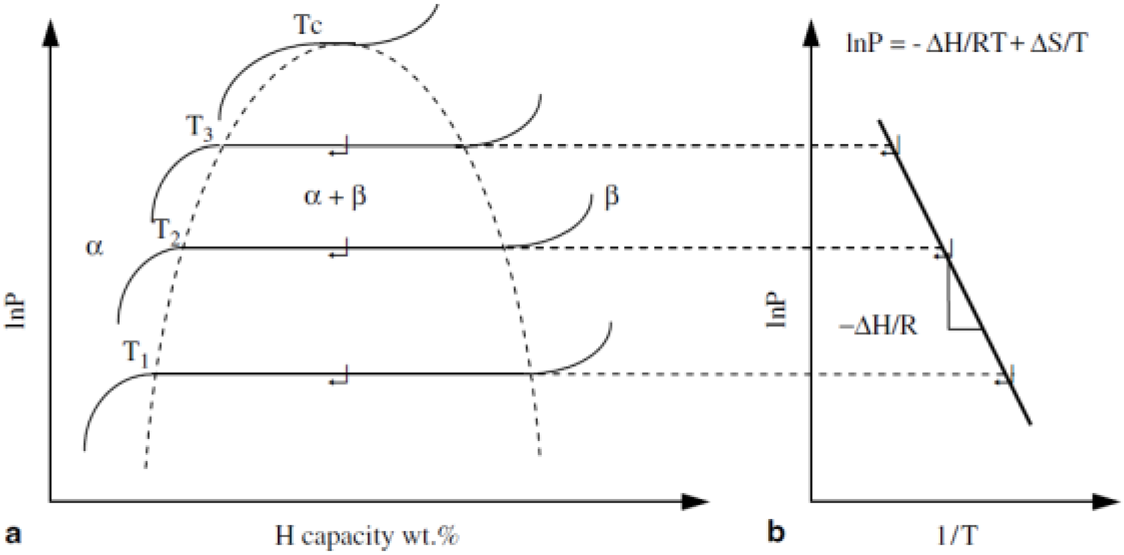

Fig. 1-3 (a) Pressure-concentration-temperature and (b) Van't Hoff plot [7].

The relationship between plateau pressure P and temperature T is given by the well-known Van’t Hoff equation:

$$\ln\left(\frac{p}{p_o}\right) = -\frac{\Delta H}{RT} + \frac{\Delta S}{R} \qquad (1.2)$$

where p_o is the atmospheric pressure, ΔH and ΔS are the enthalpy and entropy changes of the hydrogenation/dehydrogenation reactions, respectively, T is the absolute equilibrium temperature, and R is the ideal gas constant. The enthalpy of absorption and desorption processes, ΔH, can be determined from the slope (-ΔH/R) using the Van't Hoff plot presented in Figure 1.3 b. While the M-H bond strength (the stability of the metal-hydrogen bond) is an important factor in determining the operating temperature of the metal hydride and could be characterized by the enthalpy term, the change from a molecular hydrogen gas to dissolved atomic hydrogen corresponds to the entropy term. If one substitutes the pressure 1 bar (or 1 atm) in the above equation, the equilibrium temperature ($T_{plateau}$) is required to give a mid-plateau pressure of 1 atm H_2 and provide the relationship between ΔH and ΔS in the following form:

$$\Delta H = \Delta S T_{plateau} \qquad (1.3)$$

The hydride formation enthalpy (ΔH) per mole H_2 as a function of the plateau temperature at 1 bar is plotted for a number of hydrides in Figure 1.4 [7] and based on their results, all the data points fit very well in a simple straight line whose slope is equal to ΔS (~130 kJ/mol K). Another significant point that can be understood from Figure 1.4 is that only those hydrides that have an enthalpy lower than 50 kJ/mol-H_2 under 1 bar have a practical desorption temperature for PEM FC (75-100 °C) [7]. Therefore, the enthalpy term is one of the most important factors characterizing any hydride.

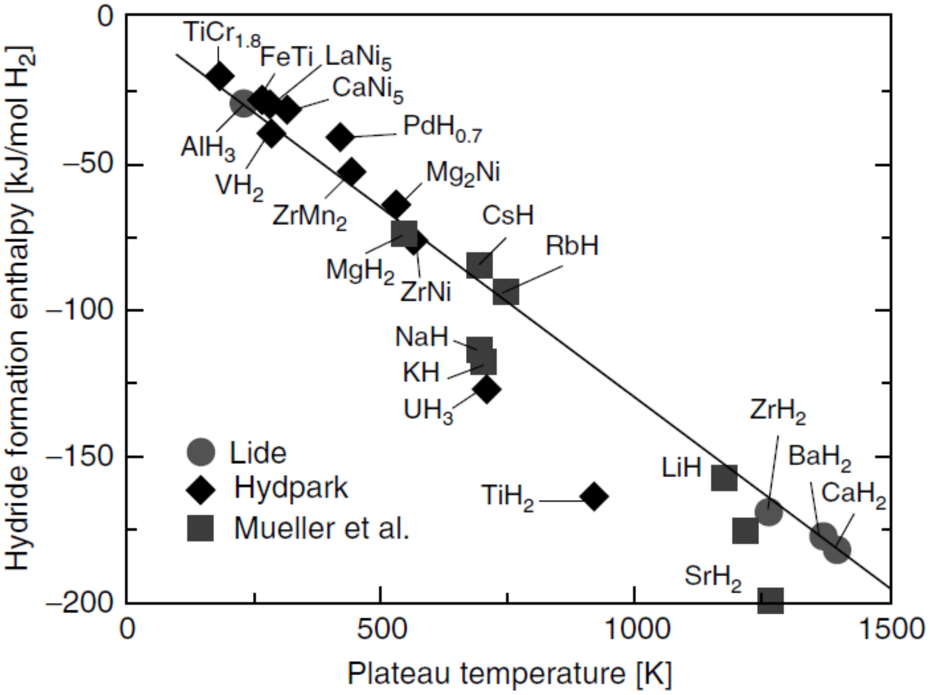

Fig. 1-4 Hydride formation enthalpy, ΔH per mole H_2, as a function of plateau temperature at 1 bar. The plateau temperature is calculated from reported thermodynamic parameter using the Van't Hoff equation [7].

1.5 Kinetics

Thermodynamics can indicate only whether or not a reaction is possible. However, these thermodynamic considerations do not tell us about the rapidity of H_2 release during dehydrogenation, which is a kinetic property. The rate of hydrogen absorption or desorption into/from a hydride compound is measured by kinetics. The rate of reaction in hydrogen storage can be influenced by many factors, such as the particle size, the size of grains residing within the particles, and the various catalytic and non-catalytic additives. Hydrogen moves in a metal hydride via atomic diffusion, first, through grain boundaries (which may be formed within the powder particles) and subsequently through the interstitial sites of the host metal structure [10]. Thus, any factor that increases the rate of a diffusion-controlled mechanism can increase the rate of dehydrogenation and hydrogenation reactions [11]. A typical example is the formation of a nanograin within the hydride powder particles by high energy ball milling, a procedure discussed later in the text [11, 16, 17].

Various nanometric catalytic additives can accelerate the rate of reaction and thus limit the time available for hydrogen atoms to diffuse and contribute to the growth of nucleating hydride nanocrystals. An example of enhanced sorption kinetics is the rapid absorption and desorption that occur during Mg-hydride formation in multiphase composite materials based on Mg, Mg_2Ni and La. A combination of the above concepts was ascribed to the improved kinetics measured in these composite materials [18]

In general, ball milling of various hydrides in order to produce nanostructured materials enhances their hydrogen storage properties. This presents a new mechanical activation route to the synthesising and manufacturing of nanomaterials for hydrogen storage. The observations made show that both the particle and grain size equally rapidly decrease with even short processing in high energy ball mills [7].

1.6 Nanostructuring of hydrides by mechanical milling

Nanocrystalline materials are single-phase or multi-phase, and their crystal size is of the order of a few (typically 1-100) nanometers in at least one dimension.

In nanostructured hydrides, a hydrogen molecule, H_2, dissociates into two hydrogen atoms on contact with a free powder surface, especially if the hydride contains metallic elements or catalytic additives on the free powder surfaces. The molecules then enter the bulk material as dissociated hydrogen atoms through the grain boundary channels. Therefore, the specific surface area and the fraction of material that belong to the grain boundaries are important parameters. Nanostructuring reduces both the particle and grain size of nanograins (crystallites) residing in the particles, thereby increasing the specific surface area of particles and the volume fraction of grain boundary materials.

High-energy ball milling is the most effective nanotechnology top-down approach for the synthesis of both nanoparticles and nanograins. The advantage of milling in the synthesis of nanocrystalline materials lies in its ability to produce bulk quantities of materials in the solid state using simple equipment at room temperature. Generally, the repeated fracturing, deformation and welding of powder particles during milling increase crystal defects such as vacancies and dislocations, as well as the volume fraction of grain boundaries. The increase in local temperature during ball milling, together with the high number of defects, aids the diffusion of solute elements into the host matrix to form a new solid solution [19, 20]. In addition, these defects can raise the free energy of the system, making it accessible to the formation of thermodynamically metastable phases. The defects can also lower the activation energy of reactions limited by poor kinetics [7]. Therefore, nanostructured materials are the best and easiest solution to addressing both thermodynamic and kinetic problems in hydrogen storage.

Among the processes used to produce advanced materials, ball milling is both well-known and commonly used. Due to the chaotic movement of balls, conventional ball milling (planetary or shakers, Fig 1.5) induces chaotic modes of milling where ball impact is mixed with shearing. However, using a magneto-mill (Uni-Ball-Mill Model 5), the trajectory of ball movement can be controlled by a magnetic field imposed by a FeNdB magnet, as shown in Fig 1.6. This control is valuable, as researchers can change the mode of mechanical action (impact or shear) by changing the orientation of the magnets.

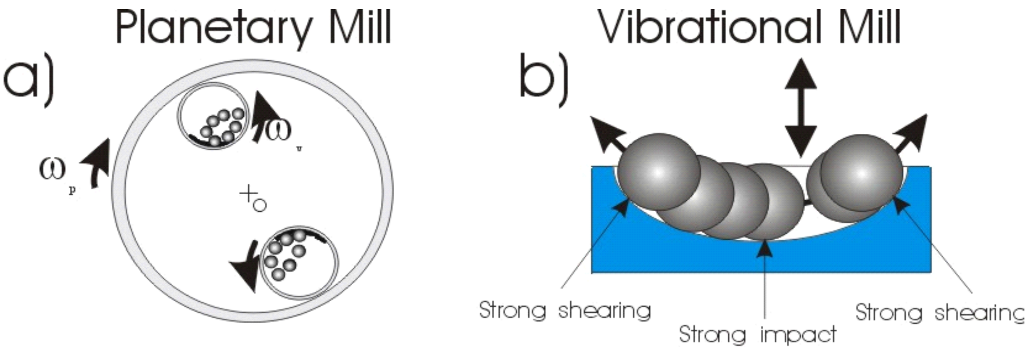

Fig. 1-5. Motion of balls in (a) a planetary and (b) a vibrational mill [7].

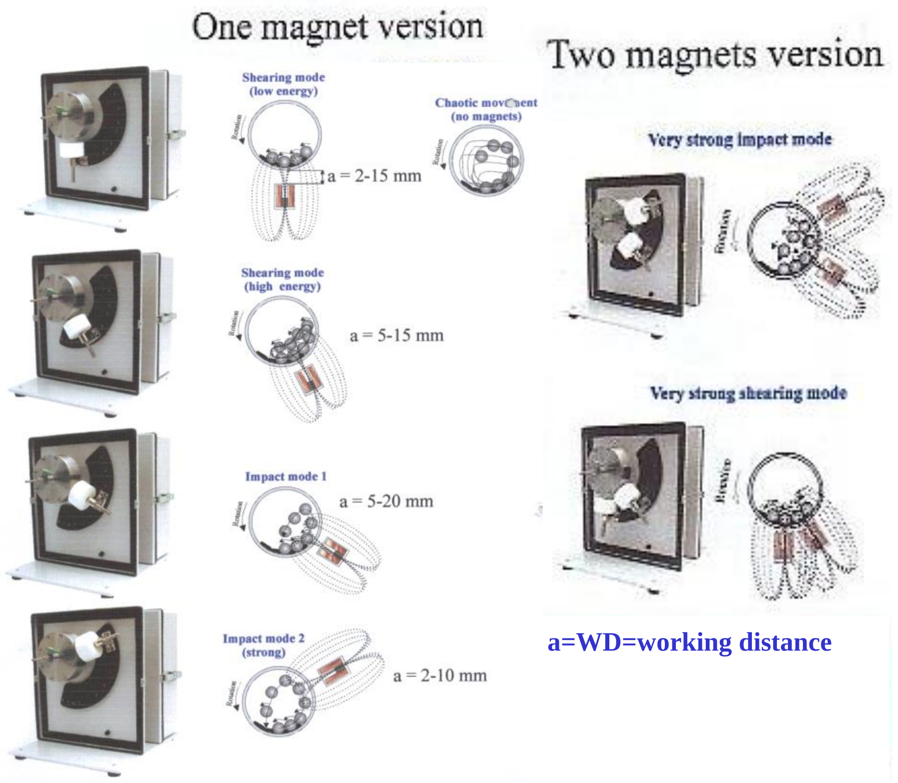

Fig. 1-6 Various controlled modes of milling available in the Uni-Ball-Mill 5 [7].

1.7 Complex hydrides

The term “complex” hydride is rather liberally applied to a rather large group of hydrides by various authors. In the broadest sense, these are hydrides composed of anionic metal-complex hydrogen or a non-metal-hydrogen complex bonded to a cationic alkali or transition metal. Hence, the entire large group can be roughly subdivided into two categories: salts of $[AlH_4]^-$, $[BH_4]^-$, i.e., alanates, amides and borohydrides and transition metal (TM) complex hydrides that have anoionic $[TMH_X]^-$ complexes such as $[FeH_6]^{4-}$ attached to a cationic light metal, e.g., Mg^{2+}, in Mg_2FeH_6 [7]. Complex hydrides have much higher hydrogen storage capacity than transition metal hydrides and also have higher hydrogen coordination numbers than simple metal/intermetallic hydrides. Since complex hydrides have both hydrogen storage capacity and desirable absorption/desorption thermodynamic/kinetics, they are considered to be the best candidates for onboard hydrogen storage applications [7, 10].

1.7.1 Metal borohydrides

Metal borohydrides have been recognized as a potential candidate for hydrogen storage due to their high hydrogen capacity. Most of the borohydrides crystalize in a complex lattice that can be found in two notable borohydrides, lithium borohydride ($LiBH_4$) and sodium borohydride ($NaBH_4$). Both are easily available commercially, with theoretical total gravimetric hydrogen capacities of 18.4 and 10.6 wt%, respectively, and they are potential candidates for on-board hydrogen storage applications. However, both suffer from thermodynamic and kinetic deficiencies that severely limit their practical use [7, 15].

1.7.1.1. Lithium borohydride ($LiBH_4$)

Lithium borohydride is one of the potentially interesting solid-state hydrogen storage materials due to its very high theoretical gravimetric hydrogen capacity (~ 18.5 wt. % H_2).

At ambient condition, its structure has been reported to have orthorhombic symmetry in which each $(BH_4)^-$ anion is surrounded by four lithium Li^+ cations and each Li^+ by four $(BH_4)^{-,}$ both in a tetrahedral configuration. An orthorhombic room temperature structure of $LiBH_4$ is transformed into a hexagonal polymorphic structure with increasing temperature. The interesting fact is that through this polymorphic transformation, the structure becomes smaller along orthorhombic α (hexagonal c) and expands in the orthorhombic b×c plane (hexagonal basal plane); therefore, the high temperature structure is more symmetric and less distorted with respect to bond lengths and bond angles [21].

This transformation can be seen as a first endothermic peak at around 110 °C in the DSC thermal desorption spectrum, and is accompanied by a small release of hydrogen (~ 0.3 wt. % H_2). $LiBH_4$ melts at 280 °C and dehydrogenates slowly according to the following reaction [7] which is illustrated by using differential scanning calorimetry with the heating rate of 2 $Kmin^{-1}$ in Fig. 1.7 a:

$$LiBH_4 \rightarrow LiH+B+3/2H_2 \qquad (1.4)$$

However, the complete dehydrogenation of $LiBH_4$ requires high temperature (above 650 °C). Thus, four endothermic peaks can be observed in the thermal desorption spectrum of pure $LiBH_4$:

1- Polymorphic transformation from orthorhombic to hexagonal at around 110 °C
2- Melting of the hexagonal structure at around 280 °C
3- The first hydrogen desorption reaction at around 490 °C
4- The second hydrogen desorption reaction at around 680 °C [22]

In the literature, the enthalpy and entropy changes of reaction (1.4) are reported as 74 kJ/mol H_2 and 115 J/K.mol H_2, respectively [23]. However, this high enthalpy changes for dehydrogenation results at dehydrogenation temperatures in excess of ~ 400 °C. Accelerating the dehydrogenation rate of $LiBH_4$ with certain metal catalysts has been investigated. Xia et al.. [24] demonstrated that although the Ni addition increased the desorption rate of $LiBH_4$ as shown in Figure 1.7, it did not reduce the enthalpy. They calculated the enthalpy and entropy of a $LiBH_4$-Ni composite and consequently the equilibrium temperature (393.2°C) at standard pressure, and showed that it was similar to that of pure $LiBH_4$. Thus, their results suggest that the Ni addition has no significant effect on changing the thermodynamic properties of $LiBH_4$ [24]. Similarly, non-metal catalysts have shown the same effect on $LiBH_4$ [25].

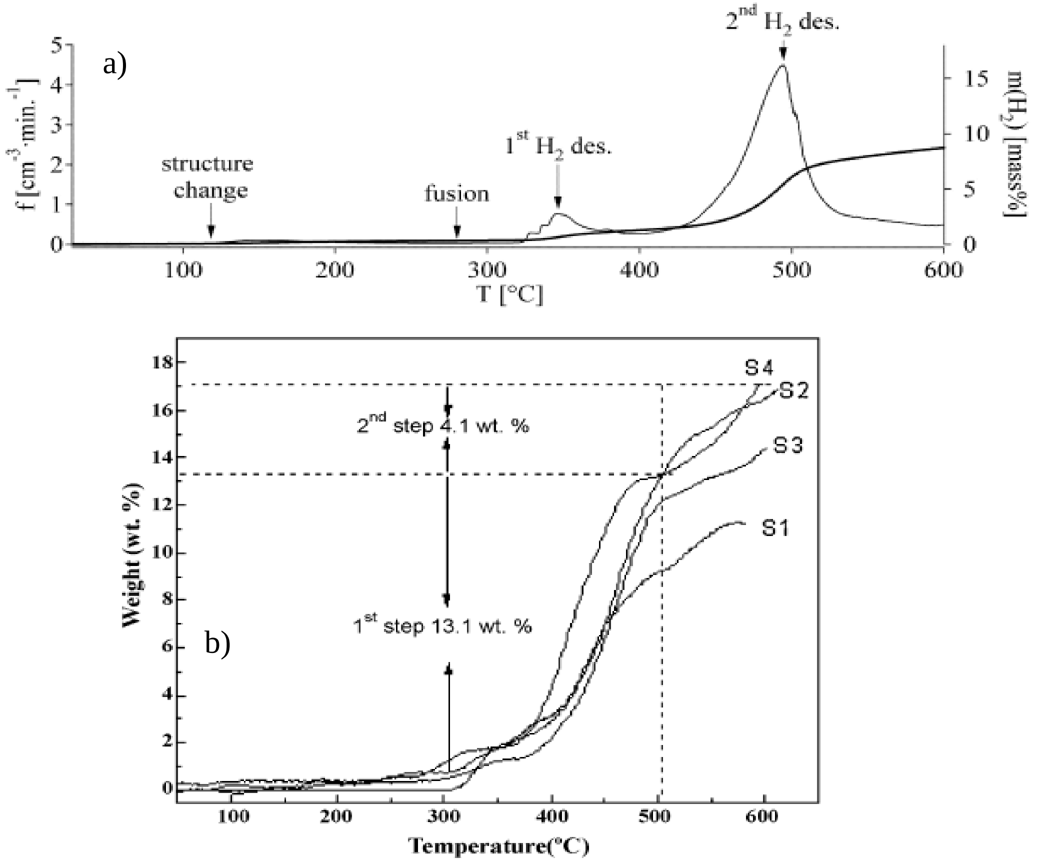

Fig. 1-7 a) Thermal desorption spectra of $LiBH_4$ with the heating rate of 2 K°min^{-1} [54] b) hydrogen desorption curves of $LiBH_4$ (S1) and $LiBH_4$-Ni with the mole ratio of 2:1 (S2), 4-1 (S3) and 6:1 (S4) [24].

1.7.1.2. Sodium borohydride ($NaBH_4$)

Sodium borohydride has recently become a new center of interest as a possible hydrogen source, as a result of its large theoretical gravimetric hydrogen capacity (10.6 wt. %). In the past twenty years, many efforts have been directed toward the application of $NaBH_4$. Unfortunately, dehydrogenation of this pristine borohydride is not easy due to its relatively high enthalpy change for dehydrogenation. Drozd et al. [26] investigated an $NaBH_4$-$Mg(OH)_2$ composite in a 1:2 mass ratio during ball milling and reported that the release of hydrogen upon heating is a result of an exothermic reaction. Varin et al.[27] studied the $NaBH_4$+$2Mg(OH)_2$ system in more detail without and with a nanometric nickel additive. They reported that H_2 desorption started at 240 °C. They estimated that the apparent activation energy was about 152-157 kJ/mol. Finally, they pointed out that, based on their results, the nano-Ni additive may not be the optimal catalyst for this system. Stasinevich and Egorenko [28] investigated the thermal hydrogen desorption from $NaBH_4$ under various hydrogen pressures, in order to clarify the thermodynamics of reactions. They observed that, for the range of hydrogen pressure (1-10atm), the melting of the compound occurred at about 505°C, a temperature lower than that of the desorption reaction.

1.8. Synthesis of new borohydrides using mechano-chemical activation synthesis (MCAS)

The unfavorable thermodynamics of $LiBH_4$ and $NaBH_4$ can be overcome to some extent by converting them to other borohydrides with better thermodynamics. One group of hydrides of potential interest for solid state hydrogen storage is based on selected transition metal borohydrides. A preliminary assessment of their thermodynamic suitability for hydrogen storage from the viewpoint of dehydrogenation enthalpy change and resulting equilibrium temperature was reported by Nakamori et al. [29, 30]. They synthesized various metal borohydrides using the mechano-chemical activation synthesis (MCAS) which occurs during high energy ball milling of complex metal hydrides mixed with appropriate metal di-or tri-chlorides, MCl_n, In essence, this is a "metathesis" reaction in solid state instead of the one which uses diethyl ether as a solvent [7, 15]. If a complex metal borohydride $LiBH_4$, which by itself is unsuitable for solid state hydrogen storage [7, 15], is ball milled with a metal (M) chloride, MCl_n, the following general "metathesis" reaction occurs during the milling:

$$nLiBH_4 + MCl_n \rightarrow M(BH_4)_n + nLiCl \qquad (1.5)$$

where M is Cr, Mg, Mn, Zr, Ti, V, Zn, Ca, Sc, or Al [31, 32].

Nakamori et al. [29, 30] also reported that the hydrogen desorption temperature (T_d) of $M(BH_4)_n$, decreases with increasing values of the Pauling electronegativity, χ_P, of metal M in borohydride. They noted that the desorbed gas for M= Ca, Sc, Ti, V and Cr ($\chi_P \leq 1.5$) was hydrogen only, while that for M= Mn, Zn and Al ($\chi_P \geq 1.5$) contained a mix of diborane gas (B_2H_6) and hydrogen.

1.8.1 Synthesis of manganese borohydride $Mn(BH_4)_2$ using $LiBH_4$ and $MnCl_2$

A metal borohydride potentially of interest for solid state hydrogen storage is $Mn(BH_4)_2$, which can be synthesized by (MCAS) during ball milling similarly to reaction (1.5) by following metathesis reaction

$$MnCl_2 + nLiBH_4 \rightarrow Mn(BH_4)_2 + 2LiCl + (n-2)LiBH_4 \qquad (1.6)$$

However, the presence of LiCl, which is always formed as a "dead weight salt" by-product, and retained $LiBH_4$ (if n>2) lessens the quantity of the available capacity of H_2 in the product. The capacity of hydrogen in the case of n=2 (no retained $LiBH_4$) is 4.76 wt% H_2, and would be even less in the case of n>2.

It has been proposed [5-11, 31] that the nanocomposite ($Mn(BH_4)_2$+2LiCl) synthesized in reaction (1.6) in a case of n=2 decomposes with a release of H_2 according to reaction (1.7).

$$Mn(BH_4)_2+2LiCl \rightarrow Mn+B+4H_2+[2LiCl] \qquad (1.7)$$

As mentioned, the maximum theoretical capacity of reaction (1.7) is 4.76 wt.% H_2.

However, the release of diborane gas (B_2H_6) in a mixture with H_2 was reported [9, 10, 14] and was observed using combined gas mass spectrometry (MS) and thermogravimetric analysis (TGA)

To date, several studies have focused mainly on the synthesis of an $Mn(BH_4)_2$•LiCl composite [32-36] using MCAS. The release of B_2H_6 simultaneously with hydrogen upon decomposition is the main disadvantage of $Mn(BH_4)_2$ [36, 37]. This release of B_2H_6 is not acceptable because it reduces the purity of the evolved hydrogen and results in a loss of boron, which in turn reduces the reversible formation of borohydrides in the succeeding rehydrogenation [37]. Previous studies have not identified an efficient way to completely suppress B_2H_6 formation during the decomposition process. Varin et al. [36] reported that the intensity of the corresponding peak of H_2 released using gas mass spectrometry was 200-600 times bigger than the one for B_2H_6 gas for $Mn(BH_4)_2$. Song et al. [37] studied the release of B_2H_6 from $Mn(BH_4)_2$ that had been synthesized through the MCAS of MnF_2 and $LiBH_4$. They suggested that adding $LiNH_2$ could suppress the release of B_2H_6, and no trace of B_2H_6 was observed when the $LiNH_2$ reached 5 wt.%. They also reported a significant decrease in the decomposition temperature of $Mn(BH_4)_2$ in which 5wt.% $LiNH_2$ reduced the decomposition temperature from 138 ºC for an undoped sample to 111 ºC for one with 5wt.% $LiNH_2$. However, they mentioned that using $LiNH_2$ did not improve the kinetic of dehydrogenation in $Mn(BH_4)_2$/LiF composites.

The possible kinetic acceleration of $Mn(BH_4)_2$ dehydrogenation using additives during MCAS and thermal dehydrogenation also has not been investigated. In addition, no research to date has studied the possibility of removing LiCl from the composite of $Mn(BH_4)_2$•LiCl synthesized by MCAS. A search of the literature reveals only a few studies have investigating the synthesis of different hydrides free of salt using solvent-mediated synthesis (wet) method. $Mg(ALH_4)_2$ was obtained based on the metathesis reaction of $NaAlH_4$ and $MgCl_2$ in diethyl ether (Et_2O) and subsequent purification using Soxhlet extraction [38]. Using the same method, $Eu(BH_4)_2$ and $Sm(BH_4)_2$ free from solvent (dimethyl sulfide) and LiCl were also achieved [39]. Pure $Mg(BH_4)_2$ was obtained using the reaction of Et_3NBH_3 and MgH_2 [40]. The reaction of $MnCl_2$ with $M(BH_4)_2$ ($M=Li^+$, Na^+, K^+) in Et_2O was also studied in [41]. Richter et al. successfully synthesized solvent-free $Mn(BH_4)_2$ through the reaction of $MnCl_2$ with $LiBH_4$ in a toluene/dimethylsulfide mixture at RT. However, they could not extract pure $Mn(BH_4)_2$ using THF as a solvent because THF removal needs a high temperature, which causes the borohydride to decompose [42]. The First attempt to remove salt from the product of MCAS has been done by Mamatha et al. [43], who investigated removing the NaCl from a $Mg(AlH_4)_2$+2NaCl mixture and the LiCl from a $Ca(AlH_4)_2$-2LiCl mixture, in both cases by using Et_2O and THF in a Soxhlet apparatus. They also claimed that complex removal of THF could not be achieved. The results reported in the literature in these publications will be discussed thoroughly later on together with the results obtained in the present work.

1.8.2 Synthesis of Iron borohydride $Fe(BH_4)_2$ using $LiBH_4$ and $FeCl_2$

A number of other potential market applications exist for simple H_2 generation systems rather than “on board” reversible storage systems, and some of them could be even recharged “off board”, supplying H_2 at ambient and slightly elevated temperatures, in the commercial, non-automotive sectors of the economy. For example, they could be utilized to supply fuel cells in such applications as stationary auxiliary power systems, portable electronic devices, off-road vehicles, lawn mowers, auxiliary devices in air transportation, coastal and international shipping, bulk hydrogen storage and many others. In the course of our experimental work on fast hydrogen-generating hydride systems, I noticed a high proclivity of the ($LiBH_4$-$FeCl_2$) hydride/halide system to rapidly generate H_2 during ball milling at ambient temperature, without any external heating. The literature on this particular hydride/halide system is very scarce. In the past 60 years, only three papers have been published [44-46] on the ($LiBH_4$-$FeCl_2$) system in which the authors investigated reactions occurring between $LiBH_4$ and the transition metal chlorides $NiCl_2$, $CoCl_2$ and $FeCl_2$. Nearly 60 years ago, Schaeffer et al. reported, for the first time, the formation of $Fe(BH_4)_2$ in a solvent (wet) reaction in diethyl ether between $LiBH_4$ and $FeCl_3$ (not with $FeCl_2$ as in the present work). They observed that the newly formed hydride, accompanied by LiCl, rapidly decomposed, releasing mainly hydrogen. They also noticed that the color of the extracted residue changed from white for an original mixture of $Fe(BH_4)_2$ and LiCl, into a black, highly pyrophoric substance after the decomposition and release of hydrogen.

More recently, Myakishev and Volkov [44] employed (MCAS) in a solid state during ball milling for the mixture of $LiBH_4$ and anhydrous chlorides such as $FeCl_2$, $NiCl_2$ and $CoCl_2$ as reactants. Ball milling was carried out at room temperature in a vibratory vacuum ball mill. After milling with $FeCl_2$, they reported that iron borohydride, $Fe(BH_4)_2$ was synthesized through the following reaction:

$$LiBH_4+0.5FeCl_2 \rightarrow 0.5Fe(BH_4)_2+LiCl \quad (1.9)$$

It was simultaneously decomposing during ball milling without any trace of diborane gas (B_2H_6) according to:

$$0.5Fe(BH_4)_2+LiCl \rightarrow 0.5Fe+B+[LiCl]+2H_2 \quad (1.10)$$

where the brackets for [LiCl] mean that LiCl takes no part in the decomposition reaction, acting only as a “dead-weight” by-product. Thus, the total reaction during the synthesis and simultaneous decomposition of $Fe(BH_4)_2$ is a combination of Eqs. (1.9) and (1.10). The maximum theoretical hydrogen capacity of the combined reaction is 4.73 wt.% with respect to the total molar mass of both reactants in Eq. (1.9) (remembering that LiCl is a “dead weight” product that reduces the total H_2 capacity). The theoretical gravimetric H_2

capacity of pure $Fe(BH_4)_2$ is a whopping 9.43 wt.%. Very recently, Zhang and Liu [46] investigated the effect of metal chlorides such as $CoCl_2$, $NiCl_2$ and $FeCl_2$ on the dehydrogenation behavior of $LiBH_4$. They reported the formation of metal borides Co_2B and Ni_4B_3 after dehydrogenation with $CoCl_2$ and $NiCl_2$ but did not report the formation of any specific boride for the $FeCl_2$ additive. Only the desorption of H_2 gas, without a trace of B_2H_6, was observed after dehydrogenation of the ($LiBH_4$-$FeCl_2$) system. They suggested that the thermal destabilization of $LiBH_4$ in a mixture with the investigated metal chlorides was due to the formation and rapid decomposition of the respective complex metal borohydrides, although no further details were presented and discussed. No attempts whatsoever were made in refs. [44, 46] to quantify the mechanical dehydrogenation process although the authors used ball milling for the synthesis.

1.8.3 Synthesis of titanium borohydride using $LiBH_4$ and titanium florides (TiF_3)

Titanium borohydride, $Ti(BH_4)_3$ has an excellent theoretical gravimetric H_2 capacity of 13.1 wt.% (molar mass 92.39 g/mol). It was first time synthesized by Hoekstra and Katz [47] using such reactants as lithium borohydride ($LiBH_4$) and titanium tetrachloride ($TiCl_4$) at a low temperature of -45°C under vacuum. The obtained product was a green solid with a calculated empirical formula of $Ti_{1.00}B_{2.96}H_{12.00}$ ($Ti(BH_4)_3$). Interestingly, the authors reported a release of diborane, B_2H_6, gas during the synthesis reaction. The successful synthesis of $Ti(BH_4)_3$ was of a great importance because, for the first time, $Ti(BH_4)_3$ was shown to be able to exist as a solid material at low temperatures and to quickly decompose at close to room temperature. Jensen et al. [48] synthesized the diadducts $Ti(BH_4)_3(PMe_3)_2$ and $Ti(BH_4)_3(PEt_3)_2$ by the reaction of trialkylphosphines with thermally unstable $Ti(BH_4)_3 \bullet Et_2O$, which was prepared in diethyl ether (Et_2O) from the $LiBH_4$ and $TiCl_4$ reactants. These complexes were stable at room temperature for a few days. The authors managed to obtain the XRD data for the $Ti(BH_4)_3(PMe_3)_2$ adduct: monoclinic, space group *Pnma*, a=10.757(1), b=11.145(2) and c=14.270(3) Å, and a density of 0.950 g/cm^3. From the obtained density and molar mass of 92.39 g/mol, one can roughly estimate the volumetric H_2 capacity of $Ti(BH_4)_3$ as being equal to about 124 kgH_2/m^3, which is a very high volumetric capacity indeed. More recently, Soloveichik reported [49] the synthesis of $Ti(BH_4)_3$ by the reaction of $LiBH_4$ with $TiCl_4$ or $TiCl_3$ and isolation by low temperature vacuum sublimation. He also mentioned that Ti fluoride salts did not react, which was erroneous as will be shown later. The synthesized $Ti(BH_4)_3$ was a white volatile solid. Electron diffraction in the gas phase showed a monomer molecule with tridentate BH_4^- groups. The hydride was thermally unstable and decomposed to TiB_2, H_2, and B_2H_6 at 20°C [49].

A few authors added a small amount of halides such as $TiCl_3$ and TiF_3 to $LiBH_4$ [50-53] with the aim of destabilizing $LiBH_4$ and reduce its high dehydrogenation temperature [54]. It has been observed that TiF_3 reduced the onset of dehydrogenation temperature of the investigated systems. The literature on this particular hydride system is very scare. Only two papers have been published [55, 56] on the ($LiBH_4$-TiF_3) system, a paper [52] on the ($LiBH_4$-TiF_3-SiO_2) and one [57] on the ($LiBH_4$-TiF_3-Fe_2O_3) system which will be discussed thoroughly later on together with the obtained results of the present work.

Apparently, data and their interpretation reported in the available literature on the ($3LiBH_4+TiF_3$) system are at least unclear and on occasion quite contradictory. Furthermore, no behavior of the ($3LiBH_4+TiF_3$) mixture during ball milling, e.g. the phenomenon of mechanical dehydrogenation [15, 58], has ever been investigated as a function of the milling energy input (kJ/g).

1.8.4 Synthesis of titanium borohydride using $LiBH_4$ and titanium chlorides ($TiCl_2$ and $TiCl_3$)

As mentioned, high enthalpy changes during the dehydrogenation of $LiBH_4$ results in dehydrogenation temperatures in excess of around 400 ºC. Reducing either the dehydriding temperature or improving the kinetic of dehydrogenation of $LiBH_4$ by mixing it with different additives that act as catalysts has received considerable critical attention since relatively large quantities of H_2 can be generated “on demand”. Some authors have investigated the destabilization of $LiBH_4$ by adding small amounts of transition metal halides such as $TiCl_3$, TiF_3 and $CoCl_2$ to $LiBH_4$ [46, 50, 54, 55, 59-67]. Zuttel et al., for example, reported that the addition of SiO_2 to $LiBH_4$ caused the initial dehyrding temperature to drop from 400 to 200 ºC [54, 63]. Jin et al. [59] studied the hydrogen desorption and absorption properties of two destabilized systems $6LiBH_4+CeH_2/CaH_2+0.2TiCl_3$. Pinkerton et al. [64] employed $NiCl_2$ or $FeCl_2$, and Tang et al. added $CoCl_2$ [61] as the catalysts for the ($2LiNH_2$+$LiBH_4$) hydrogen storage system. Vajo et al. [62] modified the thermodynamics of a ($LiBH_4$+MgH_2) system with 2-3 mol % of $TiCl_3$ used as a catalyst. Zhang et al. reported that $LiBH_4$ was significantly destabilized by the addition of $FeCl_2$, $CoCl_2$ and $NiCl_2$, resulting in major hydrogen desorption at temperature between 230 ºC and 300 ºC [46]. Sun et al. investigated the effect of Mg_3La and $TiCl_3$ on $LiBH_4$ and showed that the addition of $TiCl_3$ can improve the dehydrogenation performance of the powder mixture [60]. Au et al. reported that doping of $LiBH_4$ with some metal halides made $LiBH_4$ very unstable, releasing H_2 even at 60 ºC. They demonstrated that ($LiBH_4$+0.2$MgCl_2$)+0.1$TiCl_3$ was the most affective material, among others tried, and starts desorbing 5wt.% of H_2 at 60 ºC [50]. In an examination of the effects of three different Ti-based additives ($TiCl_3$, TiF_3 and TiO_2) on the dehydrogenation temperature of the $LiBH_4$/CaH_2 systems, Yang et al. found that $TiCl_3$ lowers the hydrogen desorption temperature more than the others, and that the higher the level of $TiCl_3$, the lower the dehydrogenation temperature [67]. In exploring the hydrogen-storage properties of the mixed complex hydride $LiBH_4$-$NaAlH_4$ system, Shi et al. [66] experimented both with and without a doping $TiCl_3$ additive. The doped system showed a significantly lower temperature for hydrogen release than the undoped system did. Dehydrogenation of the milled $LiBH_4$/CaH_2/$TiCl_3$ was investigated by Liu et al. [65]. They showed that adding $TiCl_3$ significantly lowers the reaction temperature of $6LiBH_4$/CaH_2/x$TiCl_3$ by around 40 ºC, especially at higher concentrations (they added $TiCl_3$ to the system by the x= 0.00 to 0.25). Fang et al. showed that thermodynamically stable $LiBH_4$ can be effectively destabilized by milling with TiF_3 in a 3:1 molar ratio in which samples could rapidly release over 5 wt.% H_2 at 70 to 90 ºC [55]. In general, if $TiCl_3$ is replaced with MCl_n in reaction (1.5), it has been proposed that $Ti(BH_4)_3$ may also be generated, as an intermediate compound through an ion-exchange reaction between $LiBH_4$ and $TiCl_3$, resulting in LiCl and $Ti(BH_4)_3$, which can occur according to the following reaction [60, 65, 68]:

$$3LiBH_4+TiCl_3 \rightarrow Ti(BH_4)_3+3LiCl \qquad (1.11)$$

All previous studies have mentioned that $Ti(BH_4)_3$ decomposes very fast due to its unstable structure under the ambient environment, which is why no one have been able to provide evidence in support of $Ti(BH_4)_3$'s existence after MCAS. The results presented in these publications will be discussed and compared with the results of my work.

2. Objectives

There is number of other potential market applications for H_2 generation systems, rather than reversible storage, at ambient and slightly elevated temperatures, for which “on board” rehydrogenation is not critical. For example, those solid state H_2 systems can utilize disposable H_2 cartridges of various sizes which could be regenerated “off board” after usage. As pointed out in the recent review, those novel solid state hydrogen generation systems could be utilized in various capacities in such applications as, for example, stationary auxiliary power systems, off-road vehicles (forklifts, street sweepers etc.), locomotives, submarines, coastal and international shipping, auxiliary devices in air transportation, lawn mowers, disposable cartridges for long duration, low power military devices (e.g. WFC20 soldier power system: [69], portable electronic devices, bulk hydrogen storage and many others. The objective of the proposed work is now focused on studying and finding suitable borohydride systems which provide for high theoretical hydrogen capacity irreversible hydride systems for relatively fast hydrogen generation “on demand” either under mechanical or thermal energy input which could be synthesized in solid state by mechano-chemical activation synthesis (MCAS). To accomplish this objective, MCAS has been applied for the synthesis of the following metal-non-metal complex hydrides: $Mn(BH_4)_2$ (theoretical H_2 capacity 9.5 wt.%), $Fe(BH_4)_2$ (theoretical H_2 capacity 9.4 wt.%) and $Ti(BH_4)_2/Ti(BH_4)_3$ (theoretical H_2 capacity 13.1 and 10.4 wt.%, respectively) using either $LiBH_4$ as precursors and suitable metal chlorides as reactants as listed and explained for each system below. Their microstructure and hydrogen storage properties have been investigated.

2.1 Nanostructured $LiBH_4$-$MnCl_2$

This study investigated the effect of the total energy input injected into the initial ($MnCl_2$+n$LiBH_4$) mixture for only two molar ratios, n = 2 and 3, on the microstructural evolution and resulting mechanical and thermal dehydrogenation properties of the synthesized $Mn(BH_4)_2$/LiCl (n=2) or $Mn(BH_4)_2$/LiCl/$LiBH_4$ (n=3) systems.

To gain a deep insight into the nano-scale of the product, the microstructure was investigated by transmission electron microscopy (TEM). Selected area diffraction pattern (SADP) is a useful method for gaining a better understanding of phase transformations that occur during processing.

As mentioned before, the release of B_2H_6 during decomposition of $Mn(BH_4)_2$ is not acceptable due to the decreasing purity of the evolved hydrogen and resulting loss of boron, which in turn reduces the reversible formation of borohydrides in the succeeding rehydrogenation [37]. The effects of Ni, graphene and $LiNH_2$ addition on suppressing the formation of B_2H_6 during decomposition of $Mn(BH_4)_2$ as well as the effects of additives on the kinetic acceleration of the dehydrogenation of $Mn(BH_4)_2$ during milling and thermal dehydrogenation are also studied.

Finally, a simplified technique for removing LiCl, which is a salt (deadweight) in the product of MCAS powder ($Mn(BH_4)_2 \bullet LiCl$), is developed in order to increase the quantity of hydrogen released from the product.

2.2 *Nanostructured $LiBH_4$-$FeCl_2$*

In the course of my experimental work on fast hydrogen-generating hydride systems, I noticed a high proclivity of the ($LiBH_4$-$FeCl_2$) hydride/halide system to rapidly generate H_2 during ball milling at ambient temperature, without any external heating. The major scientific objective of this work is to investigate and understand in more detail the H_2 generation behavior from the $LiBH_4$ and $FeCl_2$ system in a 2:1 stoichiometric ratio (equivalent to 1:0.5) during ball milling with varying milling energy inputs.

2.3 *Nanostructured $LiBH_4$-TiF_3*

In view of the number of discrepancies in the published data and the overall scarcity of published papers on the ($3LiBH_4+TiF_3$) system, the major scientific objective of this work is to investigate and understand in more detail the H_2 generation behavior from the $LiBH_4$ and TiF_3 system in a 3:1 stoichiometric ratio during ball milling with varying milling energy inputs and during subsequent thermolysis. In addition, we are investigating the effect of potential catalytic additives such as ultrafine filamentary nickel (Ni) which, in its submicrometric and nanometric form, has been found to be a very effective catalyst for metal and complex hydride systems [7, 15, 58] and graphene which was recently investigated as an additive for improving sorption behavior of $LiBH_4$ [70]. The ($3LiBH_4+TiF_3$) system is quite attractive as a potential efficient hydrogen generator at low temperatures and deserves a full understanding.

2.4 *Nanostructured $LiBH_4$-$TiCl_2$/$TiCl_3$*

No previous studies have reported the dehydrogenation during milling (mechanical dehydrogenation) of ($LiBH_4$-$TiCl_3$) powder mixtures, nor has the addition of $TiCl_2$ to $LiBH_4$ been investigated in the literature. To address these omissions, this chapter of my thesis attempts to show and compare the hydrogen-generation behavior from the mixtures ($LiBH_4$-$TiCl_2$) and ($LiBH_4$-$TiCl_3$) during milling with varying milling energy inputs. It also provides microstructural evaluation of the synthesized and dehydrogenated powders.

3. Experimental

3.1 Materials

The as-received materials used in this work are listed in the Table 3.1.

Table. 3-1. Chemical hydrides and additives materials used in this work.

Material	**Purity (%)**	**Provider**
$LiBH_4$	95	Alfa Aesar
TiF_3	98	Alfa Aesar
$TiCl_3$	78.5	Alfa Aesar
$TiCl_2$	99.98	Sigma aldrich
$FeCl_2$	99.5	Alfa Aesar
$MnCl_2$	99.99	Alfa Aesar
Ultrafine filamentary carbonyl nickel (Ni)	99	Cnem
Graphene oxide platelets (flakes) (FL-RGO), referred to as “graphene”	contains ~9.6 wt.% % of oxygen and ~1 wt.% H_2	Nanomaterials (http://www.nanomaterials.pl)
$LiNH_2$	95	Sigma aldrich
Et_2O	99.0	Sigma aldrich

3.2. Chemical compositions

Table. 3.2 listed the starting materials compositions for synthesising composites.

Table. 0-2. Chemical compositions of the studied systems

System	**n**	**Additive**
n$LiBH_4$+$MnCl_2$	2, 3	---
n$LiBH_4$+$MnCl_2$	2	5wt.% Ni, graphene and $LiNH_2$
n$LiBH_4$+$FeCl_2$	2	---
n$LiBH_4$+TiF_3	3	---
n$LiBH_4$+TiF_3	3	5wt.% Ni, graphene and $LiNH_2$
n$LiBH_4$+$TiCl_3$	3	---
n$LiBH_4$+$TiCl_2$	2	---

3.3. Milling procedure

Mechano-chemical activation synthesis (MCAS) of mixtures was carried out for different milling times in ultra-high purity hydrogen gas atmosphere (purity 99.999%: O_2< 2 ppm; H_2O< 3 ppm; CO_2< 1 ppm; N_2< 6 ppm; CO<1 ppm; THC<1 ppm) at ~300 kPa pressure in the magneto-mill Uni-Ball-Mill 5 manufactured by A.O.C. Scientific Engineering Pty Ltd, Australia [71-73]. The milling was carried out under a strong impact mode (IMP68) with two magnets positioned at 6 and 8 o'clock, at the distance from the vial of ~10 and ~2 mm, respectively, as shown in Figure 3.1. The ball-to-powder weight ratio (R) with 4 steel balls was 132 and the rotational speed of milling vial was ~200 rpm. In the magneto-ball mill Uni-Ball-Mill 5, the milling energy can be controlled by changing the angular positions of one or two strong NdFeB magnets and changing the number of hard steel balls (mass 65 g and 25 mm in diameter each) in a milling vial [7, 71-73]. In a recent Ref. [74] a semi-empirical method of calculating milling energy in the magneto-ball mill Uni-Ball-Mill 5 was reported, in particular, the quantity of milling energy, $Q_{TR(R)}$ per unit mass•hour (kJ/gh) which is injected into and stored in a milled powder for each particular milling mode with a fixed ball-to-powder mass ratio, R. For the milling mode IMP68-4B-R132 which was applied in the present work, the injected energy per hour is Q_{TR132}=72.8 kJ/gh (Table 5 in Ref. [74]). Then the total milling energy input, Q_{TR} (kJ/g), can be calculated. Table 3.3 shows the total milling energy input, Q_{TR} (kJ/g), applied for different systems used in my work.

After loading with powder, an air-tight milling vial with an O-ring, equipped with a pressure valve mounted in the lid, was always first evacuated and then purged several times with ultra-high purity argon (Ar) gas (99.999% purity) before final pressurization with H_2. During milling the vial was continuously cooled by an air fan and the milling process. The release of hydrogen during ball milling was monitored and estimated from the pressure increase in the milling vial measured by a pressure gage using an ideal gas law [7] and expressed in wt.% with respect to the total weight of powder sample with the accuracy ±0.1 wt.% H_2.

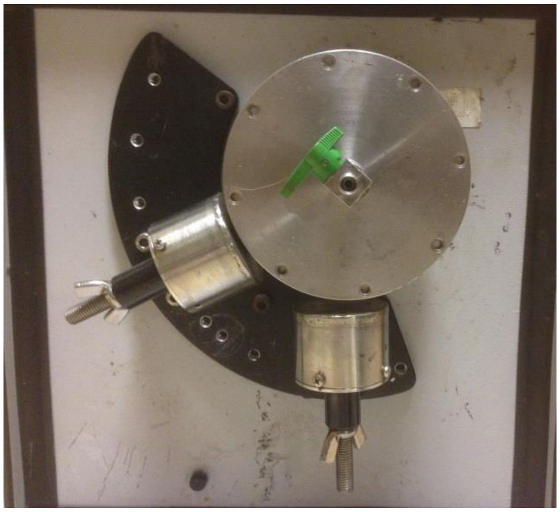

Fig. 3-1 An optical photo showing the angular position of magnets at 6 and 8 o'clock (IMP 68) for ball milling in the Uni-Ball-Mill 5.

The powder samples were handled in a glove box containing a moisture-absorbing Drierite granulated compound. Before handling, the glove box was purged a few times with high purity argon gas (99.999% purity) in order to minimize any possible contamination by moisture or oxygen from air.

Table. 3-3. The total milling energy input, Q_{TR} (kJ/g), applied for the studied systems

System	**Time of milling (min)**	**milling energy input, Q_{TR} (kJ/g)**
($2LiBH_4$+$MnCl_2$)	30, 120, 300	36.4, 145.6, 364
($3LiBH_4$+$MnCl_2$)	30, 120, 300	36.4, 145.6, 364
($2LiBH_4$+$MnCl_2$)+ 5wt.% Ni/ graphene/ $LiNH_2$	60	72.8
($2LiBH_4$+$MnCl_2$) prepared for solvent extraction	60	72.8
($2LiBH_4$+$FeCl_2$)	2, 5, 15, 30	2.43, 6.07, 18.2, 36.4
($3LiBH_4$+TiF_3)	60, 300	72.8, 364
($3LiBH_4$+TiF_3) + 5wt.% Ni/ graphene	60, 300	72.8, 364
($2LiBH_4$+$TiCl_2$)	30, 60	36.4, 72.8
($3LiBH_4$+$TiCl_3$)	30, 60	36.4, 72.8

3.4. Solvent extraction procedure

Figure 3.2 shows a schematic of solvent extraction performed in this work. The ball milled $2LiBH_4$+$MnCl_2$ powder was mixed with diethyl ether (Et_2O) with the mass ratio of 1:4 and subsequently stirred for 2h at room temperature (RT) with a rotational speed of 225 rpm in order to dissolve the newly formed $Mn(BH_4)_2$ in the Et_2O solvent and separate it from salt (LiCl and NaCl). The suspension after stirring was injected into a 60 ml syringe and filtered with a 0.2µm syringe filter. The filtering was done to collect salt at the filter and allow suspended $Mn(BH_4)_2$ to pass through the filter. In order to extract $Mn(BH_4)_2$ from the suspension in Et_2O, an evaporation process was carried out on the suspension after filtering, at room temperature and also on a hot plate at different temperatures of 32 °C, 42 °C and 52 °C, accompanied by simultaneous vigorous stirring at 1000 rpm to agitate the solution. The dry powder product after evaporation at this stage is refereed to hereafter as 1st Ext, with additional notation to note the different temperatures used (e.g., 1st EXT at 42 °C). After characterization and thermally evaluation of the product, the powder left after the 1st extractions at different temperatures was mixed with di ethyl ether again with the same mass ratio (1:4), stirred for the same time and, finally filtered for the second time. Similarly, the suspension after the 2nd extraction was kept at different temperatures for evaporation. The dry powder after this process is hereafter referred to as 2nd EXT, with an additional notation for the different temperatures used (e.g., 2nd EXT at 42 °C). The solvent extraction procedure was also carried out in the glove box, which was first purged and subsequently filled with high-purity argon gas (99.999% purity). It is worth to note that Et_2O was employed as a solvent because LiCl is poorly soluble in Et_2O while $Mn(BH_4)_2$ is efficiently soluble in this solvent [41].

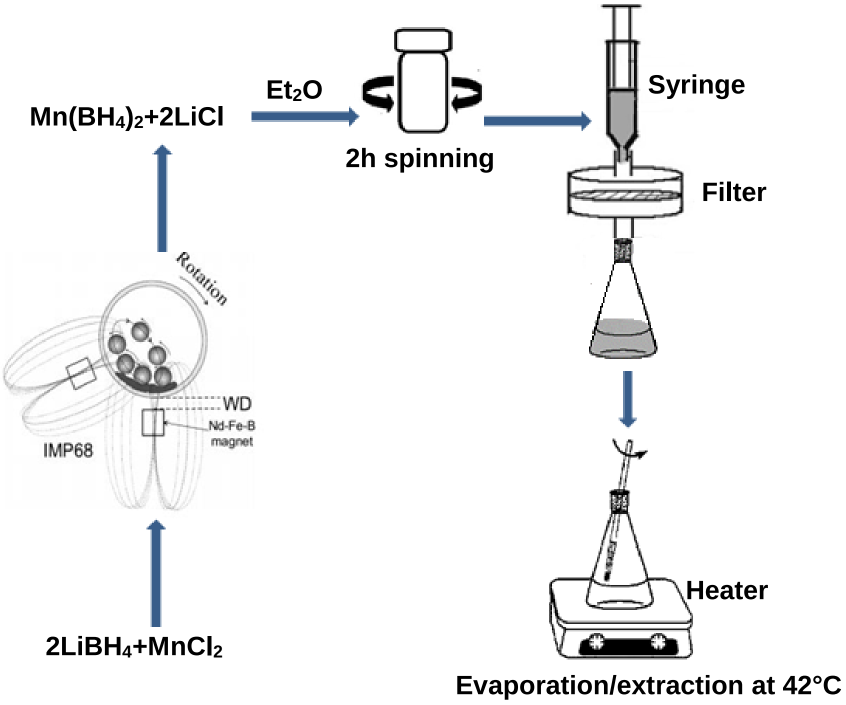

Fig. 3-2 A schematic explaining the solvent extraction methodology employed in the present work used for a separation of $Mn(BH_4)_2$ from the mixture with LiCl (Adapted from [75]).

3.5 Hydrogen storage properties

The hydrogen thermal desorption/absorption was evaluated by means of a second generation volumetric Sieverts-type apparatus custom-built by A.O.C. Scientific Engineering Pty Ltd., Australia [76]. This apparatus, built entirely of austenitic stainless steel, allows loading of a powder sample into a stainless steel reactor in a glove box under high purity argon and its subsequent transfer to the main unit in a sealed reactor without any exposure to the environment. Approximately 30-40 mg sample was used in a desorption test. Before starting the desorption test, the inner tubing of the apparatus was evacuated and purged four times with hydrogen. The furnace of the apparatus was heated separately to the desired test temperature and subsequently inserted onto a tightly sealed powder sample reactor inside which an atmospheric pressure of 1 bar H_2 was kept. The powder sample in the reactor reaches the furnace temperature in ~400s in the temperature range of 100-200 °C which is negligible compared to desorption completion time. Hence, the test can be considered as "isothermal". Desorption curves were corrected for the hydrogen gas expansion due to the increase in temperature. The amount of desorbed hydrogen was calculated from the ideal gas law as described in detail in [7] and expressed in wt.% with respect to the total weight of powder sample. The calibrated accuracy of desorbed hydrogen capacity is about ±0.1 wt.% H_2 and that of temperature reading and stabilization ±0.1 °C.

The apparent activation energy for volumetric hydrogen desorption was estimated using the registered dehydrogenation curves by applying a simple Arrhenius equation [7] following Sandrock et al. [77]

$$k = k_o e^{-E_A / RT} \tag{3.1}$$

where k is the rate of hydrogen desorption in convenient engineering terms of wt%H_2/h measured from the slope of the volumetric hydrogen desorption curves registered by the Sieverts-type apparatus (the selected linear portion of each pertinent dehydrogenation curve was fitted by a linear equation obtaining its slope) [78], E_A is the activation energy in kJ/mol, R is the gas constant (8.314472 J/mol K) and T is absolute temperature (K). The measured rates were plotted in the Arrhenius form as ln k vs. 1000/RT.

Characterization of the synthesised powder

3.6. X-Ray diffraction

A Bruker D8 X-ray diffractometer using a monochromated CuKα_1 radiation (λ= 0.15406 nm) with an accelerating voltage of 40 kV and a current of 30 mA was used for investigating phase transformation and the crystalline properties of powders. A custom made brass holder with Cu/glass plates and Kapton window transmittable to X-rays in the upper part of that was used to hold the sample in the X-ray machine.

The Williamson-Hall method [79] in the following form was used to evaluate the crystallite size of LiF and the lattice strain:

$$\beta \cos\theta = 0.9\lambda/D + 2A\varepsilon \sin\theta \qquad (3.2)$$

Where β is the full width at the half maximum intensity (FWHM) of a diffraction peak, θ is the Brag diffraction angle, λ is the wavelength, A is a constant = 1 and D and ε are the average crystallite size and lattice strain, respectively. The best fit line drowns of $\beta \cos\theta$ versus $2\sin\theta$ which were calculated for several peaks. The slope of $\beta \cos\theta$ vs. $2\sin\theta$ provided the average lattice strain while the average crystallite size was estimated from the intersection of this line at $\sin\theta = 0$.

3.7. Scanning electron microscopy (SEM)

A LEO 1550 high resolution, field emission scanning electron microscope (FESEM) employing a secondary electron mode (SE) with the accelerating voltage of 10 kV was used to asses the morphology of nanocomposite powder after MCAS. Samples were dispersed on a sticky carbon tape in an argon atmosphere glove box and then quickly transferred into the SEM sample holder.

The particle size of powders was estimated from the SEM micrographs using the ImageJ software by Softonic [80].

3.8. Differential scanning calorimetry (DSC)

The differential scanning calorimetry (DSC) analysis was conducted simultaneously with the thermogravimetric analysis (TGA) on a Setaram Sensys Evo 3d analyzer (France). The analyser was coupled with a quadrupole mass spectrometer Hiden Analytical (United Kingdom). Each powdered sample (~10-30 mg) was loaded into a alumina crucible of 100 µl volume and covered with alumina powder almost to the top of the crucible to prevent the oxidation and hydrolysis during the quick transfer to the analyzer and also to avoid a volatile foaming and flowing out of the crucible if the powder sample melted. After loading to the analyzer, each sample was flushed with high purity helium gas (<10 ppm O_2 and H_2O, BIP quality, Air Products) for 90 min and after that heating of sample was performed from 30 to 520°C with the rate of 5°C/min. Carrier helium gas flow was set to 28 ml/min. Hydrogen and diborane gas (B_2H_6) level was measured with the use of mass spectrometer by analyzing the intensity of ions with the m/z=2 (H_2), 27 (B_2H_6), 26 and 24 ratio. For the purpose of graph plotting the measured pressure of escaping gases was normalized by the mass of the powder sample.

3.9. Fourier transform infrared spectroscopy (FT-IR)

The Fourier transform infrared spectroscopy (FT-IR) measurements were performed with a Nicolet 6700 apparatus at room temperature in the wavenumber range 600-3500 cm^{-1} to examine the features of chemical bonding states of samples. The FT-IR apparatus was put in a glove bag and purged continuously with high purity (5N) nitrogen. The glove bag was opened and the glass vial containing a powder sample was inserted into a glove bag. After closing the glove bag the sample was dispersed onto the sample holder and inserted in the machine under nitrogen atmosphere. Subsequently, further measurements were carried out under the atmosphere of high purity (5N) nitrogen gas. The measurement was carried out in DRIFTS mode. The raw data, with automatic background subtraction, were plotted. The resolution was 4 cm^{-1} for all data and the units on the plots are Kubelka-Munk units.

3.10. Transmission electron microscopy (TEM)

Samples for high resolution transmission electron microscopy (HR TEM) were prepared by two different methods. The first one was a wet method where a proper solvent was required that allows for dispersing the agglomerates into individual powder particles by ultrasonication. The diethyl ether (Et_2O) solvent was adopted in this work which was already used for solvent (wet) chemical separation of complex alanate hydrides from salts [43]. The ball milled powder was dispersed in Et_2O and distributed on an amorphous carbon grid.

The second one was a dry method in which the dry powders were directly dispersed onto the amorphous carbon grids.

In both methods, preparations were done outside such that the samples were in air for a few minutes during the transfer to the microscope. Electron microscopy studies were performed with a HR TEM FEI Titan microscope at 300 kV (λ=0.0197 Å), equipped with a CEOS image corrector and an Oxford INCA X-sight EDS system and the energy filter

Gatan Tridiem GIF. Samples were imaged using a Gatan LN_2 holder which decreased the beam induced sample damage of the hydride powder. A fast Fourier transform (FFT) was used for obtaining digital selected-area electron diffraction patterns (SAEDPs) from the high resolution TEM micrographs by applying the ImageJ software [80]. The grain (crystallite) size of the $Mn(BH_4)_2$ and LiCl phases from the HR TEM images was estimated as the equivalent circle diameter, $ECD=(4A/\pi)^{1/2}$, where A represents the projected particle area which was measured using the ImageJ software [80]. The corrected sample standard deviation for an average ECD value was also calculated.

4. *Nanostructured $LiBH_4$-$MnCl_2$*

4.1 Microstructure of ball milled powders after MCAS

Figure 4.1 shows the SEM micrographs of the morphology of both as-received constituent powders, $LiBH_4$ (Fig 4.1a) and $MnCl_2$ (Fig 4.1b) which were used for preparing the ($nLiBH_4+MnCl_2$) mixtures (n=2 and 3) for MCAS by ball milling. The $LiBH_4$ particles are very coarse and chunky and their color is white. In contrast, the morphology of the as received $MnCl_2$ appears to be globular, resembling agglomerates of fibrous, thinner particles. The color of $MnCl_2$ is pink.

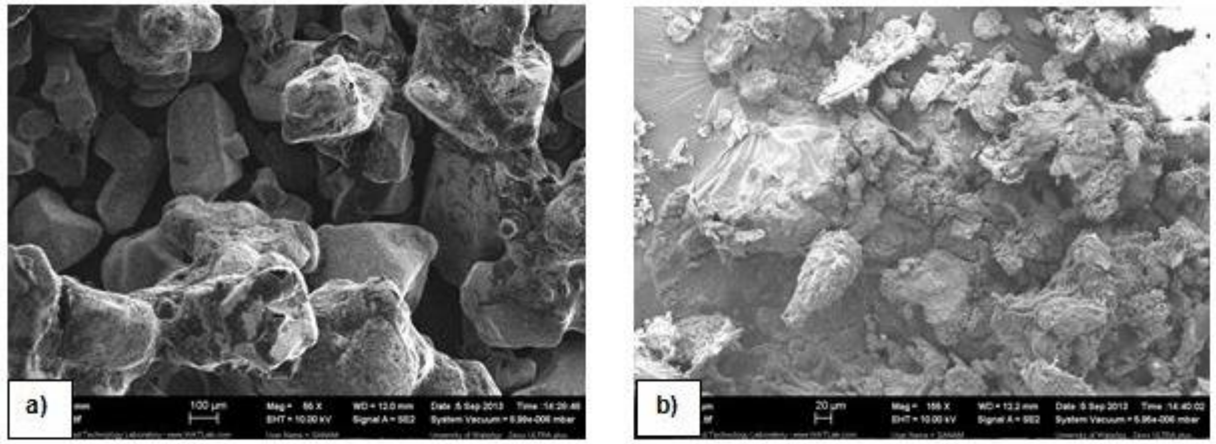

Fig. 4-1. Scanning electron micrographs of as received constituent powders (a) $LiBH_4$ and (b) $MnCl_2$ (Adapted from [81] .

Figure 4.2 shows the evolution of the powder morphology for a ($2LiBH_4+MnCl_2$) mixture (n=2), as a function of milling time, or alternatively, the total milling energy input, Q_{TR}, for 0.5h (Q_{TR}=36.4 kJ/g) (Fig 4.2a), 2h (Q_{TR}=145.6 kJ/g) (Fig.4.2b) and (c) 5h (Q_{TR}=364 kJ/g) (Fig 4.2c). It can be clearly seen that even after milling with only a small energy input in Figure 4.2a (Q_{TR}=36.4 kJ/g) the refinement of the initial powder mixture is quite dramatic especially by comparison with a huge size of the as-received $LiBH_4$ particulate in Figure 4.1a. The morphology of powder after milling with Q_{TR}=145.6 kJ/g (Fig 4.2b) seems to be thoroughly refined. However, milling with even higher Q_{TR}=364 kJ/g (Fig 4.2c) shows that a fraction of powder particles becomes severely agglomerated.

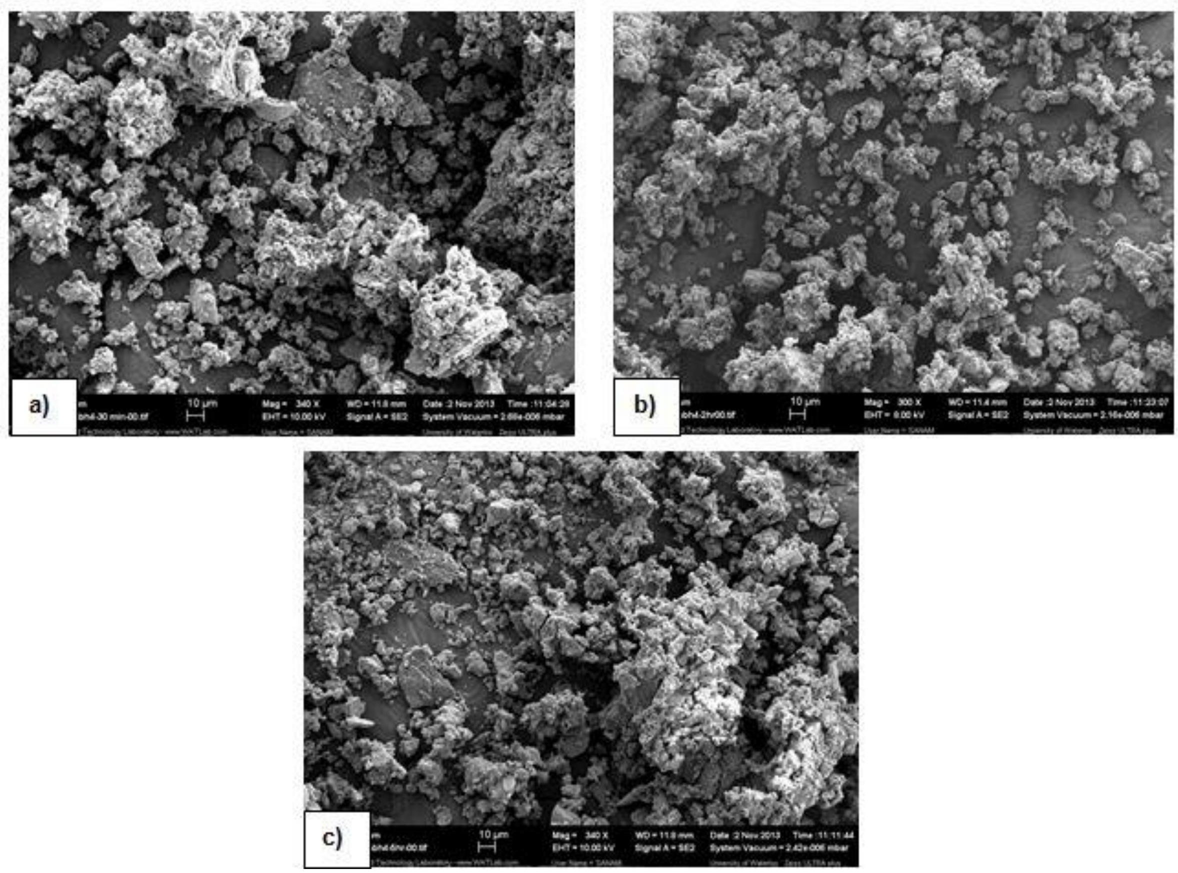

Fig. 4-2. Scanning electron micrographs of ball milled ($2LiBH_4+MnCl_2$) powders after MCAS for varying milling time or milling energy input. (a) 0.5h (Q_{TR}=36.4 kJ/g), (b) 2h (Q_{TR}=145.6 kJ/g) and (c) 5h (Q_{TR}=364 kJ/g) (Adapted from [81]).

Figure 4.3a shows the XRD patterns after ball milling (BM) with an energy input, Q_{TR}=145.6 kJ/g (2h), for the n = 2 and 3 mixtures. On the XRD pattern for the ball milled n=2 mixture after MCAS only the diffraction peaks of LiCl and $Mn(BH_4)_2$ are clearly seen. The identification of $Mn(BH_4)_2$ was based on data reported in [34, 82, 83] which show that it has a trigonal lattice structure (the space group $P3_112$) with the lattice parameters a=10.435(1) Å and c=10.835(2) Å. The pattern for the n=3 mixture is nearly identical to the n=2 with the exception that a remnant very weak and broad $LiBH_4$ peak is barely visible. The peaks of $Mn(BH_4)_2$ are broadened that confirm that the synthesized hydride is heavily nanostructured. Nearly identical XRD patterns are observed after milling with a much lower energy input, Q_{TR}=36.4 kJ/g (0.5h). It is quite remarkable that “metathesis” reaction (1.6) occurs at such a small input of milling energy Q_{TR}=36.4 kJ/g. It suggests that a thermodynamic barrier for “metathesis” reaction in a $LiBH_4/MnCl_2$ system is very low.

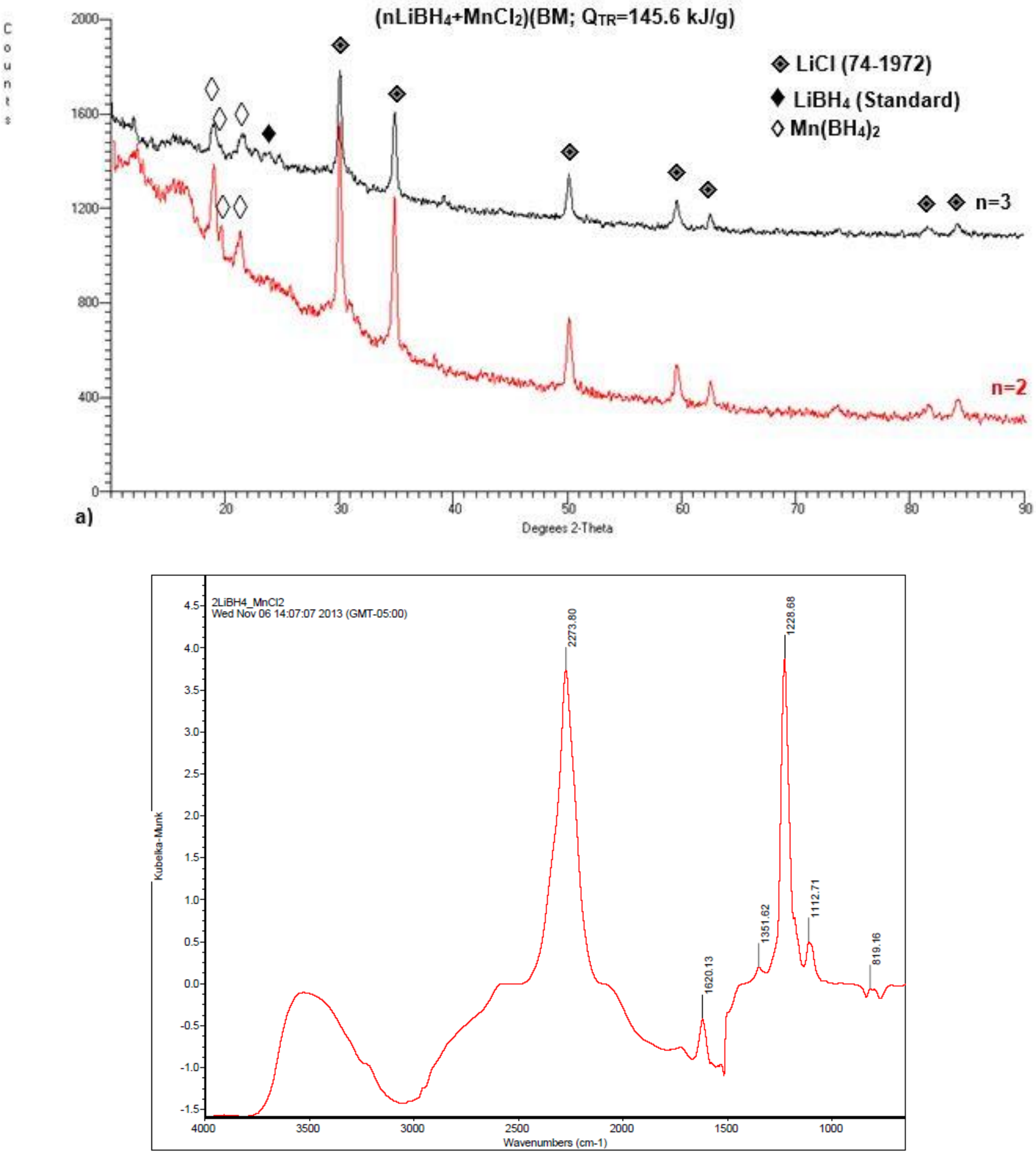

Fig. 4-3. (a) XRD patterns after ball milling (BM) with a low energy input, Q_{TR}=36.4 kJ/g, for the n=2 and 3 mixtures. (b) FT-IR spectrum for the n=2 mixture ball milled with a moderate energy input of Q_{TR}=145.6 kJ/g (Adapted from [81]).

Figure 4.3b shows the FT-IR spectrum for the n=2 mixture ball milled with an energy input of Q_{TR}=145.6 kJ/g which exactly correspond to Figure 4.3a. Table 4.1 shows in the first column the FT-IR wavelengths for all peak minima in Figure 4.3b. The second column shows the FT-IR wavelengths for all peak minima for $LiBH_4$ which was measured separately as a standard. Three FT-IR peaks in the first column in Table 4.1, 3219.66, 1721.32 and 797.38 cm^{-1}, have values very close to the FT-IR peaks for $LiBH_4$, 3221.87, 1719.43 and 796.05cm^{-1}. It is possible that those three FT-IR peaks belong to a miniscule amount of $LiBH_4$ that is not recognizable in an XRD pattern in Figure 4.3a. However, the other peaks extracted from the first and shown in the third column in Table 4.1 belong to the MCAS synthesized $Mn(BH_4)_2$ hydride.

Table. 4-1. FT-IR wavenumbers (cm^{-1})(accuracy=± 2 cm^{-1}) of as-received $LiBH_4$ and the ball milled ($2LiBH_4+MnCl_2$) nanocomposite after 2h ball milling (Q_{TR}=145.6 kJ/g).

($2LiBH_4+MnCl_2$) **(this work)**	**$LiBH_4$** **(this work)**	**$Mn(BH_4)_2$**
	3485.02	
	3436.13	
	3387.73	
	3221.87	
3219.66	2686.50	
2958.91	2628.26	-
2562.00	2356.90	2958.91
2273.92	2279.88	2562.00
1721.32	2182.12	2273.92
1620.17	1719.43	-
1575.83	1689.20	1620.17
1526.71	1638.47	1575.83
1352.74	1603.17	1526.71
1228.91	1529.60	1352.74
1113.08	1503.24	1228.91
1035.45	1437.30	1113.08
963.04	1313.64	1035.45
818.97	1294.19	963.04
797.38	1249.15	818.07
721.57	1177.91	-
	1107.85	721.57
	1075.91	
	1009.00	
	960.57	
	796.05	
	659.19	

The two important parameters that provide quantitative information about microstructural evolution/refinement during ball milling, such as the average powder particle size and the average size of grains (crystallites) residing in powder particles, were both estimated. Table 4.2 shows particle size of the milled powder and crystallite (grain) size for the $Mn(BH_4)_2$ synthesized hydride and a LiCl salt as a function of the milling energy input, Q_{TR}. It is clearly seen that the average particle size of 7.5±2.6 µm is the smallest one after milling for 2h with Q_{TR}=145.6 kJ/g. After milling for 5h with Q_{TR}=364 kJ/g the average particle size increases to 16.1±6.3 µm. This is in an excellent agreement with Figure 4.2b and c that show the initial dramatic particle refinement and subsequently a profound agglomeration of particulate, respectively. So the average particle size of 16.1±6.3 µm after ball milling with Q_{TR}=364 kJ/g is due to the presence of a fraction of larger powder agglomerates. However, it must be kept in mind that the individual powder particles forming an agglomerate could be much smaller than the average value.

Also, it is apparent from Table 4.2 that the synthesized $Mn(BH_4)_2$ hydride is nanocrystalline exhibiting a crystallite (grain) size within the range from ~21 to ~14 nm which clearly decreases with increasing milling energy input, Q_{TR}. The crystallite (grain) size of LiCl is very close to 30 nm regardless of the milling energy input, Q_{TR}. In this manner a nanocomposite containing both nanocrystalline constituents, the $Mn(BH_4)_2$ hydride and LiCl salt, has been synthesized

Table. 4-2. Experimentally estimated particle and crystallite (grain) sizes with standard deviations for a ($2LiBH_4$+$MnCl_2$) mixture as a function of milling time and the milling energy, Q_{TR}, injected into powders which was calculated according to Ref. [74]. Ball milling under IMP68-4B-R132 mode.

Powder	**Milling time (h)**	**Injected energy Q_{TR} (kJ/g)**	**Particle size±standard deviation (µm)**	**Crystallite (grain) size±standard deviation (nm) for $Mn(BH_4)_2$**	**Crystallite (grain) size±standard deviation (nm) for LiCl**
As-rec $LiBH_4$	0	0	238.5±109.7	-	-
As-rec $MnCl_2$	0	0	19.1±9.8	-	-
$2LiBH_4$+$MnCl_2$	0.5	36.4	14.9±6.6	21±5.0	34.2±1.6
$2LiBH_4$+$MnCl_2$	2	145.6	7.5 ±2.6	18±1.0	30.6±5.6
$2LiBH_4$+$MnCl_2$	5	364.0	16.1± 6.3	14±0.5	29.8±3.3

For the sake of clarity, it must be mentioned that I did not carry microstructural investigations for the ($3LiBH_4$+$MnCl_2$) mixture because it eventually showed worse dehydrogenation properties than that with n=2 as will be shown in the following sections. In order to confirm if there is a release of H_2 during ball milling as has been observed in our laboratory for other ball milled hydrides [15, 74, 78, 84], the hydrogen desorption during ball milling of the ($nLiBH_4$+$MnCl_2$) mixtures was continuously monitored. Figure 4.4 shows that H_2 desorption from both mixtures with n=2 and 3up to 2h of milling is minimal. However, for the n=2 mixture there is a gradual acceleration of mechanical dehydrogenation to the extent that the quantity of desorbed H_2 increases from about 0.3 after 2h to 0.7 wt.% after 5h of ball milling.

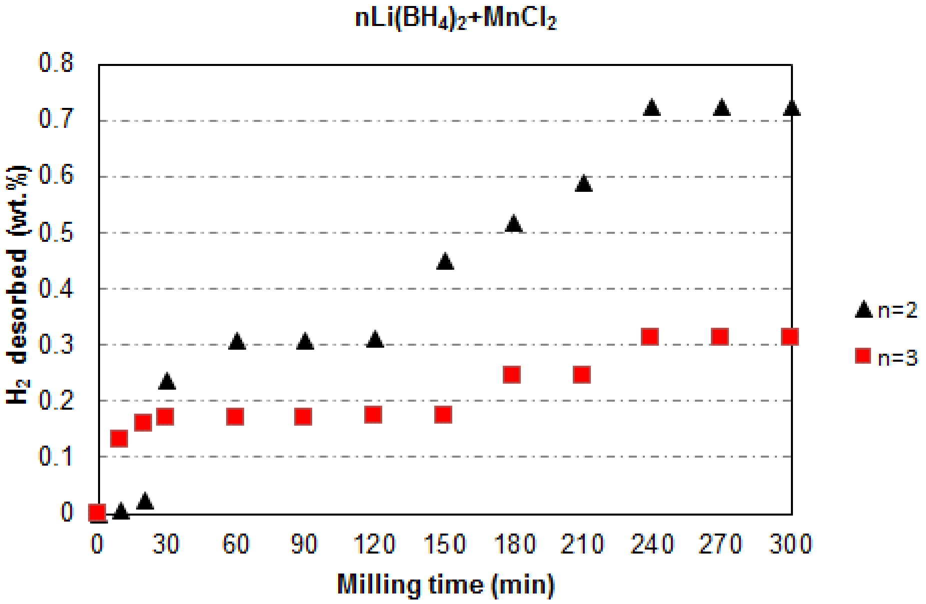

Fig. 4-4. The quantity of H_2 desorbed during milling of the initial ($2LiBH_4$+$MnCl_2$) and ($3LiBH_4$+$MnCl_2$) mixtures (adapted from [81].

4.1.1 Thermal behavior in DSC during continuous heating

Figure 4.5a shows the DSC curves for the ball milled n=2 and 3 nanocomposites during continuous heating up to 250 °C. For both of them there are two endothermic peaks observed. The first one is very small for n=2 but much larger for n=3 having the area of 3.47 and 21.49 J/g, with the peak maximum temperature of 100.3 and 102.7 °C, respectively. The second peak with the peak maximum temperature of 139.9 and 137.4

°C for n=2 and 3, respectively, has slightly larger area of 67.21 J/g for n=2 than that of 58.11 J/g for n=3.

Figure 4.5b shows DSC curves for the n=2 and 3 nanocomposites which were first heated to 123°C and subsequently cooled to room temperature. It is clearly observed that the smaller endothermic peak with the maximum at 100.8 and 103.2 °C for n=2 and 3, respectively, is reversible although with a very large thermal hysteresis having the maximum peak temperature at 67.2 °C for n=3 on cooling. So, for n=3 the thermal hysteresis is 36 °C. For n=2 the cooling peak is much diffused and hardly visible in Fig. 4.5b.

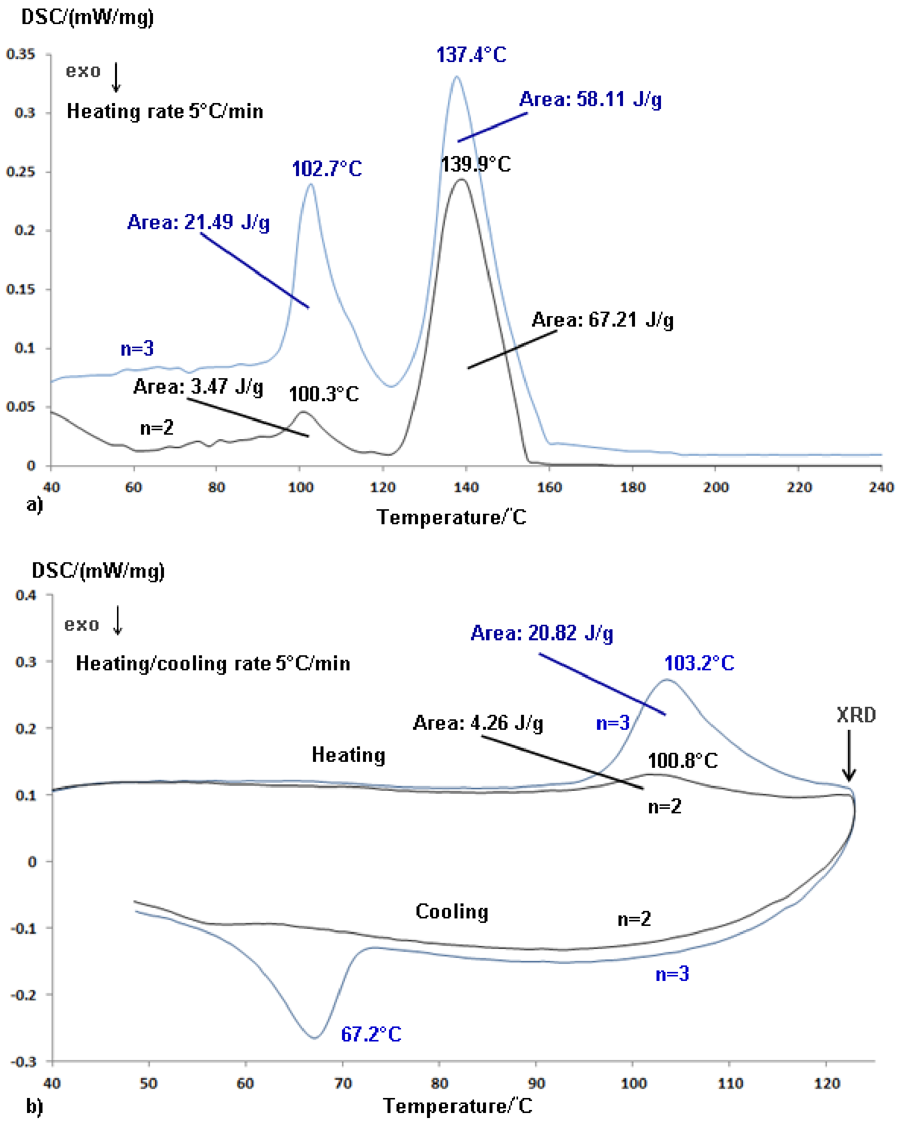

Fig. 4-5. DSC curves for the n=2 and 3 nanocomposites ball milled with Q_{TR}=145.6 kJ/g. (a) DSC at 5°C/min heating rate up to 250°C/min and (b) at 5°C/min heating rate up to 123 °C and then cooling to room temperature (Adapted from [81]).

The DSC thermal behavior observed in Figure 4.5 can be interpreted as follows. The first low temperature endothermic peak at around 100 °C is most likely due to a polymorphic transformation of $LiBH_4$ which at room temperature exists as an orthorhombic phase (space group *Pnma*) and undergoes a first-order phase transition to a hexagonal phase (space group $P6_3mc$) [85, 86]. The transformation temperature has been quoted in the literature as occurring at the 105-108°C range, although, without specifying the heating rate used in the experiments [85, 86]. Züttel et al. [54] claimed that the lattice transformation of $LiBH_4$ was associated with a small H_2 desorption of about 0.3 wt.% although the mechanism of desorption was not provided. On cooling, the transformation is reversible as can be seen in Figure 4.5b with a large temperature hysteresis. The $LiBH_4$ transformation peak at about 100 °C on heating and 67.2 °C on cooling for the ball milled n=3 nanocomposite is much larger than that for the n=2 nanocomposite because the former has a 1 mol of retained $LiBH_4$ in the microstructure according to Reaction (1.6). The small peak at 100.3 °C in Figure 4.5a for the ball milled n=2 nanocomposite is a bit surprising because at that molar ratio entire $LiBH_4$ is supposed to be reacted according to reaction (1.6). Apparently, reaction (1.6) was not completed 100% and a miniscule amount of $LiBH_4$ was retained in the microstructure after MCAS although the $LiBH_4$ peaks are not observed in the XRD pattern for the ball milled n=2 nanocomposites in Fig. 4.3a. That indicates that, indeed, the quantity of $LiBH_4$ retained in the ball milled n=2 nanocomposite must have been very small, beyond the XRD resolution.

Apparently, the DSC peaks observed in Figure 4.5a at 139.9 and 137.4 °C for the ball milled n=2 and 3 nanocomposites, respectively, are due to dehydrogenation of the MCAS synthesized $Mn(BH_4)_2$ according to the either of reactions (1.7) or (1.8).

In order to confirm the correctness of the DSC thermal behavior observed in Figure 4.5 and discussed above, the XRD patterns shown in Figure 4.6 were obtained from DSC samples heated up to 123 and 250°C followed by cooling down to room temperature (see an XRD arrow in Figure 4.5b). It is clearly seen that the n=2 and 3 nanocomposites heated to 123 °C still show the presence of the XRD peaks of the MCAS synthesized $Mn(BH_4)_2$. The XRD pattern for the n=2 sample heated to 250 °C does not show any diffraction peaks of $Mn(BH_4)_2$ which confirms that a low temperature DSC peak at around 100 °C in Figures 4.5a and b, is unrelated to the decomposition of $Mn(BH_4)_2$ but, instead, corresponds to a polymorphic transformation of $LiBH_4$ while the peaks at around 140 °C in Figure 4.5a correspond to the liberation of H_2 due to the decomposition of $Mn(BH_4)_2$. In addition, the XRD pattern after heating to 250 °C shows no presence of the peaks of Mn and B as required by Reactions (1.7) or (1.8). That could be due to the amorphous structure of both elements after dehydrogenation which will be investigated by TEM and EDS in the next section (4.2).

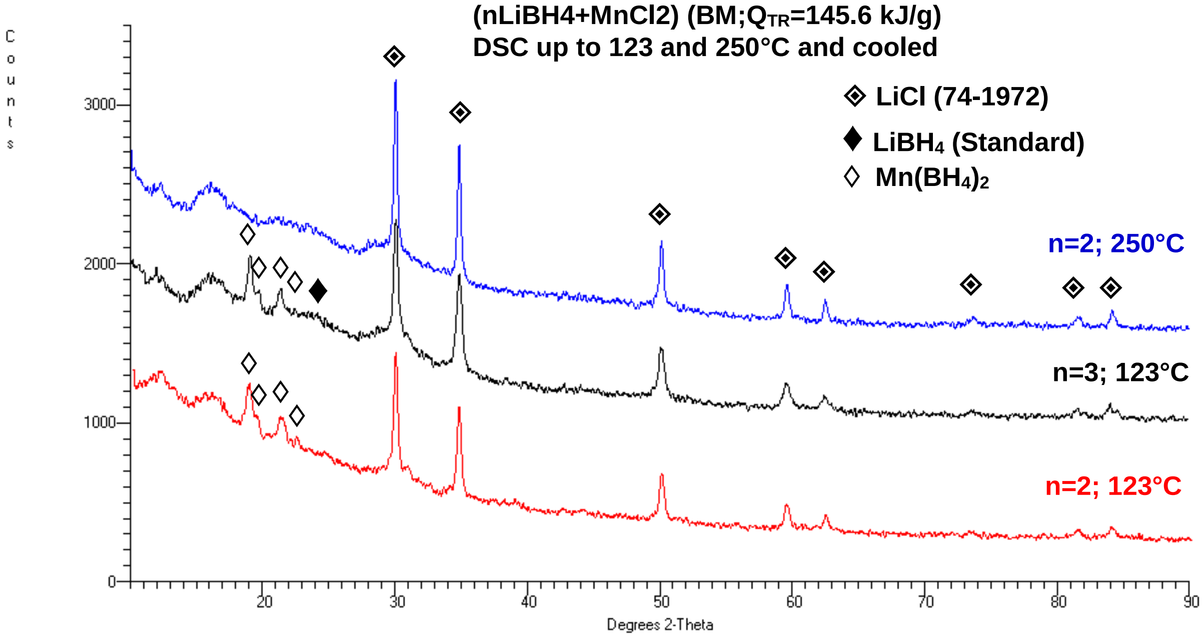

Fig. 4-6. XRD patterns for the n=2 and 3 nanocomposites ball milled with Q_{TR}=145.6 kJ/g after DSC run up to 123 °C and then cooling to room temperature (adapted from [81]).

4.1.2 Isothermal dehydrogenation

Figure 4.7 shows dehydrogenation curves at varying temperatures of 100, 150 and 200°C for the n=2 nanocomposite ball milled with two levels of energy input Q_{TR}=36.4 and 145.6 kJ/g. The rate of dehydrogenation is quite rapid at 100°C and clearly increases with the initial increase of milling energy input. As observed in Fig. 4.7a and b, for the energy input Q_{TR}=36.4 (Fig 4.7a) and 145.6 kJ/g (Fig 4.7b), the quantity of 4 wt.% H_2 is desorbed within about 5 and 2 h, respectively. It is interesting to note that if the milling energy input further increases to Q_{TR}=364 kJ/g (Table 4.2) the rate of dehydrogenation decreases such that 4 wt.% H_2 is now desorbed within 10 h (the dehydrogenation curve is not shown here). This behavior will be discussed later.

Figures 4.7a to 4.7f also show that the maximum H_2 desorption quantity at 100 and 200°C is very similar and does not exceed ~4.5 wt.% (or 9.5 wt.% with respect to the content of $Mn(BH_4)_2$.) The maximum theoretical H_2 capacity for the n=2 mixture ($2LiBH_4+MnCl_2$) is 4.76 wt.% (Table 1 in Ref. [36]).

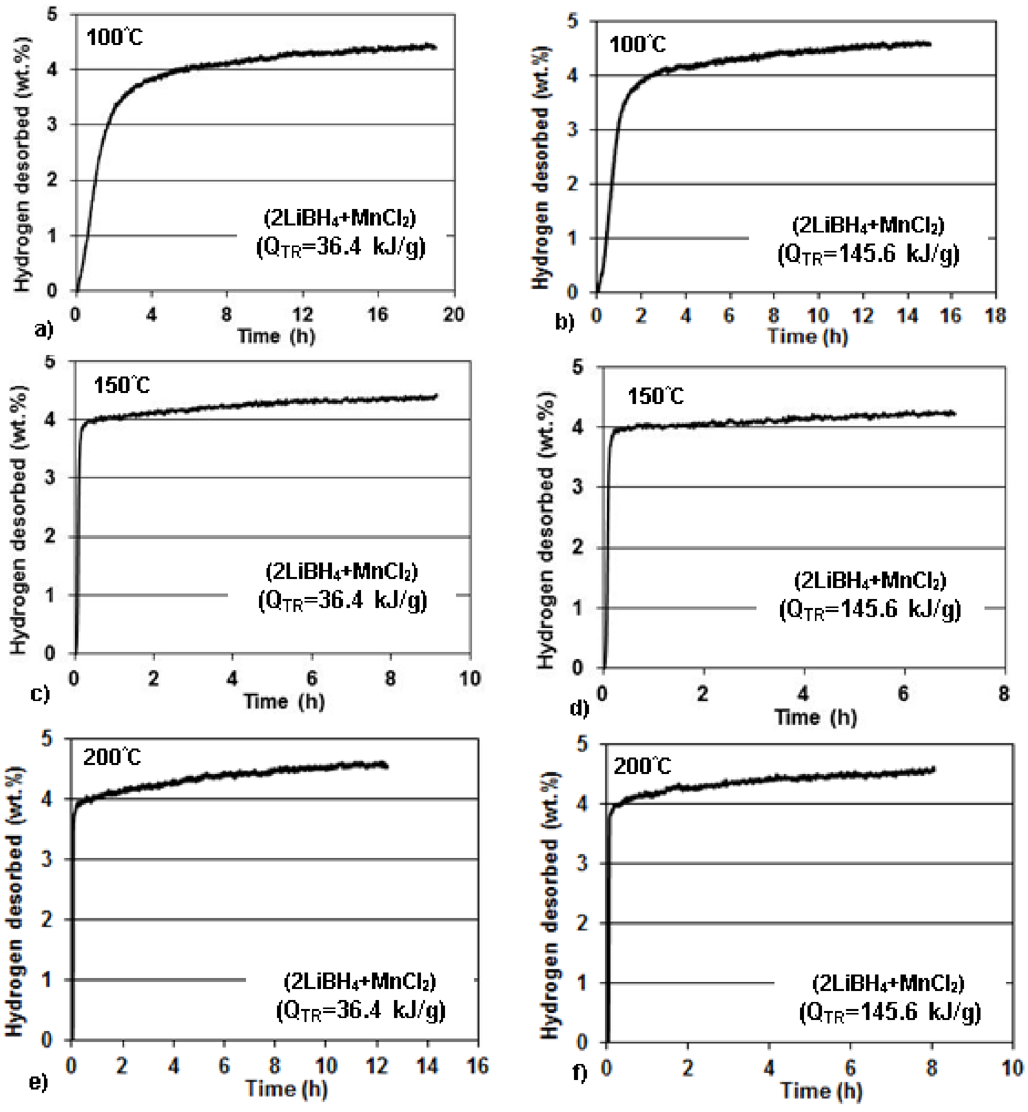

Fig. 4-7. Dehydrogenation curves for the n=2 nanocomposite ball milled with the energy input Q_{TR}=36.4 and 145.6 kJ/g at (a) 100°C, (b) 150°C and (c) 200°C. The microstructure of the powders after complete dehydrogenation was analyzed using XRD (adapted from [81]).

Figure 4.8 shows XRD patterns for the n=2 and 3 nanocomposites initially ball milled with the energy input of Q_{TR}=36.4 kJ/g (0.5h) after dehydrogenation at 100°C for 18.7 h (n=2, the end of the dehydrogenation curve in Fig. 4.7a) and 20.3 h (dehydrogenation curve not shown here), respectively. By comparison with Figure 4.3a just after the MCAS synthesis, it is clearly seen that no peaks of $Mn(BH_4)_2$ are visible in Figure 4.8 which means that the synthesized hydride completely decomposed during dehydrogenation at

100°C according to reaction (1.7) or (1.8). Similarly, to Figure 4.6 after a 250°C DSC run, no peaks of Mn and B from either of reactions (1.7) and (1.8) are observed in Figure 4.8. That confirms that both elements are amorphous after dehydrogenation. However, the presence of either amorphous or crystalline Mn and B could be unambiguously verified by TEM in the next section (4.2).

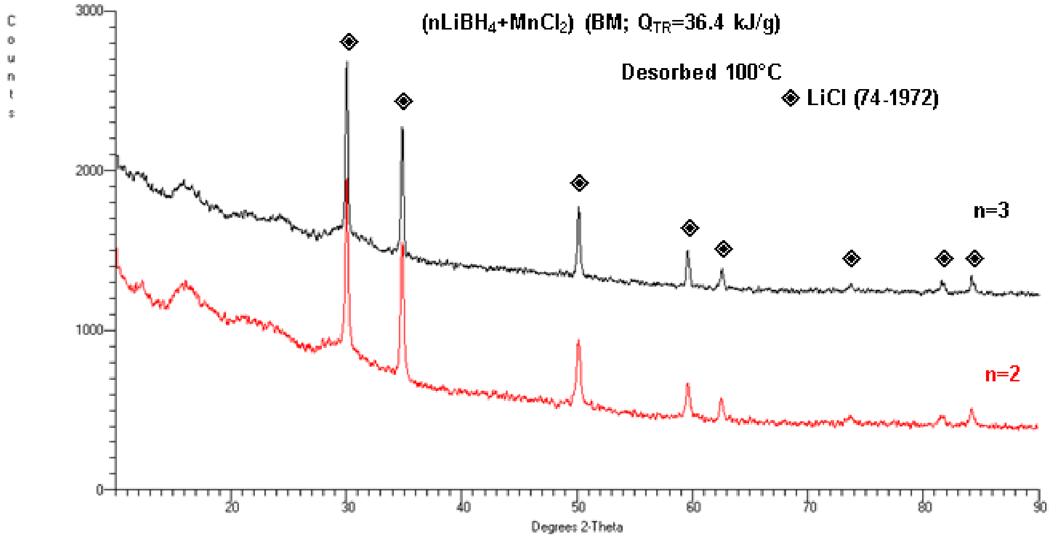

Fig. 4-8. XRD patterns for the n=2 and 3 nanocomposites ball milled with the energy input of Q_{TR}=36.4 kJ/g (0.5h) after dehydrogenation at 100°C for 18.7 h (the end of the dehydrogenation curve in Fig.4.7a) (adapted from [81]).

The dehydrogenation curves, as those shown in Figure 4.7, were used for estimation of the apparent activation energy for dehydrogenation for the ball milled n=2 and 3 nanocomposites.

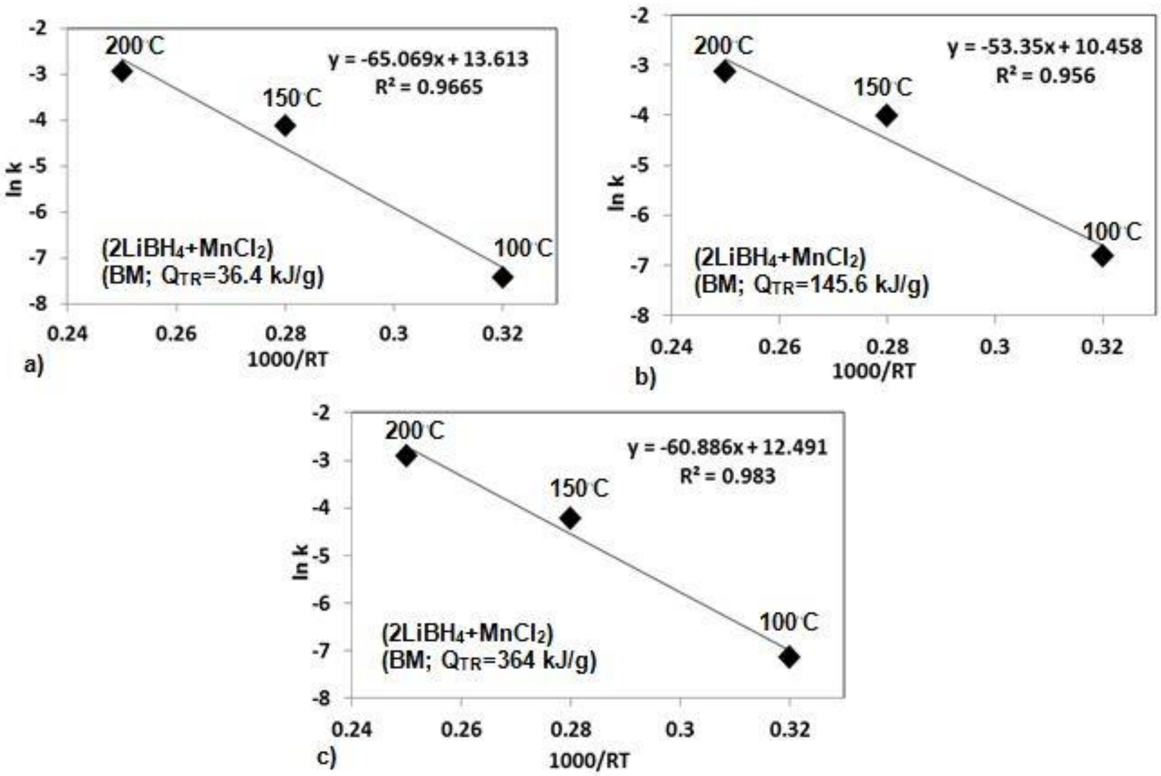

Fig. 4-9. The Arrhenius plots for calculating the apparent activation energy for dehydrogenation of the n=2 ($2LiBH_4$+$MnCl_2$) nanocomposite ball milled with increasing milling energy input (a) Q_{TR}=36.4 kJ/g, (b) Q_{TR}=145.6 kJ/g, (c) Q_{TR}=364 kJ/g (adapted from [81]).

Figure 4.10 shows the pertinent Arrhenius plots and Figure 4.11a shows the plot of the estimated apparent activation energy for dehydrogenation as a function of the milling energy input, Q_{TR}.

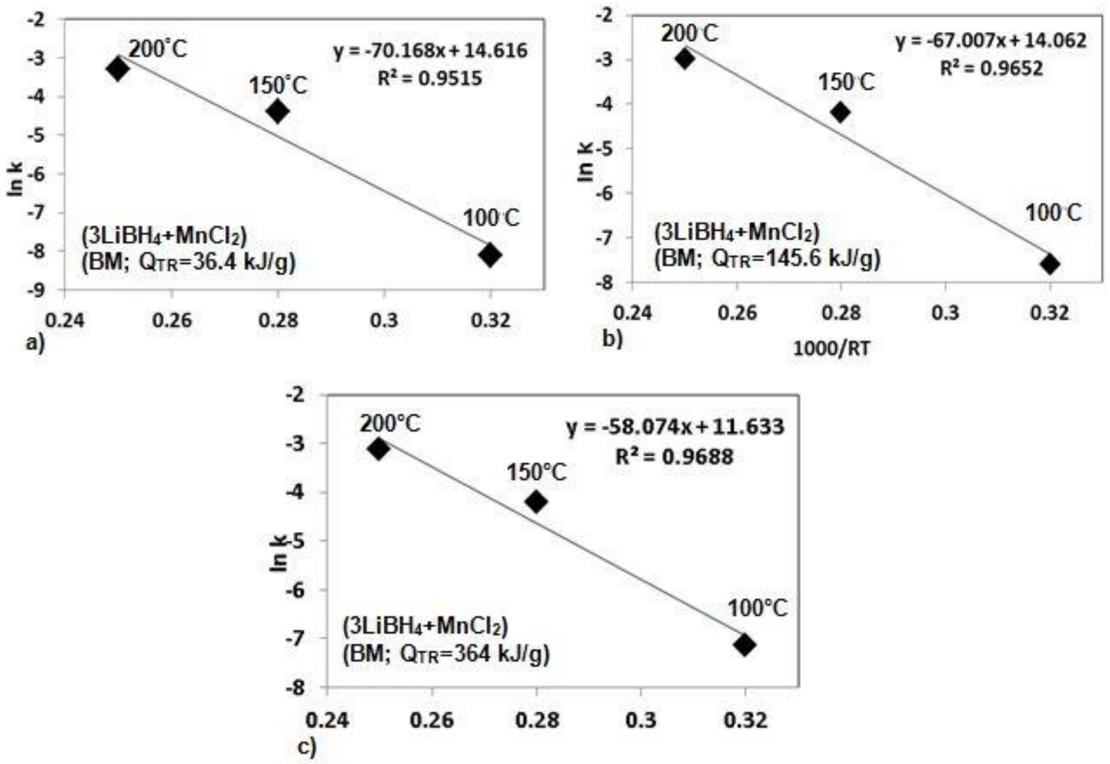

Fig. 4-10. The Arrhenius plots for calculating the apparent activation energy for dehydrogenation of the n=3 ($3LiBH_4+MnCl_2$) nanocomposite ball milled with increasing milling energy input (a) Q_{TR}=36.4 kJ/g, (b) Q_{TR}=145.6 kJ/g, (c) Q_{TR}=364 kJ/g (adapted from [81]).

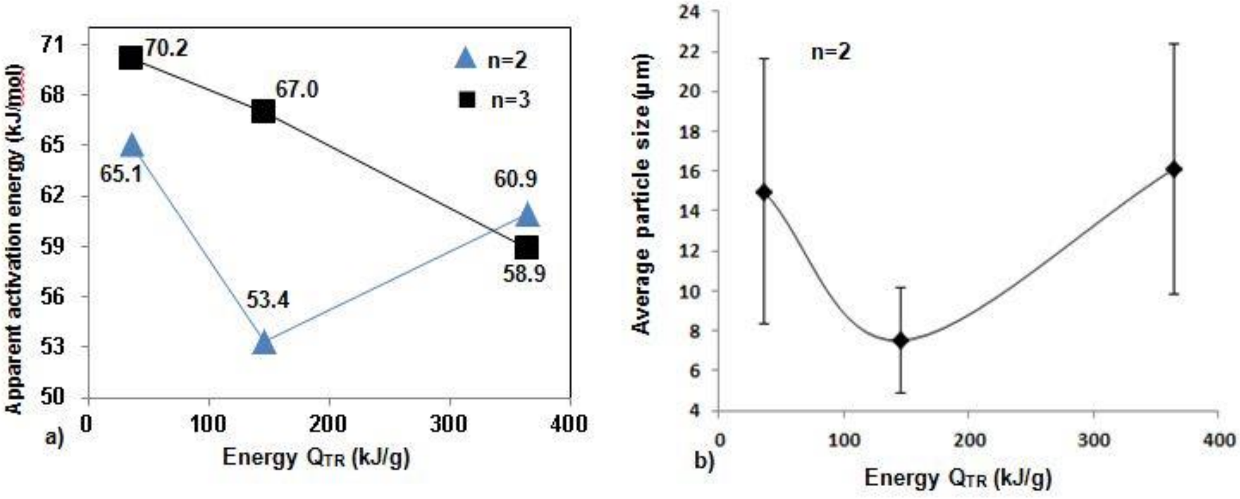

Fig. 4-11. (a) Apparent activation energy for dehydrogenation for the ball milled n=2 and 3 nanocomposites as a function of the milling energy input, Q_{TR}. (b) Variation of the particle size for the n=2 nanocomposite as a function of the milling energy input, Q_{TR} (adapted from [81]

The first important observation in Figure 4.11a is that for the milling energy input Q_{TR}=36.4 and 145.6 kJ/g the apparent activation energy for dehydrogenation for the ball milled n=3 nanocomposite is slightly higher than that for the n=2 nanocomposite. For the highest milling energy input Q_{TR}=364 kJ/g, both the n=2 and 3 nanocomposites have quite similar apparent energies for dehydrogenation on the order of 60 kJ/mol. Since the apparent activation energy for the n=3 nanocomposites is higher than that for the n=2 nanocomposite we did not investigate the microstructure of the former as mentioned earlier. It is clear that the n=2 stoichiometry in the initial mixture is the best from the standpoint of the lowest apparent activation energy.

The second important observation in Figure 4.11a is that the apparent activation energy for dehydrogenation for the n=3 nanocomposite decreases monotonically with increasing milling energy input, Q_{TR}, whereas the apparent activation energy for the n=2 nanocomposite decreases from about 65 kJ/mol for Q_{TR}=36.4 kJ/g to about 53 kJ/mol for Q_{TR}=145.6 kJ/g and then increases for the Q_{TR}=364 kJ/g. This rather unusual behavior is clearly explained by Figure 4.11b which shows the variations of the average particle size of the ball milled n=2 nanocomposite as a function of the milling energy input, $Q_{TR.}$ From Table 4.2 it is clear that initially the average particle size decreases by particle refinement during ball milling down to 7.5 ±2.6 µm for the milling energy input Q_{TR}=145.6 kJ/g but with further milling it increases again reaching the average size 16.1± 6.3 µm for the milling energy input Q_{TR}=364 kJ/g. In other words, the apparent activation energy for dehydrogenation of nanocrystalline $Mn(BH_4)_2$ is strongly dependent on the average particle size for the ball milled n=2 nanocomposite such that it increases with increasing average powder particle size. Interestingly, the apparent activation energy for dehydrogenation doesn’t seem to be dependent on the average crystallite (grain) size for the n=2 nanocomposite which gradually decreases with increasing milling energy input (Table 4.2).

The third observation from Figure 4.11a is that by comparison to previous study in Ref. [36] the apparent activation energy values for dehydrogenation obtained in this work are about 30-50 kJ/mol lower (depending on the milling energy input) than those reported in Ref. [36]. It seems that ball milling in the present work was much more effective than that in Ref. [36] which resulted in a more refined average particle size.

4.1.3 Long term slow dehydrogenation at room temperature

Figure 4.12 shows dehydrogenation curves obtained at 100°C for the n=2 and 3 nanocomposites ball milled up to a constant milling energy input Q_{TR}=145.6 kJ/g and subsequently stored for a varying time durations at room temperature under a slight overpressure of argon. It is observed that the n=2 nanocomposite doesn't release H_2 during storage up to 28 days (Figures 4.12a and b) but within 80 days it releases a small amount of about 0.5 wt.% H_2 and subsequently stabilizes up 120 days of further storage. The ball milled n=3 nanocomposite doesn't release H_2 within 124 days of storage. The observed behavior is in agreement with the preliminary results which reported in Ref. [36]. Apparently, the nanocrystalline $Mn(BH_4)_2$ hydride synthesized by MCAS during ball milling of the n=2 and 3 mixtures is a very stable hydride during low temperature storage.

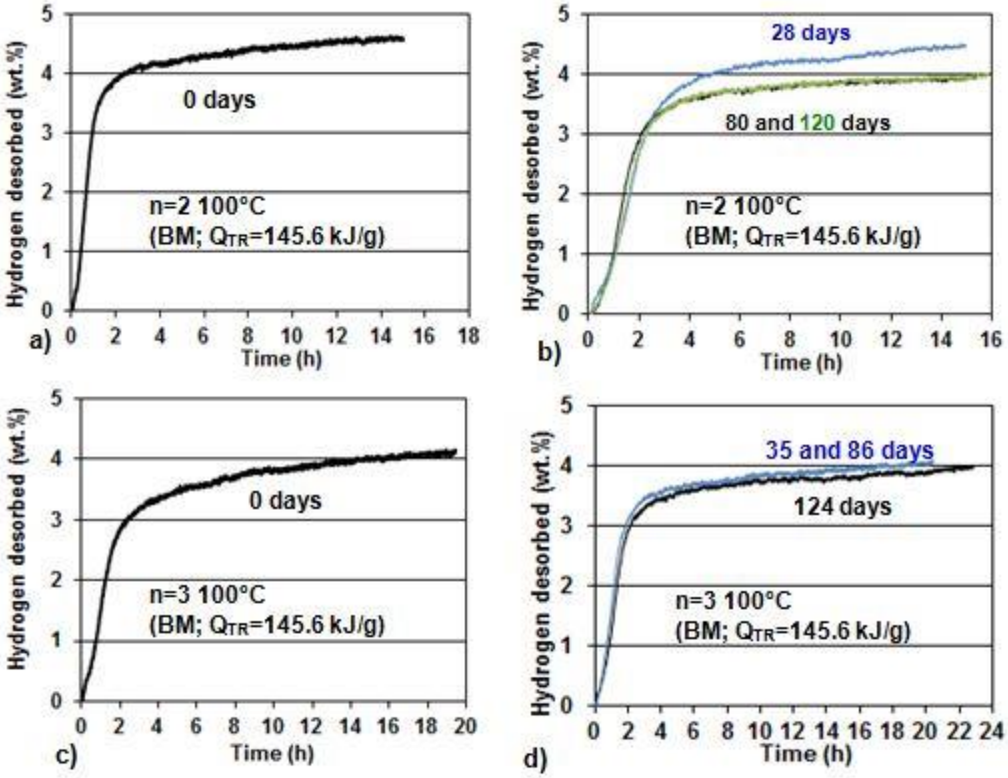

Fig. 4-12. Dehydrogenation curves obtained at 100°C for the n=2 and 3 nanocomposites ball milled up to a constant milling energy input Q_{TR}=145.6 kJ/g and subsequently stored at room temperature for a varying time duration under a slight overpressure of argon (adapted from [81]).

4.2 *High resolution transmission electron microscopy (TEM), energy-dispersive X-ray spectroscopy (EDS)*

In order to obtain a detailed insight into the microstructure of the ($Mn(BH_4)_2$+2LiCl) mixture, just after the synthesis by MCAS as well as after subsequent thermal dehydrogenation (thermolysis), using high resolution transmission electron microscopy (HR TEM) combined with energy-dispersive X-ray spectroscopy (EDS) for elemental mapping of the microstructure and X-ray diffraction. It must also be pointed out that, so far, HR TEM investigations have never been reported for those borohydrides synthesized by MCAS during ball milling. TEM and EDS studies has been done only for the n=2 ($2LiBH_4$+$MnCl_2$) nanocomposite ball milled with the milling energy input Q_{TR}=145.6 kJ/g (2h).

4.2.1 *TEM and EDS studies of nanocrystalline manganese borohydride ($Mn(BH_4)_2$ after MCAS*

Fig. 4.13a shows the SEM secondary electron image of powder after ball milling with the energy input Q_{TR}=145.6 kJ/g. Figs. 4.13b and c show the results of the EDS chemical analysis from two selected areas of the BM mixture, where the EDS spectrum of boron (B), chlorine (Cl) and manganese (Mn) are clearly observed. The spectra of carbon (C) and oxygen (O) are most likely arising from a carbon tape used as a substrate for powders analysis. Since the EDS detector cannot detect presence of elements with atomic number less than 5, the spectrum of Li in this experiment is not detected. The EDS spectra for the ball milled powder sample show the presence of Mn and Cl which, most likely, reside in the synthesized $Mn(BH_4)_2$ and LiCl phases, respectively, that were formed during ball milling as a result of MCAS according to reaction (1.6).

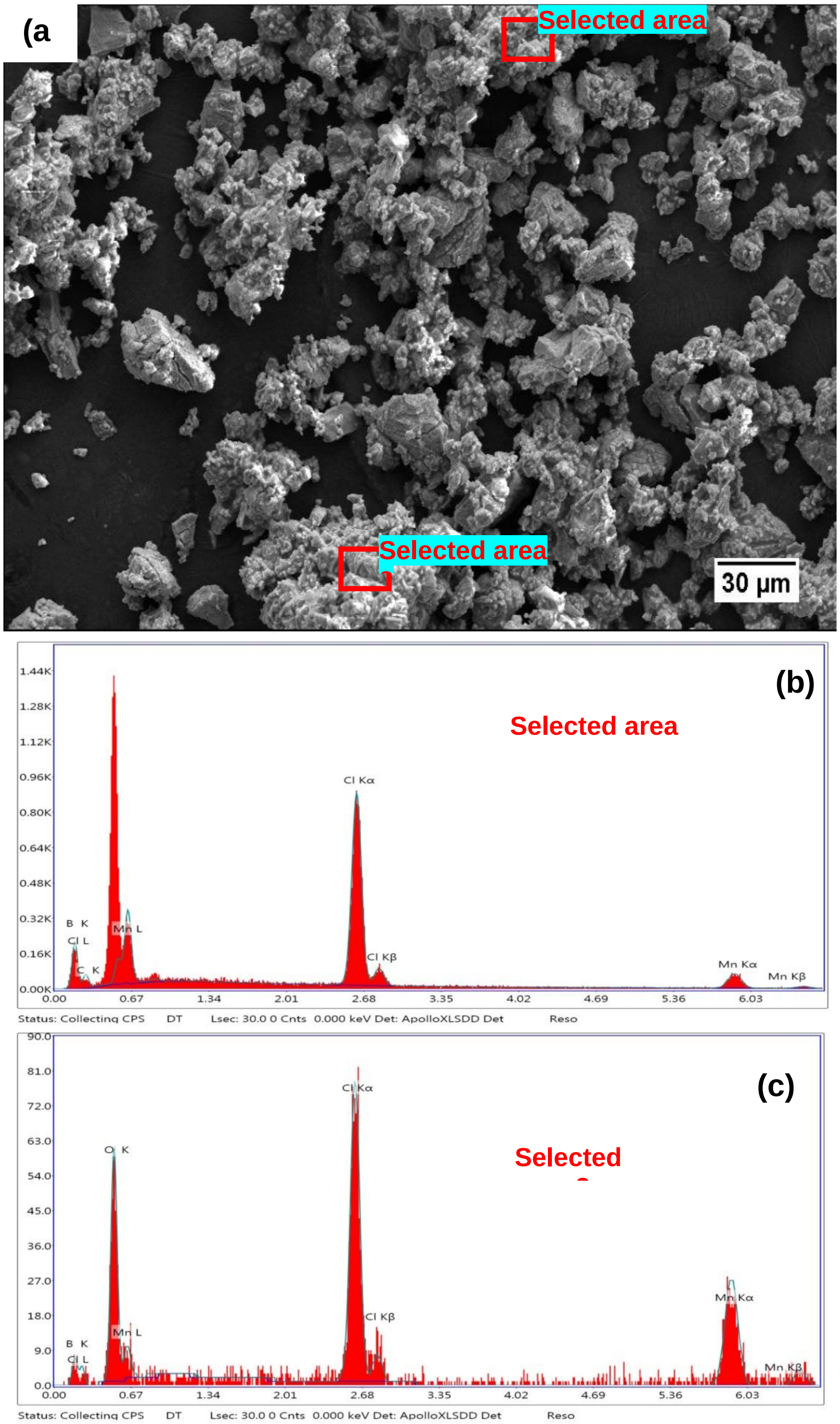

Fig. 4-13. Scanning electron micrographs of ball milled (2LiBH$_4$+MnCl$_2$) powders after MCAS and (b) energy dispersive X-ray spectroscopy (EDS) of the selected area of SEM micrograph after MCAS (adapted from [87].

Figure 4.14 shows the XRD patterns of the as-received ($2LiBH_4$+$MnCl_2$) powder mixture and the same mixture after ball milling. Since new sample was ball milled for the TEM and EDS studies, XRD was carried out again to confirm formation of both the $Mn(BH_4)_2$ and LiCl after MCAS by ball milling. The as-received pattern shows the diffraction peaks of orthorhombic $LiBH_4$ (space group Pnma, a=7.17858(4), b=4.4368e 2(2), c=6.80321(4) Å) [21] and rhombohedral $MnCl_2$ (space group R-3m, a=3.7061, b=3.7061, c=17.569 Å) [88]. It can be seen that after 2 h ball milling with the energy input Q_{TR}=145.6 kJ/g, the diffraction peaks of the constituent powders disappeared while $Mn(BH_4)_2$ and LiCl peaks evolved.

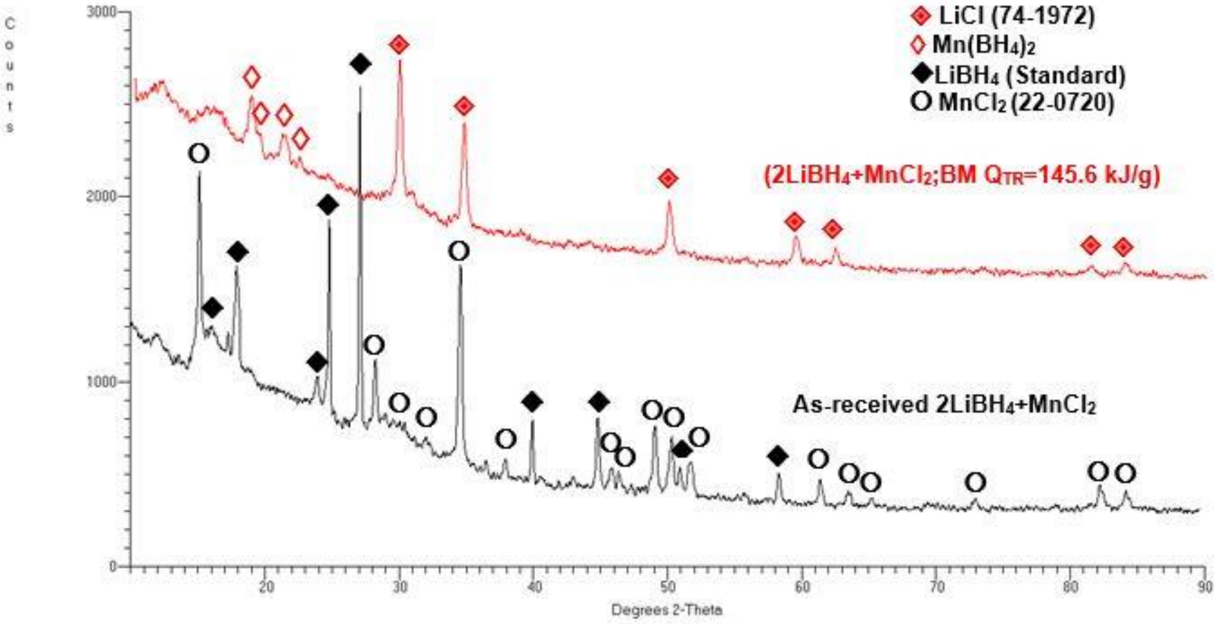

Fig. 4-14. XRD patterns of the as received ($2LiBH_4$+$MnCl_2$) mixture and the same mixture after ball milling with an energy input Q_{TR}=145.6 kJ/g (2 h) [87].

As mentioned earlier, the diethyl ether (E_2O) solvent was used in a wet method in order to breakdown the powder sample into smaller pieces, most ideally, into individual particles having thickness transparent to the electron beam. The transmission electron microscopy (TEM) micrographs of the synthesized powder prepared by a wet method using Et_2O are shown in Fig. 4.15. It appears that the Et_2O solvent reacted with the ball milled powder damaging the surface of powder particles. Apparently, the wet method using Et_2O seems not to be suitable for extracting individual powder particles form the synthesized powder for TEM study. It was discarded from further consideration.

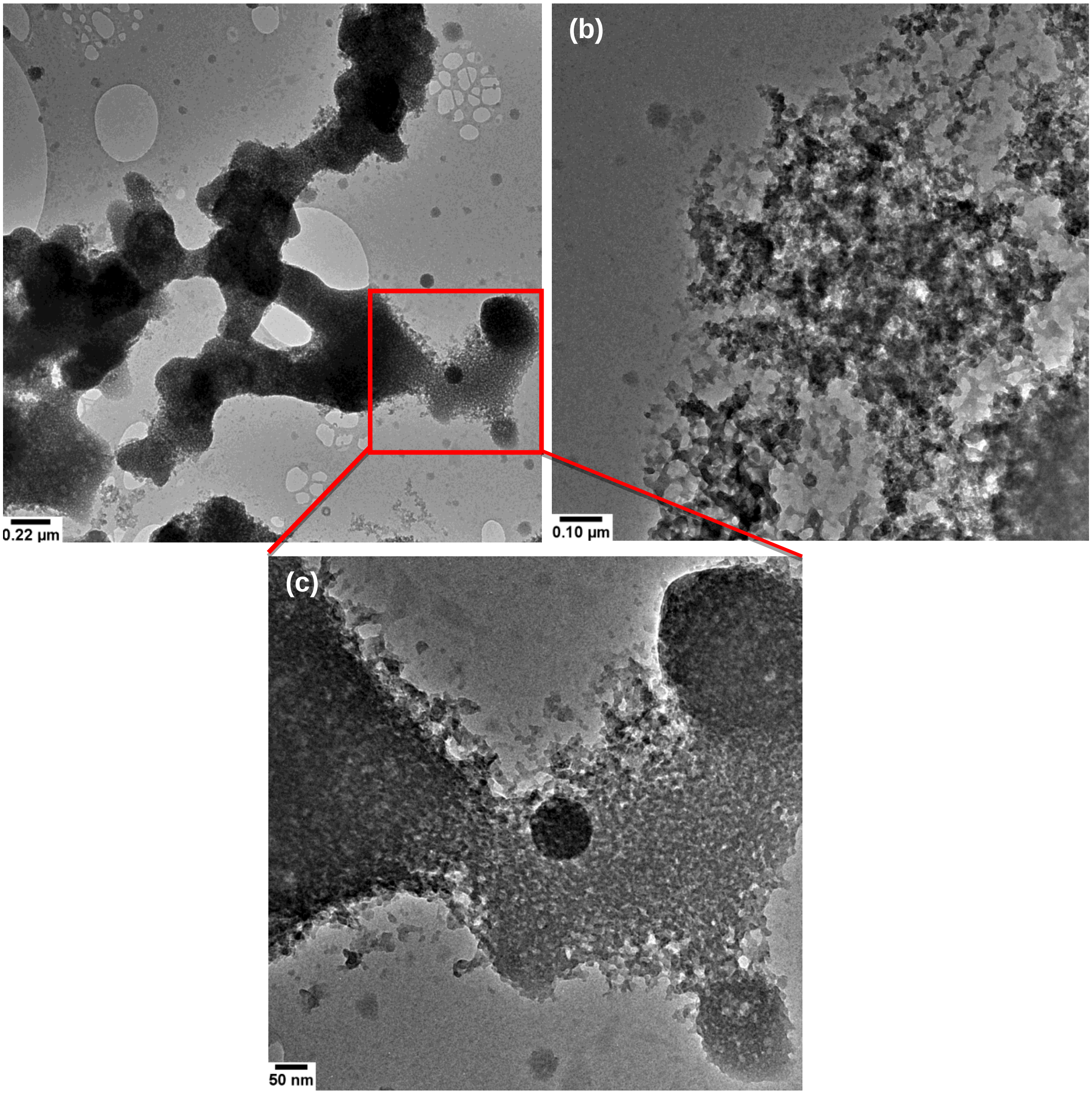

Fig. 4-15. TEM micrograph of ($2LiBH_4$+$MnCl_2$) powder mixture after ball milling with an energy input Q_{TR}=145.6 kJ/g (2h) (wet method) at different magnifications adapted from [87].

Figure 4.16a presents the TEM micrograph of two partially overlapped powder particles, a smaller one with ECD=0.63 and a larger particle with ECD=1.14 µm, which were extracted from the synthesized nanocomposite ($Mn(BH_4)_2$+2LiCl) powder without using any solvent (dry method). The sample looks much better although it shows some degree of beam damage and the presence of amorphous material. Apparently, the dry method is much more effective for extracting much less undamaged particles from the synthesized powder than the wet method. Fig. 4.16b shows the selected area electron diffraction pattern (SAEDP) from the larger particle area indicated by a red arrow in Fig. 4.16a. A number of interplanar spacings ($d_{(hkl)}$), which are shown in the left upper corner of Fig. 4.16b, corresponding to various diffracting (hkl) planes in the crystalline lattice of the LiCl phase, were experimentally calculated from the SAEDP and they are depicted by calculated powder ring patterns in the SAEDP in Fig. 4.16b analogous to those obtained from X-ray powder diffraction. Each calculated ring corresponds to a interplanar spacing, $d_{(hkl)}$. They are clearly consistent with the crystal lattice spacings from ICDD (JCPDC) card # 74-1972 for LiCl which is used as a standard in our XRD analysis.

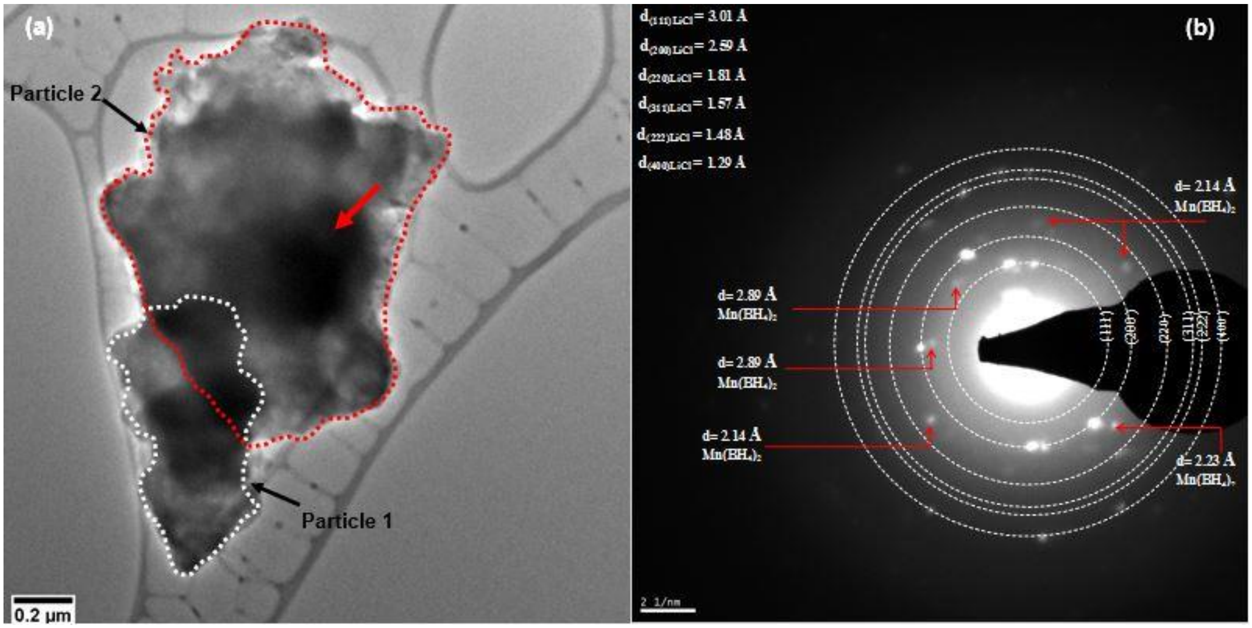

Fig. 4-16. (a) TEM micrograph of two partially overlapping powder particles which were extracted without using solvent (dry method) from the synthesized nanocomposite ($Mn(BH_4)_2$+2LiCl). (b) Corresponding selected area diffraction (SAED) pattern (adapted from [87]).

Figure 4.17a shows high-resolution TEM image of individual nanograins/crystallites residing in one of the particles in Fig. 4.16a. The area on the image exhibiting the same orientation of the lattice planes, visible under high resolution, was corresponding to one individual nanograin and the contours of nanograins are delineated by a broken line. Subsequently, the digital diffraction using a fast Fourier transform (FFT) from the entire image, that includes all nanograins visible within the frame, was performed and is shown in the top inset. The calculated diffraction rings using the ImageJ software, visible on the digital diffraction in Fig. 4.17b, were identified as corresponding to LiCl by calculating the ratio of the diameter of the second ring further from the center, corresponding to the LiCl (200) lattice plane and inverse of its lattice spacing, ($1/d_{(200)}$), to the diameter of the first ring near the center, corresponding to the LiCl (111) lattice plane ($1/d_{(111)}$), which is equal to 1.15. This particular ratio exactly fits with the ratio of $d_{(111)}/d_{(200)}$ of the FCC structure of LiCl phase in our material. Since $Mn(BH_4)_2$ has diffraction spots at lower 2θ angles or correspondingly larger $d_{(hkl)}$ spacings (Table 4.3) than LiCl, it must have diffraction spots closer to the center of FFT diffraction pattern in the inset as compared to LiCl. As a results, the 4 digital white diffraction spots identified by the arrows in the inset in Fig. 4.17b are corresponding to $Mn(BH_4)_2$. Subsequently, each individual nanograin was identified as belonging either to LiCl or $Mn(BH_4)_2$ based on respective digital diffraction using FFT performed on each individual nanograin and subsequent calculation of the ring diameter/interplanar spacing ratios. The grains countoured by a dotted red line correspond to LiCl and their digital diffraction spots all have the ratio near 1.15, characteristic of an FCC-type lattice (LiCl). The nanograins delineated by a white dotted line belong to $Mn(BH_4)_2$ and their FFT diffraction spots always appear at one of the positions of the 4 FFT diffraction spots near the center (see white arrows) and they do not exhibit the FCC ratios.

For additional confirmation of the correctness of the FFT analysis in Fig. 4.17a, an TEM SAEDP was taken exactly from the area of nanograins visible in Fig. 4.17a and is shown in Fig 4.17c. A number of interplanar spacings ($d_{(hkl)}$), which are shown in the left upper corner of Fig. 4.17c, corresponding to various diffracting (hkl) planes in the crystalline lattice of the LiCl phase, were experimentally calculated from the SAEDP and they are overlaid with the calculated powder ring patterns in Fig. 4.17c.

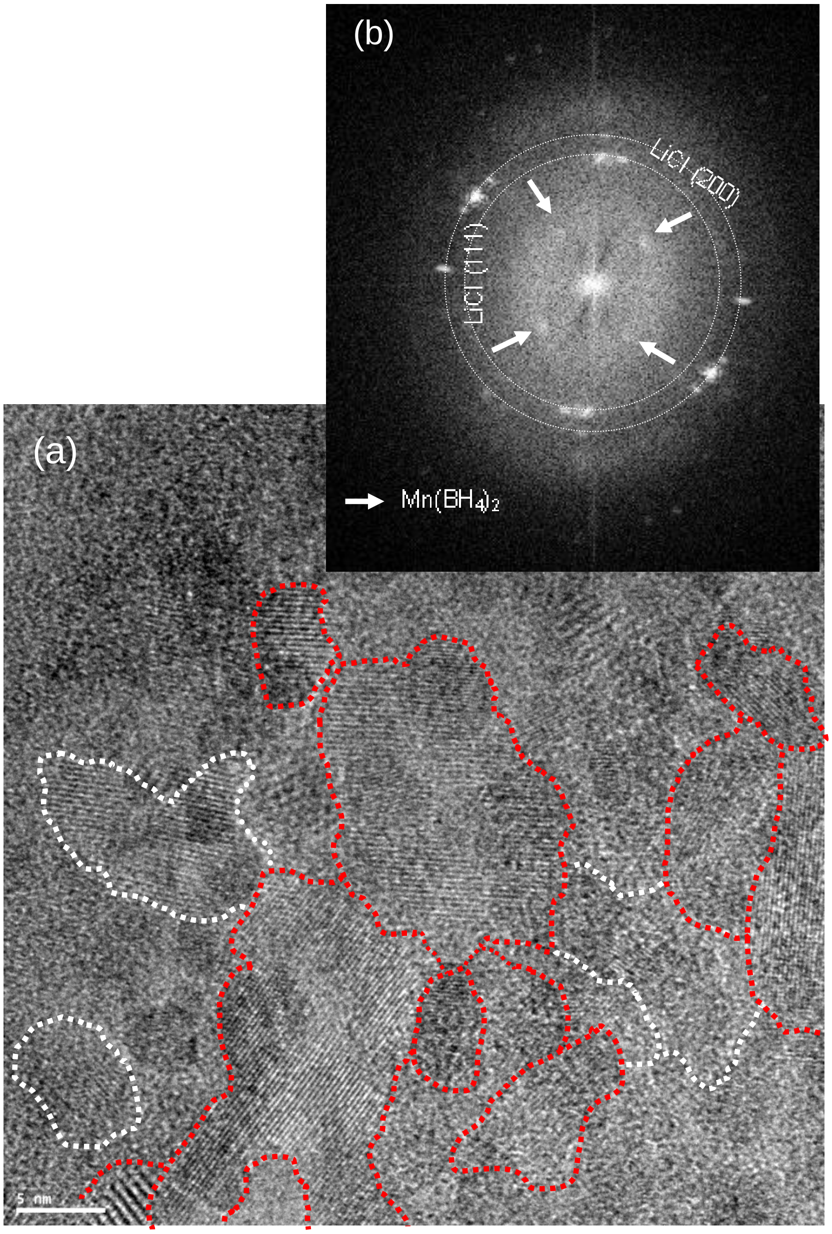
(b)
LiCl (200)
LiCl (111)
Mn(BH$_4$)$_2$
(a)
5 nm

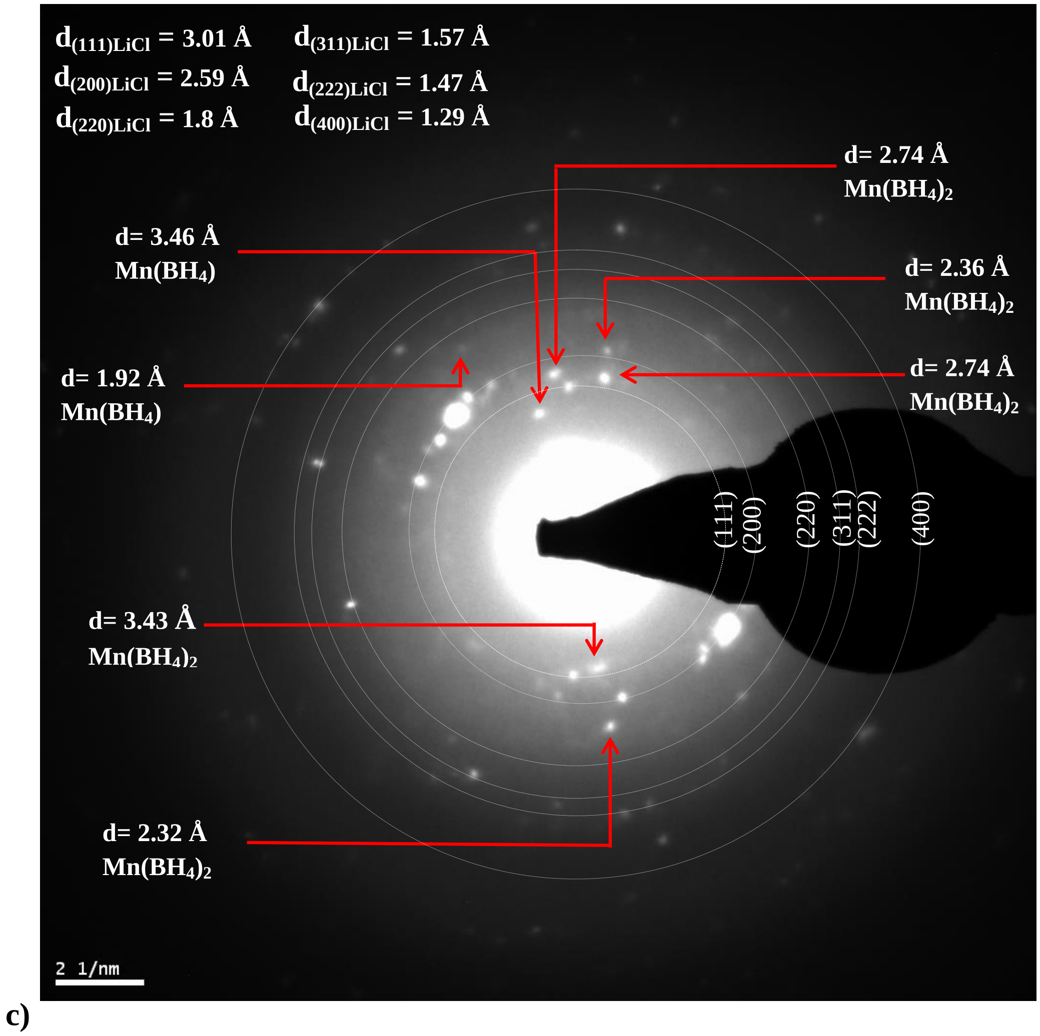

Fig. 4-17. (a) High resolution TEM image of a particle extracted from the synthesized nanocomposite ($Mn(BH_4)_2$+2LiCl) powder (marker is 5 nm). (b) A digital SAEDP using a fast Fourier transform (FFT) of the whole image in (a). (c) SAEDP from the particle imaged in (a) (adapted from [87]).

For the unambiguous identification of $Mn(BH_4)_2$ from the electron diffraction SAEDPs in Fig. 4.16b and 4.17c, we used the 2θ values extracted from the synchrotron radiation diffraction pattern reported in [36] for the synthesized ($Mn(BH_4)_2$+2LiCl) nanocomposite which are tabulated in the first column in Table 4.3. Using the synchrotron 2θ values and the synchrotron radiation wavelength from [36] the plane spacings $d_{(hkl)}$ for $Mn(BH_4)_2$ were calculated from the Bragg's law and are also listed in the second column in Table 4.3. The third column in Table 4.3 contains the $d_{(hkl)}$ values experimentally obtained from the SAEDPs in Fig. 4.16b and 4.17c. Unfortunately, a large background in the scattered intensity at low angles in the SAEDP in Fig. 4.16b and 4.17c does not allow to recognize the first few diffraction spots corresponding to the highest intensity peaks for $Mn(BH_4)_2$ at 2θ= 18.9, 19.5 and 21.2° which correspond to the $d_{(hkl)}$ interplanar spacing larger than 3.46 Å (Table 4.3). However, the other diffraction spots for $Mn(BH_4)_2$ at larger 2θ angles ($d_{(hkl)}$ smaller than 3.46 Å) are well visible in Fig. 4.16b and 4.17c and are summarized in the third column in Table 4.3. The experimental $d_{(hkl)}$ interplanar spacings for $Mn(BH_4)_2$, obtained from the electron SADPs in Fig. 4.16b and 4.17c, are in good agreement with the corresponding interplanar spacings calculated from the synchrotron radiation diffraction (the reader can compare the second and third column in Table 4.3). This excellent agreement confirms unambiguously the presence of crystalline $Mn(BH_4)_2$ after mechano-chemical synthesis, in the microstructure of the ball milled samples.

I calculated the average nanograin/crystallite size (expressed as ECD) of each constituent phase LiCl and $Mn(BH_4)_2$ from several HR TEM micrographs which exhibited a number of LiCl and $Mn(BH_4)_2$ grains similar to those visible in Fig. 4.17a. From the digital SAED patterns using FFT on a few HR TEM micrographs (similar to an example in Fig. 4.17c), I was able to identify fourteen grains of LiCl and eleven grains of $Mn(BH_4)_2$. For LiCl and $Mn(BH_4)_2$ the average ECD equals 14.1±3.7 and 10.0±2.9 nm, respectively. By comparison, the crystallite size for LiCl and $(MnBH_4)_2$, synthesized in the powder ball milled with Q_{TR}=145.6 kJ/g, was estimated by using the Scherrer formula from the XRD patterns to be equal to 30.6±5.6 and 18±1 nm, respectively, as reported in the previous section (4.1). The average ECD values for both the LiCl and $(MnBH_4)_2$ phases, estimated using HR TEM technique, are apparently smaller than the average crystallite size values estimated from the XRD Scherrer formula. This could be envisaged because two dissimilar methods were used for estimating a nanograin size which is well discussed in [89-91]. The important finding is that the HR TEM grain size analysis performed in this work confirms that both the LiCl and $Mn(BH_4)_2$ phases are nanocrystalline after being formed during mechano-chemical synthesis of the initial ($2LiBH_4+MnCl_2$) mixture.

Table. 4-3. Experimental 2θ values (from [36]) and calculated lattice spacings, $d_{(hkl)}$ for $Mn(BH_4)_2$ from synchrotron radiation, calculated 2θ angles X-ray radiation and SADP of from this work.

Experimental 2θ values from synchrotron radiation (λ=0.73065 Å) pattern in [36] for n=2	**Calculated $d_{(hkl)}$ (Å) for $Mn(BH_4)_2$ from the Bragg's law using λ=0.73065 Å for synchrotron**	**Experimental $d_{(hkl)}$ (Å) for $Mn(BH_4)_2$ from SAEDP in this work**
4.714	8.88311	---
7.992	5.24238	---
8.937	4.68901	---
9.207	4.55178	---
10.017	4.18454	---
10.584	3.96095	---
12.12	3.46051	3.46
12.201	3.43790	3.43
14.360	2.92291	2.89
15.340	2.73719	2.74
17.771	2.36530	2.36
18.090	2.32380	2.32
18.850	2.23091	2.23
19.681	2.13769	2.14
20.360	2.06701	---
21.631	1.94696	---
21.840	1.92847	---

4.2.2 TEM and EDS studies of nanocrystalline manganese borohydride ($Mn(BH_4)_2$) after thermal dehydrogenation

As illustrated in Fig. 4.8, the XRD pattern for the synthesized nanocomposite ($Mn(BH_4)_2$+2LiCl) after dehydrogenation and comparing it with Fig. 4.3a and 4.14 (just after MCAS) it can be seen that no peaks of $Mn(BH_4)_2$ are visible anymore while the LiCl peaks remains very strong. It is to be noted that no X-ray diffraction peaks of pure elemental Mn and B are visible in 4.8 as would be theoretically expected due to the proposed paths of thermal decomposition in both reactions (1.7) and (1.8).

Figures 4.18a and c show the TEM micrographs for the same synthesized nanocomposite ($Mn(BH_4)_2$+2LiCl) after thermal dehydrogenation at 100°C for 18.7 h whose XRD pattern is already shown in Fig. 4.8. Nearly round-shaped nanoscale particles are clearly visible in a larger agglomeration. The corresponding SAED patterns from the areas indicated by the red arrows in Figs. 4.18a and c are shown in Figs. 4.18b and d, respectively. Electron diffraction spots corresponding to the lattice planes of LiCl such as (111), (200), (220), (311) and (222), identified using ICDD (JCPDC) card # 74-1972, are clearly observed distributed on the calculated diffraction rings corresponding to randomly oriented nanoparticles in Figs. 4.18a and c.

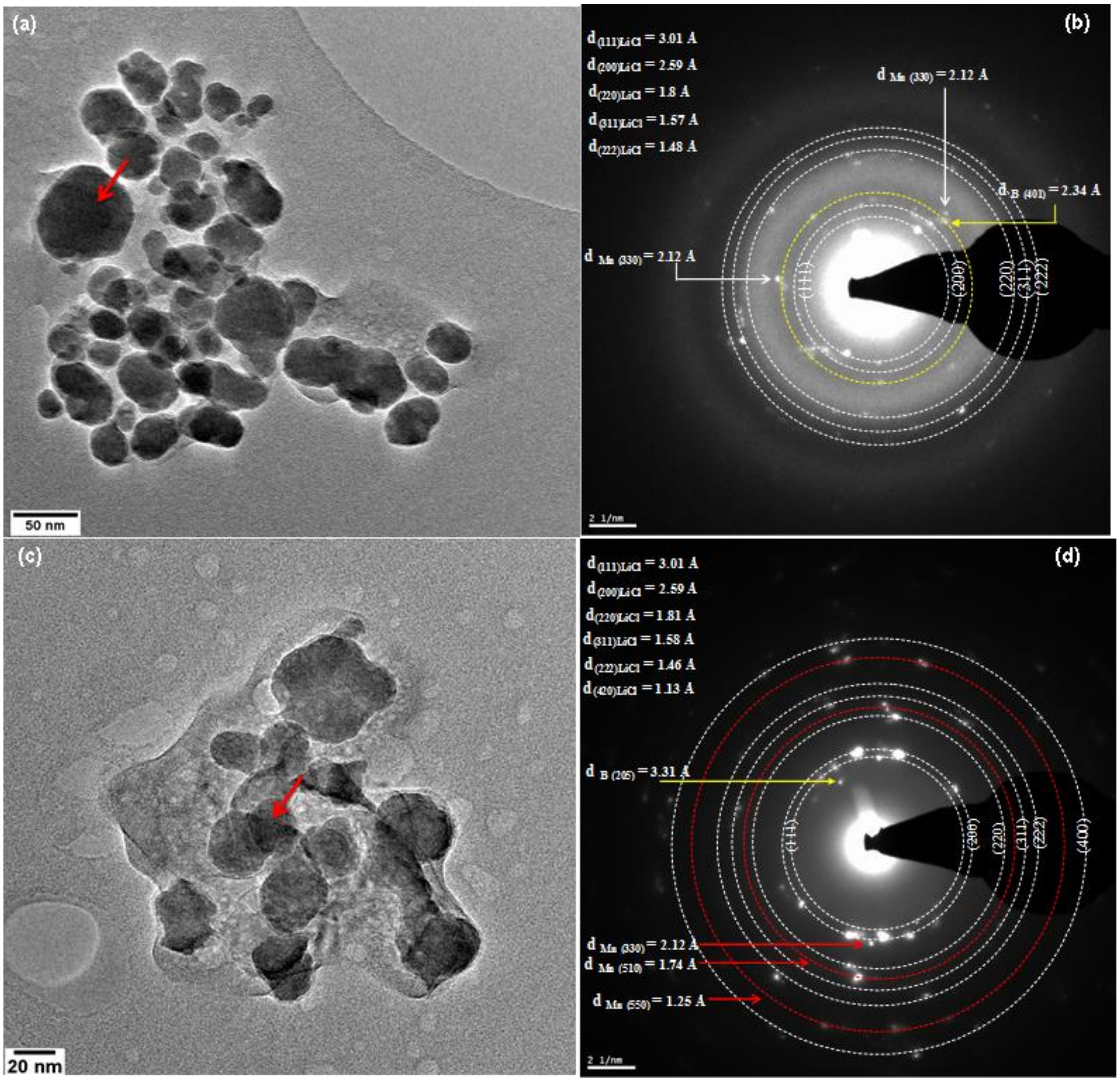

Fig. 4-18. (a, c) TEM micrograph of the synthesized nanocomposite ($Mn(BH_4)_2$+2LiCl) (dry condition) after dehydrogenation at 100°C (18.7 h) and (b, d) corresponding selected SAED patterns (adapted from [87]).

However, the most interesting finding is that a number of electron diffraction spots corresponding to crystalline α-Mn (space group I3m) and β-B rhombohedral (space group R3m) are also identified using ICDD (JCPDC) card #32-0637 and #11-0618, respectively. The most intense diffracting planes for α-Mn are collected in Table 4.4 including the lattice spacings ($d_{(hkl)}$), diffraction angles (2θ) and peak intensities.

According to Table 4.4 the strongest peak (100%) of α-Mn is assigned to the (330) plane with the $d_{(330)}$ spacing of 2.10 Å. The SAED patterns of annealed powder in Fig. 4.18b and d show strong diffraction spots of α-Mn corresponding to the diffraction planes (330), (510) and (550) (Table 4.4) distributed on the calculated diffraction rings which were calculated by the ImageJ software [80] based on the scale of the corresponding SAED pattern.

Table. 4-4. Interplannar spacing and Bragg diffraction angle 2θ for α-Mn as copmpared to experimentally observed TEM SAED patterns.

α-Mn ICDD (JCPDC) card #32-0637		**(SAEDP) This work**
$d_{(hkl)}$ (Å)	**I [%]**	**$d_{(hkl)}$ (Å)**
2.10110	100.0	2.12
1.89900	25.0	-
1.81900	9.0	-
1.74750	14.0	1.74
1.28640	4.0	-
1.26050	7.0	1.25

The first three strongest diffraction peaks of β-B occur at small diffraction angles of 2θ=11.12, 17.51 and 19.02° and conversely at larger $d_{(hkl)}$ spacings whose corresponding electron diffraction spots would be located very close to the center of SADPs in Fig. 4.18b and d. Unfortunately, they cannot be discerned in the respective SAED patterns because of the presence of a background coming from the fact that the particles are very small and distributed over an amorphous carbon film in Figs. 4.18b and d. Nevertheless, two electron diffraction spots from the lattice planes (205) and (401) with the lattice spacing $d_{(401)}$=2.34 Å and $d_{(205)}$=3.31 Å, belonging to β-B, are clearly detected in the SAED patterns in Figs. 4.18b and d.

The evidence that both Mn and B exist in the dehydrogenated powder as crystalline phases α-Mn and β-B, respectively, is another important finding in this work. It was shown earlier that the XRD pattern of the dehydrogenated ($Mn(BH_4)_2$+2LiCl) nanocomposite shown in Fig. 4.8 does not show any visible Bragg diffraction peaks belonging to crystalline Mn or B. In the cases where no crystalline diffraction peaks are present it is often assumed “a priori” that the decomposition products of $Mn(BH_4)_2$ are amorphous [35, 42]. However, to the contrary, the SAED patterns clearly show that both Mn and B products exit after dehydrogenation of $Mn(BH_4)_2$ in a crystalline form. For the sake of clarity, it is to be noted that in [36] very small but recognizable diffraction peaks of α-Mn after dehydrogenation of the synthesized mixtures ($nLiBH_4+MnCl_2$) where n=5, 9 and 23 was observed. No XRD peaks corresponding to crystalline α-Mn have ever been observed for the molar ratio n=2. Neither XRD peaks of crystalline β-B have ever been observed after dehydrogenation of $Mn(BH_4)_2$ for any molar ratio n in the ($nLiBH_4+MnCl_2$) mixture [7, 15, 33-36, 58].

In general, it must be pointed out that from either of decomposition reactions (1.7 and 1.8) the quantity of LiCl after desorption is 2 moles in the total mass of powder which is much larger than only 1 mole of Mn or B. Therefore, LiCl will be well detectable by XRD in contrast to Mn/B whose quantity could be insufficient to be detectable by XRD although Mn/B are detectable by electron diffraction which is capable of analyzing very small powder particles. The SAEDPs in Fig. 4.18a, c were taken from powder particles (red arrows) having sizes on the order of 20-50 nm. Since the SAEDPs show diffraction spots of LiCl, α-Mn and β-B, all these phases must have nanometric sizes to be confined within the 20-50 nm sized particles.

Additional support for the presence of nanometric sized α-Mn and β-B after thermal dehydrogenation of the ($(MnBH_4)_2+MnCl_2$) nanocomposite and decomposition of $Mn(BH_4)_2$ is provided by the EDS elemental distribution map for all elements: Cl (red), Mn (green) and B (blue) in Fig. 4.19a and particularly by the individual elemental maps for Cl (Fig. 4.19b), Mn (Fig. 4.19c) and B (Fig. 4.19d) from the powder thermally dehydrogenated at 100°C for 18.7 h whose XRD pattern is already shown in Fig. 4.8 and HR TEM images and SAED patterns are shown in Fig. 4.18.

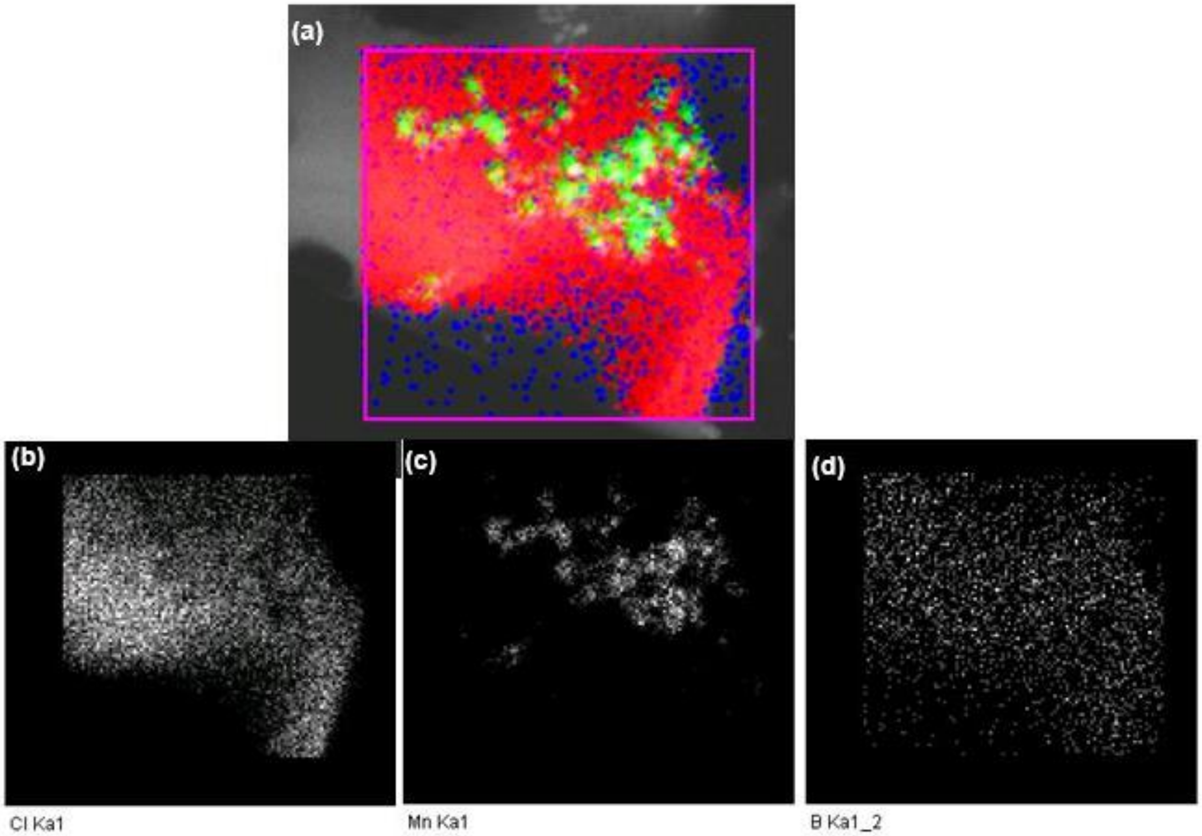

Fig. 4-19. (a) The energy X-ray dispersive spectroscopy (EDS) elemental distribution map after dehydrogenation at 100°C (18.7 h) and decomposition of $Mn(BH_4)_2$ for all elements: Cl (red), Mn (green) and B (blue)). Individual elemental distribution maps for (b) Cl, (c) Mn and (d) B (adapted from [87]).

For comparison to Fig. 4.19 the same EDS elemental distribution maps were taken from a synthesized nanocomposite ($Mn(BH_4)_2$+$MnCl_2$) after ball milling and are shown in Fig. 4.20.

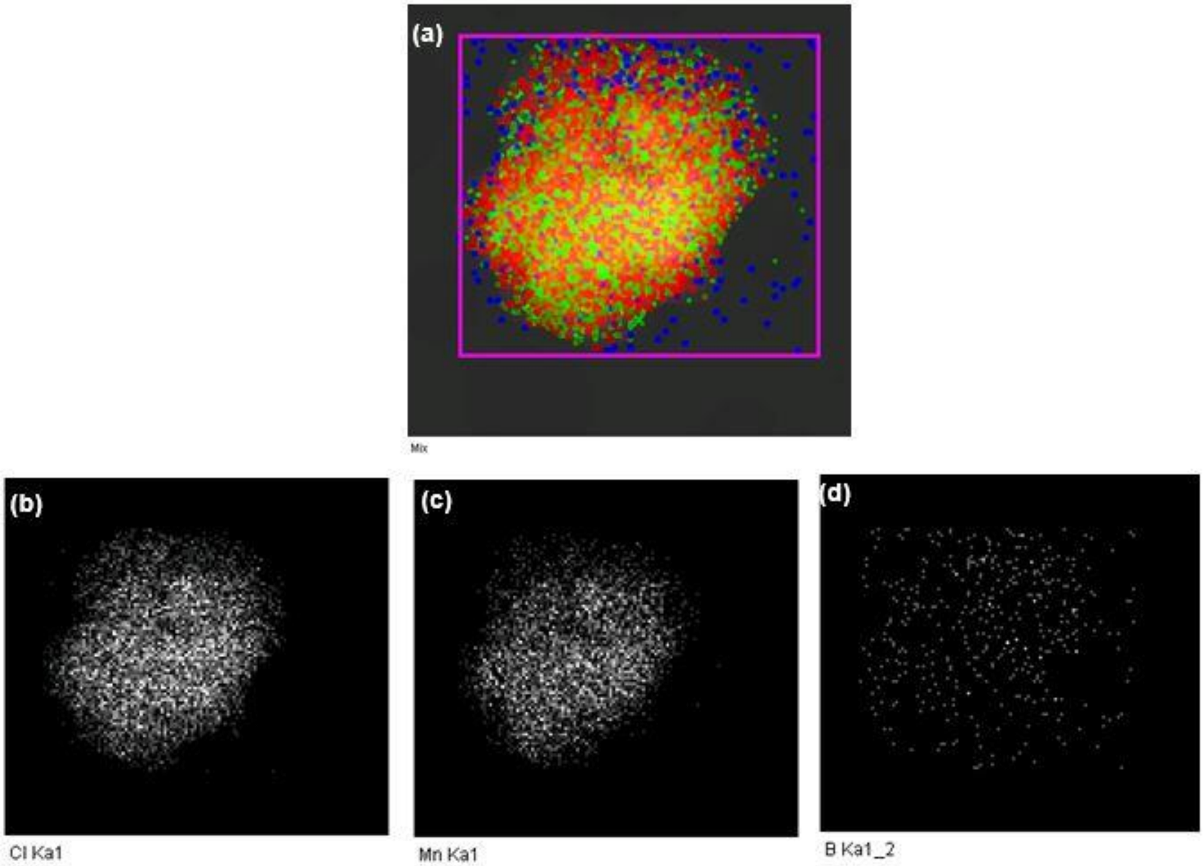

Fig. 4-20. (a) The energy dispersive X-ray spectroscopy (EDS) elemental distribution map for the synthesized nanocomposite ($Mn(BH_4)_2$+2LiCl) after ball milling with an energy input Q_{TR}=145.6 kJ/g (2 h) for all elements: Cl (red), Mn (green) and B (blue)). Individual elemental distribution maps for (b) Cl, (c) Mn and (d) B (adapted from [87]).

It is clearly seen, especially from individual EDS elemental maps that both the $MnK_{\alpha1}$ (Fig. 4.20c) and $BK_{\alpha1}$ (Fig. 4.20d) elements are very uniformly dispersed in the ball milled powder containing the synthesized $Mn(BH_4)_2$ phase while after thermal decomposition of $Mn(BH_4)_2$ the Mn element, as can be seen in its $MnK_{\alpha1}$ elemental map (Fig. 4.19c), is agglomerated into clusters, most likely, forming the α-Mn nanograins. There is no such a pronounced clustering observed in the elemental $BK_{\alpha1}$ map (Fig. 4.19d) for dispersion of β-B after decomposition of $Mn(BH_4)_2$ as compared to its dispersion after ball milling in the elemental $BK_{\alpha1}$ map in Fig. 4.20d.

A high resolution TEM image of the synthesized nanocomposite after thermal dehydrogenation (Fig. 4.17 and 4.18) is shown in Fig. 4.21a which was taken from one of the powder particles visible in Fig. 4.18c. Nanograins with different crystal orientations, which are contoured by a broken line, can be clearly seen. Employing FFT from the rectangle area indicated in Fig. 4.21a identifies those nanograins as belonging to LiCl. The digital diffraction patterns obtained using FFT in Fig. 4.21b presents two calculated electron diffraction rings which exactly conform to the diffraction pattern of the FCC LiCl structure.

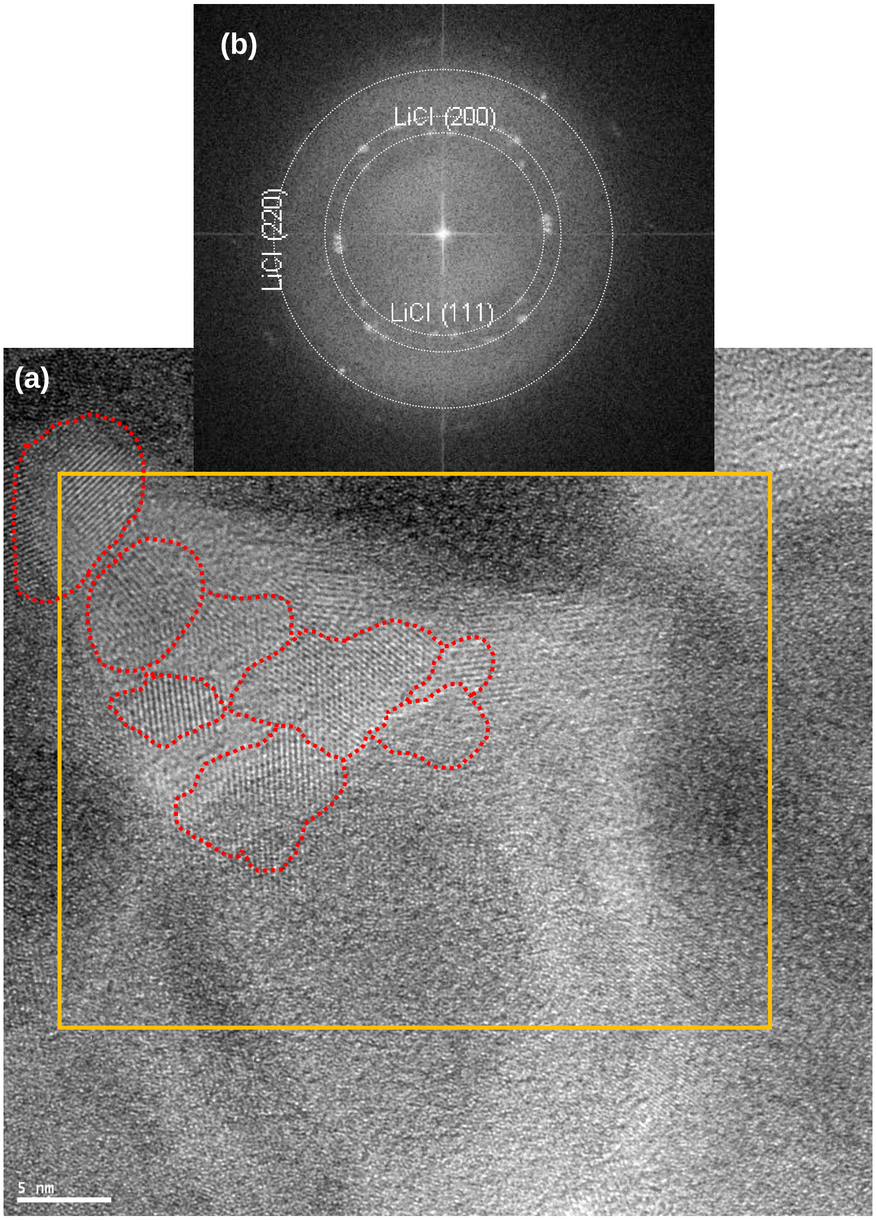

Fig. 4-21. (a) High resolution TEM micrograph of the initial synthesized nanocomposite ($Mn(BH_4)_2$+2LiCl) after thermal dehydrogenation at 100°C for 18.7 h. (b) A digital SAEDP using a fast Fourier transform (FFT) of the area inside the box in (a) (marker 5 nm) (adapted from [87]).

The average ECD for the LiCl nanograins visible in Fig. 4.21a was estimated as being equal to 6.1±1.8 nm. This value correlates well with the nanograin size of the LiCl phase after MCAS synthesis observed in the ball milled powder particles (Fig. 4.17).

4.3. Effect of additives on ($2LiBH_4$+$MnCl_2$) nanocomposite ball milled with the milling energy input Q_{TR}=72.8 kJ/g (1h)

In this section, the effects of ultrafine filamentary carbonyl nickel (Ni), graphene and $LiNH_2$ addition on suppressing the formation of B_2H_6 during decomposition will be discussed. In addition, the influence of doping with 5wt.% of additive on the decomposition kinetics of the dehydrogenation of $Mn(BH_4)_2$ during milling and thermal dehydrogenation is investigated.

4.3.1. Effects of additives on microstructural evaluation during mechanical and isothermal dehydrogenation of ($2LiBH_4$+$MnCl_2$)

The release of H_2 during one-hour ball milling for the sample without and with additives is illustrated in Fig. 4.22. As shown, almost no H_2 is desorbed during BM of the sample with 5 wt.% graphene. However, the addition of 5 wt.% Ni increases the amount of H_2 during BM to 0.48wt.%. On other hand, the sample without an additive released 0.2 wt.% H_2 after 1h BM, which is nearly identical to the amount of H_2 desorbed during the BM investigated in the previous section on the ($nLiBH_4$+$MnCl_2$) system. Adding 5wt.% $LiNH_2$ causes an increase in the quantity of H_2 released from 0.2 (for $2LiBH_4$+$MnCl_2$) to 0.25 wt.% H_2 for ($2LiBH_4$+$MnCl_2$)+5 wt.% $LiNH_2$.

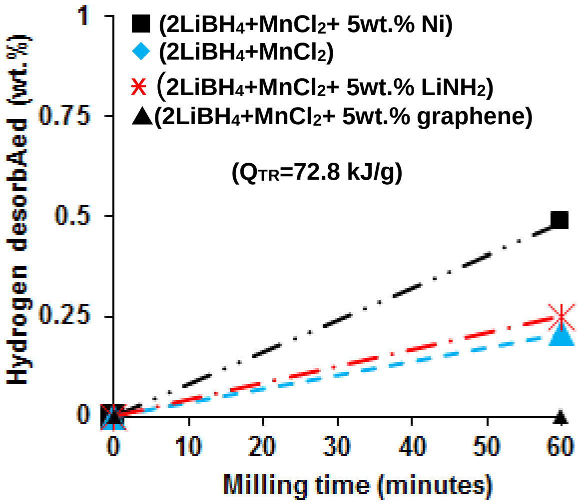

Fig. 4-22. The quantity of H_2 desorbed during milling of the initial ($2LiBH_4$+$MnCl_2$) powder mixtures without and with additives.

Fig 4.23 shows the XRD pattern of the ($2LiBH_4+MnCl_2$) nanocomposite ball milled with the milling energy input Q_{TR}=72.8 kJ/g (1h) compared with the one with 5 wt.% Ni.

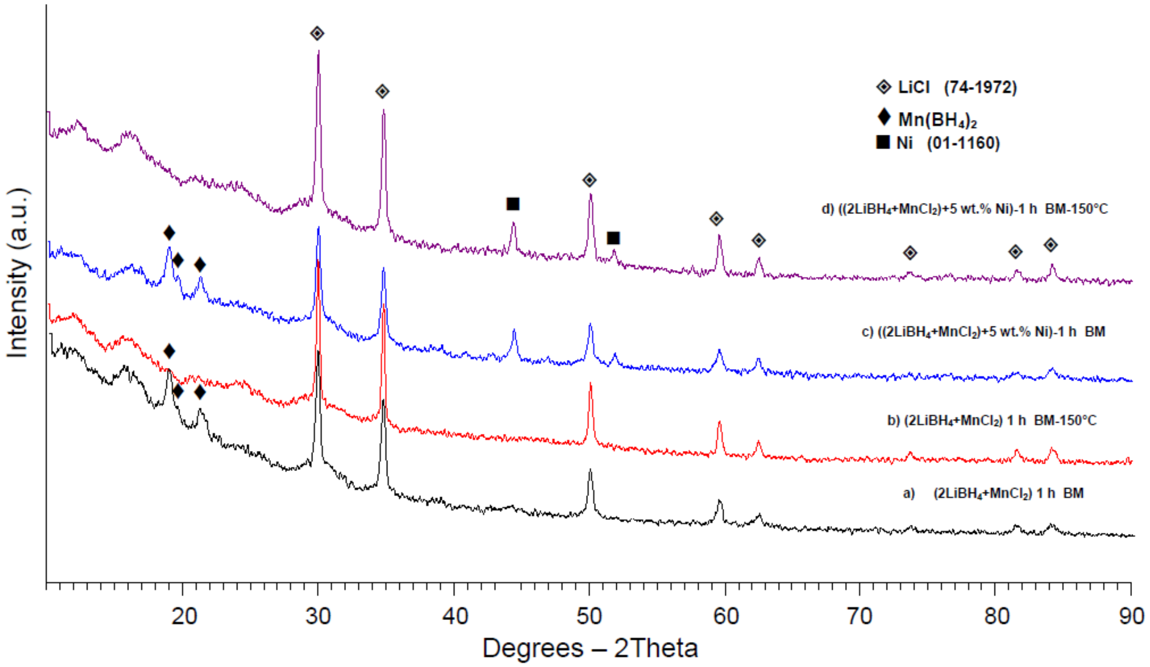

Fig. 4-23. XRD patterns of the $2LiBH_4+MnCl_2$ powder mixtures (a) ball milling (BM) with an energy input, Q_{TR}=72.8 kJ/g, for, (b) after isothermal dehydrogenation at 150 °C, (c) ball milling (BM) with an energy input, Q_{TR}=72.8 kJ/g, for the ($2LiBH_4+MnCl_2$)+5 wt.% Ni powder mixtures and (d) after isothermal dehydrogenation at 150 °C.

The XRD pattern for the sample with 5 wt.% graphene (Fig. 4.24) is nearly identical to the sample with no additive. No graphene XRD peaks are observed in Fig. 4.24 either, most likely due to transformation of graphene to amorphous structure after milling; whereas Ni peaks are visible in Fig. 4.23c and d.

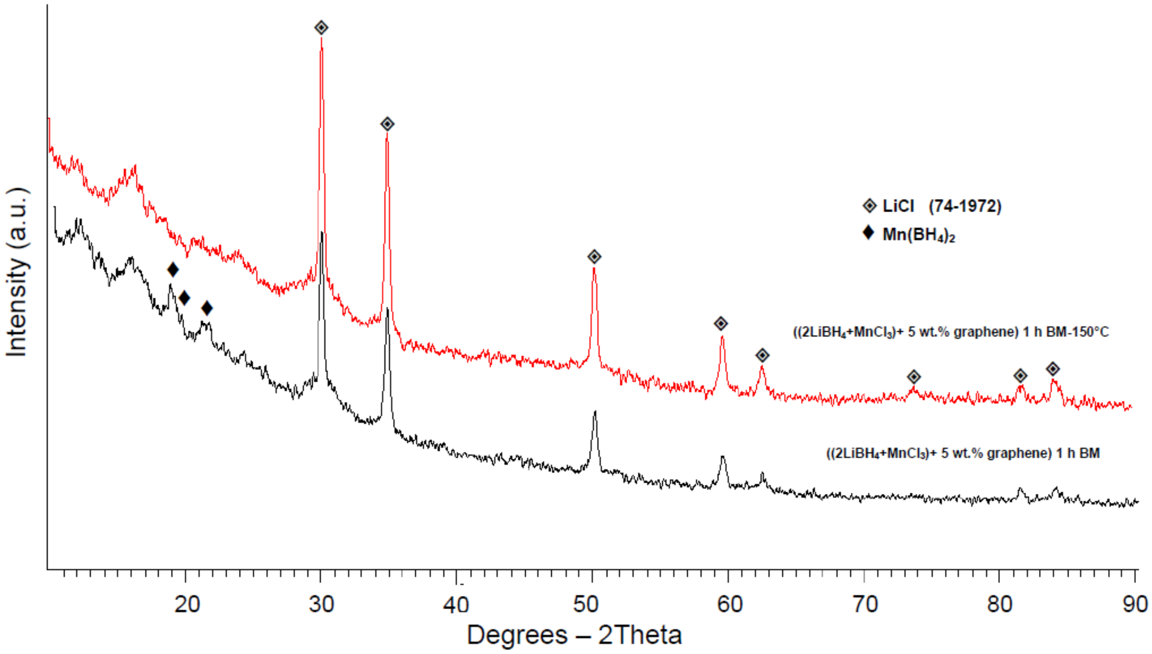

Fig. 4-24. XRD patterns of the mixture $(2LiBH_4+MnCl_2)$ +5 wt.% graphene ball milled for 1h (Q_{TR}=72.8 kJ/g) and after dehydrogenation at 150 °C.

Fig. 4.25 illustrates the XRD patterns of the milled powder mixture with 5 wt.% $LiNH_2$ with an energy input, Q_{TR}=72.8 kJ/g (1h) compared to the one after isothermal dehydrogenation at 100 °C. Complete transformation of the as-received powder mixture to $Mn(BH_4)_2$ and LiCl is observed after BM, whereas the LiCL peaks are the only XRD peaks which can be seen after thermal treatment.

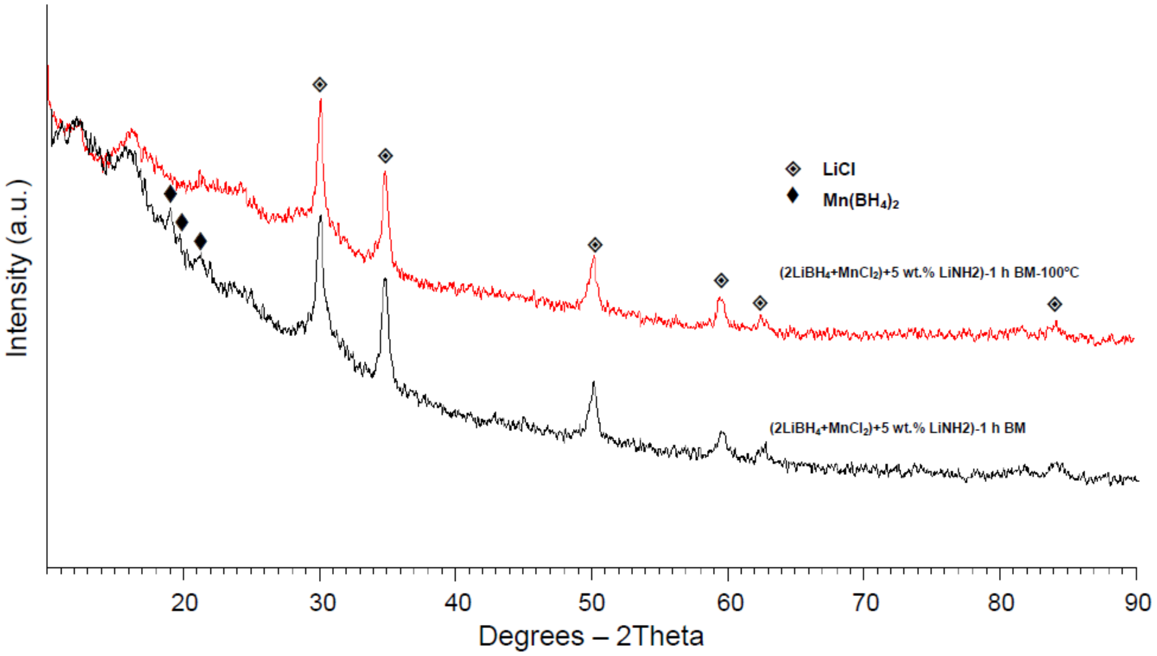

Fig. 4-25. XRD patterns of the mixture (2LiBH$_4$+MnCl$_2$) +5 wt.% LiNH$_2$ ball milled for 1h (Q$_{TR}$=72.8 kJ/g) and after dehydrogenation at 100 °C.

The FT-IR spectra for the (2LiBH$_4$+MnCl$_2$)+5 wt.% LiNH$_2$ with an energy input, Q$_{TR}$=72.8 kJ/g (1h) is shown in Fig. 4.26b and can be compared with the reference FT-IR spectrum for a (2LiBH$_4$+MnCl$_2$) sample ball milled with Q$_{TR}$=145.6 kJ/g (2h) containing a synthesized, crystalline Mn(BH$_4$)$_2$ hydride (which is already shown in Fig. 4.3) and shown in Fig. 4.26a again.

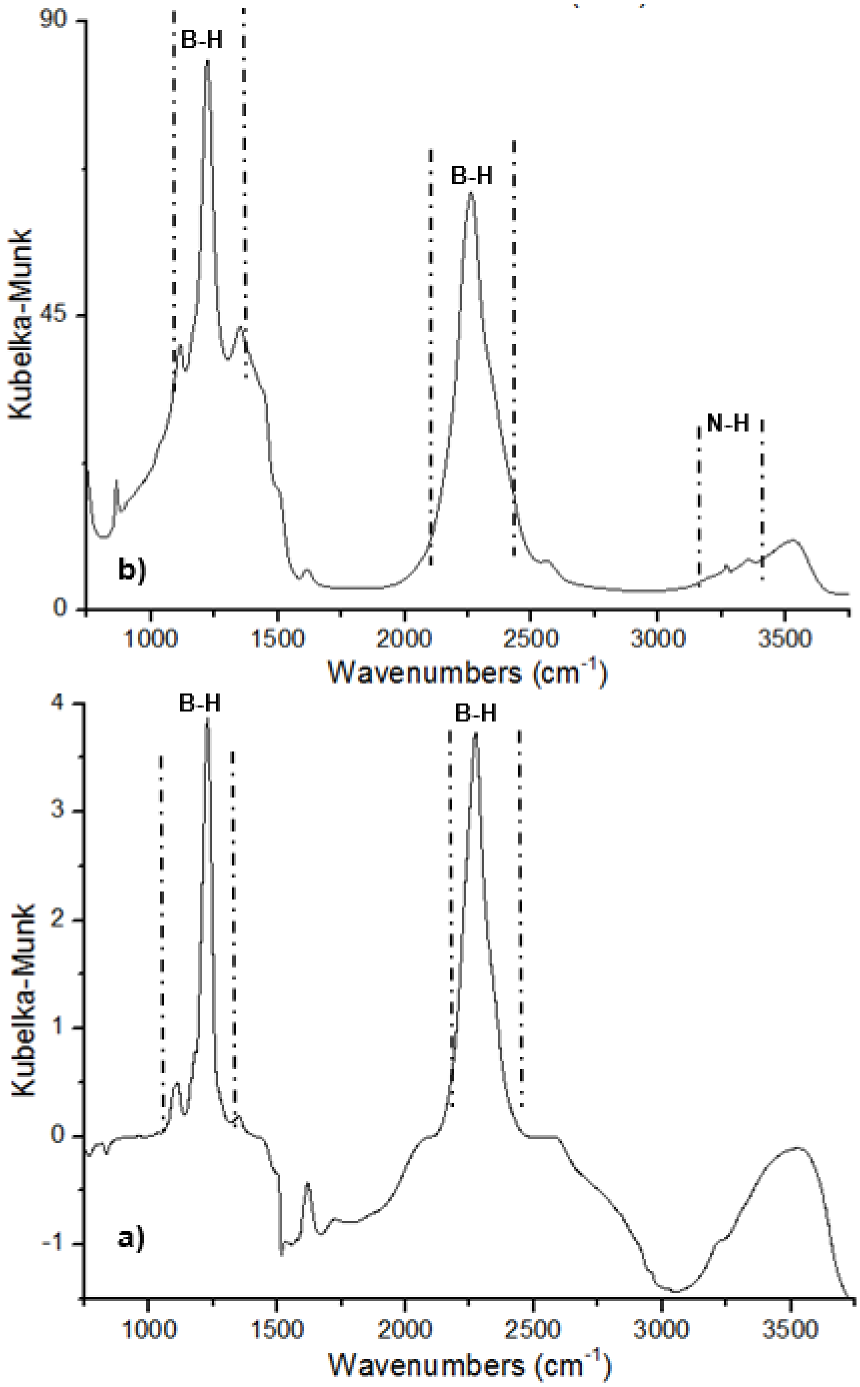

Fig. 4.26. (a) Reference FT-IR spectrum for a ($2LiBH_4$+$MnCl_2$) sample ball milled with Q_{TR}=145.6 kJ/g (2h) containing a synthesized, crystalline $Mn(BH_4)_2$ hydride (b) FT-IR spectrum for a ($2LiBH_4$+$MnCl_2$)+5 wt.% $LiNH_2$ sample ball milled with a milling energy input Q_{TR}=72.8 kJ/g (1h).

The FT-IR measurement shown in Fig. 4.26 strongly supports the presence of $Mn(BH_4)_2$ in this sample. Two IR active modes of B-H bending in the range of 1050-1350 cm^{-1} and stretching in the range of 2150-2400 cm^{-1} [92-94] are obvious in the FT-IR spectrum of the sample after 1h BM. The reference FT-IR spectrum for the crystalline $Mn(BH_4)_2$ synthesized by the MCAS of ($2LiBH_4+MnCl_2$) BM for 2h in Fig 4.26a shows a clear comparison of the bending and stretching bond of B-H formed after milling of ($2LiBH_4+MnCl_2$)+5 wt.% $LiNH_2$. The vibration of the N-H stretch bond in the range of 3290-3360 cm^{-1} is also seen in the sample with 5 wt.% $LiNH_2$ due to the presence of $LiNH_2$ in the mixture [37].

4.3.2. Effect of additives on thermal decomposition properties of ($2LiBH_4+MnCl_2$)

Gas mass spectrometry as well as DSC/TGA results during temperature programmed desorption (TPD) up to 500°C of the 1h ball milled samples without additive ($2LiBH_4+MnCl_2$) are shown in Fig. 4.27 (a and b) and can be compared to those with ($2LiBH_4+MnCl_2$)+5 wt.% graphene in Fig. 4.27 (c and d), with ($2LiBH_4+MnCl_2$)+5 wt.% Ni in Fig. 4.27 (e and f) and finally the ($2LiBH_4+MnCl_2$)+5 wt.% $LiNH_2$ in Fig. 4.27 (g and h). Release of H_2 as a principal gas as well as a miniscule quantity of borane B_2H_6 are observed for all 4 samples. Actually, hydrogen release started at 100 °C, with a maximum intensity at around 140-160°C. The ratio of H_2 to B_2H_6 is 493 up to 200°C (Fig. 4.27 (a)) for the ($2LiBH_4+MnCl_2$) sample, which is increased to 722 by adding 5 wt.% graphene (Fig. 4.27 (c)). Fig. 4.27 (g) shows the ratio of 3213 (H_2/B_2H_6) for the ($2LiBH_4+MnCl_2$)+5 wt.% $LiNH_2$ powder mixture. Gas mass spectrometry of the sample with 5wt.% Ni (Fig. 4.27e), however, shows greatly suppressed B_2H_6 (H_2/B_2H_6= 4667). The DSC curve of the ($2LiBH_4+MnCl_2$) after 1h BM sample (Fig. 4.27 (b)) exhibits a huge endothermic peak, with the maximum at around 150 °C. The principle endothermic peak and its maximum is profoundly shifted to a much higher temperature range (maximum at 168 °C) by adding 5wt.% graphene ((Fig. 4.27 (d)). In contrast, the sample with 5wt.% Ni shifted slightly to a lower temperature, with the maximum at about 146 °C ((Fig. 4.27b). Fig. 4.27 (h) shows the DSC curve of the sample with 5wt.% $LiNH_2$; a sharp exothermic peak occurred at 120 °C and then a small endothermic peak at nearly133 °C. However, the DSC of the ($2LiBH_4+MnCl_2$)+5 wt.% $LiNH_2$ sample (Fig. 4.27h) shows a huge exothermic peak (120 ºC) before the characteristic endothermic peak for decomposition of $Mn(BH_4)_2$ at (133 °C) indicating that the decomposition mechanism of this sample occurs through overlapping of exothermic and endothermic reactions.

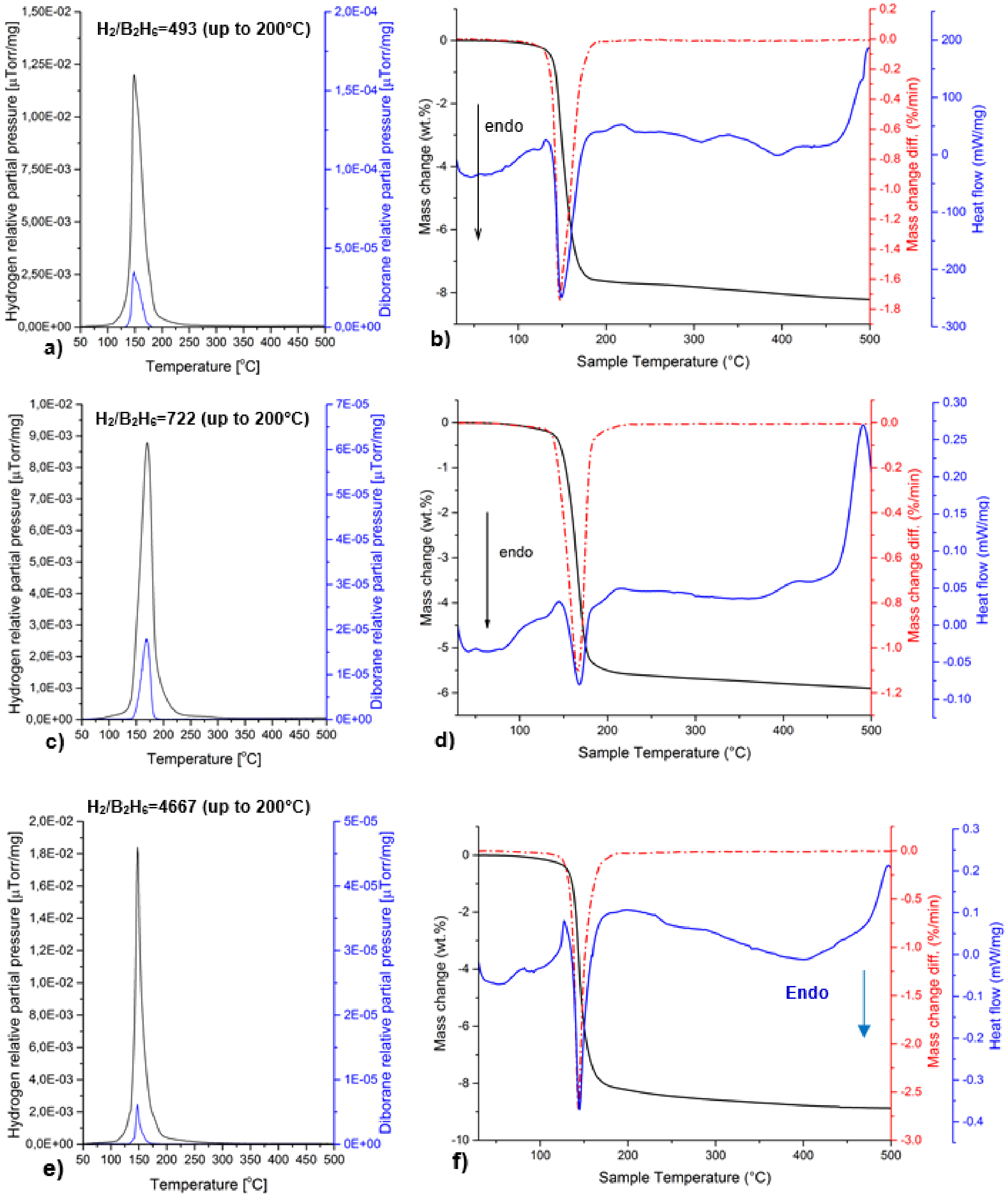

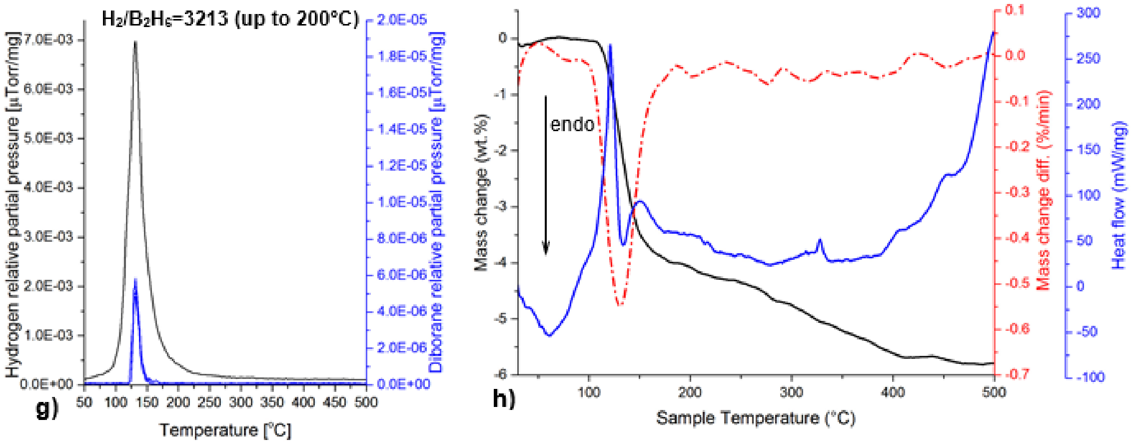

Fig. 4.27. (a) Mass spectrometry (MS) gas desorption spectra and (b) TG and DSC curves for a ($2LiBH_4+MnCl_2$) sample ball milled for 1h, (c) (MS) gas desorption spectra and (d) TG and DSC curves for a ($2LiBH_4+MnCl_2$) +5 wt.% graphene, (e) (MS) gas desorption spectra and (f) TG and DSC curves for a ($2LiBH_4+MnCl_2$) +5 wt.% Ni, (g) (MS) gas desorption spectra and (h) TG and DSC curves for a ($2LiBH_4+MnCl_2$) +5 wt.% $LiNH_2$.

Fig. 4.28 shows the dehydrogenation curves of different samples obtained at different temperatures. Fig. 4.28 (a) shows isothermal dehydrogenation curves of the ($2LiBH_4+MnCl_2$)+5 wt.% graphene at 100, 150 and 200 °C with an energy input, Q_{TR}=72.8 kJ/g (1h). Dehydrogenation curves of ($2LiBH_4+MnCl_2$)+5 wt.% Ni and ($2LiBH_4+MnCl_2$)+5 wt.% $LiNH_2$ are also shown in Fig. 4.28 (b) and (c), respectively. As mentioned earlier, the theoretical capacity of reaction (1.6) is 4.76 wt.% H_2, which will be reduced to 4.53 wt.% H_2 by adding 5 wt.% additive to the as-received materials. The total quantity of desorbed hydrogen at 100 °C is 3.83 for the sample with 5wt.% graphene, 4.03 wt.% H_2 for the sample with 5wt.% Ni and 4.28 wt.% H_2 for the sample with 5wt.% $LiNH_2$.

It is apparent that using 5wt.% additives (Ni, graphene, $LiNH_2$) can minimize the release of B_2H_6 during isothermal dehydrogenation. Adding 5wt.% additives to the powder mixture leads to increased intensity ratio of the corresponding peaks of H_2 to B_2H_6. $LiNH_2$ and Ni better suppress the release of B_2H_6 than graphene. However, it seems that Ni does not reduce the decomposition temperature of $Mn(BH_4)_2$, while 5wt.% graphene increases the decomposition temperature of $Mn(BH_4)_2$ from 150 to 168 °C. On the other hand, $LiNH_2$ is able to reduce the decomposition temperature of $Mn(BH_4)_2$, shown by the endothermic peak in DSC, significantly from 150 °C to 133 °C (Fig. 4.27 (h)). It is worth noting that the N-H stretch bond in pure $LiNH_2$ is at the wave numbers range of 3500-3700 cm^{-1}, which is shifted to the higher range of 3290-3360 cm^{-1} by doping the ($2LiBH_4$+$MnCl_2$) sample with 5wt.% $LiNH_2$. A similar result was observed by Song et al. [37]. They reported that compared to pure $LiNH_2$, the characteristic peaks of the N-H stretch bonds in $LiNH_2$-doped $3LiBH_4/MnF_2$ composites shifted toward higher wavenumbers, which suggests that the combination of BH_4^- and NH_2^- has taken place during the doping process.

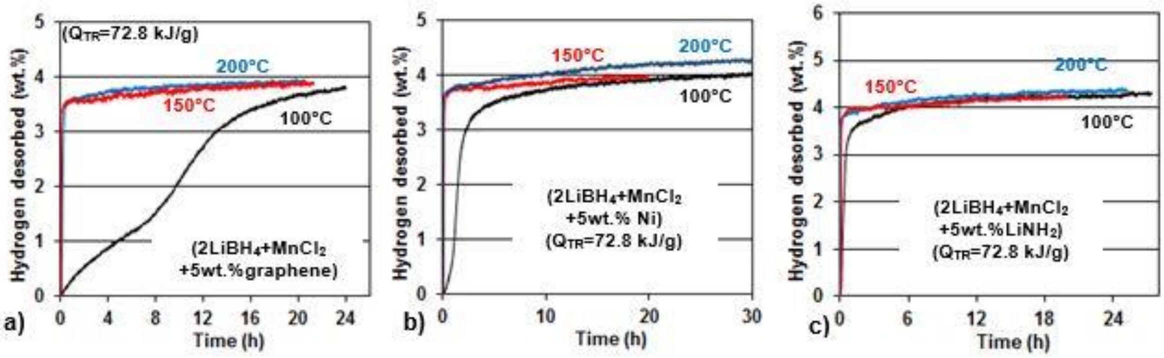

Fig. 4.28. Desorption curves of a) ($2LiBH_4$+$MnCl_2$) +5 wt.% graphene ball milled for 1h (Q_{TR}=72.8 kJ/g) and after dehydrogenation at 100, 150 and 200 °C, b) ($2LiBH_4$+$MnCl_2$) +5 wt.% Ni ball milled for 1h (Q_{TR}=72.8 kJ/g) and after dehydrogenation at 100, 150 and 200 °C, c) ($2LiBH_4$+$MnCl_2$) +5 wt.% $LiNH_2$ ball milled for 1h (Q_{TR}=72.8 kJ/g) and after dehydrogenation at 100, 150 and 200 °C.

The apparent activation energy values calculated for the isothermal dehydrogenation for the ($2LiBH_4$+$MnCl_2$) milled with an energy input, Q_{TR}=72.8 kJ/g (1h) at three different temperatures (100 ºC, 150 ºC and 200 ºC) are shown in Fig. 4.29a and compared to those with 5wt.% additives. Fig. 4.29b compares the isothermal dehydrogenation curves of the sample without additive and those with additives at 100 °C. The sample with graphene tends to release hydrogen at a lower rate. The faster kinetic of desorption at 100 °C can be seen for the sample with $LiNH_2$ compared with the sample without additive from Fig. 4.29.

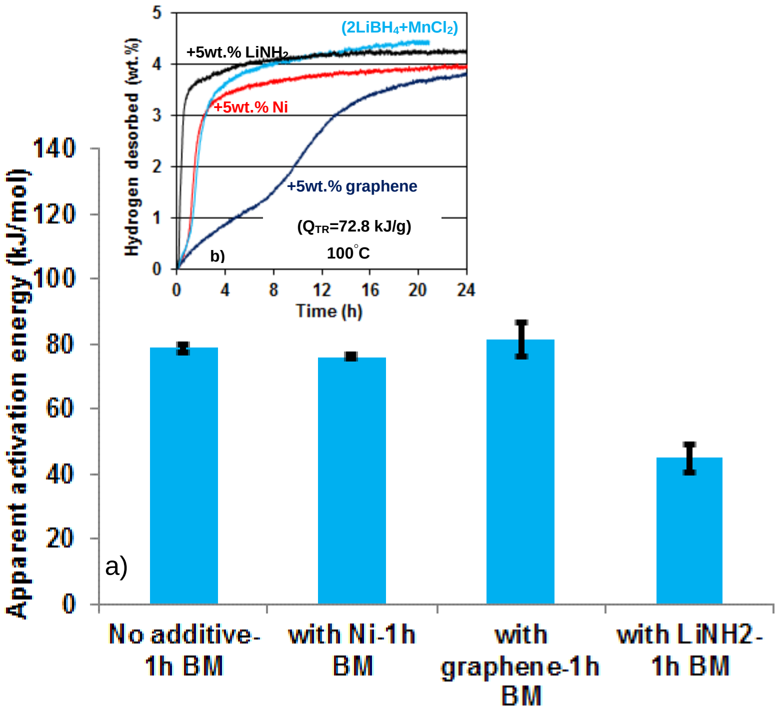

Fig. 4.29. a) Apparent activation energy (kJ/mol) for dehydrogenation for the samples with and without additives after 1h BM and b) comparison of isothermal dehydrogenation curves at 100 °C for the sample with and without additives.

The dehydrogenation curves in the range of 100 ºC to 200 ºC such as those shown in Fig. 4.28, were taken to estimate the apparent activation energy for dehydrogenation of the ball milled composites. As shown in Fig. 4.29, the apparent activation energies for dehydrogenation of the sample without additive and the one with 5wt.% Ni are quite similar. As compared to 78.9±1.2 kJ/mol for an undoped ($2LiBH_4$+$MnCl_2$) powder mixture, the activation energy of 76.1±0.6 kJ/mol for a 5wt.% Ni- doped ($2LiBH_4$+$MnCl_2$) composite indicates that 5wt.% Ni yields no obvious improvement in the kinetics of dehydrogenation. Graphene, however, has a slightly higher apparent activation energy for dehydrogenation (81.5±5.2 kJ/mol), which was expected since the $2LiBH_4$+$MnCl_2$+5wt.% graphene shows very slow dehydrogenation at 100ºC compared to other samples illustrated in Fig. 4.29b. The most striking observation to emerge from the apparent activation energy comparison is that 5wt.% $LiNH_2$ can reduce the apparent activation energy to 44.9±4.3 kJ/mol. This reduction may result from the destabilizing of the B-H bonds in ($2LiBH_4$/$MnCl_2$) during BM through the electrostatic attraction between

H^- in BH_4^- and H^+ in NH_2^-, with consequent lower decomposition temperature and faster dehydrogenation [37].

4.4 Solvent extraction of ($2LiBH_4+MnCl_2$) nanocomposite ball milled with the milling energy input Q_{TR}=72.8 kJ/g (1h)

In this section, simple solvent-extraction method was used to remove or decrease the quantity of LiCl, which is a salt in the product of MCAS powder ($Mn(BH_4)_2$•LiCl), in order to increase the capacity of hydrogen released from the product.

4.4.1 Evaluation of the microstructure of ($2LiBH_4+MnCl_2$) powder mixture after solvent extraction

Fig. 4.30 illustrates the XRD pattern of the 1st and 2nd Ext powder mixture without additives at RT and 42 °C as described in the Experimental section. The XRD pattern of the powder that could not pass through the filter during the solvent extraction process is also shown in Fig. 4.30e. XRD diffraction of the 1st EXT at 42°C sample after isothermal dehydrogenation at 100 ºC is illustrated in Fig. 4.30f.

Comparing the XRD pattern of the sample after BM (Fig. 4.23) with the one after solvent extraction (Fig. 4.30 (a-d)), with the one after isothermal dehydrogenation (Fig. 4.30 e), and with the powder left in the filter during filtration, five broad themes emerged:

1. The LiCl peaks became weaker (lower intensity) after 1st EXT than the one after MCAS
2. 2nd EXT shows further reduction in the intensity of LiCl peaks regardless of the solvent extraction temperature
3. The most striking result to emerge from the XRD of the solvent extraction powders is that $[\{Li(Et_2O)_2\}Mn_2(BH_4)_5]$ crystallizes in the powder after extraction. The identification of $[\{Li(Et_2O)_2\}Mn_2(BH_4)_5]$ was based on the data reported in [41], which shows that it has a monoclinic space group C2/c (Table. 2 in ref [41]).
4. $[\{Li(Et_2O)_2\}Mn_2(BH_4)_5]$ peaks that formed due to the solvent extraction have completely disappeared after isothermal dehydrogenation, indicating that the newly formed phase is fully decomposed.

5. LiCl is the only phase characterized from the XRD pattern of the powder inside of the filter that could not pass through the filter.

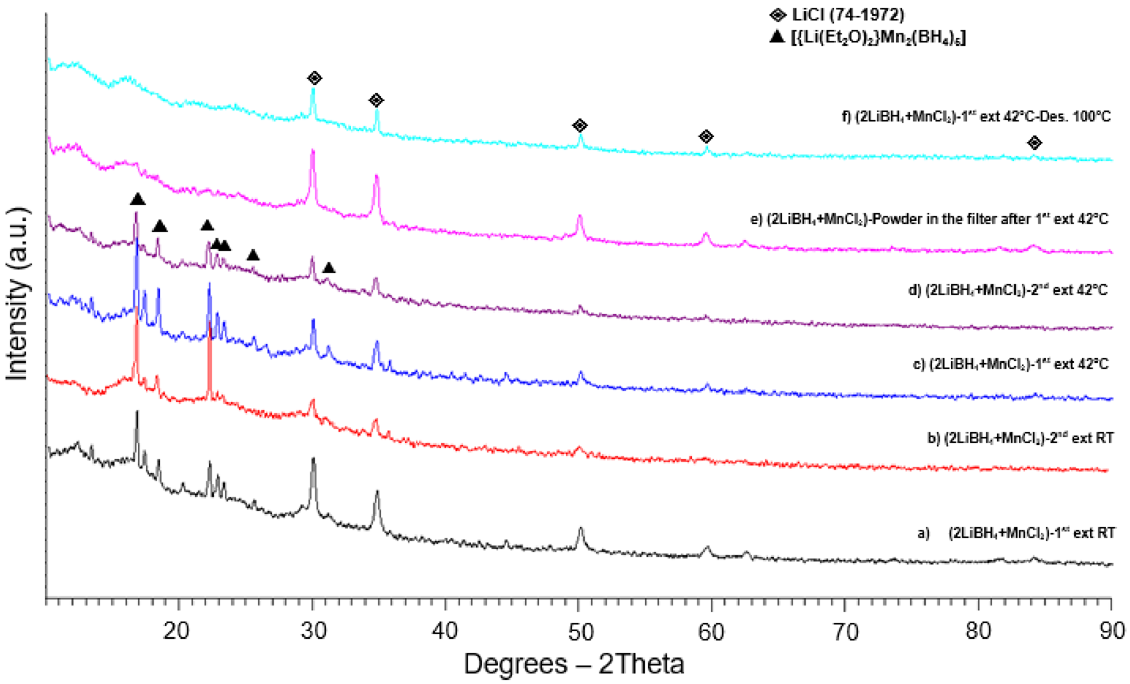

Fig. 4.30. XRD patterns of ($2LiBH_4$+$MnCl_2$) powder mixtures after (a) milled and first solvent extracted at RT (b) milled and second solvent extracted at RT (c) milled and first solvent extracted at 42 °C (d) milled and second solvent extracted at 42 °C (e) Powder in the filter after first solvent extraction of ($2LiBH_4$+$MnCl_2$) powder mixtures and (f) after isothermal dehydrogenation at 100 °C of first extracted sample at 42 °C.

Fig. 4.31 shows the XRD peaks after 1st EXT of the powder mixture with 5wt.% Ni and Graphene. A scenario similar to the one for the sample without additives (Fig. 4.30) is seen in both powder mixtures with Ni and graphene after solvent extraction: the LiCl peaks' intensity becomes weaker, whereas the [{Li(Et_2O)$_2$}Mn_2(BH_4)$_5$] crystallized after solvent extraction. In addition, peaks of [{Li(Et_2O)$_2$}Mn_2(BH_4)$_5$] disappear after isothermal dehydrogenation. The XRD pattern of the powder inside of the filter after the extraction of ($2LiBH_4$+$MnCl_2$)+5 wt% Ni, as shown in Fig. 4.31 (e), indicates that neither Ni or LiCl can pass through the filter. Apparently, the size of Ni after 1h BM and solvent extraction is not small enough to pass through the filter.

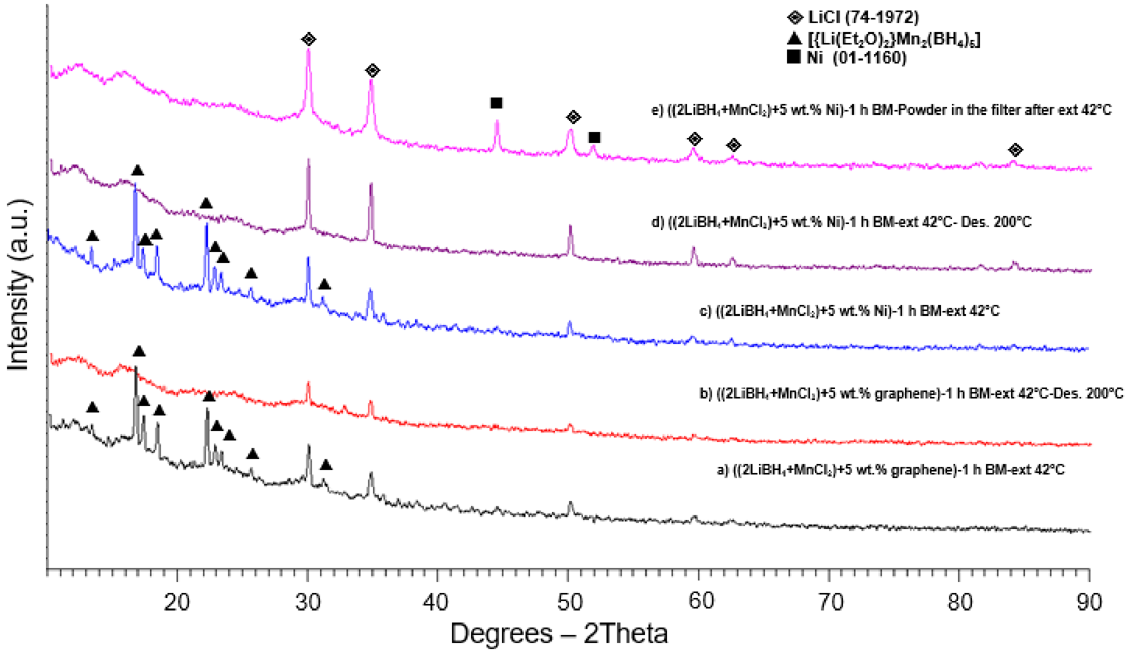

Fig. 4.31. XRD patterns of a) (2LiBH$_4$+MnCl$_2$) +5 wt.% graphene-1h BM extracted at 42°C b) after dehydrogenation of sample (a) at 200 °C, c) (2LiBH$_4$+MnCl$_2$) +5 wt.% Ni-1h BM extracted at 42°C, d) after dehydrogenation of sample (c) at 200 °C and e) powder in the filter through extraction of sample c.

The FT-IR spectra for the (2LiBH$_4$+MnCl$_2$) after the 1st EXT sample are shown in Fig. 4.32b and can be compared with the reference FT-IR spectrum for a (2LiBH$_4$+MnCl$_2$) sample ball milled with Q_{TR}=145.6 kJ/g (2h) containing a synthesized, crystalline Mn(BH$_4$)$_2$ hydride (which is already shown in Fig. 4.3 and Fig. 4.26a) and shown in Fig. 4.32a again.

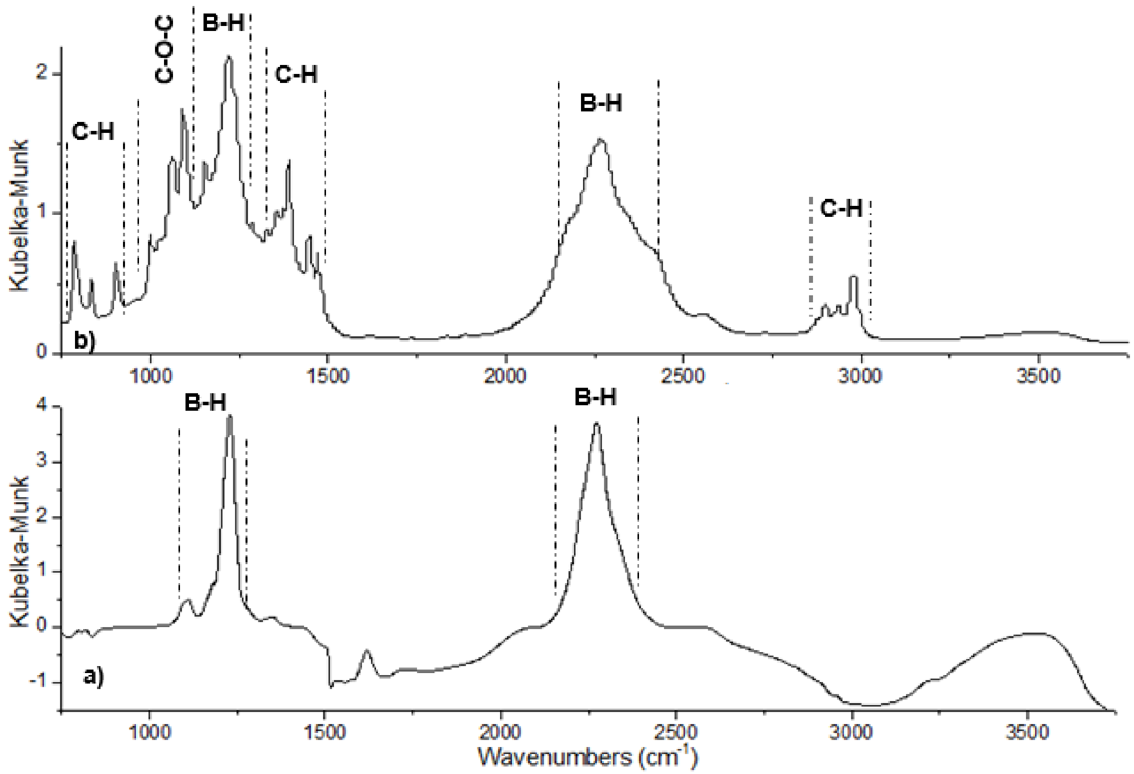

Fig. 4.32. (a) Reference FT-IR spectrum for a ($2LiBH_4$+$MnCl_2$) sample ball milled with Q_{TR}=145.6 kJ/g (2h) containing a synthesized, crystalline $Mn(BH_4)_2$ hydride (b) FT-IR spectrum for a ($2LiBH_4$+$MnCl_2$) sample ball milled with a milling energy input Q_{TR}=72.8 kJ/g (1h) and extracted at 42°C.

As mentioned in the literature review (section 1.8.1), very little was found on the removal of salt from the composite powder after MCAS. Soxhlet apparatus had been used for removing NaCl and LiCl from the MCAS powders of $Mg(AlH_4)_2$-2NaCl and $Ca(AlH_4)_2$-2LiCl, respectively [43]. As pointed out in the section 1.8.1, the authors reported that an extraction method using Et_2O as a solvent in the Soxhlet apparatus led to crystallization of the $Mg(AlH_4)_2{\bullet}Et_2O$ adduct from the solvent. They could remove Et_2O after further heating in vacuum [43].

Turning now to the experimental evidence, [$\{Li(Et_2O)_2\}Mn_2(BH_4)_5$] is a crystalline phase which has been formed and detected by XRD of the extracted powders, as shown in Fig. 4.30. Crystalization of the [$\{Li(Et_2O)_2\}Mn_2(BH_4)_5$] has recently been reported by Tumanov et al. [41]. They studied the reaction of $MnCl_2$ with $M(BH_4)_2$ ($M=Li^+$, Na^+) in Et_2O and reported that [$\{M(Et_2O)_2\}Mn_2(BH_4)_5$] ($M= Li^+$, Na^+) was the crystalline phase elucidated by XRD. For the unambiguous identification of [{$Li(Et_2O)_2$}$Mn_2(BH_4)_5$] from the XRD in Fig. 4.30 and 4.31, I used the 2θ values extracted from the synchrotron radiation diffraction pattern reported in [41] for the synthesized powder after reaction of 0.7 g $Li(BH_4)_2$ and 2.52g LiCl in 120 ML Et_2O, which are tabulated in the first column in Table 4.5. Using the synchrotron 2θ values and the synchrotron radiation wavelength from [41], the plane spacings $d_{(hkl)}$ for [{$Li(Et_2O)_2$}$Mn_2(BH_4)_5$] were calculated using Bragg's law and are listed in the second column in Table 4.5. The $d_{(hkl)}$ values experimentally obtained from the XRDs in Figs. 4.30 are listed in the third column in Table 4.5. Excellent agreement can be seen from comparison of the plane spacing calculated from the synchrotron radiation (second column) and the one from XRD (third column). The largest $d_{(hkl)}$ observable from the XRD pattern in this work is 8.838 Å, because the scan range of XRD starts at 2θ=10°. One of the issue that emerges from the XRD pattern of the extracted powder presented in Fig. 4.30 is that the peaks of LiCl (in lower intensity) can still be seen even after filtration. There are two likely causes for this: 1) although LiCl is extremely poorly soluble in pure Et_2O, it can be efficiently trapped by the [$Mn(BH_4)_2$-Et_2O] system, consequently increasing the solubility; and; 2) LiCl particles smaller in size than the filter (0.2μm) may form and therefore cannot be filtered out [41]. Two IR characteristic bands for the BH_4^- groups in the range of 1050-1350 cm^{-1} and in the range of 2150-2400 cm^{-1} strongly support the presence of borohydride in the sample extracted at 42 ºC, illustrated in Fig. 4.32b. Modes of C-H bending in the range of 750-900 cm^{-1} and stretching in the ranges of 1390-1470 and 2900-2980 cm^{-1}, and the typical C-O-C stretch band in the range of 1000-1090 cm^{-1} exhibit a set of characteristic bands for the Et_2O molecules (Fig. 4.32b) [43, 95].

The presence of Ni could improve the kinetics of dehydrogenation in the extracted samples. Unfortunately, I was unable to obtain Ni used as additive in the final product of the extracted sample since, as detected by XRD in Fig. 4.31 (c) and (e), Ni could not pass through the filter and remained in it. The possible explanation of the lack of Ni in the extracted sample can be interpreted by looking at the SEM images in Fig. 4.33. Generally, Ni was supposed to pass through the filter due to the lower particle size than the filter. However, as illustrated in Fig. 4.33c, the morphology of the powder kept in the filter is severely agglomerated compared to the extracted samples after filtration (Fig.

4.33 a and b), indicating that Ni particles became agglomerated through BM and mixing with Et_2O.

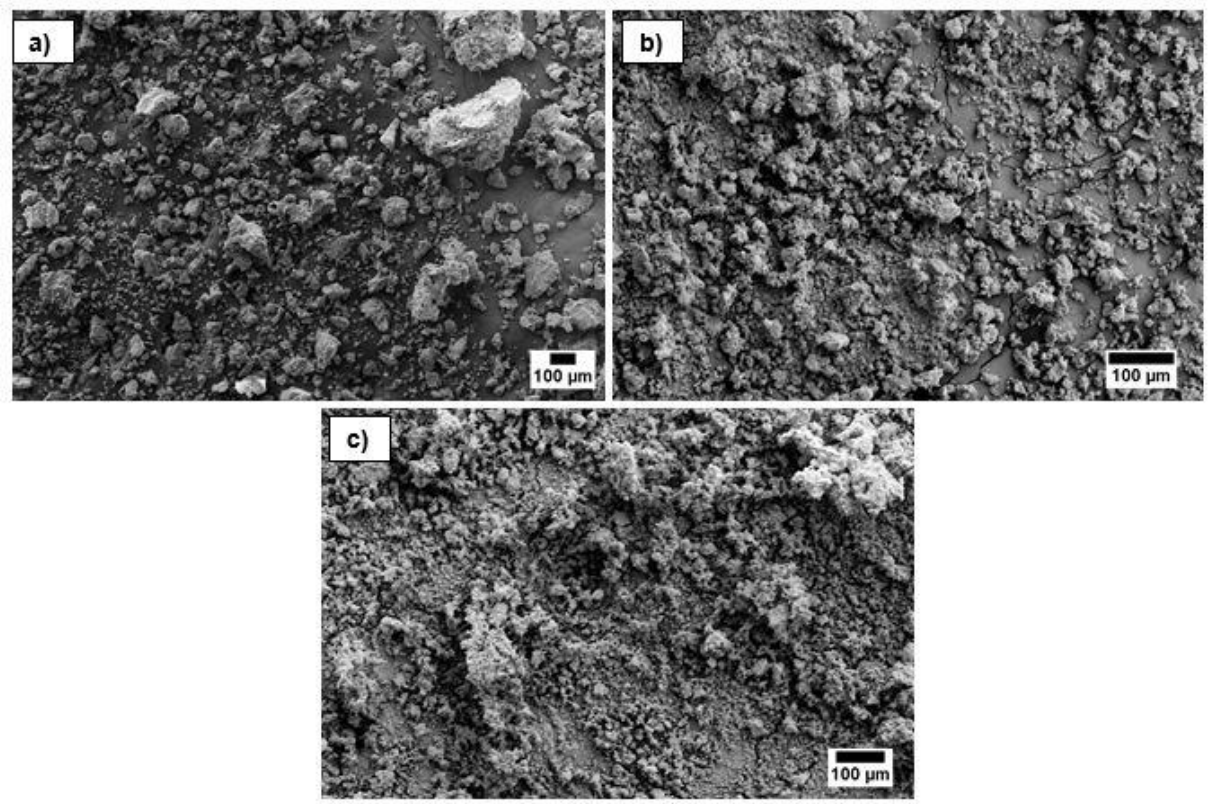

Fig. 4.33. SEM micrograph a) ($2LiBH_4$+$MnCl_2$) milled for 1h and after first extraction at 42 °C b) ($2LiBH_4$+$MnCl_2$)+5 wt.% Ni after 1h BM and extraction at 42 °C, c) powder left in the filter during the solvent extraction process of the ($2LiBH_4$+$MnCl_2$)+5wt.% Ni.

4.4.2 Thermal properties of the solvent extracted samples

Gas mass spectrometry as well as DSC/TGA results during temperature programmed desorption (TPD) up to 500°C of the extracted sample (EXT-$2LiBH_4$+$MnCl_2$) without additive are illustrated in Fig. 4.34 (a and b). Release of H_2 as a principal gas as well as a miniscule quantity of borane B_2H_6 is observed for this sample. Actually, hydrogen release started at 100 °C, with a maximum intensity at around 140-160°C. The ratio of H_2 to B_2H_6 for the sample after extraction has not been calculated, unfortunately, due to the high mass lost (~ 33%) during thermal analysis (Fig. 4.34a). As can be seen in DSC of the sample after solvent extraction is illustrated in 4.34 (b), the first big endothermic peak starts at around 72 °C, with the maximum at about 100 °C, and the second one is at its maximum at about 130 °C.

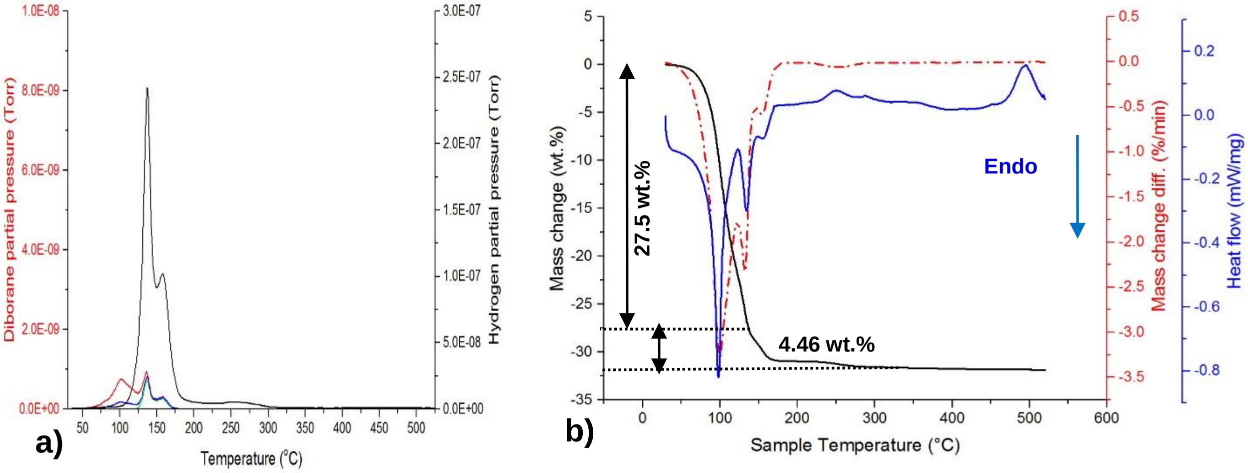

Fig. 4.34. (a) Mass spectrometry (MS) gas desorption spectra and (b) TG and DSC curves for a (2LiBH$_4$+MnCl$_2$) after first extraction at 42 °C.

Fig. 4.35 presents the quantities of hydrogen desorbed after isothermal dehydrogenation at 100 °C and 200 °C for (2LiBH$_4$+MnCl$_2$), before and after solvent extraction, in two bar graphs. Fig. 4.35a shows the total quantity of H_2 desorbed after full desorption, while the one after 18h desorption is illustrated in Fig. 4.35b. The quantity of hydrogen desorbed after full isothermal dehydrogenation with the corresponding time of full desorption are presented in Table 1A (second column, Appendices). The times to reach 3, 4 and 5 wt.% H_2 for (2LiBH$_4$+MnCl$_2$) milled with an energy input, Q_{TR}=72.8 kJ/g (1h) as well as those after 1st and 2nd solvent extraction at different temperatures are also summarized in Table 1A. This table also shows that, among all samples, after 1st extraction at different temperatures, extraction at 42 °C has the maximum quantity of H_2 desorbed, 5.14 and 5.72 wt.% H_2 at 100 °C and 200 °C isothermal dehydrogenation, respectively. However, after 2nd extraction, the sample extracted at 32 °C exhibit maximum desorption after isothermal dehydrogenation at 100 °C (5.47 wt.%), while the one after 2nd extraction at 42°C shows maximum desorption at 200 °C (5.41 wt.%).

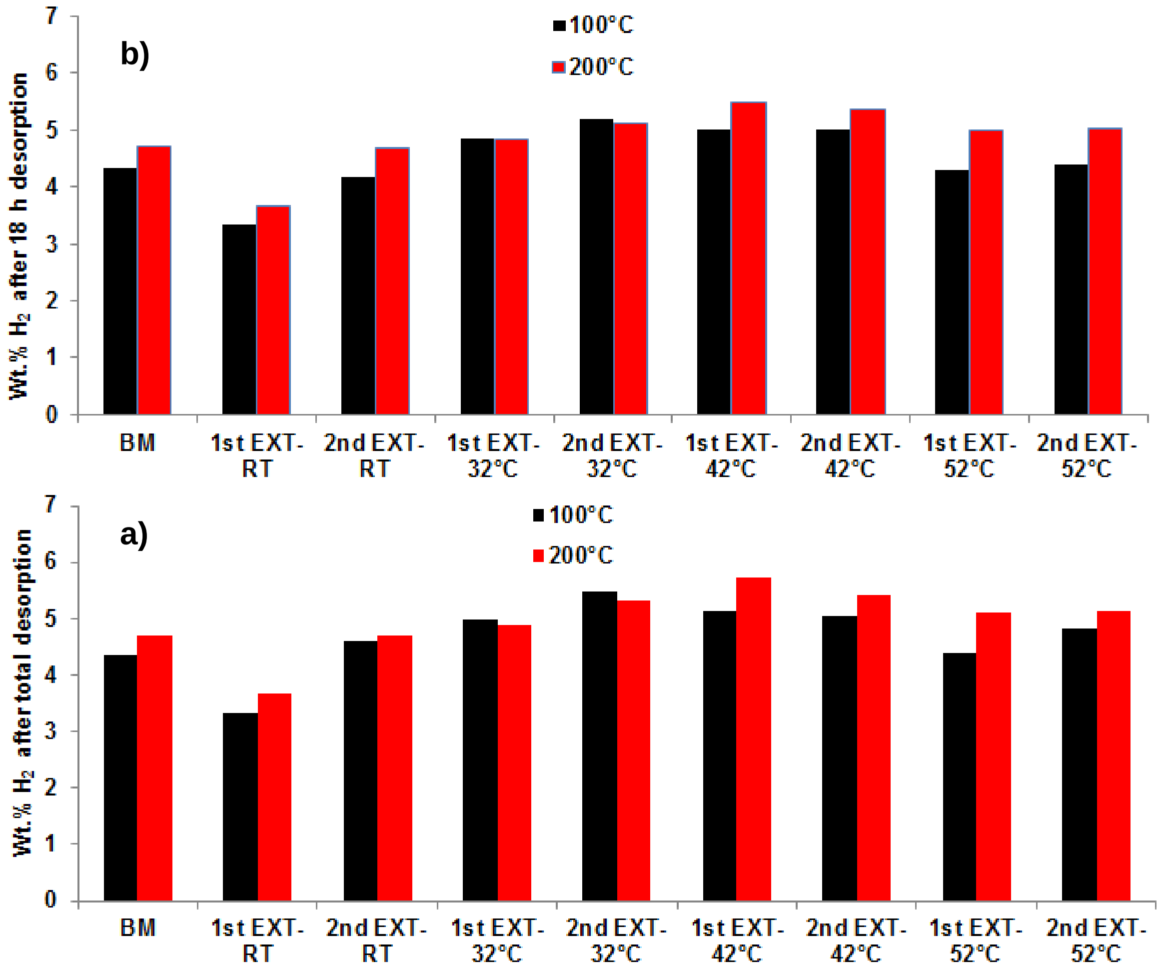

Fig. 4.35. Quantity of hydrogen desorbed after a) full desorption and b) after 18h desorption of isothermal dehydrogenation at 100°C and 200°C for ($2LiBH_4$+$MnCl_2$) before and after solvent extraction.

Fig. A.1 (a) shows the dehydrogenation curves of the samples after 1st extraction at 42 °C without and with additives. The extraction process, however, seems not to have worked for the samples with additive, as shown in the XRD pattern of the sample with additive after solvent extraction (Fig. 4.31). As shown in Fig. 4.31 (c), the Ni peaks were not observed in the XRD pattern of the suspended powder after extraction of ($2LiBH_4$+$MnCl_2$)+5 wt.% Ni, but they were seen in the XRD pattern of the powder in the filter (Fig. 4.31 (e)), indicating that extraction of the sample with additives does not work as expected. Fig. A.1 (b) compares the isothermal dehydrogenation behaviors at 100 °C of ($2LiBH_4$+$MnCl_2$) after the first extraction at RT and different higher temperatures (32-52 °C). The maximum quantity of desorbed H_2, as mentioned earlier from the bar graph in Fig. 4.35 and Table 1A and the one shown in Fig. .1A (b) is observed in the sample after solvent extraction at 42 °C.

Fig. 4.36 shows the quantities of hydrogen desorbed at 100 and 200 °C as a function of the evaporation rate measured during evaporating of the suspended powder after filtering during the 1st (Fig. 4.36a) and 2nd (Fig. 4.36b) extraction processes. The evaporation rate increases with increasing temperature, so that extraction at RT has the lowest and the one at 52°C has the highest rate.

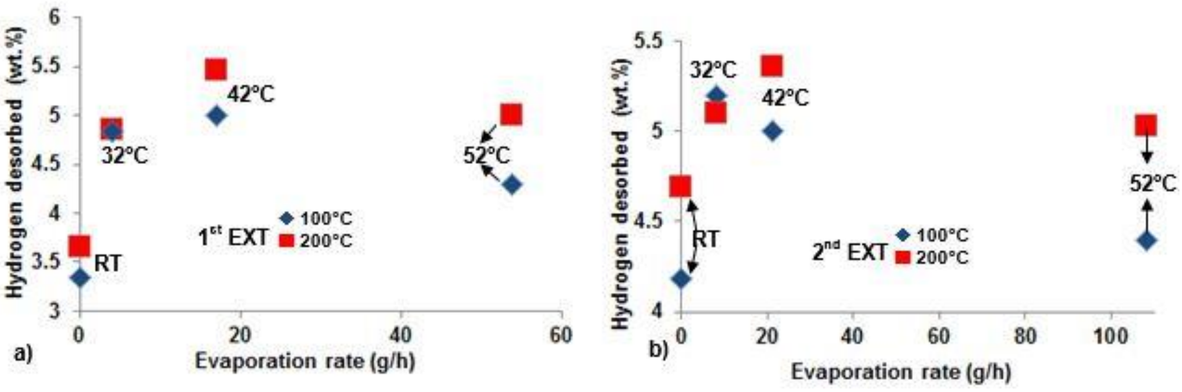

Fig. 4.36. Quantity of hydrogen desorbed at isothermal dehydrogenation of 100 and 200°C as a function of evaporation rate measured during evaporating of the suspended powder after filtering a) during 1st extraction and b) during 2nd extraction process.

The authors in [43] suggested that evaporation of the molecules of Et_2O breaks the coordination environment around the Li^+ atoms and consequently leads to collapse of the structure with the formation $Mn(BH_4)_2$. A similar mechanistic trend is observed through heating of the extracted samples. As shown Fig. 4.30f, the $[\{Li(Et_2O)_2\}Mn_2(BH_4)_5]$ peaks disappeared after isothermal dehydrogenation. In addition, as can be seen in Fig. 4.34b, two decomposition steps are observed in the TG analysis of the solvent extracted sample at 42 ºC. The first step in the range of 70-116 ºC and the mass loss of 27.5 wt.% corresponds to the evolution of Et_2O. The second step has an endothermic peak corresponding to the decomposition of $Mn(BH_4)_2$ starting at 125 ºC, with the maximum at about 136 ºC and the mass loss of 4.46 wt.%.

As mentioned in the experimental section, drying of the suspension after filtering was done at RT, as well as high temperatures (32-52 ºC). Apparently, the quantity of H_2

desorbed from the powder mixture at both 100 and 200 °C after solvent extraction has the relative dependency to evaporation rate of the suspension up to 42 °C. However, raising the evaporation rate by increasing the extraction temperature from 42 °C to 52 °C leads to a reduced quantity of hydrogen desorbed, meaning that the optimum temperature for the solvent extraction process is around 42 °C. A possible explanation for this might be the desorption of some quantity of H_2 with an increase in temperature to 52°C. Similar behavior is seen for the sample after 2^{nd} extraction method and desorption at 200°C.

4. 5 Summary of findings

1. After milling the stoichiometric ($2LiBH_4+MnCl_2$) mixture (n=2) with a small total milling energy input Q_{TR}=36.4 kJ/g the refinement of the initial powder mixture is quite dramatic achieving the average particle size of 14.9±6.6 μm. After further milling with Q_{TR}=145.6 kJ/g the average particle size is reduced to 7.5±2.6 μm but it increases to 16.1±6.3 μm after a total milling energy input of Q_{TR}=364 kJ/g due to a profound agglomeration of milled particulate.
2. As a result of the mechano-chemical activation synthesis (MCAS) occurring during ball milling of the ($2LiBH_4+MnCl_2$) and ($3LiBH_4+MnCl_2$) mixtures (n=2 and 3), a nanocrystalline $Mn(BH_4)_2$ hydride is synthesized which is accompanied by nanocrystalline LiCl which constitutes a “dead-weight” for the microstructure.
3. The crystallite (grain) size of the synthesized nanocrystalline $Mn(BH_4)_2$ hydride attains 21±5.0 nm for the total milling energy input Q_{TR}=36.4 kJ/g and then is further reduced to 18±1.0 nm for Q_{TR}=145.6 kJ/g and finally to 14±0.5 nm for Q_{TR}=364 kJ/g.
4. The crystallite (grain) size of LiCl is very close to 30 nm regardless of the milling energy input, Q_{TR}.
5. Thermal decomposition of $Mn(BH_4)_2$ is endothermic with a peak maximum at about 140°C.
6. The rate of isothermal dehydrogenation of the nanocrystalline $Mn(BH_4)_2$ is quite rapid at 100°C and clearly increases with the initial increase of the total milling energy input, Q_{TR}. The maximum quantity of H_2 desorbed at 100 and 200°C is very similar and doesn’t exceed ~4.5 wt.%.

7. The apparent activation energy for dehydrogenation of nanocrystalline $Mn(BH_4)_2$ is strongly dependent on the average particle size for the ball milled powder such that it increases with increasing average powder particle size.

8. The synthesized nanocrystalline $Mn(BH_4)_2$ hydride is very stable and does not excessively release H_2 during long-term storage at room temperature for over 120 days under a slight overpressure of argon.

9. Both X-ray diffraction and TEM selected area electron diffraction patterns (SAEDPs) clearly confirm the presence of the $Mn(BH_4)_2$ and LiCl phases in the synthesized nanocomposite. No other phases were detected. Both $Mn(BH_4)_2$ and LiCl are nanocrystalline phases because bright field high-resolution TEM imaging of the synthesized composite powder particles reveals the presence of nanograins belonging to LiCl and $Mn(BH_4)_2$.

10. The grain sizes expressed as the equivalent circle diameters (ECD) of LiCl and $Mn(BH_4)_2$, estimated from the high-resolution TEM micrographs, are within the range of 14.1±3.7 nm and 10.0±2.9 nm, respectively.

11) The XRD patterns of the thermally dehydrogenated ($Mn(BH_4)_2$+2LiCl) nanocomposite do not exhibit any visible Bragg diffraction peaks belonging to either crystalline α-Mn or β-B. In contrast, the SAED patterns and EDS elemental maps provide convincing evidence that both Mn and B exist in the dehydrogenated powder as nanometric sized phases α-Mn and β-B, respectively. Apparently, the lack of Bragg diffraction peaks in an XRD pattern is insufficient evidence that the Mn and B elemental products of $Mn(BH_4)_2$ thermal dehydrogenation can be classified as being amorphous.

12. The addition of 5wt.% ultrafine filamentary Ni increases the amount of H_2 during BM in comparison with the sample without additives. Graphene additive, however, decreases the quantity of H_2 desorbed during BM. Adding 5wt.% $LiNH_2$ causes a slight increase in the quantity of H_2 released from 0.2 (for $2LiBH_4$+$MnCl_2$) to 0.25 wt.% H_2 for $2LiBH_4$+$MnCl_2$+5wt.% $LiNH_2$.

13. Using 5wt.% additives can minimize the release of B_2H_6 during isothermal dehydrogenation. Adding 5wt.% additives to the powder mixture leads to increased intensity ratio of the corresponding peaks of H_2 to B_2H_6. $LiNH_2$ and Ni suppress the release of B_2H_6 better than graphene does.

14. Ni does not reduce the decomposition temperature of $Mn(BH_4)_2$, while 5wt.% graphene changes it to 168 °C from 150 °C. On other hand, $LiNH_2$ is able to reduce the decomposition temperature of $Mn(BH_4)_2$ significantly, from 150 °C to 133 °C.

15. As compared to 78.9±1.2 kJ/mol for the apparent activation energy for the dehydrogenation of an undoped $2LiBH_4$+$MnCl_2$ powder mixture, the activation energy of 76.1±0.6 kJ/mol for a 5wt.% Ni-doped $2LiBH_4$+$MnCl_2$ composite indicates that 5wt.% Ni yields no obvious improvement in the kinetic of dehydrogenation. Graphene, however, slightly increases the apparent activation energy for dehydrogenation (81.5±5.2 kJ/mol).

16. The most notable observation to emerge from the apparent activation energy comparison is that 5wt.% $LiNH_2$ can reduce the apparent activation energy to 44.9±4.3 kJ/mol.

17. A crystalline $[\{Li(Et_2O)_2\}Mn_2(BH_4)_5]$ phase was detected by XRD of the solvent-extracted ($2LiBH_4$+$MnCl_2$) powder mixture.

18. Thermal dehydrogenation of solvent extracted sample leads first to the evolution of Et_2O and then to the decomposition of $Mn(BH_4)_{2.}$

5. Nanostructured ($LiBH_4$-$FeCl_2$)

5.1. Mechanical dehydrogenation and evolution of microstructure at room temperature

Figure 5.1a shows a scanning electron micrograph of the as received $FeCl_2$ reactant. The crystals are irregularly shaped, some of them rod-shaped, having thickness of about 10 µm, although more regular than the $MnCl_2$ crystals, but smaller than the $LiBH_4$ crystals.

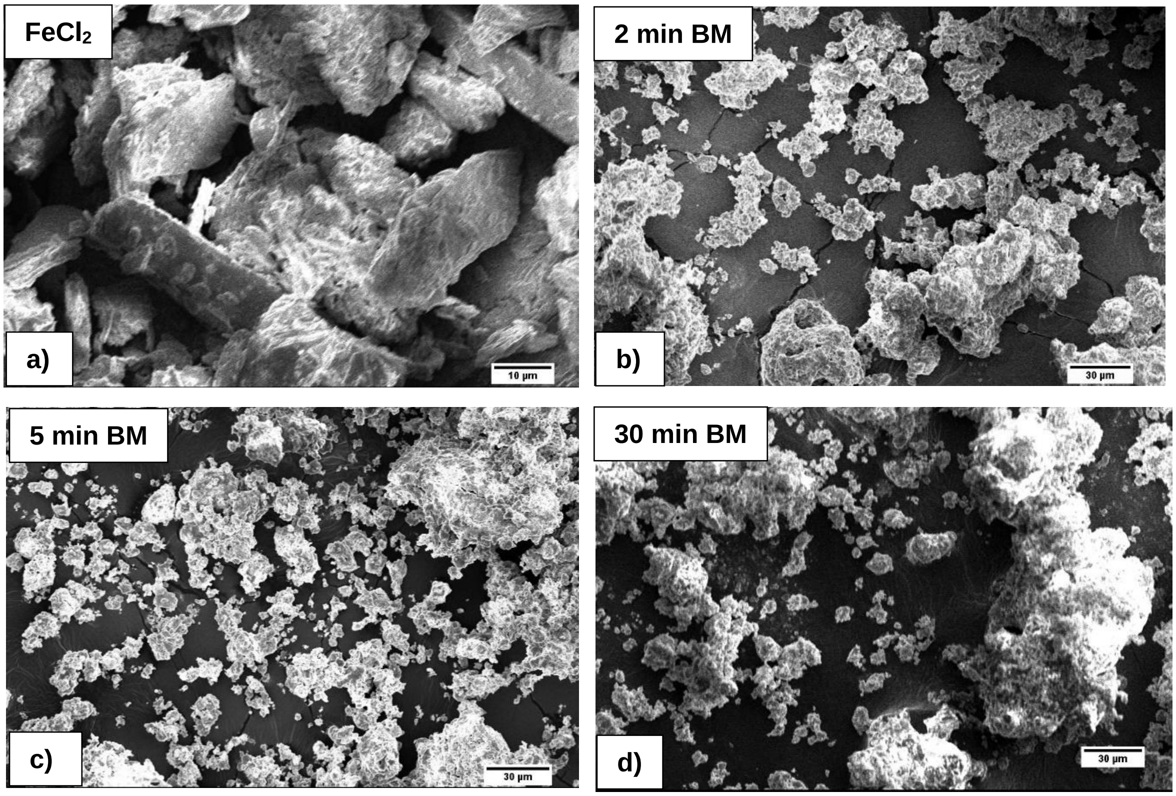

Figure 5-1. Scanning electron micrographs of (a) as received $FeCl_2$ and ball milled powders of the ($2LiBH_4$+$FeCl_2$) mixture after MCAS for varying milling time equivalent to varying milling energy input, Q_{TR}. (b) 2 min (Q_{TR}=2.43 kJ/g), (c) 5 min (Q_{TR}=6.07 kJ/g) and (d) 30 min (Q_{TR}=36.4 kJ/g) (adapted from [96]).

Figures 5.1b, c and d show the evolution of morphology of the initial ($2LiBH_4$+$FeCl_2$) mixture during short ball milling durations in the magneto-mill, Uni-Ball-Mill 5, as a function of milling time or alternatively, energy input, Q_{TR}. As can be seen, the energy input injected into the powder mixtures is, in general, rather small. Nevertheless, even after injecting barely Q_{TR}=2.43 kJ/g of milling energy, the ($2LiBH_4$+$FeCl_2$) mixture is already very thoroughly milled although it exhibits a few agglomerated powder particles.

By comparison, a similar powder mixture ($2LiBH_4$+$MnCl_2$), investigated in section 4.1 for the synthesis of $Mn(BH_4)_2$ by MCAS, exhibited a pronounced agglomeration after milling at a much higher energy input, Q_{TR}, from 145.6 to 364 kJ/g. It seems that the mixture ($2LiBH_4$+$FeCl_2$) may be prone to forming agglomerates even at a very low milling energy input.

As mentioned in section 4 for the MCAS synthesized mixture ($2LiBH_4$+$MnCl_2$), nearly no H_2 was observed to be released during ball milling (mechanical dehydrogenation phenomenon). In contrast, the present ($2LiBH_4$+$FeCl_2$) mixture quickly mechanically dehydrogenates, even after injecting a very small milling energy input, Q_{TR}. Fig. 5.2a and b show the H_2 release curves after holding the ($2LiBH_4$+$FeCl_2$) samples for 1h at room temperature (RT; 20-22 °C) in an H_2 filled milling vial (~300 kPa) and subsequent milling for 2 and 5 min, respectively (the following desorption curves at 100 °C are also shown that will be thoroughly discussed).

Storage of the ($2LiBH_4$+$FeCl_2$) mixture for 1h at RT results in only modest release of about 0.5 (Fig. 5.2a) to 0.8 wt.% H_2 (Fig. 5.2b). It shows that the investigated mixture is reasonably stable at RT and not volatile. During BM, the mixture previously held at RT, additionally mechanically dehydrogenates 0.33 and 1.4 wt.% H_2 after injecting a very small quantity of milling energy, Q_{TR}=2.43 (Fig. 5.2a) and 6.07 kJ/g (Fig. 5.2b), respectively.

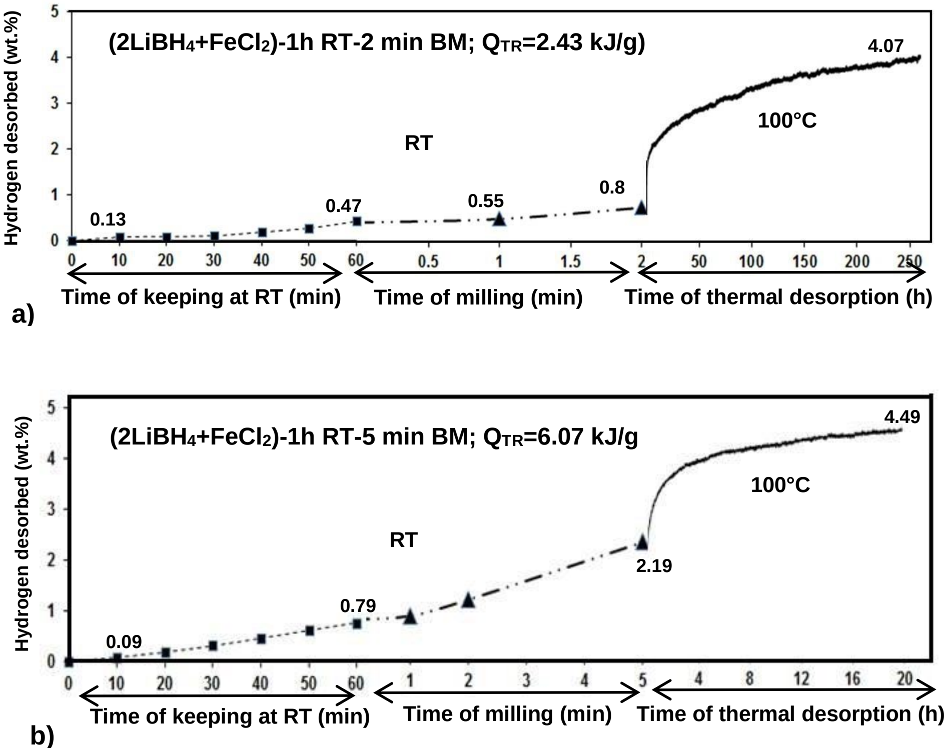

Figure 5-2. ($2LiBH_4$+$FeCl_2$), held at RT for 1h and subsequently ball milled (BM) for (a) 2 min (Q_{TR}=2.43 kJ/g) and (b) 5 min (Q_{TR}=6.07 kJ/g) and dehydrogenated after BM under 1 bar H_2 at 100 °C (adapted from [96]).

The XRD patterns are shown in Fig. 5.3. The XRD pattern for the initial mixture of as received powders shows only the Bragg diffraction peaks of $LiBH_4$ and $FeCl_2$. The peaks of $LiBH_4$ were identified using our own standard pattern of as received $LiBH_4$ while the peaks of $FeCl_2$ were identified using ICDD (JCPDS) card #01-1106. However, it must be pointed out for clarity, that the intensity of the (003) $FeCl_2$ peak at 2θ=15.2°, in the XRD pattern in Fig. 5.3, is 100% and the intensity of the (104) $FeCl_2$ peak at 2θ=35.3° is 54%. This is exactly opposite to the values reported in the ICDD card # 01-1106 which shows 100% intensity for the (104) and 63% for the (003) $FeCl_2$ peak. Furthermore, the interplanar spacing $d_{(003)}$ of the (003) plane calculated from our XRD pattern (Fig. 5.3) comes out at 5.82 Å as opposed to 5.90 Å reported in the card #01-1106. All the other interplanar spacings for $FeCl_2$ calculated from our XRD pattern agree very well with those reported in the card # 01-1106. The noted discrepancies may arise due to the fact that the XRD data reported in the card # 01-1106 were determined using $MoK\alpha_1$ radiation as opposed to CuKα_1 radiation used in the present work although the exact cause is not clear.

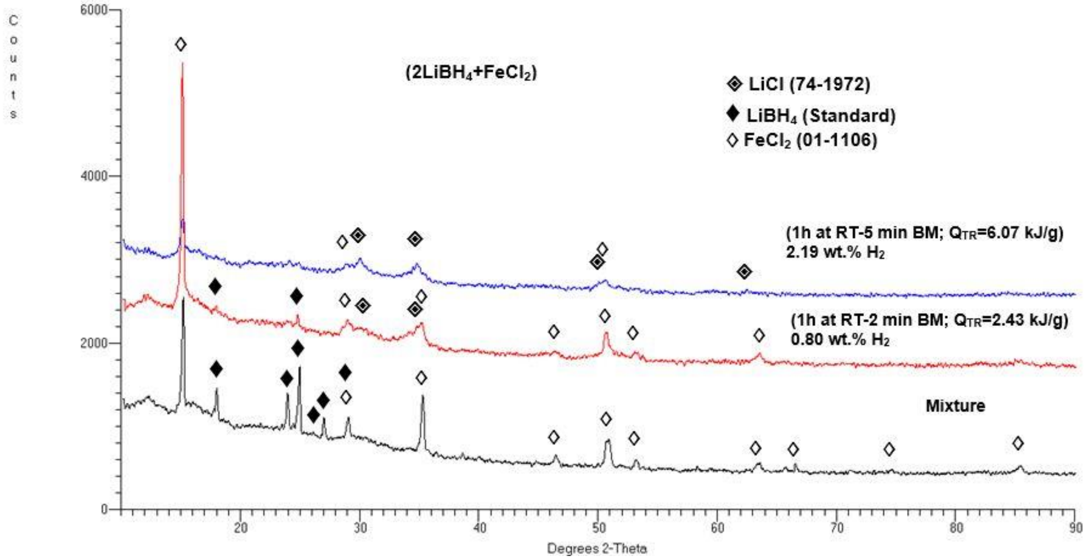

Figure 5-3. XRD patterns corresponding to samples from Fig. 6.2 (adapted from [96]).

The mixture (1h RT+2min BM) (Fig. 5.2a), shows very weak peaks of remaining $LiBH_4$, relatively strong peaks of $FeCl_2$ and weak LiCl peaks which indicate an early stage of LiCl formation. The mixture (1h RT+5min BM) that released the total of 2.19 wt. % H_2 (Fig. 5.2b), shows no $LiBH_4$ peaks, still a relatively strong principal $FeCl_2$ peak (003) at $2\theta=15.2°$ and small but clearly visible LiCl peaks. The results of XRD analysis are collected in Table A.2 (Appendices). No presence of any other crystalline phase is observed in Fig. 5.3 after BM. Interestingly, both powders were attracted to a permanent magnet after ball milling.

Figure 5.4 shows the effects of increasing milling energy input on the mechanical dehydrogenation of samples that were directly ball milled without a prior storage at RT. A minimal amount of 0.33 wt.% H_2 is released due to mechanical dehydrogenation after injection of 2.43 kJ/g milling energy (Fig. 5.4a) which increases to 0.87 wt.% H_2 after injecting nearly 3-fold quantity of milling energy (6.07 kJ/g) (Fig. 5.4b). The quantity of H_2 released because of mechanical dehydrogenation rapidly increases to 2.80 (Fig. 5.4c), 3.50 (Fig. 5.4d) and 4.02 wt.% (Fig. 5.4e) after injecting 12.14, 18.2 and 36.4 kJ/g of milling energy input, respectively. Since the total theoretical H_2 capacity of the

($2LiBH_4$+$FeCl_2$) mixture is 4.73 wt.%, injecting barely 36.4 kJ/g of milling energy input leads, at nearly room temperature, to mechanical dehydrogenation of about 85% of the theoretical H_2 capacity (Fig. 5.4e), or even slightly higher if one takes into account the purity corrected total capacity

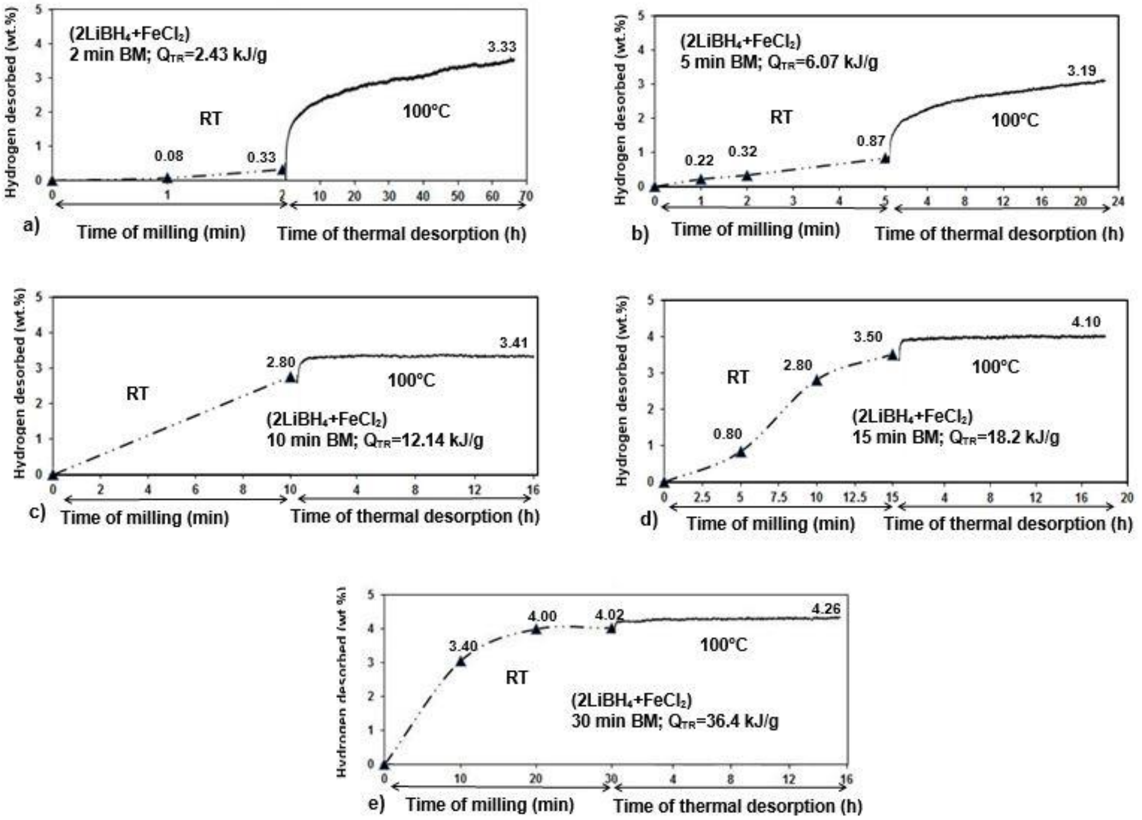

Fig. 5.4. Hydrogen desorption curves for ($2LiBH_4$+$FeCl_2$) after (a) 2 min BM (Q_{TR}=2.43 kJ/g), (b) 5 min BM (Q_{TR}=6.07 kJ/g), (c) 10 min BM (Q_{TR}=12.14 kJ/g), (d) 15 min BM (Q_{TR}=18.20 kJ/g) and (e) 30 min BM (Q_{TR}=36.40 kJ/g). All milled powders were subsequently dehydrogenated at 100°C and the pertinent curves are shown (adapted from [96]).

Finally, it must be added that the ($2LiBH_4$+$FeCl_2$) mixture, originally white in color, gradually converted to black during ball milling (MCAS). This occurred even after barely 2 min of milling although the originally white color was nearly preserved when the mixture was just held for 1h at RT in the glove box.

Figure 5.5 shows the XRD pattern as a function of milling energy input (milling time) for samples whose mechanical dehydrogenation curves are shown in Fig. 5.4. It is clearly seen that the peaks of $LiBH_4$ disappear just after the milling energy input reaches 2.43

kJ/g while the peaks of $FeCl_2$ disappear after about 12.14 kJ/g of milling energy input. The peaks of LiCl become visible after the injection of 6.07 kJ/g milling energy. Such a rapid disappearance of the $LiBH_4$ peaks without yet visible formation of LiCl suggests that $LiBH_4$ becomes highly disordered by ball milling.

It is to be pointed out that the ($2LiBH_4+FeCl_2$) hydride mixture exhibits, so far, the most rapid rate of mechanical dehydrogenation while the other hydride mixtures such as ($1LiAlH_4+LiNH_2$) [84, 97] and ($3LiAlH_4+MnCl_2$) [97] have slightly lower rates of mechanical dehydrogenation. For all these three hydride systems the milling energy input which induces a copious H_2 release because of mechanical dehydrogenation is, indeed, very small (about 36.4 kJ/g) as compared to other hydride mixtures investigated in our laboratory and mentioned above.

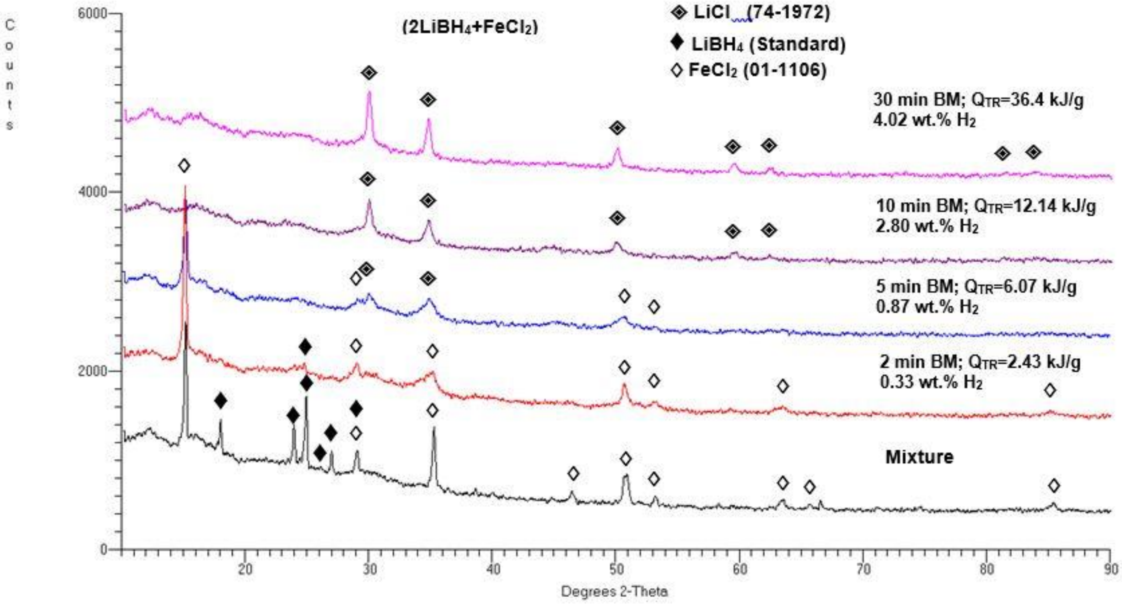

Fig. 5.5. XRD patterns of the ($2LiBH_4+FeCl_2$) mixture ball milled (BM) with increasing milling energy input Q_{TR} (milling time) (adapted from [96].

Fig. 5.6a shows the FT-IR spectrum of a ($2LiBH_4+FeCl_2$) sample ball milled for 5 min with a milling energy input Q_{TR}=6.07 kJ/g compared with the reference FT-IR spectrum of $LiBH_4$ [93]. The FT-IR spectrum of $2LiBH_4+FeCl_2$ is illustrated again in Fig. 5.6b to have the spectrum in much more detail. This particular sample desorbed about 0.87 wt.% H_2 during milling for 5 min. Its corresponding XRD is shown in Fig. 5.5 and indicates the presence of LiCl and retained, unreacted $FeCl_2$. As mentioned above, unreacted $LiBH_4$ is in an amorphous state. For comparison. All samples after ball milling were attracted to a permanent magnet which indicates that a ferromagnetic constituent resides in their microstructure.

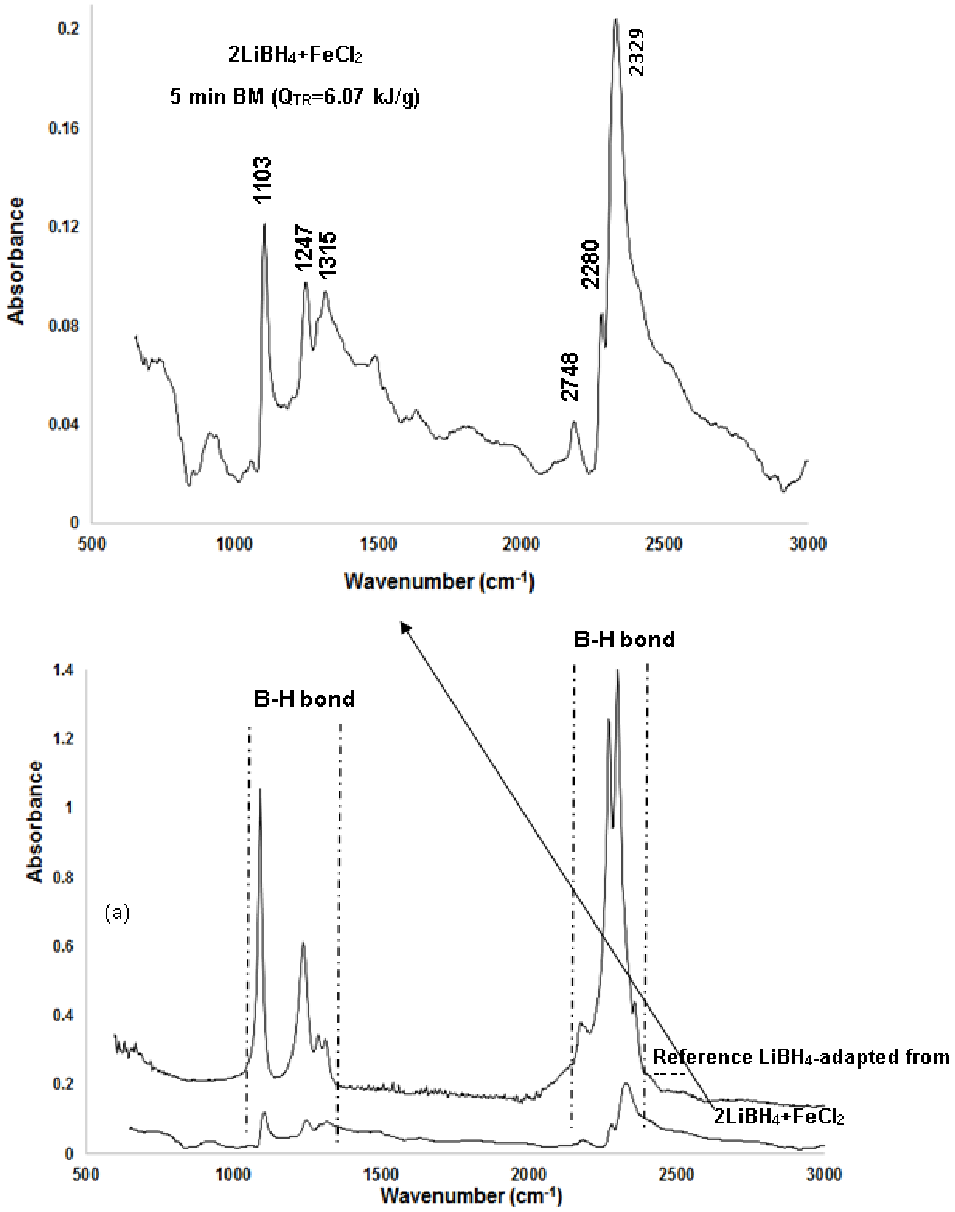

Fig. 5.6 (a) FT-IR spectrum for as-received $LiBH_4$ (top one) compared with a ($2LiBH_4$+$FeCl_2$) sample ball milled with a milling energy input Q_{TR}=6.07 kJ/g (5 min) (the bottom one) and (b) ($2LiBH_4$+$FeCl_2$) sample ball milled with a milling energy input Q_{TR}=6.07 kJ/g (5 min) (adapted from [96]).

5.2. DSC thermal behavior

Figure 5.7a shows a DSC curve for a ($2LiBH_4$+$FeCl_2$) mixture which was just mixed by shaking in a glass vial and not ball milled (non-BM) exhibiting a moderate size endothermic peak with the maximum at about 120 °C (Table A.2) and a large, narrow, principal exothermic peak with the maximum at 282 °C (Table A.2). The latter is irreversible on cooling which means that it is related to thermal desorption of hydrogen. Fig. 5.7b shows that the first, smaller, endothermic peak for both the non-BM and BM samples is fully reversible upon cooling although with a substantial hysteresis. The reversible behavior of an endothermic peak is exactly the same as observed, for the ball milled ($nLiBH_4$+$MnCl_2$; n=2 and 3) mixture during subsequent DSC measurements (Fig. 4.5b). The endothermic peak arises due to a polymorphic transformation of $LiBH_4$ which at room temperature exists as an orthorhombic phase (space group *Pnma*) and undergoes a first-order phase transition to a hexagonal phase (space group $P6_3mc$) [21, 54].

Fig. 5.7c shows that after ball milling with varying energy inputs the endothermic peak is still visible at around 115-117 °C (Table A.2) but the principal exothermic peak becomes very wide and its maximum is profoundly shifted to a much lower temperature range of about 204-206 °C for the energy input 6.07-12.14 kJ/g (Table A.2). The shift is about 80 °C in magnitude as compared to a non BM mixture in Fig. 5.7a. Such a substantial shift of a principal H_2 desorption peak has never been reported in the literature.

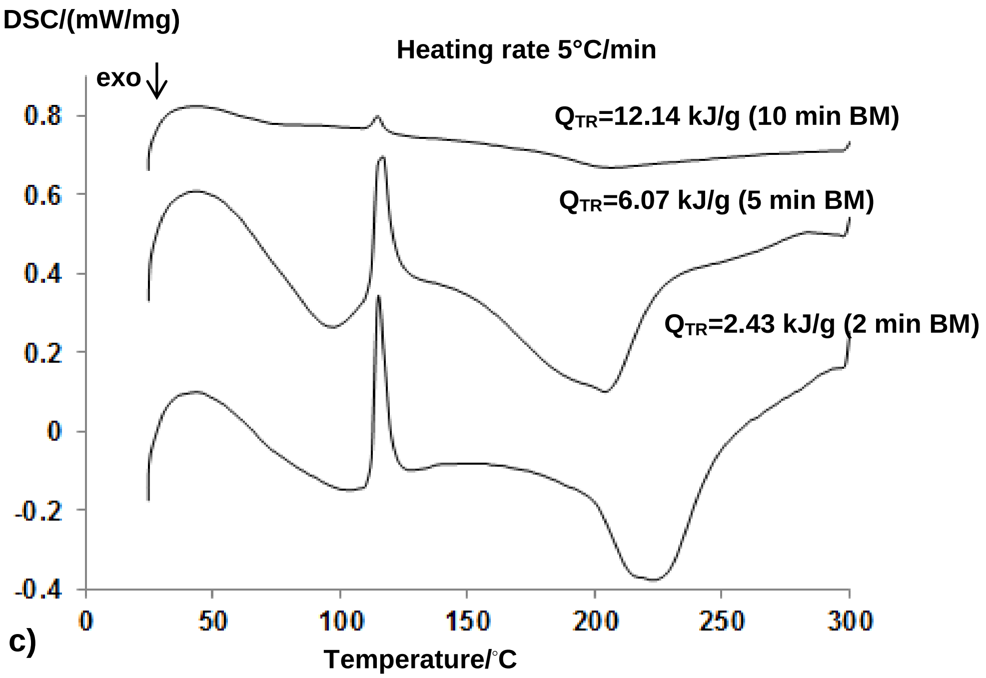
DSC/(mW/mg)
Heating rate 5°C/min
exo ↓
Q_{TR}=12.14 kJ/g (10 min BM)
Q_{TR}=6.07 kJ/g (5 min BM)
Q_{TR}=2.43 kJ/g (2 min BM)
0.8
0.6
0.4
0.2
0
-0.2
-0.4
0
50
100
150
200
250
300
Temperature/°C
c)

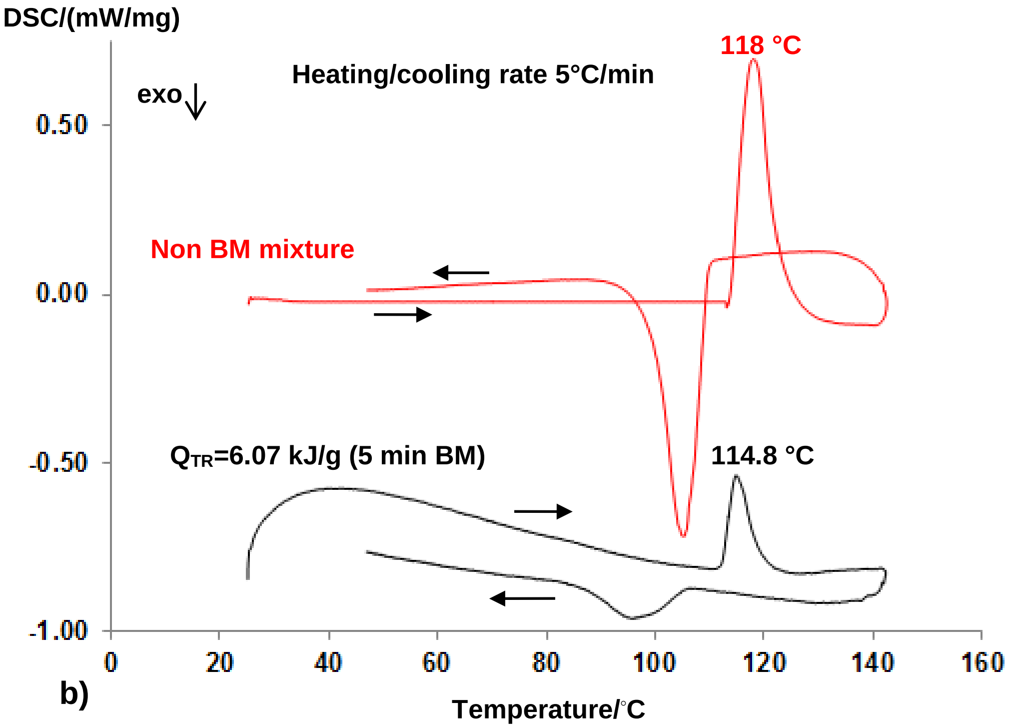
DSC/(mW/mg)
118 °C
Heating/cooling rate 5°C/min
exo ↓
Non BM mixture
Q_{TR}=6.07 kJ/g (5 min BM)
114.8 °C
0.50
0.00
-0.50
-1.00
0
20
40
60
80
100
120
140
160
Temperature/°C
b)

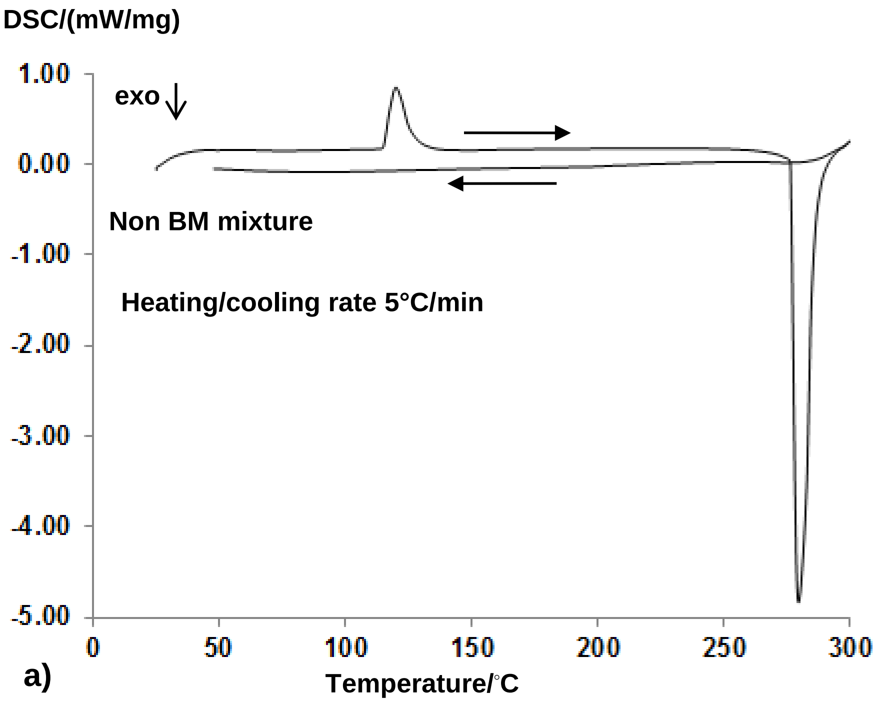

Fig. 5.7. DSC traces of the ($2LiBH_4$+$FeCl_2$) mixture (a) non-BM mixture, (b) ball milled (BM) with increasing milling energy input Q_{TR} (milling time), and (c) low temperature DSC segment showing comparison of DSC peaks corresponding to a polymorphic transformation of $LiBH_4$. Samples milled with Q_{TR}=2.43 and 6.07 kJ/g (2 and 5 min) were held at RT for 1h under argon atmosphere (Adapted from [96]).

5.3. Isothermal dehydrogenation

As already shown in Fig. 5.2 and 5.4, the BM powders were subsequently isothermally dehydrogenated at 100 °C. For comparison, isothermal dehydrogenation of both BM and non-BM powders was also carried out at 250 °C. Table A.4 summarizes the quantities of H_2 desorbed during ball milling and isothermal dehydrogenation at 100 and 250 °C.

Figure 5.8 shows desorption curves obtained at 100, 110, 120 and 250 °C for the BM ($2LiBH_4$+$FeCl_2$) samples (5 min) with a total injected energy input, Q_{TR}=6.07 kJ/g, which resulted in mechanical dehydrogenation of 0.87 wt.% H_2 (Fig. 5.4b and Table A.1). It is seen that the BM samples show a rather sluggish dehydrogenation rate at the temperature range 100-120 °C. The total quantity of desorbed hydrogen within 20 h is just slightly over 2 wt.%. For comparison, a desorption curve at 100 °C for the BM ($2LiBH_4$+$MnCl_2$) sample, in which the crystalline $Mn(BH_4)_2$ hydride was formed through MCAS, is also shown. For the ($2LiBH_4$+$MnCl_2$) sample the dehydrogenation rate is much faster than that for the ($2LiBH_4$+$FeCl_2$) sample and the quantity of H_2 desorbed within 20 h is over 4 wt.%. The dehydrogenation rate for the ($2LiBH_4$+$FeCl_2$) sample increases at 250 °C although it decelerates rapidly after about 1 h and the total H_2 desorbed within 20 h is still much lower than that desorbed at 100 °C for the reference BM ($2LiBH_4$+$MnCl_2$) sample. I attempted to estimate the apparent activation energy of desorption at the range 100-120 °C from the dehydrogenation curves in Fig. 5.8 but the obtained results were unreliable because of lack of sufficiently linear desorption rate at the beginning of the dehydrogenation curves. It should also be pointed out that the thermal dehydrogenation rate at 100-120 °C for the BM ($2LiBH_4$+$FeCl_2$) samples as shown in Fig. 5.8 is much lower than that observed during ball milling where 4.02 wt. H_2 is desorbed in just 0.5h of ball milling (Fig. 5.4e).

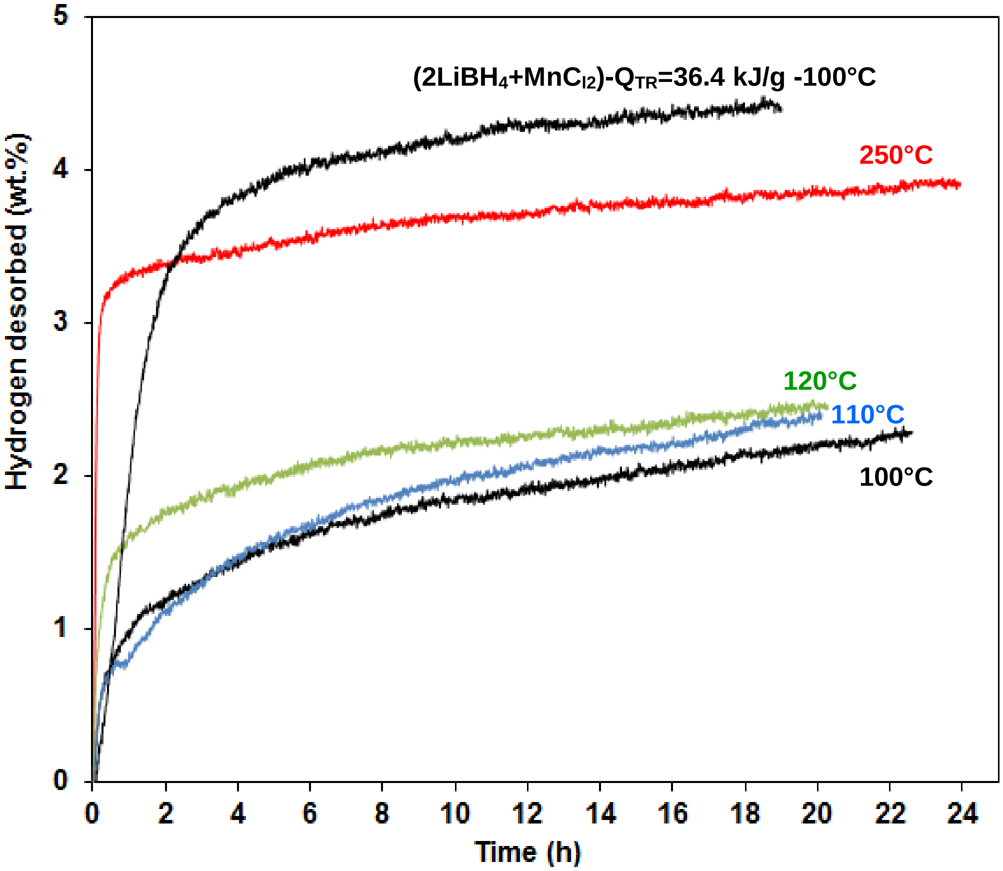

Fig. 5.8. Isothermal dehydrogenation curves at 100, 110, 120 and 250 °C for the ($2LiBH_4$+$FeCl_2$) pre-ball milled with the energy input Q_{TR}=6.07 kJ/g (5 min) compared with a dehydrogenation curve for the ($2LiBH_4$+$MnCl_2$) at 100°C from section 4 (adapted from [96]).

Figure 5.9 shows the XRD patterns for the BM samples after dehydrogenation at 100 °C for various quantities of milling energy input during milling and dehydrogenation time length. It is clearly seen that for the milling energies from 2.43 to 12.14 kJ/g the XRD patterns show residual principal peaks of $FeCl_2$ still visible after dehydrogenation for 42.4 to 66.3h. That explains qualitatively the sluggishness of desorption in the non-linear portion of desorption curves in Fig. 5.8. Apparently, because of short milling duration, $FeCl_2$ is not completely reacted with amorphous $LiBH_4$ during ball milling. Fig. 5.10 shows an XRD pattern after dehydrogenation of the 5 min BM sample at 250 °C for 122h. No residue $FeCl_2$ peaks are visible which means that retained $FeCl_2$ after BM reacted fully at high temperature.

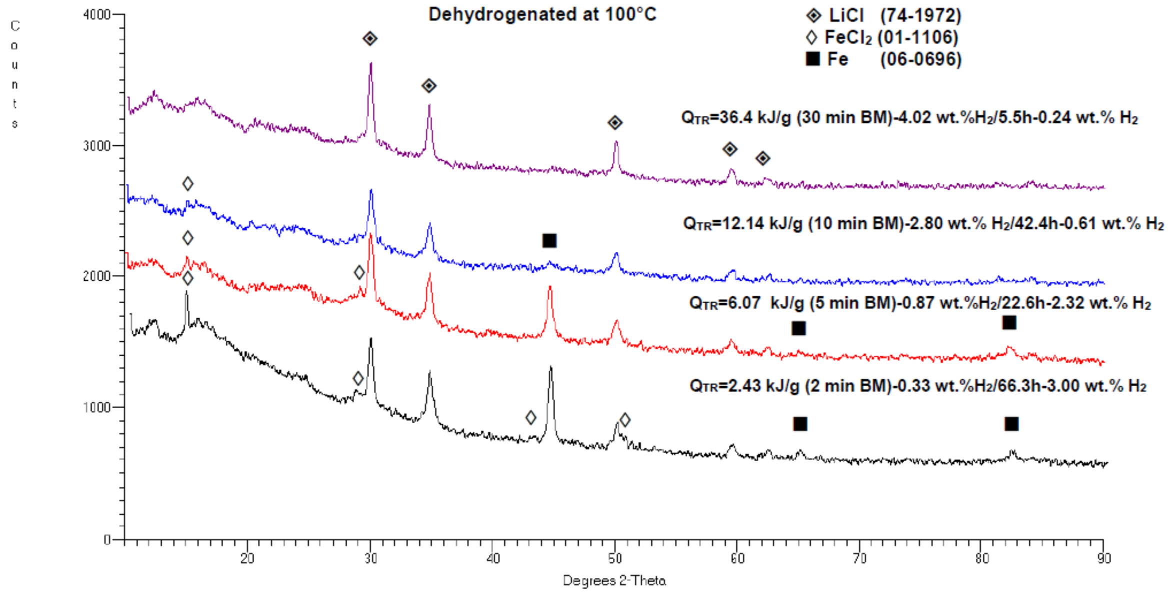

Fig. 5.9. XRD patterns after isothermal dehydrogenation at 100 °C for the BM samples with varying energy inputs. The quantities of H_2 mechanically dehydrogenated during ball milling and those thermally dehydrogenated after corresponding dehydrogenation time are shown (Adapted from [96]).

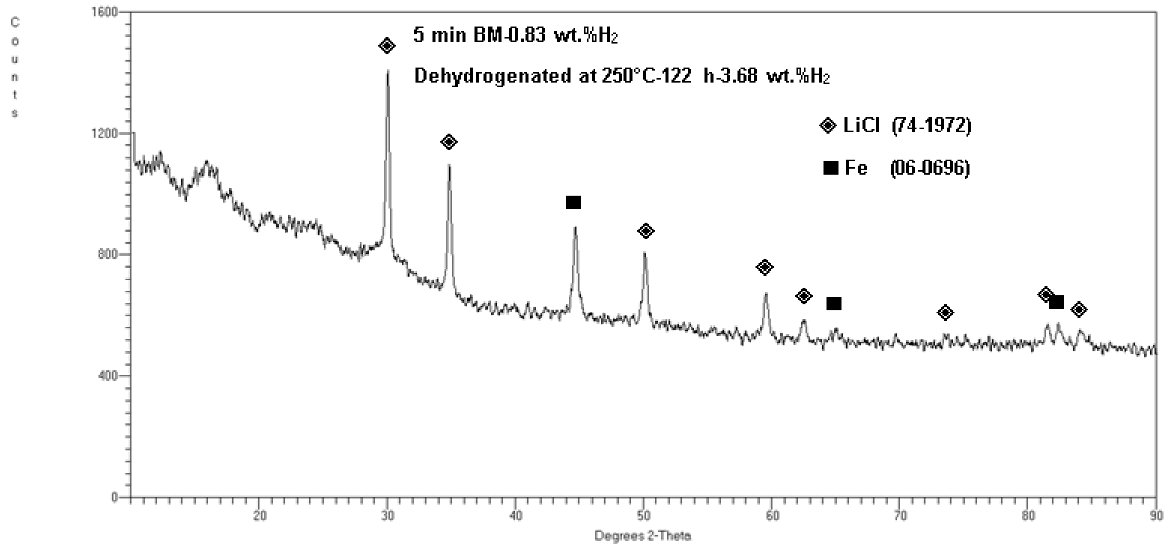

Fig. 5.10. XRD pattern after isothermal dehydrogenation at 250 °C for the BM sample processed with the energy input of 6.07 kJ/g (5 min BM) (Adapted from [96]).

The BM samples dehydrogenated for 22.6, 42.4 and 66.3 h at 100 °C exhibit strong diffraction peaks of crystalline α-Fe in Fig. 5.9 while the BM samples dehydrogenated for 15.5 and 17.7 h do not show any peaks of crystalline Fe which must exist in an amorphous state as it was formed during ball milling. Apparently, if thermal reaction at 100 °C occurs in the BM samples, Fe remains amorphous if the dehydrogenation time is too short, being within the range 15.5-17.7 h while crystalline α-Fe is formed if the duration of dehydrogenation reaction is longer, within the range 22.6-66.3 h. Also, the XRD pattern in Fig. 5.10 for the 5 min BM ($2LiBH_4$+$FeCl_2$) sample, dehydrogenated at 250 °C for 122h, shows strong diffraction peaks of crystalline α-Fe. The above observations strongly suggests that for the BM samples, initially amorphous Fe, crystallizes into α-Fe during dehydrogenation for a specific time which is roughly longer than about 17.7 h at 100 °C. For BM samples dehydrogenated at 250 °C amorphous Fe becomes definitely crystalline α-Fe after 122 h (Fig. 5.10). Regardless of whether or not the crystalline α-Fe peaks were observed on an XRD pattern the BM samples after dehydrogenation at 100 and 250 °C, the samples were always strongly attracted to a permanent magnet confirming their ferromagnetic character.

The non-BM samples at 250 °C desorbs only 3.0 wt.% H_2 (Fig. 5.11) within 18 to 32 h (as calculated from the original data sheets) in contrast to the 5 min BM sample which at the same temperature desorbs the same amount of H_2 (Fig. 5.8) within barely 0.2 h (as calculated from the original data sheet). Apparently, ball milling for 5 min accelerated the H_2 desorption rate at 250 °C over 100 times.

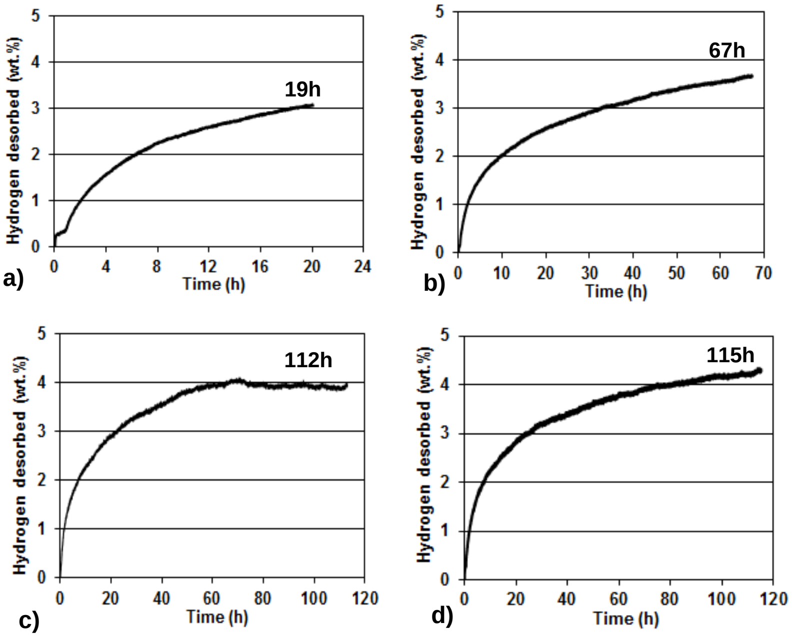

Fig. 5.11. Desorption curves for the non-ball milled (non-BM) samples (only mixed) at 250 °C with increasing length of dehydrogenation, (a) 19 h, (b) 67 h, (c) 112 h and (c) 115 h (Adapted from [96]).

Fig. 5.12 shows the XRD patterns for the non-BM samples dehydrogenated at 250 °C with increasing dehydrogenation time. It is clearly seen that after 19 h of dehydrogenation, a strong $FeCl_2$ peak is still visible whose intensity gradually decreases with increasing duration of dehydrogenation until it becomes very weak but still discernible after 112 h of dehydrogenation. Another interesting feature in Fig. 5.12 is no presence of diffraction peaks of crystalline α-Fe even after a long time dehydrogenation of 115h which means that initially amorphous Fe doesn’t crystallize in the non-BM samples even during a very long dehydrogenation time. The non-BM samples dehydrogenated at 250 °C were also strongly attracted to a permanent magnet after dehydrogenation. Apparently, there must be amorphous Fe present in the microstructure of dehydrogenated samples from Fig. 5.12.

Amorphous Fe can be ferromagnetic. It is well known for over 30 years that amorphous Fe and Fe-based alloys exhibit ferromagnetic/magnetic properties [98]. Furthermore, it was reported that amorphous nanostructured Fe particles about 20-30 nm in size and nanoplatelets were ferromagnetic [99, 100]. This also explains why the ($2LiBH_4$+$FeCl_2$) mixtures after BM are attracted to a permanent magnet as mentioned in the previous section. They must contain amorphous Fe after ball milling.

For samples exhibiting crystalline α-Fe peaks, the grain (crystallite) size is determined and listed in Table A.5. Apparently, crystalline α-Fe is nanometric, exhibiting the grain (crystallite) size within the 27-47 nm range. There is an observed tendency in Table A.5 of decreasing size with increasing milling energy input from 2.43 to 6.07 kJ/g.

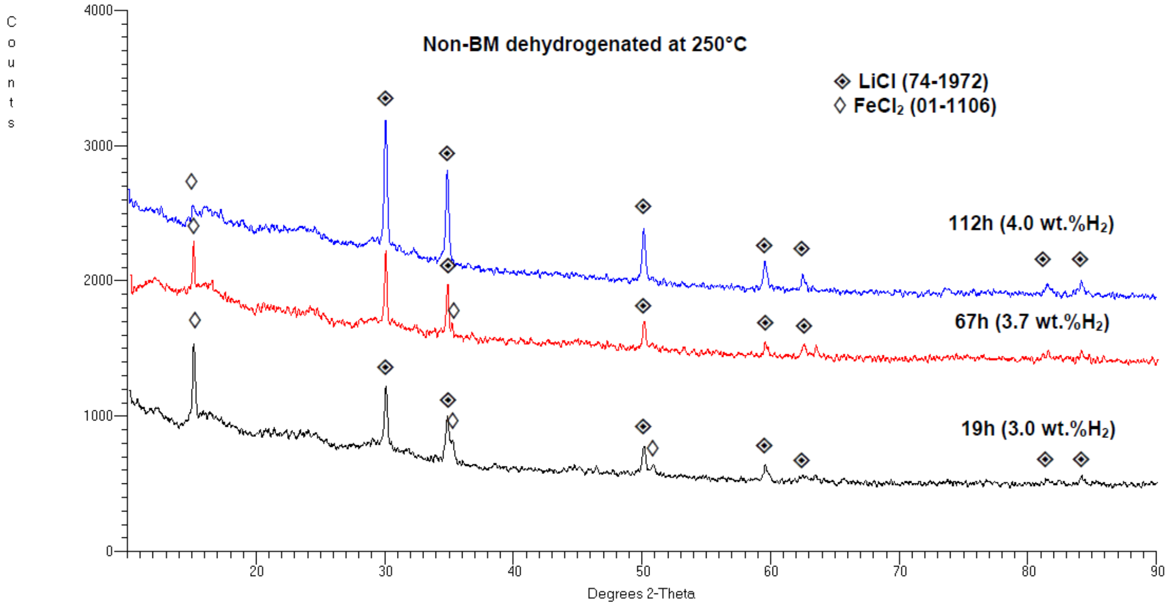

Fig. 5.12. XRD patterns for the non-ball milled (non-BM) samples after dehydrogenation at 250°C for varying times shown (Adapted from [96]).

5.4. Discussion

5.4.1. Mechanical dehydrogenation and evolution of microstructure at room temperature

Within a general framework of events described in the introduction (1.8.2 section), the experimental results presented in the preceding section seem to be in an apparently good agreement with mechano-chemical reactions described by Eqs. (1.9) and (1.10). As shown in the X-ray Bragg diffraction peaks of LiCl, as a newly formed solid phase, are observed in Fig. 5.3 after BM which clearly indicates that reactions described by Eqs. (1.9) must have occurred. However, no diffraction peaks of $Fe(BH_4)_2$, that would be required by Eqs. (1.9) and (1.10) are observed. The experimental fact that samples are always ferromagnetic being attracted to a permanent magnet after ball milling clearly indicate that Fe in reaction Eq. (1.10) is formed in the amorphous state in the microstructure of BM samples. Furthermore, the presence of amorphous Fe is additionally confirmed because it eventually crystallizes forming nanocrystalline α-Fe, having the grain (crystallite) size within the 27-47 nm range.

Comparing the B-H bending and stretching bonds in the FT-IR spectrum of $2LiBH_4$+$FeCl_2$ sample, ball milled for 5 min (Fig. 5.5 a and b), with the reference FT-IR spectrum for the $LiBH_4$ (Fig. 5a) indicates the existence of $LiBH_4$ in the milled sample while $LiBH_4$ peaks was not observed in the XRD pattern of the 5h BM sample (Fig. 5.5). However, according to the phase identification by XRD, the presence of LiCl diffraction peaks which appeared after BM indicates that $FeCl_2$ reacts with $LiBH_4$ and, most likely, forms $Fe(BH_4)_2$. Similar behavior has been reported during MCAS of $LiBH_4$ with some other halides (TiF_3 and $TiCl_3$). For example, Sun et al. [60], Liu et al. [65], Au et al. [51, 101] and Fang et al. [55] reported that $Ti(BH_4)_3$ which formed during BM could not be observed by XRD and FT-IR. In all of their publications, $LiBH_4$ was only phase which identified by FT-IR while it had not been detected in the XRD pattern of the milled samples. They all claimed that new borohydride is very unstable under ambient condition and decomposed very fast. Jeon and Cho [102] also synthesised $Zn(BH_4)_2$ and found that the material decomposed very fast at RT.

In summary, for ball milling with simultaneously occurring MCAS and mechanical dehydrogenation, we stipulate that $Fe(BH_4)_2$ is formed very rapidly during BM. Simultaneously, $Fe(BH_4)_2$ decomposes under ball milling conditions forming both amorphous Fe and boron which leads to the change of color of the milled powder from white to black as originally reported by Schaeffer et al. [45] for a wet synthesis. Therefore, Eqs. (1.9) and (1.10) can now be expressed as one total reaction in the following form:

$$LiBH_4+0.5FeCl_2 \xrightarrow{(BM)} 0.5Fe(BH_4)_2+LiCl \xrightarrow{(BM)} 0.5a\text{-}Fe+a\text{-}B+2H_2+[LiCl] \qquad (5.1)$$

where [LiCl] means that this compound doesn't take part in reaction.

The hydride/halide ($2LiBH_4+FeCl_2$) system is quite remarkable in this respect that the mechanical dehydrogenation rate during ball milling (Fig. 5.4e) is much higher than the thermal dehydrogenation rate at 100-250 °C (Fig. 5.8) for the BM samples. By comparison, the quantity of 4.02 wt.% H_2 is desorbed after 0.5h of ball milling (Fig. 5.4e) while at 250 °C after the same time only 3.2 wt.% H_2 is desorbed (Fig. 5.8) from the BM sample. This is a very beneficial behavior for a rapid H_2 generator, clearly indicating that elevated temperature is not really needed for desorbing large quantities of H_2. Apparently, rapid mechanical dehydrogenation during BM is possible because of continuous formation of $Fe(BH_4)_2$ and its destabilization with the continuous mechanical energy input.

5.4.2. Thermal dehydrogenation in DSC and Sieverts-type apparatus

With regard to thermal dehydrogenation events in DSC for the non-ball milled (non-BM) and ball milled (BM) samples in Fig. 5.7c, the principal exothermic peak becomes very wide for the BM samples and its maximum is profoundly shifted by about 80 °C in magnitude to a much lower temperature range of about 204-206 °C for the energy input 6.07-12.14 kJ/g (Table A.3) as compared to a non BM mixture in Fig. 5.7a. Such a substantial temperature shift of a principal H_2 desorption peak has never been reported in the literature. It seems that ball milling accelerates thermal dehydrogenation reaction mechanisms. It can be envisaged that $Fe(BH_4)_2$ formed in BM samples initially accelerates the reaction at between $LiBH_4$ and $FeCl_2$ at elevated temperatures which starts at lower temperatures, even simultaneously with the polymorphic $LiBH_4$ transformation (Fig. 5.7a,b) and thermal reaction extends throughout a wide temperature range as reflected by wide DSC H_2 desorption peaks in Fig. 5.7c. In contrast, dehydrogenation reaction in DSC of the non-BM samples occurs through slow chemical reaction between $LiBH_4$ and $FeCl_2$:

$$LiBH_4+0.5FeCl_2 \rightarrow 0.5Fe+a\text{-}B+LiCl+2H_2 \qquad (5.2)$$

The final products are Fe and amorphous B (a-B) accompanied by hydrogen gas.

Expressing decomposition reaction through Eqs. (5.1) gives us opportunity to calculate the standard enthalpy (heat) of reaction, $\Delta H^o_{(reaction)}$, given as the difference between the standard enthalpies of formation of the products and the reactants [103] in the following form [103]:

$\Delta H^o_{(reaction)} = \Sigma\Delta H_f^0{}_{(products)} - \Sigma\Delta H_f^0{}_{(reactants)}$ (5.3)

Taking standard molar enthalpies of formation from Ref. [104]: ΔH_f^0 ($LiBH_4$)= -190.46 kJ/mol, ΔH_f^0 ($FeCl_2$)= -341.80 kJ/mol and ΔH_f^0 (LiCl)= -408.27 kJ/mol, and substituting into Eq. (1.11) one obtains:

$\Delta H^o_{(reaction)}$= [(-408.27)+0+(0.5×0)+(2×0)]-[(-190.46)+(0.5×(-341.79)]= -46.91 kJ/mol $LiBH_4$ or -23.46 kJ/mol H_2 (5.4)

That clearly shows that the thermal dehydrogenation reaction of the ($LiBH_4$+0.5$FeCl_2$) system has an exothermic character which is in an excellent agreement with the DSC H_2 desorption curves in Fig. 5.7 and further confirms the hypothesis about correctness of reaction events described by Eqs. (5.2).

Slow thermal reaction between $LiBH_4$ and $FeCl_2$ described by Eq. (5.2) is additionally supported by the dehydrogenation behavior at 100 (Fig. 5.8) and 250 °C (Fig. 5.11). The curves start with relatively rapid initial dehydrogenation step after which they desorb very slowly. This is well observed for the curve at 250 °C for a pre-ball milled (2$LiBH_4$+$FeCl_2$) for which the initial dehydrogenation rate is very fast but then after a short while the dehydrogenation rate is precipitously reduced and over 20 h duration is required to desorb 4 wt.% H_2. This peculiar behavior is explained by the fact that a small quantity of $Fe(BH_4)_2$ is formed during ball milling (Fig. 5.6), as discussed earlier, which by rapid thermal decomposition according to Eq. (5.1) accelerates the initial stage of H_2 desorption. However, after its depletion, a slow, chemical reaction of Eq. (5.2) occurs reducing the desorption rate.

In any case the thermally dehydrogenated H_2 quantity in Fig. 5.8 does not exceed the theoretical capacity of 4.73 wt.% H_2 for the system, clearly indicates that only H_2 is desorbed without the presence of diborane gas.

Furthermore, decomposition temperature of $Fe(BH_4)_2$ in reaction described by Eq. (5.1) can be roughly estimated at 1 bar H_2 pressure from the Van't Hoff equation [81]. Assuming the estimated $\Delta H^o_{(reaction)}$=23.46 kJ/mol H_2 as calculated earlier and the standard entropy of reaction, $\Delta S^o_{(reaction)}$, the same as for $LiBH_4$, which was reported as being equal to =100.2 kJ/mol H_2 [105], one obtains the equilibrium decomposition temperature equal to about -38°C. Obviously, this is not an exact value but clearly indicates that decomposition of $Fe(BH_4)_2$ can start below 0°C which agrees well with the decomposition temperature range -10 to 0 °C reported by Schaeffer et al. [45] for solvent synthesized $Fe(BH_4)_2$ and confirms that MCAS-synthesized $Fe(BH_4)_2$ is a metastable hydride which is very prone to decomposing right after its formation under a mechanical energy input.

Although a practical application aspect is beyond the scope of this section, but it is still prudent to say a few words about this particular aspect. It must be clearly reiterated, right from the beginning, that the hydride systems for hydrogen generation are not typical, reversible on board, "hydrogen storage" systems in the classical meaning of this word, as discussed in the Introduction section. In contrast, the H_2 generating systems after being exhausted and converted into elemental or other chemical species would not require reversibility "on-board" but could be chemically regenerated or converted to useful chemical compounds "off-board", i.e. in a chemical plant.

For example, it may be envisaged that the rapid mechanical dehydrogenation phenomenon observed previously in our laboratory for some hydride/hydride [84, 97], hydride/halide [97] and the $LiBH_4$-$FeCl_2$ hydride/halide systems could be applied in practical engineering terms for generating large quantities of hydrogen on demand for auxiliary power generation systems coupled with PEM fuel cells and batteries. Further possible practical applications for the rapid hydrogen generators are low power remote fuel cells or portable gas analyzers [106, 107], fuel cell off-road vehicles and cordless lawn mowers running with a fuel cell instead of hydrogen combustion engine [108]. The rapid H_2 generators can also be used in a number of chemical processes where a continuously reducing atmosphere is needed for a completion of the chemical process [15]. They could also have an application in a military sector for supplying hydrogen to micro fuel cells in portable devices needed for soldiers on a mission in remote areas [15].

Furthermore, a surprisingly very low mechanical energy input required to generate H_2 from several such systems like the ($LiBH_4$-$FeCl_2$) system investigated in this work, without the necessity for applying elevated temperatures, renders the rapid mechanical dehydrogenation phenomenon useful for powering various fuel cell-run devices mentioned above in such a way that the mechanical energy for H_2 release could even be provided by human power similarly, for instance, to pedaling a stationary bicycle.

Other hydride/hydride or hydride/halide systems with even more rapid mechanical dehydrogenation rate and higher released H_2 capacity, which could practically serve as "rapid mechanical hydrogen generators" should be sought. Several similar high H_2 capacity systems are now under investigation in our laboratory and will be reported in further publications.

Finally, the ball milled ($2LiBH_4$+$FeCl_2$) powder is not combustible if simply exposed to air containing modest moisture 20-30% moisture (humidity). However, it is combustible if in contact with a wet substrate. A small amount of the powder sprinkled on a paper towel was combusted in less than 10 s. This apparently occurs due to a contact with moisture absorbed by a paper towel. However, I always handle it under a high purity argon atmosphere.

5.3. Summary of findings

The results reported herein elucidate the effects of the total milling energy input, Q_{TR} (kJ/g), during a mechano-chemical activation synthesis (MCAS) of the ($2LiBH_4$+$FeCl_2$) mixture on its microstructural evolution and mechanical and isothermal dehydrogenation properties.

Ball milling (BM) of the ($2LiBH_4$+$FeCl_2$) mixture at room temperature (RT) results in rapid and copious mechanical dehydrogenation up to about 85% of its total theoretical H_2 capacity equal to 4.73 wt.%. The system is quite remarkable in the sense that the mechanical dehydrogenation rate during ball milling is much higher than the thermal dehydrogenation rate at the 100-250°C range. For illustration, the quantity of 4.02 wt.% H_2 is desorbed after 0.5h of ball milling while at 250°C, after the same desorption time, only 3.2 wt.% H_2 is desorbed. Therefore, the system is an excellent, ambient temperature, rapid H_2 generator. Furthermore, to achieve that remarkable H_2 desorption rate the required milling energy input is very small being equal to 36.4 kJ/g. X-ray diffraction after BM shows the presence of the crystalline LiCl diffraction peaks. FT-IR spectrum show the presence of $LiBH_4$ after ball milling. Samples milled under varying energy input are attracted to a permanent magnet. Apparently, iron borohydride, $Fe(BH_4)_2$, is rapidly synthesized by MCAS during ball milling and simultaneously decomposes, forming amorphous iron (a-Fe) and boron (a-B).

Further experiments with DSC and isothermal dehydrogenation at the temperature range 100-250°C strongly suggest that for the BM samples a $Fe(BH_4)_2$ hydride, which was formed during BM, is likely initially decomposing with a fast rate. Subsequently, a $Fe(BH_4)_2$ hydride is rapidly exhausted and a slow chemical reaction between $LiBH_4$ and $FeCl_2$ begins which for the non-BM samples starts right in the beginning of desorption.

The presence of Fe in the microstructure of the BM samples, as a product of decomposition of $Fe(BH_4)_2$, is additionally confirmed because Fe formed after thermal dehydrogenation is initially amorphous but eventually crystallizes forming nanocrystalline α-Fe after being held at dehydrogenation temperature for some time. Nanocrystalline Fe after crystallization exhibits the grain (crystallite) size within the 27-47 nm range. There is an observed tendency of decreasing Fe nanograin (crystallite) size from 47 to 27-33 nm with increasing milling energy input from 2.43 to 6.07 kJ/g. Some potential applications are also briefly discussed.

6. ($LiBH_4$-TiF_3) system with catalytic additives

6.1. Mechanical dehydrogenation and evolution of microstructure at room temperature

Figure 6.1 illustrates the SEM micrographs of the morphology of as-received TiF_3 (Fig. 6.1a), graphene (Fig. 6.1b) and ultrafine filamentary Ni (Fig. 6.1c and d), respectively. By comparing the SEM micrograph of TiF_3 and that of the as-received $LiBH_4$ (already shown in Fig. 4.1a), one can see that the TiF_3 powder particles are finer than $LiBH_4$, but more agglomerated. However, the graphene powder particles are very dispersed being in a platelet (flake) form, while the ultrafine filamentary Ni powder exhibits agglomerated ball-like features (Fig. 6.1c) which exhibit filamentary morphology under a high magnification (Fig. 6.1d).

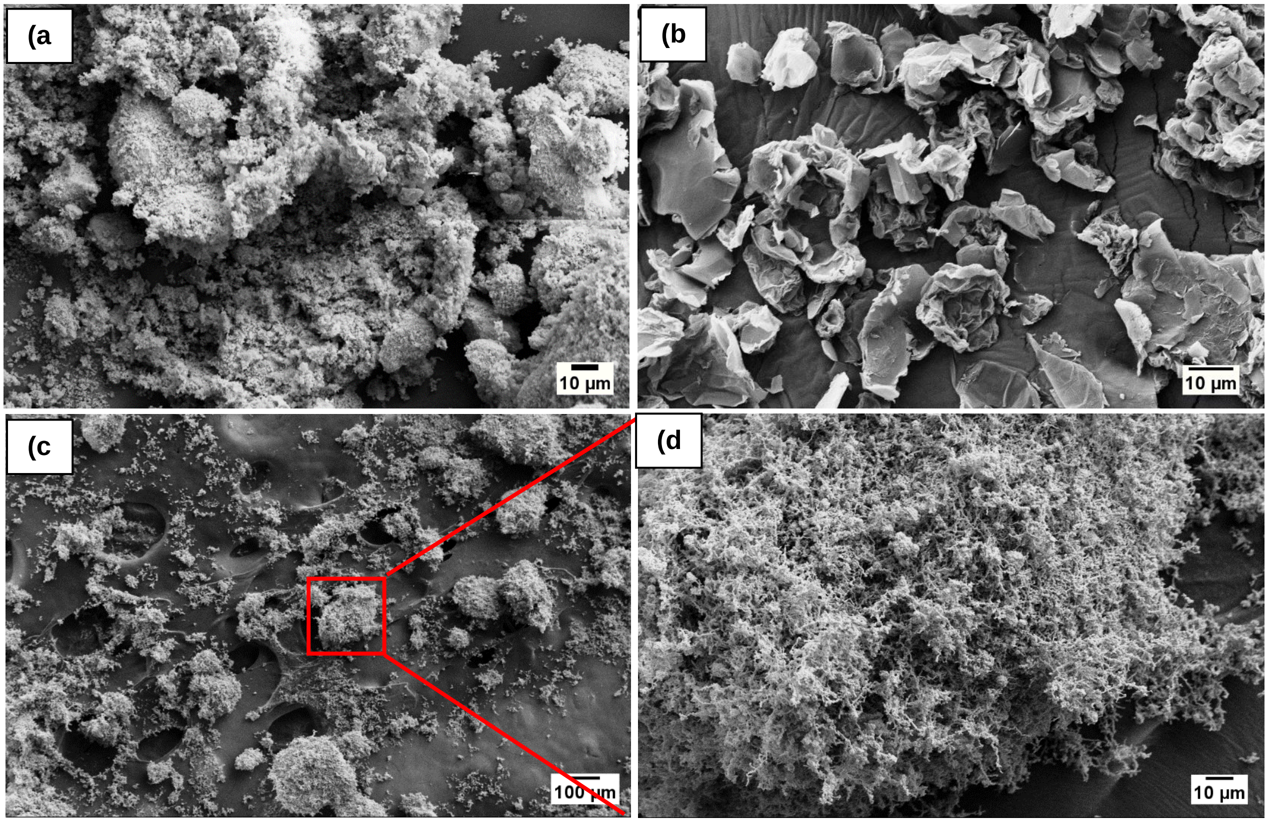

Figure 6-1. Scanning electron micrographs of as received constituent powders (a) TiF3, (b) graphene and (c and d) Ni (adapted from [109]).

A dramatic refinement of the initial powder mixture after milling, particularly in comparison to the large size of the as-received $LiBH_4$ particulate, can be clearly seen in Fig. 6.2. However, some severely agglomerated powder particles are also observed after milling. In addition, there is no significant difference between the morphology of the ball milled powder without additives and the powder with the addition of 5 wt.% Ni (Fig. 6.2e and f). However, a SEM micrograph of a sample with graphene (Fig. 6.2c and d) suggests less agglomeration when the milling time is increased from 1 to 5h although this hypothesis would have to be quantitatively supported with detailed measurements of powder particle distribution.

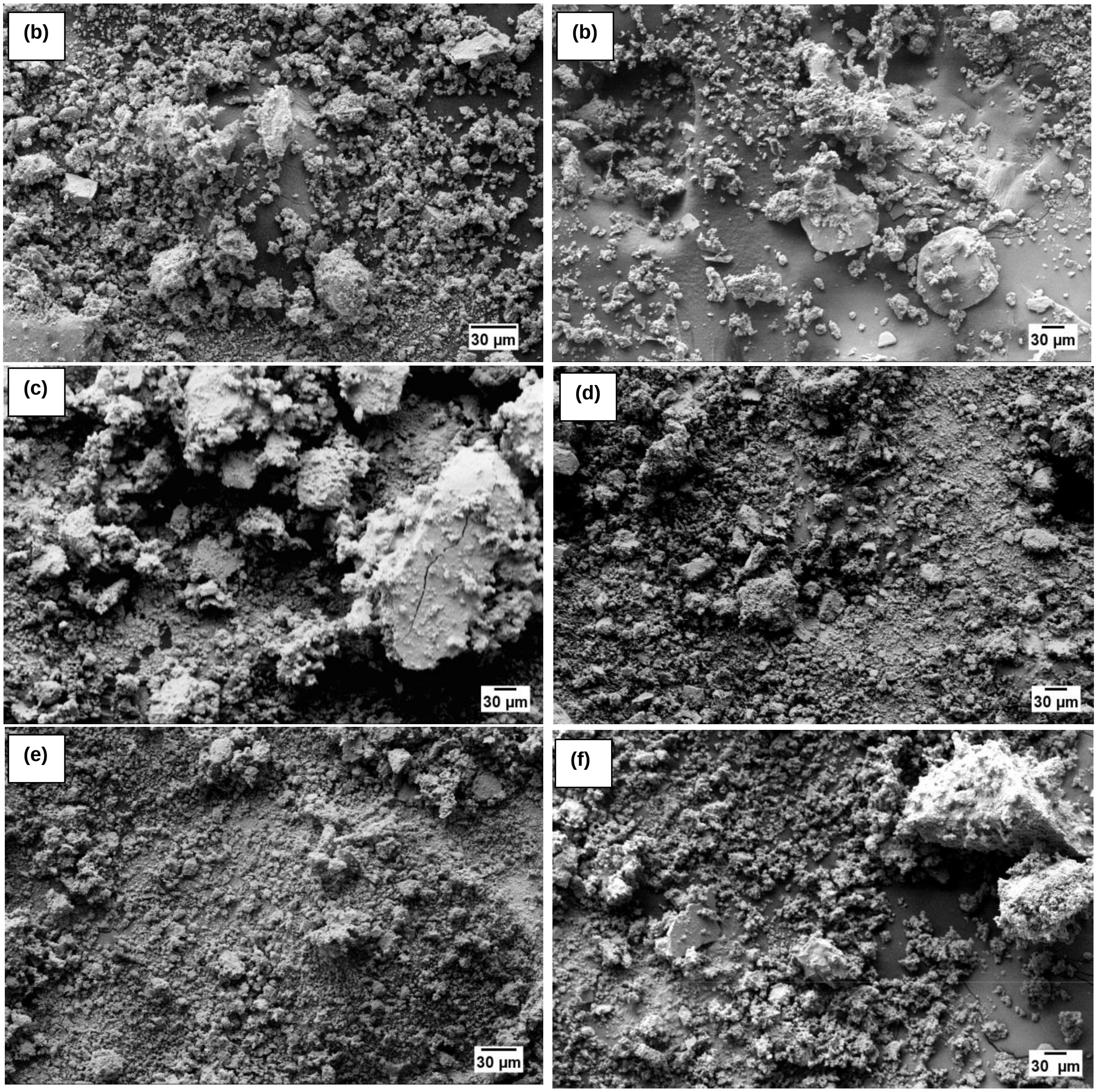

Figure 6-2. Scanning electron micrographs of ball milled (BM) powders for varying milling time (milling energy input). (a) ($3LiBH_4$+TiF_3)-1h BM, (b) ($3LiBH_4$+TiF_3)-5h BM (c) ($3LiBH_4$+TiF_3)+5 wt.% graphene-1h BM (d) ($3LiBH_4$+TiF_3)+5 wt.% graphene-5h BM (e) ($3LiBH_4$+TiF_3)+5 wt.% Ni-1h BM (f) ($3LiBH_4$+TiF_3)+5wt.% Ni-5h BM (adapted from [109]).

So far, the phenomenon of mechanical dehydrogenation for the ($3LiBH_4$+TiF_3) system has never been reported in the literature. As shown in Fig. 6. 3, the additive-free sample mechanically dehydrogenated 1.35 and 1.58 wt.% H_2 after milling with an energy input

Q_{TR}=72.8 kJ/g (1h BM) and Q_{TR}=364 kJ/g (5h BM), respectively, while the sample with ultrafine Ni mechanically dehydrogenated 1.42 and 1.97 wt.% H_2 after 1 and 5h BM, respectively. Apparently, regardless of the presence of ultrafine filamentary Ni both types of samples exhibit a similar mechanical dehydrogenation behavior during BM which shows that ultrafine Ni does not accelerate mechanical dehydrogenation rate to any measurable extent in contrast to its strong effect on the thermal dehydrogenation of hydrides containing submicrometric/nanometric Ni [7, 15]. On the other hand, a surprising aspect of mechanical dehydrogenation of the sample with graphene is that it showed less dehydrogenation up to Q_{TR}=72.8 kJ/g (1h BM) in comparison with the other two systems. However, the rate of dehydrogenation increased rapidly after 1h of milling and the quantity of desorbed H_2 reached 2.38 wt.% after the energy input reached Q_{TR}=364 kJ/g (5h BM) (Fig. 6.3). As mentioned in the Experimental section reduced graphene oxide employed in the present work contains ~1 wt.% H_2. That quantity of H_2 is, most likely, released when a large energy input of Q_{TR}=364 kJ/g (5h BM) is injected into the powder. In this context, it is to be pointed out that after longer milling reduced graphene oxide is transformed, at least, partially to a highly dispersed amorphous carbon which may enhance the release of H_2 from the original graphene structure.

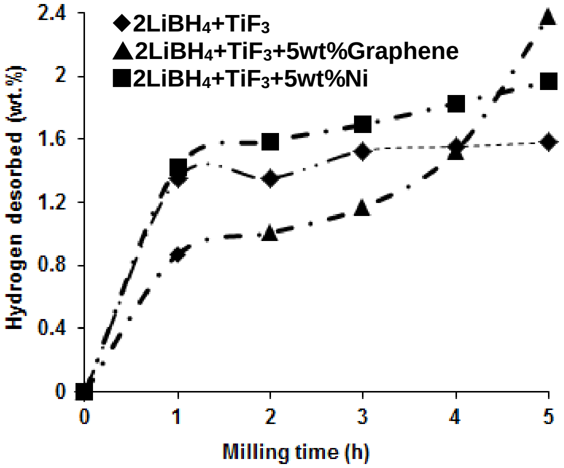

Figure 6-3. The quantity of H_2 desorbed during milling of the ($3LiBH_4+TiF_3$) powder mixture without and with additives (adapted from [109].

The XRD patterns of the samples after 1 and 5h BM and complete dehydrogenation at three different temperatures are presented in Fig. 6.4a and b, respectively. Fig. 6.4a shows the XRD patterns of the additive-free powder mixture milled with an energy input, Q_{TR}=72.8 kJ/g (1h BM) compared to those after thermal treatment. The diffraction peaks of $LiBH_4$ and TiF_3 can still be seen after 1h BM (Fig. 6.4a). Fig. 6.4b shows that after 5h BM, the peak intensities of TiF_3 are much lower than those after 1h BM, and all the peaks of $LiBH_4$ have disappeared. A trace of LiF diffraction peaks as well as very weak peaks of elemental Ti after 1 and 5h BM, in addition to the presence of TiF_3 diffraction peaks, indicate that a mechano-chemical reaction between the reactants started during BM but the amount of energy was still insufficient to complete the reaction. Moreover, Fig. 6.4a, b show that after dehydrogenation up to 100 °C the peaks of TiF_3 in both samples milled for 1 and 5h are not visible anymore, whereas the intensity of the LiF peaks substantially increased. The peaks of Ti are clearly visible as well.

The XRD pattern of the powder mixture with 5 wt.% graphene with an energy input, Q_{TR}=72.8 kJ/g (1h) and 364 kJ/g (5h), are shown in Fig. 6.4c and Fig. 6.4d, respectively. During BM, the diffraction peaks of $LiBH_4$ disappeared, whereas the TiF_3 peaks are still visible. The LiF diffraction peaks which began to appear during BM becomes stronger after dehydrogenation at various temperatures (Fig. 6.4c and Fig. 6.4d), while the lack of TiF_3 peaks after thermal desorption indicates a similar phase transition as that for the additive-free samples. Fig. 6.4e illustrates the XRD patterns of the sample with ultrafine Ni, ball milled with an energy input Q_{TR}=72.8 kJ/g (1h) compared to a sample after dehydrogenation at 60 °C. Diffraction peaks of Ni as well as TiF_3, LiF and Ti are clearly seen after 1h BM while dehydrogenation at 60 °C led to the disappearance of the TiF_3 peaks. Similar behavior can be seen for the sample containing Ni after BM with an energy input 364 kJ/g (5h) in Fig. 6.4f.

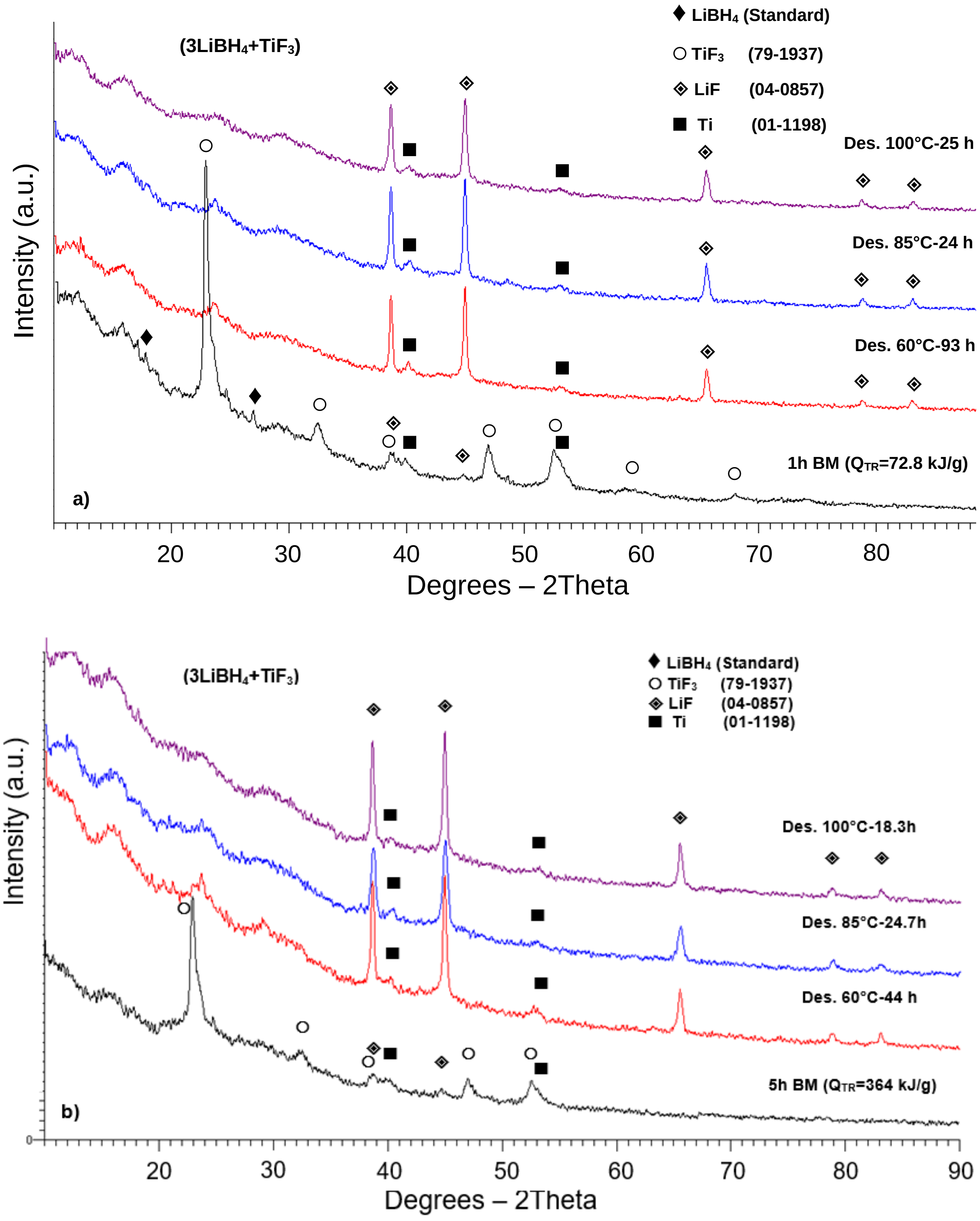

(3LiBH₄+TiF₃)
♦ LiBH₄ (Standard)
○ TiF₃ (79-1937)
◈ LiF (04-0857)
■ Ti (01-1198)
Des. 100°C-25 h
Des. 85°C-24 h
Des. 60°C-93 h
1h BM (Q_TR=72.8 kJ/g)
a)
Intensity (a.u.)
Degrees – 2Theta
20
30
40
50
60
70
80
(3LiBH₄+TiF₃)
♦ LiBH₄ (Standard)
○ TiF₃ (79-1937)
◈ LiF (04-0857)
■ Ti (01-1198)
Des. 100°C-18.3h
Des. 85°C-24.7h
Des. 60°C-44 h
5h BM (Q_TR=364 kJ/g)
b)
Intensity (a.u.)
Degrees – 2Theta
0
20
30
40
50
60
70
80
90

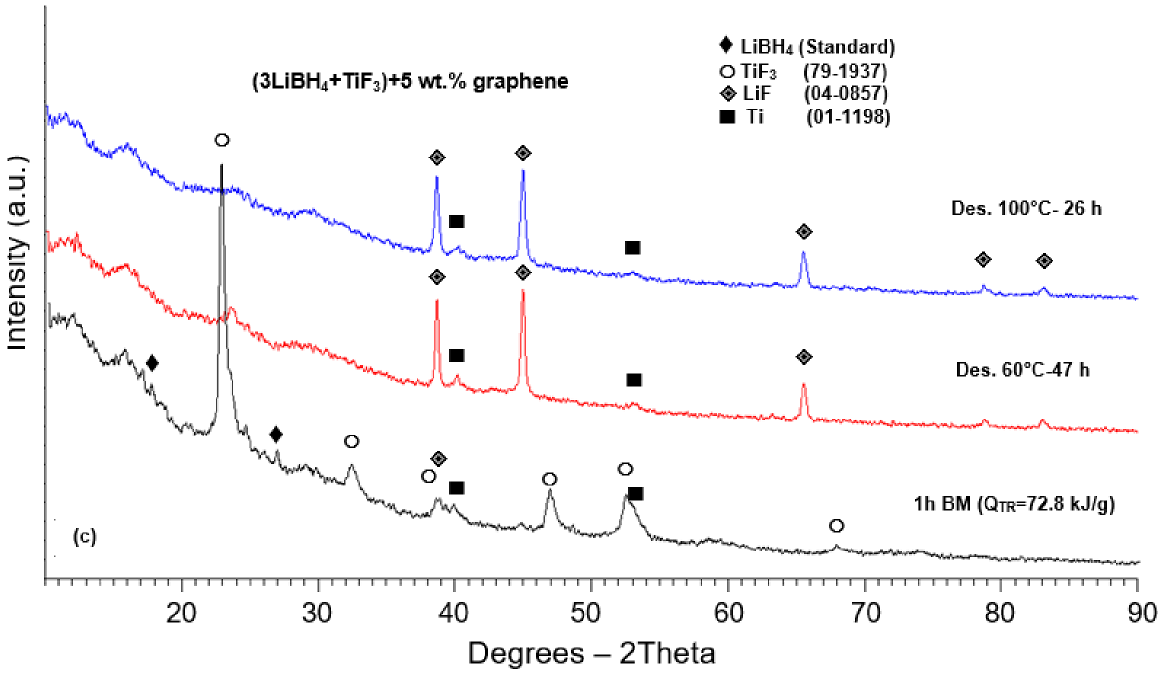
(3LiBH$_4$+TiF$_3$)+5 wt.% graphene
♦ LiBH$_4$ (Standard)
○ TiF$_3$ (79-1937)
◈ LiF (04-0857)
■ Ti (01-1198)
Des. 100°C- 26 h
Des. 60°C-47 h
1h BM (Q$_{TR}$=72.8 kJ/g)
(c)
Intensity (a.u.)
20
30
40
50
60
70
80
90
Degrees – 2Theta

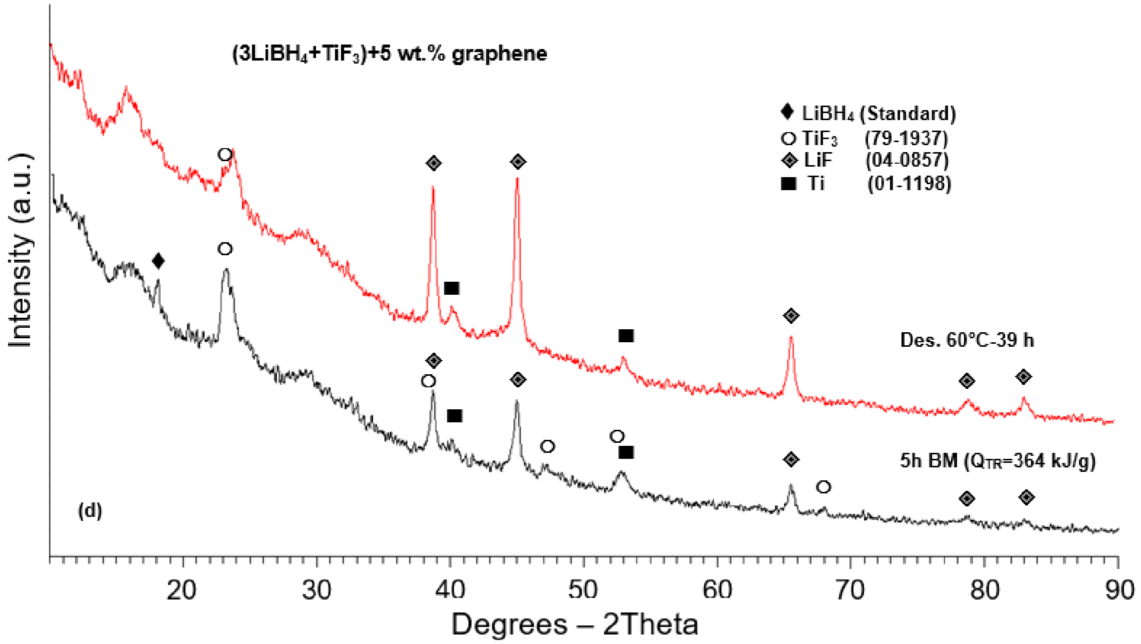
(3LiBH$_4$+TiF$_3$)+5 wt.% graphene
♦ LiBH$_4$ (Standard)
○ TiF$_3$ (79-1937)
◈ LiF (04-0857)
■ Ti (01-1198)
Des. 60°C-39 h
5h BM (Q$_{TR}$=364 kJ/g)
(d)
Intensity (a.u.)
20
30
40
50
60
70
80
90
Degrees – 2Theta

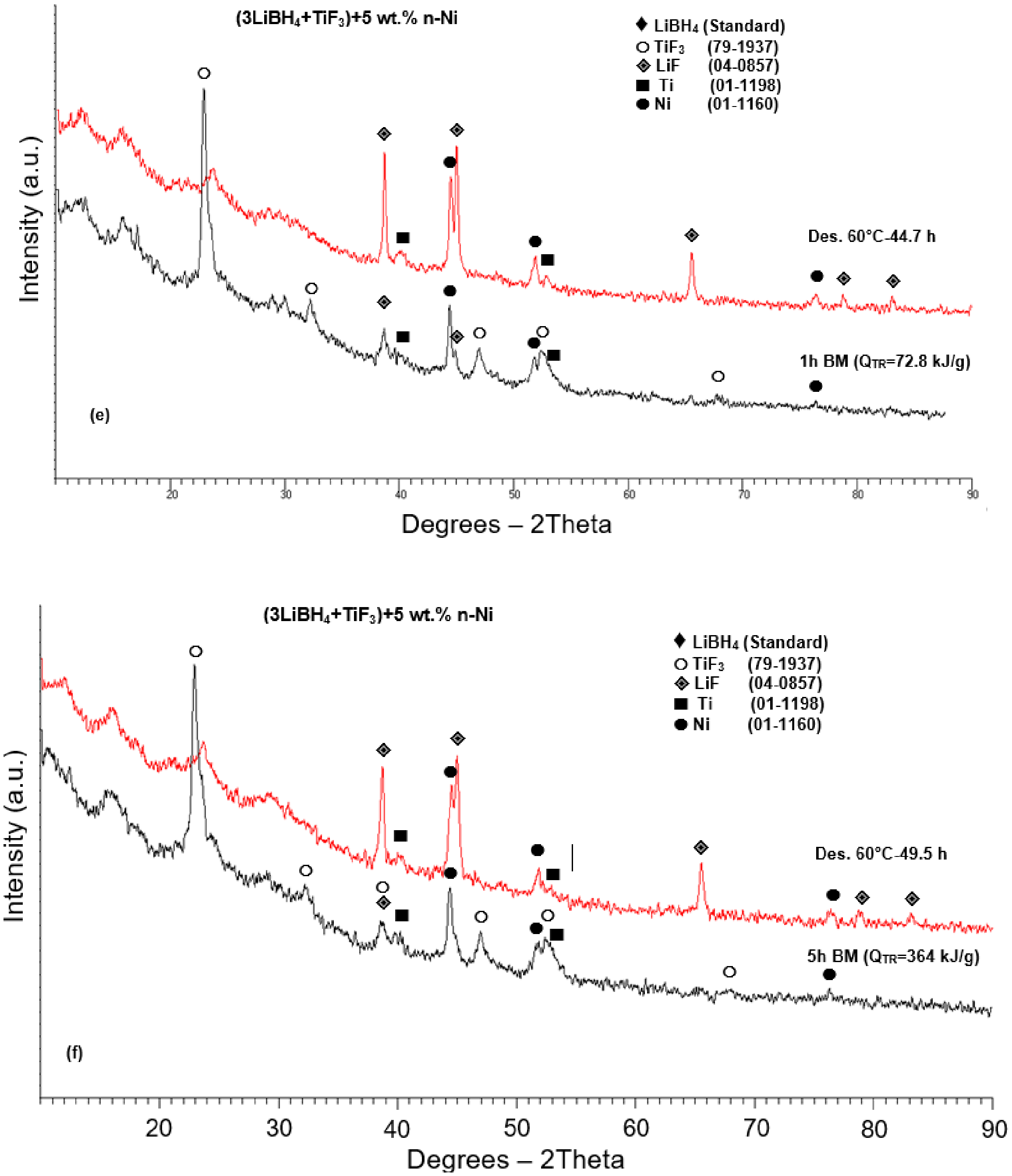

Figure 6-4. XRD patterns after ball milling (BM) and isothermal dehydrogenation at different temperatures for (a) ($3LiBH_4+TiF_3$) with an energy input, Q_{TR}=72.8 kJ/g (1h BM), (b) ($3LiBH_4+TiF_3$) with an energy input, Q_{TR}=364 kJ/g (5h BM), (c) ($3LiBH_4+TiF_3$)+5 wt.% graphene with an energy input, Q_{TR}=72.8 kJ/g (1h BM), (d) ($3LiBH_4+TiF_3$)+5 wt.% graphene with an energy input, Q_{TR}=364 kJ/g (5h BM), (e) ($3LiBH_4+TiF_3$)+5 wt.% Ni with an energy input, Q_{TR}=72.8 kJ/g (1h BM), (f) ($3LiBH_4+TiF_3$)+5 wt.% Ni with an energy input, Q_{TR}=364 kJ/g (5h BM) (adapted from [109]).

The FT-IR spectrum for the additive-free sample, ball milled with an energy input Q_{TR}= 364 kJ/g which desorbed 1.58 wt.% H_2 during milling, is shown in Fig. 6.5a, and can be compared to the samples after isothermal dehydrogenation at 60 °C for 2.2h (desorbed 1.58 wt.% H_2 during BM and additionally 0.99 wt.% H_2 during isothermal dehydrogenation) and 100 °C for 18.3h (desorbed 1.58 wt.% H_2 during BM and additionally 4.8 wt.% H_2 during isothermal dehydrogenation) in Fig. 6.5b and c, respectively. Fig. 6.5d shows the FT-IR spectrum of pure $LiBH_4$ adapted from [93].

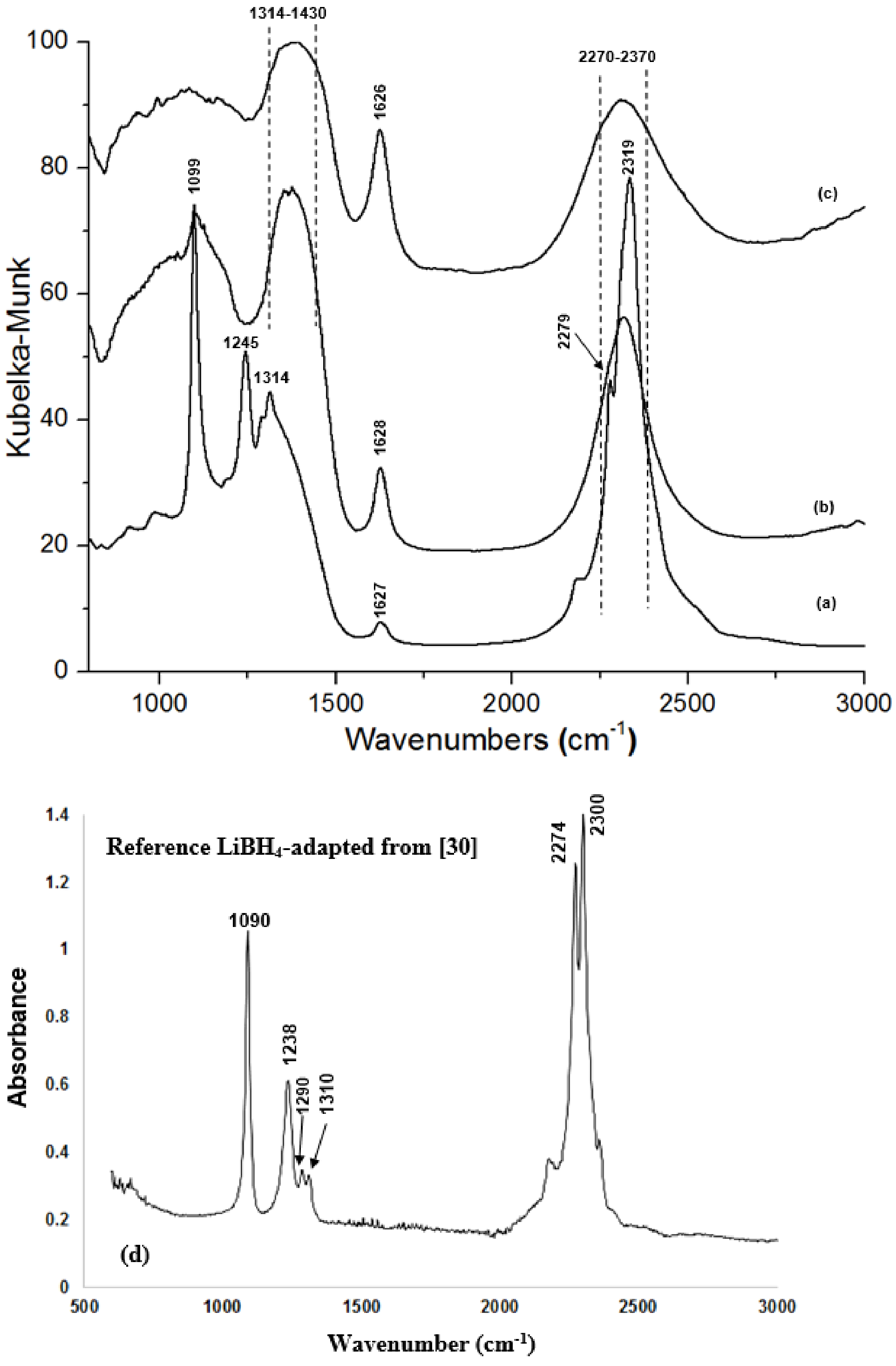

Figure 6-5. a) FT-IR spectrum for the sample without additive with an energy input of Q_{TR}= 364 kJ/g, 5h BM (desorbed 1.58 wt.% H_2), b) after 5h BM and isothermal dehydrogenation at 60 °C for 2.2h (desorbed 2.57 wt.% H_2), c) after 5h BM and isothermal dehydrogenation at 100 °C for 18.3h (desorbed 6.38 wt.% H_2) and d) pure $LiBH_4$ (adapted from [109]).

6.2. *Thermal behavior in DSC, gas mass spectrometry*

Gas mass spectrometry as well as DSC/TGA results during temperature programmed desorption (TPD) up to 500°C of the 1h ball milled additive-free samples are shown in Fig. 6.6 a, b and can be compared to those after 5h ball milled in Fig. 6.6c, d, respectively. For the sample milled with an energy input Q_{TR}=72.8 kJ/g (1h BM), the release of hydrogen starts from about 50 °C as a principal gas with a maximum intensity around 120-140 °C and is accompanied by a miniscule quantity of diborane B_2H_6 (Fig. 6.6a). The ratio of H_2 to B_2H_6 is 6015 up to 200 °C which increases to 6089 with temperature increasing to 500 °C. It is also worth noting that the release of B_2H_6 in the 1h BM sample starts around 110 °C, with a maximum intensity at around 125-135 °C, indicating that B_2H_6 may not be released at low temperatures <100 °C which strongly suggests that gas desorbed during ball milling (Fig. 6.3) is, indeed, pure H_2.

A very interesting finding is that, in contrast to 1h BM sample, gas mass spectrometry of the sample after 5h BM (Q_{TR}=364 kJ/g) does not show, within a resolution range of the MS instrument, any visible release of B_2H_6 which is also reflected in a huge intensity ratio H_2/B_2H_6=10503 (Fig. 6.6c). The DSC curve of the 1h BM sample (Fig. 6.6b) exhibits a large exothermic peak at around 125 °C and a very small overlapped exothermic peak at about 180 °C, whereas for the 5h BM sample, the maxima of the first and second overlapped exothermic peaks occur at 120 °C and 170 °C (Fig. 6.6d), respectively. The TGA mass loss up to 200°C was reduced from 3.58% to 1.44% by increasing the milling energy from 72.8 kJ/g (1h) to 364 kJ/g (5h) (compare Fig. 6.6b and Fig. 6d).

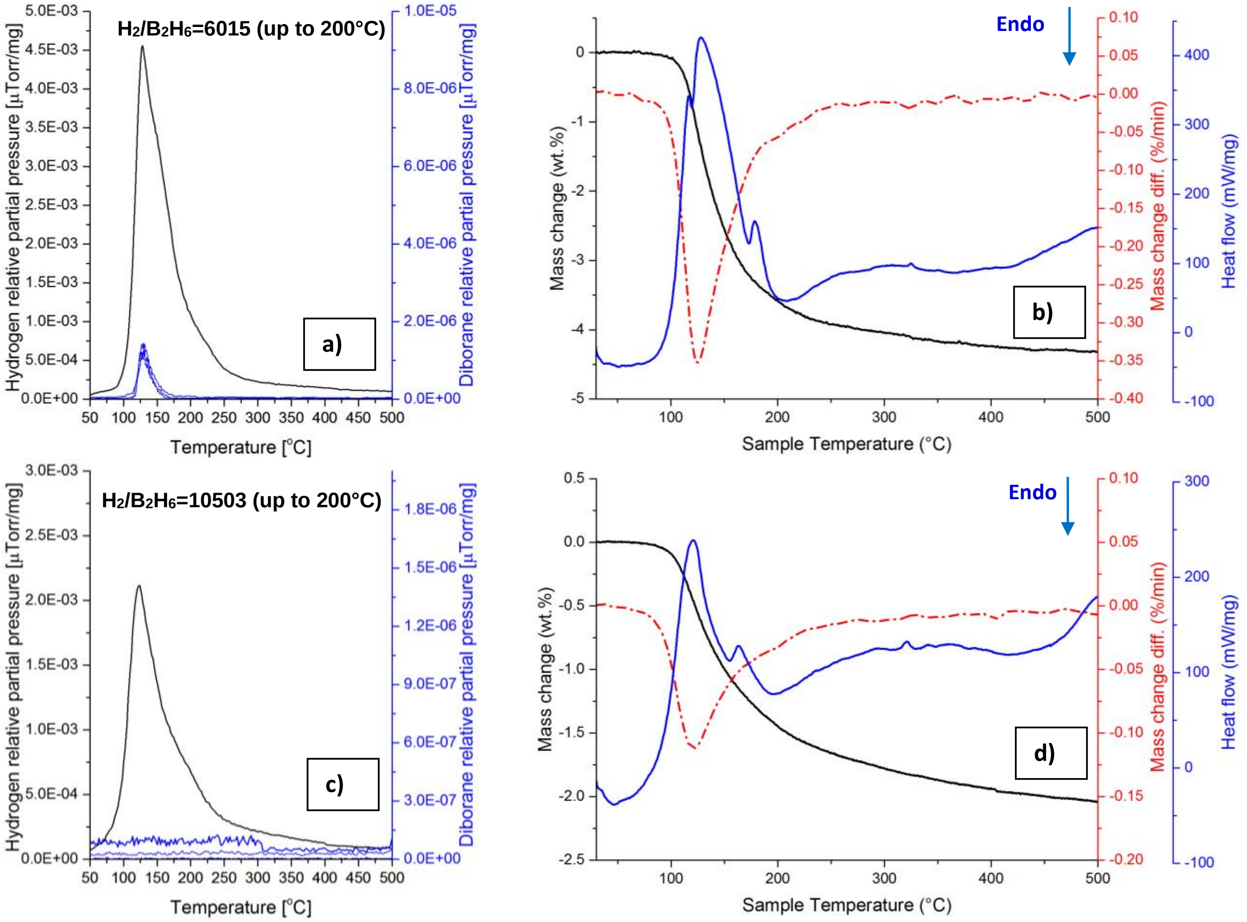

Figure 6-6. (a) Mass spectrometry (MS) gas desorption spectra for a ($3LiBH_4$+TiF_3) sample ball milled for 1h mixture. (b) TG and DSC curves (c) $3LiBH_4$+TiF_3 sample ball milled for 5h mixture (d) TG and DSC curves. Heating rate 5°C/min.

6.3. *Isothermal dehydrogenation*

Figure 6.7 shows the isothermal dehydrogenation curves at varying temperatures from 60 to 200 °C for the additive-free samples (Fig. 6.7a and b), with ultrafine Ni (Fig. 6.7c and d) and graphene (Fig. 6.7e and f) ball milled with energy input Q_{TR}=72.8 and 364 kJ/g. The quantities of H_2 desorbed during BM and subsequent isothermal dehydrogenation at varying temperatures are summarized in Table 6.1. As can be seen, the total quantity of H_2 desorbed at 60 °C within 93h is 4.52 wt.%, which increases to 5.81 wt.% at 200 °C within 20h for the 1h BM additive-free sample. On the other hand, the same powder milled for 5h (Fig. 6.7b) desorbed less hydrogen (5.58 wt.%) at 200 °C in comparison with the powder milled for 1h obviously owing to higher release of H_2 during BM. The total quantities of H_2 desorbed during BM and subsequent isothermal dehydrogenation at 200 °C for both the 1 and 5h BM samples are same (7.16 wt.%).

As mentioned in Sec. 6.1 (Fig. 6.3), the sample with 5 wt.% Ni tends to release more H_2 during BM than the additive-free one (column two of Table 6.1). It also shows a faster dehydrogenation rate than the additive-free sample during isothermal dehydrogenation (Fig. 6.7c). The time required for desorbing 4.00 wt.% H_2 for the sample with 5 wt.% Ni after 1h BM is 21.8h at 60 °C, in contrast to 30h for the additive-free sample at 60 °C.

The sample with 5 wt.% graphene milled for 1h (Q_{TR}=72.8 kJ/g) shows a slower thermal dehydrogenation rate at 60°C than all other samples, and does not even reach 4.00 wt.% H_2 after 43h thermal treatment (Fig. 6.7e). The sample with 5 wt.% graphene milled for 1h (Q_{TR}=72.8 kJ/g) shows a slower thermal dehydrogenation rate at 60°C than all other samples, and does not even reach 4.00 wt.% H_2 after 43h thermal treatment (Fig. 6.7f). However, after a short while the desorption starts saturating and the quantity of H_2 does not exceed 3 wt.% for any dehydrogenation temperature from 60 to 200 °C (Fig. 6.7f and Table. 6.1) up to 24h duration. In addition, for that sample the total H_2 quantity of 5.25 wt.% desorbed during ball milling and at 200°C (24h) is the smallest one which is partially related to the fact that it exhibited the highest amount of desorption during ball milling among all the samples (Fig. 6.3 and Table. 6.1) and also related to a very rapid saturation of desorption rate at 200°C (Fig. 6.7f). As mentioned earlier, after milling for 5h (Q_{TR}=364 kJ/g) the reduced graphene oxide additive is to a large extent reduced to highly dispersed carbon. The presence of amorphous carbon can be responsible for a dehydrogenation behavior observed in Fig. 6.7f.

Table. 6-1. Summary of hydrogen quantities desorbed due to mechanical and thermal dehydrogenation

Sample	**H_2 desorbed during BM (wt.%)**	**H_2 desorbed at 60°C (wt.%)**	**H_2 desorbed at 85°C (wt.%)**	**H_2 desorbed at 100°C (wt.%)**	**H_2 desorbed at 120°C (wt.%)**	**H_2 desorbed at 200°C (wt.%)**	**Total H_2 desorbed during BM and at 200°C (wt.%)**
($3LiBH_4$+TiF_3)-1h BM	1.35	4.52 (93.2)	4.85 (23.6)	5.30 (25)	5.52 (23.15)	5.81 (21.3)	7.16
($3LiBH_4$+TiF_3)-5h BM	1.58	4.73 (44)	4.83 (24.6)	5.04 (65)	5.29 (23.5)	5.58 (19.5)	7.16
($3LiBH_4$+TiF_3)+5wt.% Ni-1h BM	1.42	4.42 (44.7)	5.18 (96.2)	5.01 (24.8)	5.05 (20.3)	5.62 (23.5)	7.04
($3LiBH_4$+TiF_3)+5wt.% Ni-5h BM	1.97	3.92 (49.45)	4.52 (41)	4.82 (22.8)	5.27 (29.2)	5.39 (21.7)	7.36
($3LiBH_4$+TiF_3)+5wt.% graphene- 1h BM	0.87	3.62 (47)	4.78 (93.5)	4.87 (26.2)	5.08 (18.9)	6.02 (22)	6.89
($3LiBH_4$+TiF_3)+5wt.% graphene- 5h BM	2.38	2.98 (39.3)	2.96 (90.95)	2.45 (22.8)	2.86 (25.1)	2.84 (92.2)	5.22

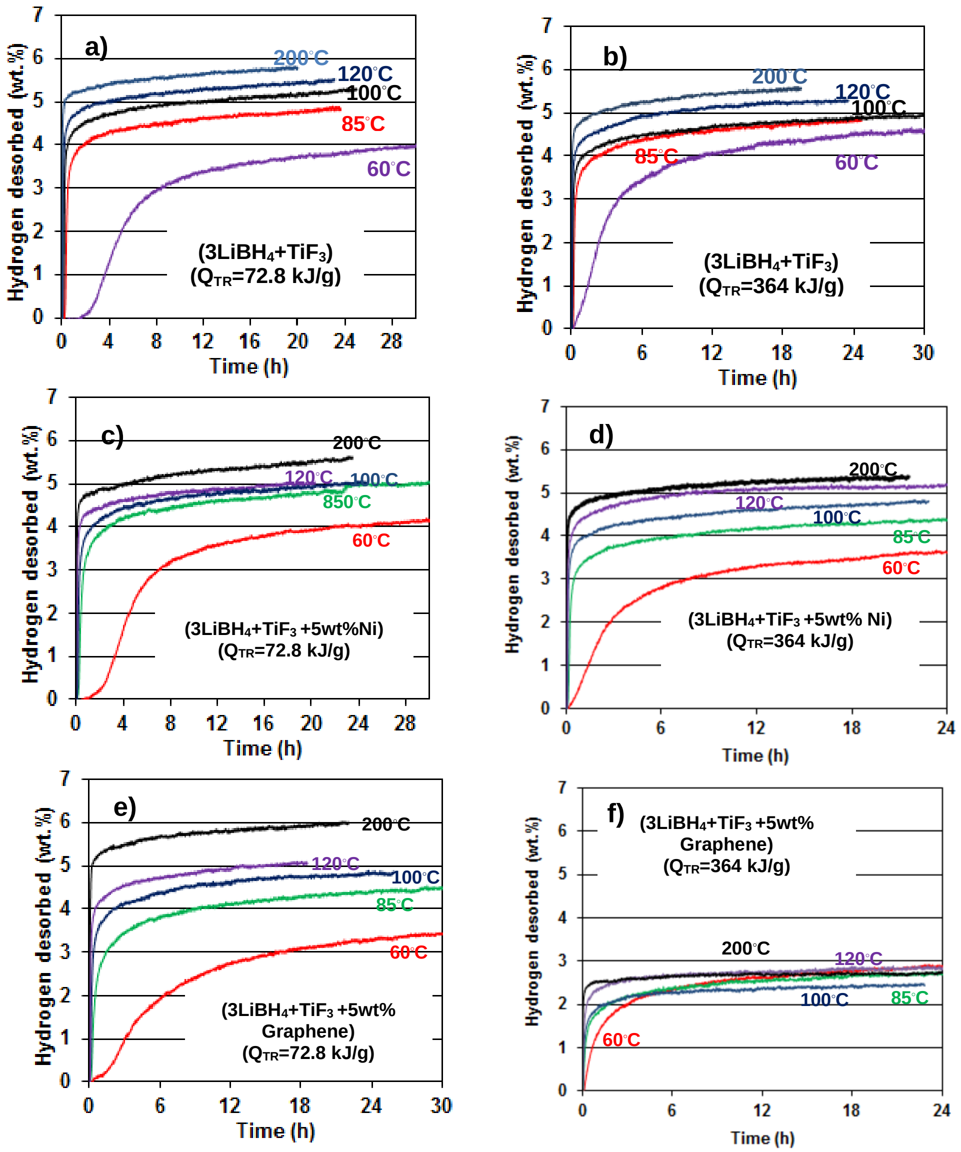

Figure 6-7. Dehydrogenation curves for (a) $3LiBH_4$+TiF_3-1h BM, (b) $3LiBH_4$+TiF_3-5h BM (c) $3LiBH_4$+TiF_3+5wt.% Ni-1h BM (d) $3LiBH_4$+TiF_3+5wt.% Ni-5h BM (e) $3LiBH_4$+TiF_3+5wt.% graphene-1h BM (f) $3LiBH_4$+TiF_3+5wt.% graphene-5h BM (adapted from [109]).

The apparent activation energy for dehydrogenation is estimated using the linear section of the dehydrogenation curves in the range of 60-120°C in Fig. 6.7 and illustrated in the bar graph shown in Fig. 6.8. The apparent activation energy for thermal dehydrogenation for the additive-free sample slightly decreases with increasing milling energy from 72.8 kJ/g (1h BM) to 364 kJ/g (5h BM). The addition of 5 wt.% Ni reduces the activation energy for the sample with a 72.8 kJ/g milling energy input (1h BM) by comparison to the additive-free sample ball milled with the same energy input (1h BM). Further milling of Ni containing sample for 5h (energy input of 364 kJ/g) leads to a slight increase in the apparent activation energy. The highest apparent energy for dehydrogenation is exhibited by a sample with 5 wt.% graphene after injection of 72.8 kJ/g milling energy (1h BM). However, as shown in Fig. 6.8, after 5h BM (Q_{TR}=364 kJ/g) the apparent activation energy of the sample with 5 wt.% graphene is dramatically reduced to about half of its value after only 1h BM (Q_{TR}=72.8 kJ/g), i.e. 42.9±3.8 vs. 95.2±1.9, respectively. Undoubtedly, this low apparent activation energy for the linear initial desorption period is related to a transformation of initial graphene into highly dispersed carbon. There are some observations published in the literature that ball milling of borohydrides, like $LiBH_4$, with carbonaceous additives substantially improves their dehydrogenation kinetics [114-116]. The explanations suggested for the effect of carbonaceous species on the enhancement of kinetics vary from the formation of Li_2C_2 during dehydrogenation [34], through a synergy of catalytic and good thermal conductivity effects [114] to heterogeneous nucleation and micro-confinement effects [115-116]. However, as can be seen in Fig. 6.7f simultaneously the dispersed carbon leads to a quick saturation of desorption manifested by a flattening of a desorption curve. This peculiar behavior may indicate a reaction between carbon and other species which rapidly exhausts its catalytic effect. Further studies are needed to elucidate the cause of that peculiar desorption behavior in Fig. 6.7f.

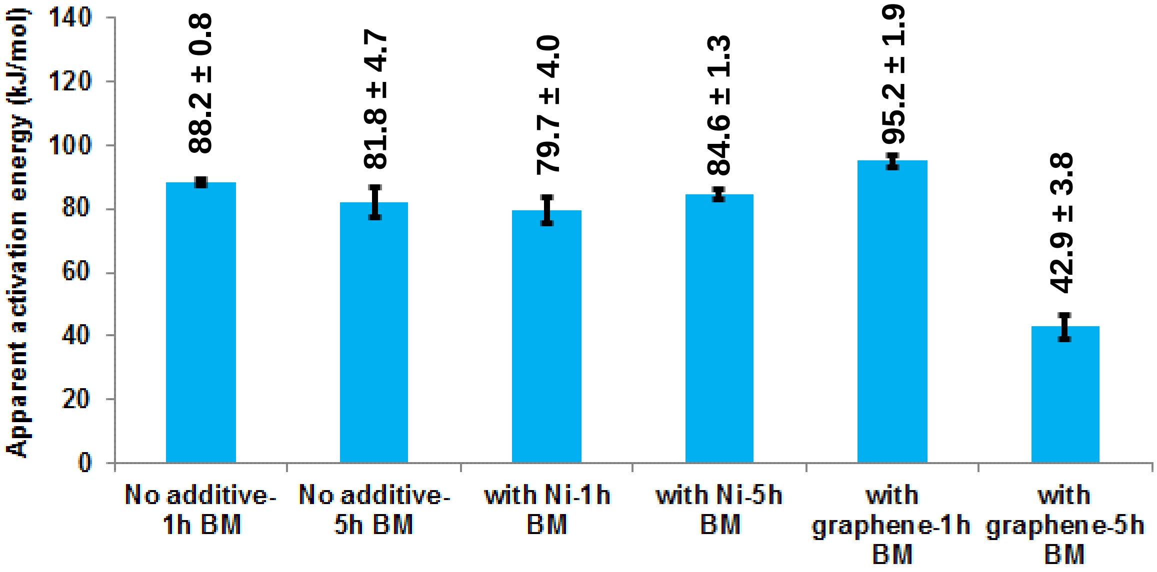

Figure 6-8. Apparent activation energy (kJ/mol) for dehydrogenation for the samples with and without additives after 1 and 5 h BM (adapted from [109]).

In order to gain the insight about the size of phases formed during dehydrogenation the crystallite size of LiF and the lattice strain after isothermal dehydrogenation at 60 °C for a specific time duration are listed in Table 7.2.

Table. 6-2. Summary of the LiF crystallite size, the lattice strain and the time of thermal dehydrogenation at 60 °C.

Sample	**Crystallite size (nm)**	**Lattice strain (%)**	**Time of desorption at 60°C (h)**
($3LiBH_4$+TiF_3)-1h BM	33.5	0.81	93.3
($3LiBH_4$+TiF_3)-5h BM	49.5	0.22	44.0
($3LiBH_4$+TiF_3)+5 wt.% Ni-1h BM	35.2	1.01	44.7
($3LiBH_4$+TiF_3+5 wt.% Ni-5h BM	36.5	1.09	49.5
($3LiBH_4$+TiF_3)+5 wt.% graphene- 1h BM	34.7	0.96	47.1
($3LiBH_4$+TiF_3)+5 wt.% graphene- 5h BM	25.2	1.35	39.4

Figure 6.9 shows dehydrogenation curves obtained at 100°C for the additive-free sample ball milled with an energy input, Q_{TR}=72.8 kJ/g (1h) and 364 kJ/g (5h) and subsequently stored for 7 and 3-month duration, respectively, at room temperature under a slight

overpressure of argon. Fig. 6.9a shows that the quantity of H_2 desorbed from the sample ball milled with an energy input, Q_{TR}=72.8 kJ/g (1h), is 5.2 wt.% H_2 within 24h, whereas at the same desorption time for the sample stored for 7 months it decreases to 2.8 wt.% H_2. Fig. 6.9b illustrates the reduction in the quantity of H_2 desorbed from the sample ball milled with an energy input 364 kJ/g (5h) from 5.00 wt.% to 1.72 wt.% in 42.5h during 3 months of storage.

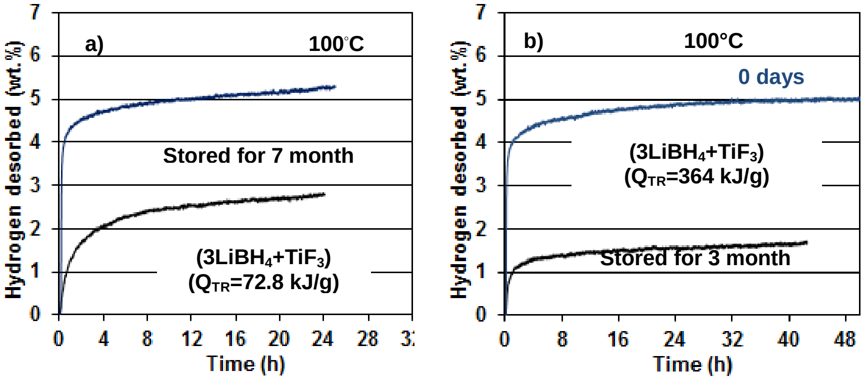

Figure 6-9. Dehydrogenation curves for $3LiBH_4+TiF_3$ at 100 °C for (a) BM for 1h and stored for 7 months and (b) BM for 5h and stored for 3 months (adapted from [109]).

6.4 discussion

As mentioned earlier, very little is found in the literature on the subject of the mechanical and thermal dehydrogenation behavior of the $LiBH_4$-TiF_3 system. Table 6.3 summarizes the milling conditions, dehydrogenation temperature and phase analysis after BM for the $LiBH_4$-TiF_3 system with varying molar ratios and with additives.

Table. 6-3. Comparison of milling conditions, heating range and phase analysis for mechanical and thermal dehydrogenation published in the literature and obtained in the present work.

Ref	System	BM	Phases after BM	Heating (°C)	Phases after heat treatment
[17]	$3LiBH_4+TiF_3$	(2h) Fritch7-Planetary 500 rpm	XRD: TiF_3	70-90	XRD: LiF XPS: $LiF+B+TiH_2$
[18]	$3LiBH_4+TiF_3$	(15 min) Planetary Qm-isp2	XRD: $TiF_3+ LiBH_4$	600	XRD: LiF XPS: $LiF+TiB_2+B$
[18]	$50LiBH_4+TiF_3$	(15 min) Planetary Qm-isp2	XRD: $TiF_3+ LiBH_4$	600	XRD: LiF+LiH
[19]	$LiBH_4$+20 wt.% Fe_2O_3+30 wt.%TiF_3	(5h) 350 rpm Qm-3sp2	XRD: TiF_3+ $LiBH_4+Fe_2O_3$	100	XRD: TiF_3+ $LiBH_4+Fe_2O_3$+LiF
[14]	$LiBH_4$ +TiF_3+20 wt.%SiO_2	(1h) 450 rpm Planetary Qm-isp	XRD: $LiF+TiB_2$	70	XRD: $LiF+TiB_2$
This work	$(3LiBH_4+TiF_3)$	(1h) 200 rpm magneto-mill	XRD: TiF_3+ $LiBH_4$+LiF+Ti	60	XRD: LiF+Ti MS: H_2 and B_2H_6
This work	$(3LiBH_4+TiF_3)$	(5h) 200 rpm magneto-mill	XRD: TiF_3+LiF+Ti	60	XRD: LiF+Ti MS: H_2

Recently, Fang et al. [55] claimed in situ formation and decomposition of amorphous $Ti(BH_4)_3$ obtained from MCAS (Table 6.3). The XRD pattern of the BM mixture exhibited only the Bragg peaks of TiF_3, which suggested that no mechano-chemical reaction occurred during milling. The authors reported no H_2 release during ball milling which is contradictory to the observations of H_2 release in this work (Fig. 6.3). Within the temperature range 70-90 °C, the authors observed about 5.0-5.6 wt.% H_2 release from the ball milled sample with an estimated apparent activation energy of ~19 kJ/mol which seems to be extremely low. DSC showed a strongly exothermic peak centered at around 90 °C, accompanied by 5.7 wt.% mass loss obtained from thermogravimetric analysis (TGA). No diborane (B_2H_6) gas was detected by gas mass spectrometry (MS) during dehydrogenation in DSC/TGA, in contrast to the report by Soloveichik [49] suggesting formation of B_2H_6. The XRD patterns after dehydrogenation exhibited only LiF diffraction peaks. The authors proposed that $Ti(BH_4)_3$ was formed at slightly elevated temperatures and decomposed according to the following reaction [55]:

$3LiBH_4+TiF_3\ (BM)\rightarrow(Thermal)\ Ti(BH_4)_3+3LiF\rightarrow3LiF+3B+5H_2+TiH_2$ (6.1)

The theoretical capacity of this reaction is 5.9 wt.% H_2, which agrees with the slightly lower observed H_2 release of ~5.0-5.6 wt.%. However, no TiH_2 diffraction peaks were detected in the XRD patterns after dehydrogenation, as required by reaction (6.1). Furthermore, one can calculate the standard enthalpy (heat) of reaction (6.1), $\Delta H^o_{(reaction)}$, given as the difference between the standard enthalpies (heats) of formation of the products and the reactants [103] in the following form:

$$\Delta H^o_{(reaction)} = \Sigma\Delta H_f^0{}_{(products)} - \Sigma\Delta H_f^0{}_{(reactants)} \qquad (6.2)$$

where ΔH_f^0 represents the standard molar enthalpy of a formation, at 25 °C, of the products and reactants in Eqs. (6.1). It should be pointed out that, by definition, the standard enthalpy of the formation of an element in its standard state is zero, $\Delta H_f^0=0$ [103]. Taking the standard molar enthalpies of the formation from Ref. [104]: ΔH_f^0 ($LiBH_4$)= -190.46 kJ/mol, ΔH_f^0 (TiF_3)= -1435.11 kJ/mol, ΔH_f^0 (LiF)= -616.93 and the most recent estimate for ΔH_f^0 (TiH_2)= -142.39 kJ/mol [104]. Substituting these values into Eq. (6.2), one obtains:

$\Delta H^o_{(reaction\ (6.1))}=$ [3×(-616.93)+(3×0)+(5×0)-142.39]-[3×(-190.46)+(-1435.11)]=+13.31 kJ/mol or +2.66 kJ/mol H_2. (6.3)

This estimate would suggest that the thermal dehydrogenation reaction (6.1) should have a weakly endothermic character, which is in a contradiction to the exothermic reaction character observed in DSC by Fang et al. [55]. However, Arita et al. [110] reported that ΔH_f^0 (TiH_2)= -179 kJ/mol, which would make the standard heat of the reaction (6.1) very weakly exothermic, with $\Delta H^o_{(reaction\ (6.1))}$= -23.3 kJ/mol or -4.7 kJ/molH_2. Therefore, such a large exothermic DSC peak in [55] still remains to be clearly explained.

More recently, Guo et al. [56] ball milled a ($3LiBH_4$-TiF_3) mixture in a planetary ball mill under argon for 15 min. The XRD patterns of the BM mixtures exhibited only the Bragg peaks of $LiBH_4$ and TiF_3, indicating that no reaction occurred during BM. Their finding is contradictory to the present results showing clearly the presence of the LiF and Ti diffraction peaks (Fig. 6.4). After dehydrogenation at 600°C, the XRD patterns exhibited only the LiF Bragg diffraction peaks, indicating that some chemical reaction occurred during thermolysis. The X-ray photo electron spectroscopy (XPS) analysis of the samples dehydrogenated at 350 and 600 °C showed some spectra peaks, interpreted by the authors as corresponding to TiB_2, TiO_2 and B_2O_2. The authors explained that the presence of oxides was a result of exposure to air when the samples were loaded into the XPS apparatus. The lack of the TiB_2 peaks on the XRD patterns was explained by the amorphous structure of TiB_2. On the basis of their results, the following thermal reaction path was proposed [56]:

$$3LiBH_4+TiF_3 \rightarrow 3LiF+TiB_2+B+6H_2 \qquad (6.4)$$

The theoretical H_2 capacity of reaction (6.4) is 7.12 wt.%. One can also estimate the standard enthalpy of reaction (6.4), $\Delta H^o_{(reaction\ (6.4))}$, taking standard molar enthalpies for $LiBH_4$, TiF_3 and LiF as those in Eq. (6.1) and that for TiB_2 as equal to -280.33 kJ/mol [104], which gives $\Delta H^o_{(reaction\ (6.4))}$= -124.6 kJ/mol or -20.77 kJ/mol H_2. A negative standard enthalpy (heat) of reaction (6.4) indicates an exothermic nature of the reaction, which was, indeed, observed by DSC in [56]. Finally, it must be pointed out that Guo et al. [56] did not investigate the isothermal dehydrogenation behavior of the BM mixtures as was done in [55]. Interestingly, reaction (6.4) is in agreement with a claim by Soloveichik [49], who suggested the formation of TiB_2 upon decomposition of $Ti(BH_4)_3$, but it does not release B_2H_6 which Soloveichik [49] also claimed to occur.

One of the interesting findings in our work is the observed release of H_2 during ball milling (Fig. 6.3). This clearly shows that mechano-chemical reaction must have occurred during ball milling. This is supported by the presence of LiF and Ti diffraction peaks after BM which strongly support the occurrence of mechano-chemical which, so far, never been reported in the literature.

Furthermore, this work clearly shows that the release of B_2H_6 during thermal dehydrogenation depends on the quantity of milling (mechanical) energy injected into the powder mixture. A thermal release of small quantities of B_2H_6 is observed for the sample milled with the energy input Q_{TR}=72.8 kJ/g (1h BM) although at a very small ratio of H_2/B_2H_6 = 6015 (Fig. 6.6a). In contrast, B_2H_6 is not observed for the 5h BM sample (Q_{TR}=364 kJ/g) (Fig. 6.6c). The FT-IR measurement shown in Fig. 6.5(a) for the 5h BM sample confirms the existence of $LiBH_4$ which was not identified by XRD, most likely, due to its amorphous structure after BM. As can be seen in Fig. 6.5(d), the FT-IR of pure $LiBH_4$ adapted from the data base of borohydrides presented on [93], strongly supports the existence of $LiBH_4$ after 5h BM. Two IR active modes of bending in the range of 1050-1350 cm^{-1} and stretching in the range of 2270-2370 cm^{-1} for $LiBH_4$ (tetrahedral bond) [93, 94, 96] are obvious in the FT-IR spectrum of the sample after 5h BM. However, the other peak within the range of 1600-1650 cm^{-1} may be related a trace of moisture present in the glove box during loading our sample into a FT-IR apparatus [39]. Interestingly, the intensity of characteristic peaks of $LiBH_4$ at 1050-1350 cm^{-1} and 2270-2370 cm^{-1} gradually decreased and their width increased with dehydrogenation of the milled powder. Isothermal dehydrogenation at 60°C for 2.2h caused a disappearance of one of the IR peaks in the bending mode (1245 cm^{-1}). The peaks at 1099 cm^{-1} became wider while those at 1314 cm^{-1} shifted to the lower wavelength. On the other hand, the dehydrogenation at 100°C for 18.3h (Fig. 5c) shows a complete disappearance in the first two peaks of B-H bending mode (1099 and 1045 cm^{-1}) and the width of shifted peak at 1314-1430 cm^{-1} increased. A comparison of FT-IR spectra of the ball milled sample (Fig. 6.5a) with the dehydrogenated ones (Fig. 6.5 c and d) indicates that the mechano-chemical reaction started during BM but the amount of energy was insufficient to complete the reaction. However, according to the above phase identification by XRD, the presence of LiF and Ti diffraction peaks which appeared after BM as well as after thermal dehydrogenation indicates that TiF_3 reacts with $LiBH_4$ and, most likely, forms $Ti(BH_4)_3$. These results are in accord with the FT-IR study done by Sun et al. [60], who investigated the formation of $Ti(BH_4)_3$ in the ($3LiBH_4+TiCl_3$) powder mixture during milling. They claimed that $Ti(BH_4)_3$ was very unstable at the ambient environment and decomposed rapidly to TiH_2, B and H_2. They only observed the signature bands of B-H using FT-IR while they could not detect $LiBH_4$ by XRD. Au et al. [50] reported that a possible reason of the $LiBH_4$ peaks disappearing during BM with halides could be due to either the reaction of $LiBH_4$ with a halide (in their case: $MgCl_2$ and $TiCl_3$) resulting in its decomposition even before heating or transformation of $LiBH_4$ to an amorphous state or both of the above. In all previous studies, it was proposed that an unstable metal borohydride $Ti(BH_4)_3$ decomposed at RT due to its unstable structure although no direct evidence in support of the existence of $Ti(BH_4)_3$ after MCAS of $LiBH_4$ and $TiCl_3$ [51, 60, 65] has ever been provided.

It is clearly seen in Fig. 6.6 that in the sample ball milled for 1h the release of B_2H_6 starts around 100-110 °C which implicates that B_2H_6 is unlikely to be released at temperatures <100 °C which strongly suggests that gas desorbed during BM was pure H_2. Therefore, assuming that, indeed, unstable $Ti(BH_4)_3$ is being formed, the first possible reaction formation/decomposition during ball milling could be as follows where $Ti(BH_4)_3$ forms and simultaneously rapidly decomposes:

$$3LiBH_4+TiF_3\xrightarrow{(BM)}Ti(BH_4)_3+3LiF\rightarrow 3LiF+6H_2+3B+Ti \qquad (6.5)$$

The theoretical capacity of this reaction is 7.1 wt.% H_2 which is much larger than even the observed 2.38 wt.% H_2, released as a result of mechanical dehydrogenation for 5h in the presence of graphene which apparently moderately accelerates mechanical dehydrogenation rate as discussed earlier. The milling energy input of 364 kJ/g is apparently still insufficient to mechanically dehydrogenate even barely 50% of the theoretical capacity of reaction (6.5). In contrast to a few other complex hydride systems such as $LiAlH_4/MnCl_2$ and $LiAlH_4/LiNH_2$ [15, 58] and $LiBH_4/FeCl_2$ [96], capable of mechanical dehydrogenation of 4-5 wt.% H_2, the present system $LiBH_4/TiF_3$ seems to be moderately resistant to mechanical dehydrogenation (Table 6.1) even with envisaged catalytic additives like Ni and graphene. However, to put it into perspective the present hydride system is more prone to mechanical dehydrogenation than the $LiBH_4/MnCl_2$ system which mechanically dehydrogenated barely 0.7 wt.% H_2 after 5h BM [81].

As shown in Fig. 6.6, the release of diborane gas, B_2H_6, is observed for the 1h BM sample but not observed for the 5h BM sample. Therefore, three alternative, general reactions could be proposed for the thermal decomposition of ($3LiBH_4+TiF_3$) system:

$3LiBH_4+TiF_3\xrightarrow{(BM)}Ti(BH_4)_3+3LiF\rightarrow Thermal\rightarrow 3LiF+xH_2+yB_2H_6+(3-2y)B+[Ti]$

(6.6)

$3LiBH_4+TiF_3\xrightarrow{(BM)}Ti(BH_4)_3+3LiF\rightarrow Thermal\rightarrow 3LiF+xH_2+yB_2H_6+zTiH_2+(3-2y)B+(1-z)[Ti]$ (6.7)

$3LiBH_4+TiF_3\xrightarrow{(BM)}Ti(BH_4)_3+3LiF\rightarrow Thermal\rightarrow 3LiF+xH_2+yB_2H_6+(1.5-y)TiB_2+(y-0.5)[Ti]$

(6.8)

where [Ti] designates Ti obtained from the first decomposition during BM. The quantity of (y) could vary from 0, which in effect reduces it to Eq. (6.5), if the release of B_2H_6 does not occur, to 1 which would greatly increase the ratio of diborane and reduces the quantity of H_2 (x=3) in released gas. The standard enthalpy for y=0 or 1 in reaction (6.6), $\Delta H^o_{(reaction\ (6.6))}$, can be estimated taking standard molar enthalpies for $LiBH_4$, TiF_3 and LiF as those in Eq. (6.1) and that for B_2H_6 as equal to +35.56 kJ/mol [104] which gives $\Delta H^o_{(reaction\ (6.6))}$ = +155.7 to +191.26 kJ/mol for 0 B_2H_6 and 1 B_2H_6, respectively. Thus, the thermal dehydrogenation of reaction (6.6) should have an endothermic character, which is in contradiction with the exothermic DSC curves shown in Fig. 6.6b and Fig. 6.6d.

Reaction (6.7) contains TiH_2 after decomposition. It was reported in [111] that TiH_2 if present in such reaction would have to decompose with two endothermic peaks at around 451 and 472 °C. However, no endothermic peaks are observed in our DSC curves (Fig. 6.6b and Fig. 6.6d). Standard enthalpy of reaction (6.7), $\Delta H^o_{(reaction\ (6.7))}$, can be estimated as above taking standard molar enthalpies for $LiBH_4$, TiF_3, LiF and TiH_2 as those in Eq. (6.1) and that for B_2H_6 in Eq. (6.5) which gives $\Delta H^o_{(reaction\ (6.7))}$= +11.35 and +46.91 kJ/mol for 0 and $1B_2H_6$, respectively.

The standard enthalpy of reaction (6.8), $\Delta H^o_{(reaction\ (6.8))}$, varies from -124.63 to +51.10 kJ/mol for 0 and 1 B_2H_6, respectively. In other words, reaction (6.8) has an exothermic character whenever number of B_2H_6 moles (y) is not larger than 0.83, which agrees with the exothermic character of the DSC curves in Fig. 6.6. However, the problem is that Eq. (6.8) requires the formation of TiB_2 which is not observed on the pertinent XRD patterns after dehydrogenation of samples without additives (Fig. 6.4 a-b) as well those with catalytic additives (Fig.6.4 c-f). If one assumes that TiB_2 is amorphous, as was also suggested by Guo et al. [56], and Ti in reaction (6.8) is nanocrystalline then this reaction agrees reasonably with the experimental results obtained in this work.

Finally, it is to be pointed out that it is observed in Fig. 6.9 that the sample ball milled with an energy input Q_{TR}=72.8 kJ/g (1h BM) desorbed after 7 months of storage about 2.4 wt.% H_2 while the sample milled with an energy input Q_{TR}=364 kJ/g (5h BM) desorbed after 3 months of storage about 3.28 wt.% H_2. In comparison with a number of ball milled nanocomposites, particularly those based on $LiAlH_4$, containing catalytic additives [15], the present system exhibits a slightly lower dehydrogenation rate during a long-term storage at room temperature. In contrast, nanocrystalline $Mn(BH_4)_2$ released only a small amount of about 0.5 wt.% H_2 within 80 days and subsequently stabilized up to 120 days of further storage [81]. As reviewed in [15, 58] there are a number of possible practical engineering applications for a long-duration hydrogen discharge for generating quantities of hydrogen on demand for auxiliary power generation systems coupled with PEM fuel cells and batteries such as low power remote fuel cells, portable gas analyzers and smartphones [15, 58, 112]. These materials can also be used in a number of chemical processes where a continuously reducing atmosphere is needed for a completion of the process [15, 58]. They could also have an application in a military sector for cartridges supplying hydrogen to micro fuel cells in portable devices needed for soldiers on a mission in remote areas [113].

6.5. Summary of findings

1. During ball milling (BM) of the ($3LiBH_4$+TiF_3) system a mechano-chemical reaction starts occurring between $LiBH_4$ and TiF_3 after injecting the energy input Q_{TR}=72.8 kJ/g (1 h BM) which accelerates with increasing milling time to 5h, Q_{TR}=364 kJ/g.

2. X-ray diffraction (XRD) shows the new phases LiF and Ti present in the microstructure together with retained TiF_3 and $LiBH_4$.

3. A mechanical dehydrogenation phenomenon occurs during mechano-chemical reaction resulting in a release of hydrogen.

3. The ultrafine Ni additive does not measurably accelerate the rate of mechanical dehydrogenation up to 5h BM (Q_{TR}=364 kJ/g).

4. Graphene does not accelerate the rate of mechanical up to 1h BM (Q_{TR}=72.8 kJ/g) but then it dramatically increases up to 5 h BM with the quantity of 2.38 wt.% H_2 finally desorbed.

5. The ball milled samples are capable of H_2 at a very low temperature of 60°C resulting in desorption of 4.52 wt.% H_2 within 93 h. The average apparent activation energy for thermal dehydrogenation equals 88.2±0.2 and 81.8±4.7 kJ/mol for samples ball milled with energy input Q_{TR}=72.8 kJ/g (1 h BM) and Q_{TR}=364 kJ/g (5 h BM), respectively.

6. The addition of 5 wt.% ultrafine Ni mildly reduces the average activation energy to 79.7±4.0 kJ/mol for sample milled with a Q_{TR}=72.8 kJ/g (1h BM) but then slightly increases to 84.6±1.3 kJ/mol after the energy input Q_{TR}=364 kJ/g (5 h BM). The highest average apparent activation energy of 95.2±1.9 kJ/mol is exhibited by a sample with 5 wt.% graphene milled with Q_{TR}=72.8 kJ/g (1h BM).

7. During thermal dehydrogenation the intensity of diffraction peaks of retained TiF_3 and $LiBH_4$ disappears while the intensity of LiF and Ti peaks dramatically increases which confirms the occurrence of a continuous thermally activated reaction between $LiBH_4$ and TiF_3 initiated during ball milling.

8. Mass spectrometry shows that the principal gas released during thermal desorption is hydrogen although the sample milled with energy input Q_{TR}=72.8 kJ/g (1 h BM) shows a miniscule quantity of diborane gas, B_2H_6, which starts around 110°C, with a maximum intensity at around 125-135°C. In contrast, the sample milled with energy input Q_{TR}=364 kJ/g (5 h BM) does not show, within a resolution range of the MS instrument, any release of B_2H_6.

9. DSC measurements show exothermic peaks for both samples regardless of milling energy input.

10. The ball milled ($3LiBH_4+TiF_3$) system is able to slowly discharge up to about 3 wt.% H_2 during a few months storage at room temperature.

7. ($LiBH_4$-$TiCl_2$) and ($LiBH_4$-$TiCl_3$) systems

7.1. Phase transformation during MCAS and thermal dehydrogenation of ($2LiBH_4$+$TiCl_2$)

One can assume the reaction of 2 moles $LiBH_4$ with one mole $TiCl_2$ according to the reaction (1.5), and propose the following reaction, similar to the one proposed for $3LiBH_4/TiCl_3$ (reaction 1.11):

$2LiBH_4+TiCl_2 \rightarrow Ti(BH_4)_2+2LiCl$ (7.1)

Regardless of the formation of $Ti(BH_4)_2$, the theoretical H_2 capacity of reaction 7.1, assuming that all 8 hydrogen atoms are released during decomposition, is 4.97 wt.% H_2 according to the following calculation:

$$\frac{8\times mollar\ mass\ of\ H\ atom}{(2\times mollar\ mass\ of\ \mathrm{LiBH_4})+(mollar\ mass\ of\ \mathrm{TiCl_2})}\times 100=\frac{(8\times 1.008)}{(2\times 21.78)+(118.77)}\times 100 = 4.97$$

wt.% H_2 (7.2)

Turning now to the results of the present work, as mentioned earlier in the section (1.8.4), the release of H_2 during the milling of (LiBH4-$TiCl_2$/$TiCl_3$) has not been reported yet. As shown in section 4, MCAS mixture of ($2LiBH_4$+$MnCl_2$) shows nearly no H_2 release during BM [81]. The mixture of ($3LiBH_4$+TiF_3) released 1.4wt.% H_2 up to 1h BM [109]. However, significant mechanical dehydrogenation was observed from the ($2LiBH_4$+$FeCl_2$) system in section 5, which was able to release 4 wt.% H_2 after 20 minutes BM [96]. Assuming all the gas released is H_2, Fig. 7.1 shows an overview of H_2 generation during BM, subsequent storage at room temperature (RT) and finally isotheral dehydrogenation at high temperatures (100 and 200 ºC). As can be seen in Fig. 7.1a, a sharp increasing trend in mechanical dehydrogenation from the mixture of ($2LiBH_4$+$TiCl_2$) up to 60 minutes BM is observed in which 2.39 and 4.17 wt.% H_2 is released up to 20 and 60 minutes BM, respectively. I tried to stop the milling and open the milling vial after 30 min BM in order to characterize the microstructure of the milled powder. However, the milled powder was severely volatile and unstable. Therefore, the powders were kept inside the milling vial at RT (Fig. 7.1c). What is interesting in this experiment is that the H_2 still continued to be released even after the BM was stopped after 30 min BM, and it reached 3.52 wt.% H_2 after 11 days storage. Comparing the mechanical dehydrogenation behavior of different halides ($MnCl_2$, $FeCl_2$, TiF_3) and $TiCl_2$

in the present work mixed with $LiBH_4$ indicates that $FeCl_2$ and $TiCl_2$ have the most impact on dehydrogenation of $LiBH_4$ during BM rather than the others. Fig. 7.1b illustrates the isothermal dehydrogenation curves of the powder mixture after 1h BM at different temperatures. The maximum quantity of H_2 released from the sample after isothermal dehydrogenation was 0.57 wt.% at 200 ºC. Thus, the total quantity of H_2 released after 1h BM and dehydrogenation at 200 ºC was 4.74 ºC. Isothermal dehydrogenation curves for the milled powder after 30 minutes BM and stored for 11 days at RT followed by dehydrogenation at 100 and 200 ºC are also shown in the final part of Fig 7.1c. The total quantity of H_2 released after 30 minutes BM, 11 days storage and isothermal dehydrogenation at 100 ºC, as illustrated in Fig. 7.1c, was 3.94 wt.% H_2 which increased to 4.23 wt.%H_2 at 200 ºC.

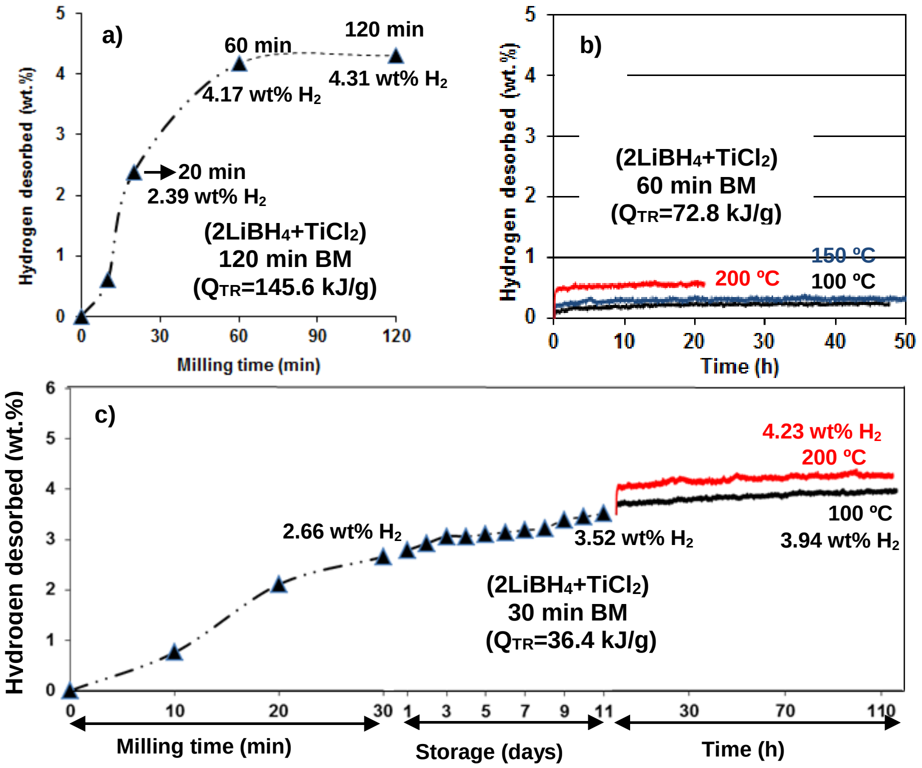

Figure 7-1. $(2LiBH_4+TiCl_2)$ ball milled (a) with an energy input, Q_{TR}=145.6 kJ/g (120 min BM), (b) with an energy input, Q_{TR}=72.8 kJ/g (60 min BM) and subsequent isothermal dehydrogenation at 100, 150 and 200 ºC under 1 bar H_2, and (c) with an energy input, Q_{TR}=36.4 kJ/g (30 min BM), held at RT for 11 days and dehydrogenated at 100 and 200 ºC under 1 bar H_2.

The SEM micrograph of the powder particles of the sample after 30 minutes BM and stored for 11 days is shown in Fig. 7.2a. Fig. 7.2b illustrates high magnification of a SEM micrograph of the agglomerated powder indicated by the red line in Fig. 7.2a. Severe agglomeration can be seen from the morphology of the milled powder in comparison with powder particles of the as-received $LiBH_4$ shown in section 4. However, I was not able to observe the morphology of the as-received $TiCl_2$ and $TiCl_3$ due to safety concerns. Both of the powders were volatile and unstable at all and started to evaporate as soon as the lid of their container was opened.

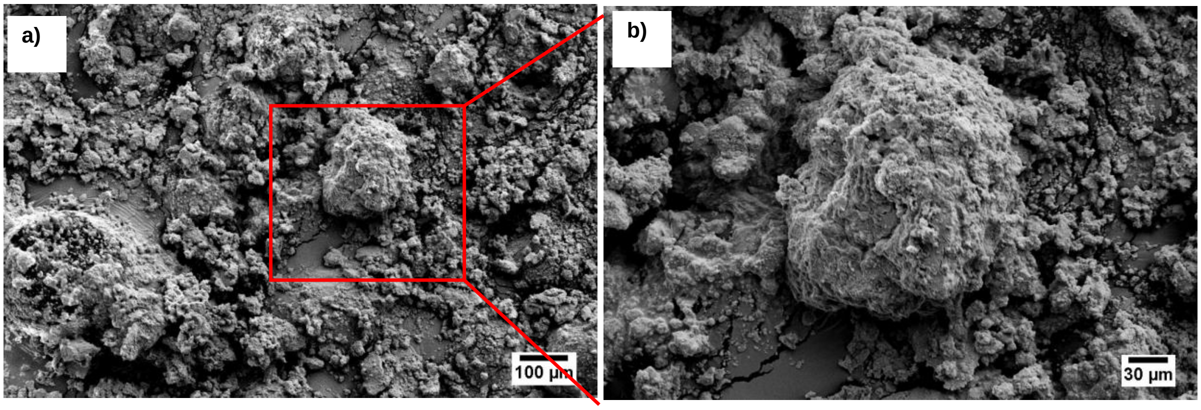

Figure 7-2. (a and b) Scanning electron micrographs of ball milled ($2LiBH_4$+$TiCl_2$) powders mixture after MCAS with an energy input, Q_{TR}=36.4 kJ/g (0.5h BM) and held at RT for 11 days.

The XRD patterns of the MCAS powders of ($2LiBH_4$+$TiCl_2$) after different milling times and different isothermal dehydrogenation temperatures are illustrated in Figure 7.3. Fig.7.3a shows the XRD of the MCAS powder with an energy input, Q_{TR}=72.8kJ/g (1h). The XRD pattern of the MCAS powder with an energy input of Q_{TR}=36.4 kJ/g (0.5h), and stored under a hydrogen atmosphere at RT in a milling vial for 11 days, is illustrated in Fig 7.3b and can be compared to those after thermal treatment shown in Fig. 7.3 (c and d). Neither of the as-received materials diffraction peaks was observed on the XRD patterns shown in Fig. 7.3. The LiCl diffraction peak is the only XRD phase pattern observed in the samples after BM and isothermal dehydrogenation, indicating that, according to reaction (7.1), a mechanochemical reaction may have started during milling. However, there are no XRD peaks corresponding $Ti(BH_4)_2$ (a proposed phase from reaction 7.1). The phase transformation will be discussed in more detail later (section 7.3) accompanied with the FT-IR results.

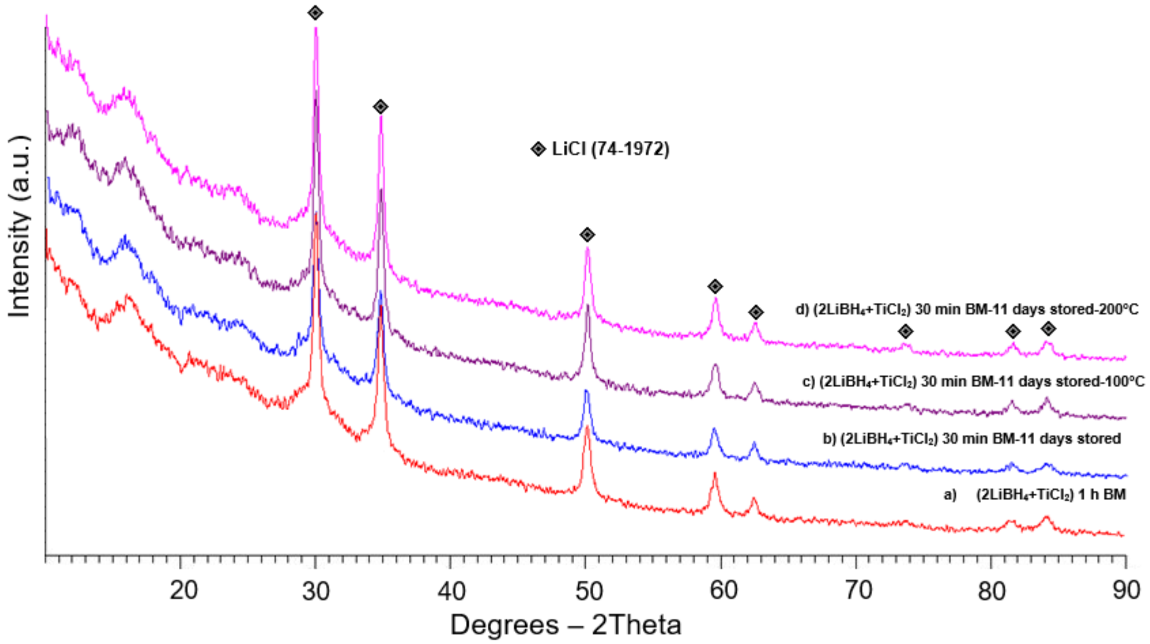

Figure 7-3. XRD patterns of the ($2LiBH_4+TiCl_2$) powder mixture (a) with an energy input, Q_{TR}=72.8 kJ/g (1h BM), (b) with an energy input, Q_{TR}=36.4 kJ/g (0.5h BM) and held at RT for 11 days (c) after isothermal dehydrogenation of the sample (b) at 100 ºC and (d) isothermal dehydrogenation of the sample (b) at 200 ºC.

7.2. Phase transformation during MCAS and thermal dehydrogenation of ($3LiBH_4+TiCl_3$)

Similar to calculation (7.2) for the reaction of $3LiBH_4$ and $TiCl_2$, one can calculate the theoretical H_2 capacity of reaction (1.11). Assuming that all 12 hydrogen atoms are released during decomposition, the theoretical H_2 capacity would be 5.51 wt.% H_2. Turning now to the experimental results, Fig. 7.4(a) illustrates the mechanical dehydrogenation of the ($3LiBH_4+TiCl_3$) powder mixture during 60 minutes BM. Unlike the $TiCl_2$, the mixture of $TiCl_3$ with 3 moles $LiBH_4$ shows slower mechanical dehydrogenation; 1.34 wt.% H_2 was desorbed during 60 min BM. I was not able to use the 60 min milled powder for isothermal dehydrogenation immediately after milling due to the unstable and volatile nature of the milled powder, so the 1h milled powder was kept inside of the milling vial for 4 days (dehydrogenation during storage was not monitored), and then the vial was opened. After being stored for 4 days, the powder was stable, indicating that during that 4 days' delay in opening of the vial dehydrogenation may have occurred. Isothermal dehydrogenation at 100 and 200 ºC was also done and is illustrated in Fig. 7.4b. The quantities of 0.83 and 1.24 wt.% H_2 were desorbed during isothermal dehydrogenation at 100 and 200 ºC, respectively. In order to monitor and measure the dehydrogenation of the milled powder during storage, BM was stopped after 30 min and the powder stored for 14 days, as illustrated in Fig. 7.4c. The milled powder with an energy input of Q_{TR}=36.4 kJ/g (30 min BM) tended to desorb H_2 very quickly up to the 7-day mark, at which point it reached 4.17 wt.% H_2. Hydrogen desorption then reached saturation point, at 4.45 wt.% H_2, and occurred no more in the remainder of the storage period. The isothermal dehydrogenation of the milled and stored samples at 100 and 200 ºC is shown in the last part of the Fig. 7.4c. The maximum quantity of H_2 for the powder mixture with an energy input of Q_{TR}=36.4 kJ/g (30 min) released during BM, storage and isothermal dehydrogenation is 5.43 wt.% H_2.

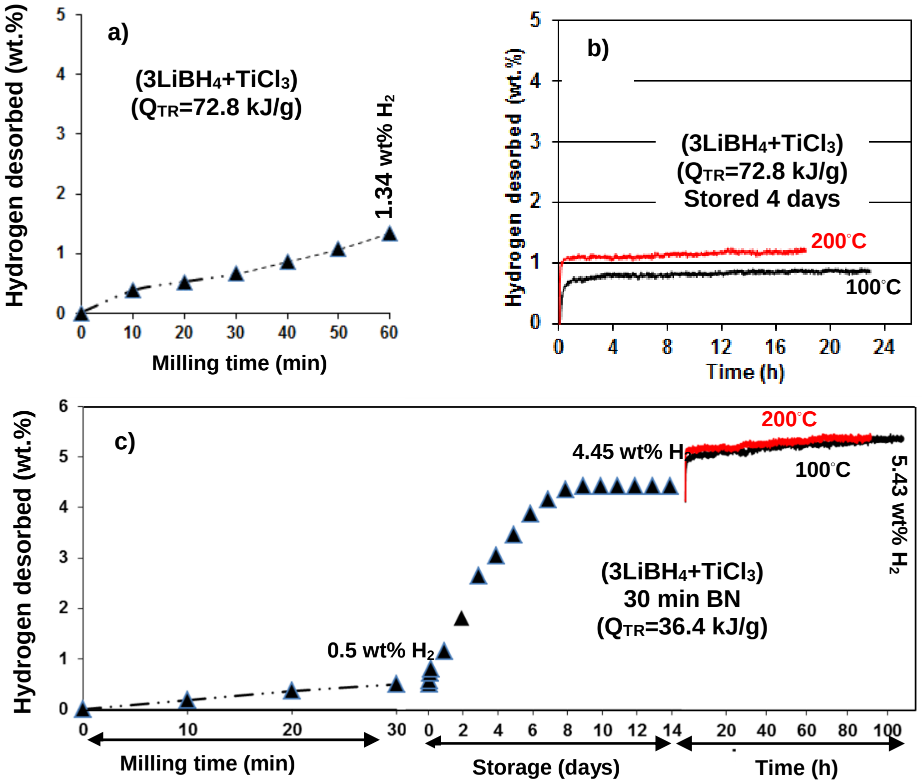

Figure 7-4. ($3LiBH_4$+$TiCl_3$) ball milled (a) with an energy input, Q_{TR}=72.8 kJ/g (60 min BM), (b) with an energy input, Q_{TR}=72.8 kJ/g (60 min BM), stored at RT for 4 days and subsequent isothermal dehydrogenation at 100 and 200 ºC under 1 bar H_2, and (c) with an energy input, Q_{TR}=36.4 kJ/g (30 min BM), held at RT for 14 days and dehydrogenated at 100 and 200 ºC under 1 bar H_2.

The SEM micrograph of the powder mixture after 30 min BM and stored for 14 days has almost the same agglomerated morphology (irregular aggregate powders) as the $2LiBH_4$+$TiCl_2$ powder mixture after BM and storage (Fig. 7.5).

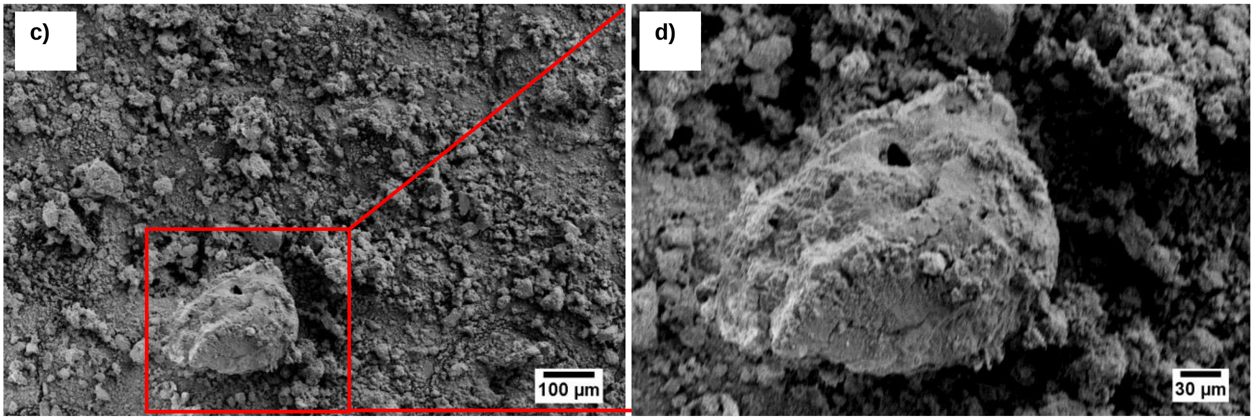

Figure 7-5. (a and b) Scanning electron micrographs of ball milled ($3LiBH_4+TiCl_3$) powders mixture after MCAS with an energy input, Q_{TR}=36.4 kJ/g (0.5h BM) and held at RT for 14 days.

Fig. 7.6a shows the XRD pattern of $3LiBH_4+TiCl_3$ with an energy input of Q_{TR}=72.8 kJ/g (60 min). The XRD pattern of the sample with an energy input of Q_{TR}=36.4 kJ/g (30 min BM) that has been stored for 14 days at RT is illustrated in Fig. 7.6b. Fig. 7.6c and d shows the XRD pattern of the isothermal dehydrogenation of the samples BMed and stored at 100 and 200 ºC, respectively. LiCl is the only phase detected in all the XRD patterns of the samples that have undergone different mechanical and thermal treatments.

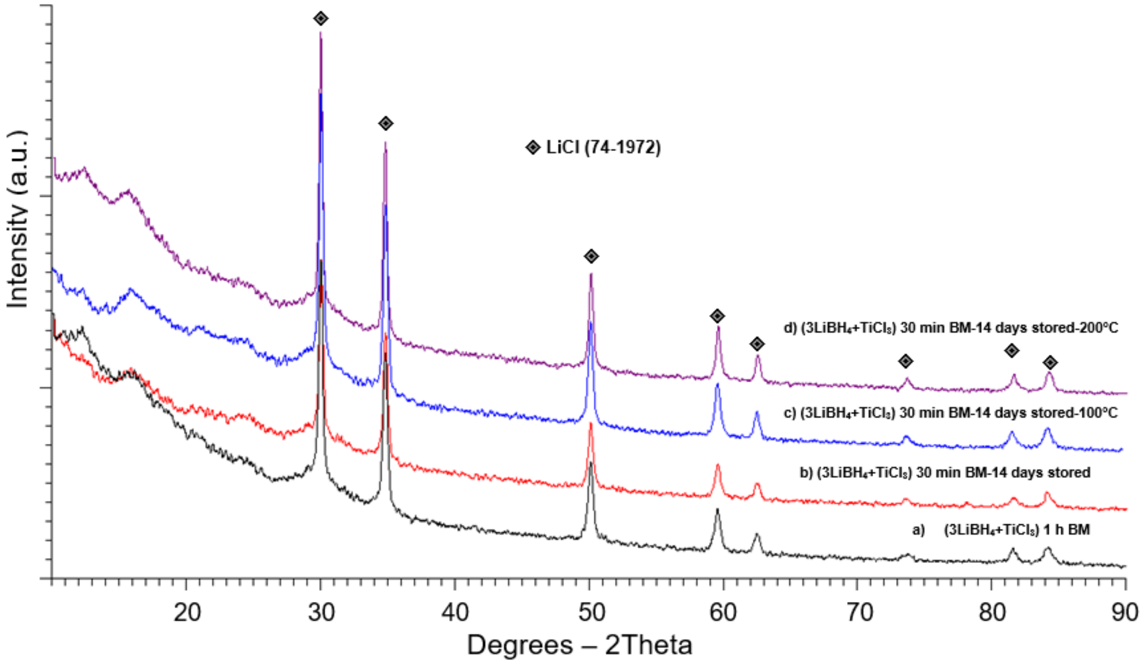

Figure 7-6. XRD patterns of the $3LiBH_4+TiCl_3$ powder mixture (a) with an energy input, Q_{TR}=72.8 kJ/g (1h BM), (b) with an energy input, Q_{TR}=36.4 kJ/g (0.5h BM) and held at RT for 14 days (c) after isothermal dehydrogenation of the sample (b) at 100 ºC and (d) isothermal dehydrogenation of the sample (b) at 200 ºC.

According to reaction (1.11), LiCl was the expected product phase with $Ti(BH_4)_3$ from the reaction of 3 moles $LiBH_4$ with one mole $TiCl_3$. Previous research on the system of $LiBH_4/TiCl_3$, in which Jin et al. [59] carried out XRD analysis, showed the LiCl and $LiBH_4$ peaks after BM while $LiBH_4$ was not observed after thermal dehydrogenation. Vajo et al. [62], however, observed LiCl, LiH and $LiBH_4$ phases after milling of a $LiBH_4$ + ½ MgH_2+$0.02TiCl_3$ powder mixture, during which $LiBH_4$ and MgH_2 disappeared through thermal dehydrogenation at 450 ºC. In the experiments on $LiBH_4/CaH_2$ mixture BM with 4, 10 and 25 mol% of $TiCl_3$, Yang et al. [114] did not show the XRD analysis of the milled sample. However, their calculations, based on HSC chemistry, showed that a reaction of $TiCl_3$ with $LiBH_4/CaH_2$, form LiCl, TiB_2 and $CaCl_2$, released the hydrogen at the same time [114]. Au et al. [101] reported that LiCl and $TiCl_3$ were the phases characterized by XRD after milling and after dehydrogenation of a $LiBH_4$+$0.2MgCl_2$+$0.1TiCl_3$ powder mixture. They claimed that the disappearing of $LiBH_4$ during milling could be due to its interaction with $MgCl_2$ and $TiCl_3$, and as a result, its decomposition even before heating, or due to the transformation of $LiBH_4$ to an amorphous state, or both of the above. Au et al. [51] reported that $TiCl_3$ disappeared while LiCl was formed from the XRD spectrum after the milling of $LiBH_4$+0.1$TiCl_3$. XRD of the dehydrided sample, however, detected LiH and LiCl. A similar scenario was reported for the ($LiBH_4$+Mg_3La+$TiCl_3$) (molar ratio= 30:3:2) system investigated by Sun et al. [60]. They stated that $Ti(BH_4)_3$, formed through the reaction of $LiBH_4$ and $TiCl_3$, is very unstable under an ambient environment and that it decomposed into TiH_2, B and H_2. However, they confirmed diffraction peaks of TiH_2 from the selected area electron diffraction pattern after 1h milling which were not identified by XRD. They suggested that the lack of TiH_2 diffraction peaks in the XRD may be due to the relatively small amount in the sample. However, in all the previous studies, it has been proposed that $TiCl_3$ reacts with $LiBH_4$ and forms unstable metal borohydride $Ti(BH_4)_3$, which decomposes at RT due to its unstable structure. No one have been able to provide evidence in support of the $Ti(BH_4)_3$ existence after MCAS [51, 60, 65]. Formation of $Ti(BH_4)_3$ through the milling of (3$LiBH_4$+TiF_3) have also claimed by Fang et al. [55]. Hoekstra and Katz were the first scientists to report the formation of $Ti(BH_4)_3$ through the interaction of (8$LiBH_4$+2$TiCl_4$) at a low temperature of -45°C under vacuum [47]. They claimed that $Ti(BH_4)_3$ decomposes very quickly at RT.

7.3. FT-IR analysis of (2$LiBH_4$+$TiCl_2$) and (3$LiBH_4$+$TiCl_3$)

Fig. 7.7a shows the FT-IR spectrum of an MCAS powder mixture of (2$LiBH_4$+$TiCl_2$) with an energy input of Q_{TR}=36.4 kJ/g (0.5h), and stored under a hydrogen atmosphere at RT in a milling vial for 11 days. The spectrum of this sample is illustrated in Fig. 7.7d separately to provide a clear view of the peak positions of the spectrum. The total quantity of H_2 released from this sample is 3.52 wt.% H_2, meaning that according to calculation (7.2), 1.45 wt.% of the capacity of H_2 has still not been released from the powder mixture. The FT-IR spectrum of (3$LiBH_4$+$TiCl_3$) with an energy input of Q_{TR}=36.4 kJ/g (0.5h), and stored under a hydrogen atmosphere at RT in a milling vial for 14 days is also illustrated in Fig. 7.7b and separately in Fig. 7.7e. The FT-IR spectrum shown in Fig. 7.7b is for the sample which desorbed 4.45 wt.% H_2, and 1.06 of H_2 has still not been released from the H_2 capacity of the powder mixture.

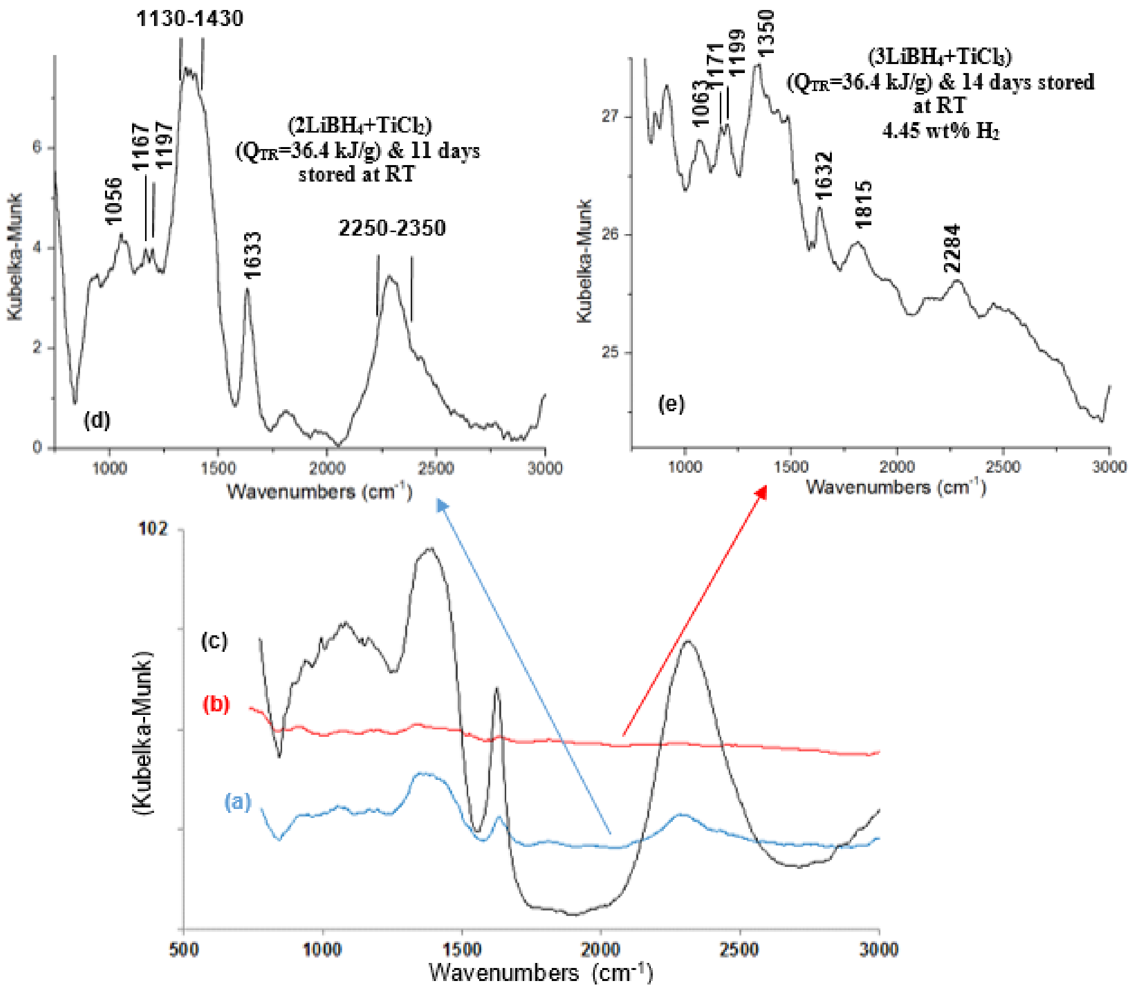

Figure 7-7. FT-IR spectrum (a and d) ($2LiBH_4$+$TiCl_2$) with an energy input of QTR=36.4 kJ/g (0.5h), and stored under a hydrogen atmosphere at RT in a milling vial for 11 days (b and e) ($3LiBH_4$+$TiCl_3$) with an energy input of QTR=36.4 kJ/g (0.5h), and stored under a hydrogen atmosphere at RT in a milling vial for 14 days (c) ($3LiBH_4$+TiF_3) 100°C for 18.3h (desorbed 4.8 wt.% H_2).

In both spectra, the B-H bending and stretching bonds of $LiBH_4$ can be seen very well. As already shown for ($3LiBH_4$+TiF_3) in section 7, the sample after 18h isothermal dehydrogenation which desorbed 2.58 wt,% H_2 of its theoretical hydrogen capacity (illustrated here again in Fig. 7.7c), had peak widening compared to the as-received $LiBH_4$, due to hydrogen release. The same scenario occured in the $LiBH_4$/$TiCl_3$ and $LiBH_4$/$TiCl_2$ systems, as can be seen in their FT-IR spectrums of Fig. 7.7. d and e, respectively. Sun et al. [60] observed similar behavior in the FT-IR spectrum of a ($3LiBH_4$+$TiCl_3$) system after BM. They mentioned that since $LiBH_4$ easily becomes amorphous during milling, it is difficult to identify the existence of $LiBH_4$ by XRD. In all previous research, the authors have claimed that the additives ($TiCl_3$, TiF_3, ZnF_2 and AlF_3) reacted with $LiBH_4$ and formed unstable metal borohydrides $Ti(BH_4)_3$, $Zn(BH_4)_2$ and $Al(BH_4)_3$ that decomposed at RT and released H_2 and B_2H_6. As a result, we can conclude that $LiBH_4$ and titanium chlorides reacted in some stepwise reactions in which $LiBH_4$ first reacted with $TiCl_2$ and $TiCl_3$ as

$$nLiBH_4 + TiCl_n \rightarrow nLiCl + Ti(BH_4)_n \qquad (7.3)$$

Then the unstable titanium borohydride decomposed immediately afterwards, at RT,

$$nLiCl + Ti(BH_4)_n \rightarrow nLiCl + TiH_2 + 2.5B{+}+(2n-1)H_2 \qquad (7.4)$$

However, we did not observe TiH_2 and B in the XRD pattern of the sample after isothermal dehydrogenation of the milled powder mixture, an observation in line with those of previous researchers. [51, 55, 59, 60, 65, 68, 101, 114]. In one case, researchers merely predicted its presence based on the HSC chemistry [67] and in other case, the selected area diffraction pattern (SADP) allowed the detection of TiH_2 and B [60]. In addition, one should expect the desorption of B_2H_6 (even a small quantity) in the products of desorption, as we have already shown for the previous systems ($LiBH_4/MnCl_2$, $LiBH_4/TiF_3$). In the case of titanium chlorides, however, as already explained, further MS analysis could not be carried out due to the unstability of the milled powder mixture. So the explanation of the decomposition behavior of the ($3LiBH_4+TiCl_3$) and ($2LiBH_4+TiCl_2$) is still unclear and needs further research.

Finally, the crystallite size and the lattice strain of the LiCl in the product of the BM sample in the both powder mixture ($LiBH_4/TiCl_2$) and ($LiBH_4/TiCl_3$) after 1h BM were calculated by the Williamson-Hall method. Based on the diffraction peaks of LiCl in XRD pattern of ($2LiBH_4+TiCl_2$) after 1h BM shown in Fig. 8.3a, the lattice strain and the LiCl crystallite size, were 0.97% and 57.8 nm, respectively. However, for the LiCl after the MCAS of ($3LiBH_4+TiCl_3$) (Fig. 7.6a), the lattice strain and LiCl crystallite size were 1.3% and 16.9 nm, respectively.

7.4. Summary of findings

1. A mechanical dehydrogenation phenomenon occurs during mechano-chemical reaction resulting in a release of hydrogen from both powder mixtures ($2LiBH_4$+$TiCl_2$) and ($3LiBH_4$+$TiCl_3$).

2. The 30 min ball milled ($2LiBH_4$+$TiCl_2$) powder mixture continued to release H_2 during storage for 11 days.

3. The ($3LiBH_4$+$TiCl_3$) mixture milled for 30 min desorbed H_2 very quickly for 7 days, at which point the H_2 quantity reached 4.17 wt. %.

5. Only LiCl XRD diffraction peaks were detected after milling as well as after isothermal dehydrogenation of both powder mixtures.

6. Based on the XRD and FT-IR results, it is likely that BM of ($LiBH_4$/$TiCl_2$) and ($LiBH_4$/$TiCl_3$) led to some stepwise reaction between $LiBH_4$ and titanium chlorides with the possibility of forming an intermediate unstable titanium borohydride which rapidly decomposed.

7. After 1h BM of ($3LiBH_4$+$TiCl_3$) and ($2LiBH_4$+$TiCl_2$) powder mixtures, the LiCl crystallite size, measured from XRD peak broadening was 57.8 and 16.9 nm, respectively.

8. Summary and recommendations

This work has explored the synthesis, characterization and fundamental nature of the desorption behavior of selected complex borohydrides and their composite systems.

Unfortunately, none of the investigated composite borohydrides can be considered a potential breakthrough candidate as a storage medium for the automotive industry since their practical gravimetric capacities are lower than the DOE targets (~10 wt.% H_2 for storage materials). However, apart from reversible storage there is number of other potential market for application of the H_2 generation systems, in the commercial, non-automotive sectors of the economy. These application involve ambient and slightly elevated temperatures. The catalyzed $LiBH_4$ with metal chlorides ($FeCl_2$, TiC_2, $TiCl_3$) may be close to the point of commercialization in disposable H_2 cartridge of various sizes that can be regenerated “off board” after usage. Most interestingly, their ability to generate hydrogen during storage at low temperatures after short milling times (less than 10 min depending on the system) make them attractive candidates for suppling fuel cell in such applications as stationary power systems, auxiliary devices in air transportation, and many others. The ($LiBH_4$+TiF_3) system is able to desorb about 4 wt.% H_2 at 60 ºC within 12 h or 3 wt. % H_2 at 85 ºC within 4 h. The capability to desorb H_2 at low temperatures makes this system a potential candidate for larger disposable cartridges which may eventually supply fuel cells in off-road vehicles that do not require a substantial driving range and/or on board reversibility. $LiNH_2$ greatly improves the hydrogen storage properties of the ($LiBH_4$+$MnCl_2$) system. Doping the ($LiBH_4$+$MnCl_2$) system with 5 wt.% $LiNH_2$ greatly reduces the apparent activation energy of the system for isothermal dehydrogenation.

References

[1] Elena D. An overview of advanced materials for hydrogen storage. Journal of Materials Processing Technology 2005;162-163:169-77.

[2] Scott DS. Smelling land : the hydrogen defense against climate catastrophe. Canadian Hydrogen Association2007.

[3] http://www.renewableenergyworld.com/hydrogen/tech.html.

[4] <Toyota2013_FullReport.pdf>.

[5] Sakintunaa B, Lamari-Darkrimb F, Hirscher M. Metal hydride materials for solid hydrogen storage: A review International Journal of Hydrogen Energy 2007;32:1121-40.

[6] Schlapbach L, Züttel A. Hydrogen-storage materials for mobile applications. Nature 414 2001:353-8.

[7] Varin RA, Czujko T, Wronski ZS. Nanomaterials for Solid State Hydrogen Storage, Springer. 233 Spring Street, New York, NY 10013, USA: Springer; 2009.

[8] Ritter JA, Ebner AD, Wang J, Zidan R. Implementing a hydrogen economy. Materials Today 2003;6:18-23.

[9] Vajo JJ, Olson GL. Hydrogen storage in destabilized chemical systems. Scripta Materialia 2007;56:829–34.

[10] Gross KJ, Carrington KR, Barcelo S, Karkamkar A, Pureal J, Ma S, et al. Recommended best practice for the characterization of storage properties of hydrogen storage materials2012.

[11] Osborna W, Markmaitreea T, Shawa LL, Hub J-Z, Kwakb J, Yangb Z. Low temperature milling of the $LiNH_2$ + LiH hydrogen storage system. International journal of hydrogen energy (2009) 34:4331–9.

[12] Zaluski L, Zaluska A, Ström-Olsen JO. Hydrogenation properties of complex alkali metal hydrides fabricated by mechano-chemical synthesis. Journal of Alloys and Compounds
1999;290:71–8.

[13] Alapati SV, Johnson JK, Sholl DS. Predicting Reaction Equilibria for Destabilized Metal Hydride Decomposition Reactions for Reversible Hydrogen Storage. The Journal of Physical Chemistry C 2007;111:1584-91.

[14] Vajoa JJ, Skeitha SL, Mertensb F, Jorgensenb SW. Hydrogen-generating solid-state hydride/hydroxide reactions. Journal of Alloys and Compounds 2005;390:55-61.

[15] Varin RA, Wronski ZS. Progress in hydrogen storage in complex hydrides. In: Gandia LM AG, Diéguez PM. , editor. Renewable Hydrogen Technologies Production, Purification, Storage, Applications and Safety: Elsevier; 978-0-444-56352-1. p. 293-332.

[16] Shawa LL, Rena R, Markmaitree T, Osborn W. Effects of mechanical activation on dehydrogenation of the lithium amide and lithium hydride system. Journal of Alloys and Compounds 2008;Volume 448:263-71.

[17] Andreasen A, Veggea T, Pedersen AS. Dehydrogenation kinetics of as-received and ball-milled $LiAlH_4$. Journal of Solid State Chemistry 2005;Volume 178:3672–8

[18] KJ G. Intermetallic materials for hydrogen storage.: University de Fribourg 1998.

[19] Bidabadi AS, Enayati M, Dastanpoor E, Varin RA, Biglari M. Nanocrystalline intermetallic compounds in the Ni–Al–Cr system synthesized by mechanical alloying and their thermodynamic analysis. Journal of Alloys and Compounds 2013;581:91-100.

[20] Bidabadi AS, Shokuhfar A, Enayati MH, Biglari M. In Situ Fabrication and Characterization of (NiCr)Al-Al_2O_3 Nanocomposite by Mechanical Alloying. Journal of Nano Research 2011;16:21-7.

[21] Soulié J-P, Renaudin G, R Černý KY. Lithium boro-hydride $LiBH_4$: I. Crystal structure. Journal of Alloys and Compounds 2002;346:200–5.

[22] Walters RT, Scogin JH. A general initial decomposition reaction for complex metal hydrides. Journal of Alloys and Compounds 2006;421:54-6.

[23] Mauron P, Buchter F, Friedrichs O, Remhof A, Bielmann M, Zwicky CN, et al. Stability and Reversibility of $LiBH_4$. Journal of Physical Chemistry B 2008;112:906–10.

[24] Xia GL, Guo YH, Wu Z, Yu XB. Enhanced hydrogen storage performance of $LiBH_4$–Ni composite. Journal of Alloys and Compounds 2009;479:545-8.

[25] MS W, PA B, R Z. Novel catalytic effects of fullerene for $LiBH_4$ hydrogen uptake and release. Nanotechnology 2009;20:204022.

[26] Drozd V, Saxena S, Garimella SV, Durygin A. Hydrogen release from a mixture of $NaBH_4$ and ($Mg(OH)_2$). International Journal of Hydrogen Energy 2007;32:3370–5.

[27] Varin RA, Parviz R. Hydrogen generation from the ball milled composite of sodium and lithium borohydride ($NaBH_4/LiBH_4$) and magnesium hydroxide ($Mg(OH)_2$) without and with nanometric Nickel (Ni) additive. International Journal of Hydrogen Energy 2012;37:1584-93.

[28] Stasinevich D, Egorenko G. Thermographic investigation of alkali metal and magnesium tetrahydroborates at pressures up to 10 atm. Russian Journal of Inorganic Chemistry 1968;13:341-3.

[29] Nakamori Y, Miwa K, Ninomiya A, Li H, Ohba N, Towata S-i, et al. Correlation between thermodynamical stabilities of metal borohydrides and cation electronegativites: First-principles calculations and experiments. Phys Rev B 2006;74:045126.

[30] Nakamori Y, Li H-W, Kikuchi K, Aoki M, Miwa K, Towata S, et al. Thermodynamical stabilities of metal-borohydrides. Journal of Alloys and Compounds 2007;446-447:296-300.

[31] Alapati SV, Johnson JK, Sholl DS. Predicting Reaction Equilibria for Destabilized Metal Hydride Decomposition Reactions for Reversible Hydrogen Storage. J Phys Chem C 2007;111:1584-91.

[32] Choudhury P, Srinivasan SS, Bhethanabotla VR, Goswami Y, McGrath K, Stefanakos EK. Nano-Ni doped Li–Mn–B–H system as a new hydrogen storage candidate. International Journal of Hydrogen Energy 2009;34:6325-34.

[33] Varin RA, Zbroniec L. The effects of ball milling and nanometric nickel additive on the hydrogen desorption from lithium borohydride and manganese chloride ($3LiBH_4 + MnCl_2$) mixture. International Journal of Hydrogen Energy 2010;35:3588–97.

[34] Černý R, Penin N, Hagemann H, Filinchuk Y. The First Crystallographic and Spectroscopic Characterization of a 3d-Metal Borohydride: $Mn(BH_4)_2$. J Phys Chem C 2009;113:9003-7.

[35] Liu R, Reed D, Book D. Decomposition behaviour of $Mn(BH_4)_2$ formed by ball-milling $LiBH_4$ and $MnCl_2$. Journal of Alloys and Compounds 2012;515:32-8.

[36] Varin RA, Zbroniec L, Polanski M, Filinchuk Y, Černý R. Mechano-chemical synthesis of manganese borohydride ($Mn(BH_4)_2$) and inverse cubic spinel (Li_2MnCl_4) in the ($nLiBH_4+MnCl_2$) (n=1, 2, 3, 5, 9 and 23) mixtures and their dehydrogenation behavior. International Journal of Hydrogen Energy 2012;37:16056-69.

[37] Song Y, Fang F, Li Y, Zhao Q, Sun D, Zhang Q, et al. Promoted hydrogen release from 3LiBH4/MnF_2 composite by doping $LiNH_2$: Elimination of diborane release and reduction of decomposition temperature. International Journal of Hydrogen Energy 2012;37:18074-9.
[38] Fichtner M, Fuhr O. Synthesis and structures of magnesium alanate and two solvent adducts. Journal of Alloys and Compounds 2002;345:286-96.
[39] Humphries TD, Ley MB, Frommen C, Munroe KT, Jensen TR, Hauback BC. Crystal structure and in situ decomposition of Eu(BH4)2 and Sm(BH4)2. Journal of Materials Chemistry A 2015;3:691-8.
[40] Chlopek K, Frommen C, Leon A, Zabara O, Fichtner M. Synthesis and properties of magnesium tetrahydroborate, Mg(BH4)2. Journal of Materials Chemistry 2007;17:3496-503.
[41] Tumanov NA, Safin DA, Richter B, Lodziana Z, Jensen TR, Garcia Y, et al. Challenges in the synthetic routes to $Mn(BH_4)_2$: insight into intermediate compounds. Dalton Transactions 2015;44:6571-80.
[42] Richter B, Ravnsbaek DB, Tumanov N, Filinchuk Y, Jensen TR. Manganese borohydride; synthesis and characterization. Dalton Transactions 2015;44:3988-96.
[43] Mamatha M, Bogdanović B, Felderhoff M, Pommerin A, Schmidt W, Schüth F, et al. Mechanochemical preparation and investigation of properties of magnesium, calcium and lithium–magnesium alanates. Journal of Alloys and Compounds 2006;407:78-86.
[44] Myakishev KG, Volkov VV. Mechanochemical synthesis of diborane (6) by the interaction of anhydrous chloride of iron (II), cobalt (II), nickel (II) with tetrahydroborates of alkaline metals. Chemistry for Sustainable Development 2006;14:375-8.
[45] Schaeffer GW, Roscoe JS, Stewart AC. The Reduction of Iron(III) Chloride with Lithium Aluminohydride and Lithium Borohydride: Iron(II) Borohydride1. Journal of the American Chemical Society 1956;78:729-33.
[46] Zhang BJ, Liu BH. Hydrogen desorption from $LiBH_4$ destabilized by chlorides of transition metal Fe, Co, and Ni. International Journal of Hydrogen Energy 2010;35:7288-94.
[47] Hoekstra HR, Katz JJ. The Preparation and Properties of the Group IV-B Metal Borohydrides. Journal of the American Chemical Society 1949;71:2488-92.
[48] Jensen JA, Girolami GS. Transition metal tetrahydridoborates as models of methane activation: synthesis and structure of Ti(BH4)3(PMe3)2. Journal of the Chemical Society, Chemical Communications 1986:1160-2.
[49] Soloveichik GL. Metal borohydrides as hydrogen storage materials. Material Matters 2 2007:11-4.
[50] Au M, Jurgensen A. Modified Lithium Borohydrides for Reversible Hydrogen Storage. The Journal of Physical Chemistry B 2006;110:7062-7.
[51] Au M, Jurgensen AR, Spencer WA, Anton DL, Pinkerton FE, Hwang S-J, et al. Stability and Reversibility of Lithium Borohydrides Doped by Metal Halides and Hydrides. The Journal of Physical Chemistry C 2008;112:18661-71.
[52] Zhang Y, Zhang W-S, Fan M-Q, Liu S-S, Chu H-L, Zhang Y-H, et al. Enhanced Hydrogen Storage Performance of $LiBH_4-SiO_2-TiF_3$ Composite. The Journal of Physical Chemistry C 2008;112:4005-10.

[53] Wang P, Ma L, Fang Z, Kang X, Wang P. Improved hydrogen storage property of Li-Mg-B-H system by milling with titanium trifluoride. Energy & Environmental Science 2009;2:120-3.

[54] Züttel A, Rentsch S, Fischer P, Wenger P, Sudan P, Mauron P, et al. Hydrogen storage properties of $LiBH_4$. Journal of Alloys and Compounds 2003;356–357:515-20.

[55] Fang ZZ, Ma LP, Kang XD, Wang PJ, Wang P, Cheng HM. In situ formation and rapid decomposition of Ti(BH4)3 by mechanical milling LiBH4 with TiF3. Applied Physics Letters 2009;94:044104.

[56] Guo YH, Yu XB, Gao L, Xia GL, Guo ZP, Liu HK. Significantly improved dehydrogenation of LiBH4 destabilized by TiF3. Energy & Environmental Science 2010;3:464-9.

[57] Zhang H, Cao Z, Sun L-X, Sun Y-J, Xu F, Liu H, et al. Improved dehydrogenation/rehydrogenation performance of $LiBH_4$ by doping mesoporous Fe_2O_3 or/and TiF_3. Journal of Thermal Analysis and Calorimetry 2013;112:1407-14.

[58] Varin. RA, Bidabadi AS. Nanostructured complex hydride systems for hydrogen generation. AIMS Energy 2015;3:121-43.

[59] Jin S-A, Lee Y-S, Shim J-H, Cho YW. Reversible Hydrogen Storage in LiBH4−MH2 (M = Ce, Ca) Composites. The Journal of Physical Chemistry C 2008;112:9520-4.

[60] Sun T, Wang H, Zhang Q, Sun D, Yao X, Zhu M. Synergetic effects of hydrogenated Mg_3La and $TiCl_3$ on the dehydrogenation of $LiBH_4$. Journal of Materials Chemistry 2011;21:9179-84.

[61] Tang WS, Wu G, Liu T, Wee ATS, Yong CK, Xiong Z, et al. Cobalt-catalyzed hydrogen desorption from the $LiNH_2$-$LiBH_4$ system. Dalton Transactions 2008:2395-9.

[62] Vajo JJ, Skeith SL, Mertens F. Reversible Storage of Hydrogen in Destabilized LiBH4. The Journal of Physical Chemistry B 2005;109:3719-22.

[63] Züttel A, Wenger P, Rentsch S, Sudan P, Mauron P, Emmenegger C. $LiBH_4$ a new hydrogen storage material. Journal of Power Sources 2003;118:1-7.

[64] Pinkerton FE, Meyer MS, Meisner GP, Balogh MP. Improved Hydrogen Release from LiB0.33N0.67H2.67 with Noble Metal Additions. The Journal of Physical Chemistry B 2006;110:7967-74.

[65] Liu D, Yang J, Ni J, Drews A. Studies of the effects of TiCl3 in LiBH4/CaH2/TiCl3 reversible hydrogen storage system. Journal of Alloys and Compounds 2012;514:103-8.

[66] Shi Q, Yu X, Feidenhans'l R, Vegge T. Destabilized $LiBH_4$−$NaAlH_4$ Mixtures Doped with Titanium Based Catalysts. The Journal of Physical Chemistry C 2008;112:18244-8.

[67] Yang H, Ibikunle A, Goudy AJ. Effects of Ti-Based Additives on the Hydrogen Storage Properties of $LiBH_4$/CaH_2 destablized system. Advances in Materials Science and Engineering 2010;2010:7.

[68] Mosegaard L, Møller B, Jørgensen J-E, Filinchuk Y, Cerenius Y, Hanson JC, et al. Reactivity of LiBH4: In Situ Synchrotron Radiation Powder X-ray Diffraction Study. The Journal of Physical Chemistry C 2008;112:1299-303.

[69] http://ardica.com/.

[70] Zhu Y, Zou J, Zeng X. Study on reversible hydrogen sorption behaviors of 3LiBH4/graphene and 3LiBH4/graphene-10 wt% CeF3 composites. RSC Advances 2015;5:82916-23.

[71] Calka A, Radlinski AP. Universal high performance ball-milling device and its application for mechanical alloying. Materials Science and Engineering: A 1991;134:1350-3.
[72] Calka A, Varin RA. Application of Controlled Ball Milling in Materials Processing. In: Srivatsan TS VR, Khor M, editor. Processing and Fabrication of Advanced Materials IX (PFAM IX). Materials Park, OH: ASM International; 2001. p. 263-87.
[73] Patent: WO9104810, US5383615, CA2066740, EP0494899, AU643949.
[74] Parviz R, Varin RA. Combined effects of molar ratio and ball milling energy on the phase transformations and mechanical dehydrogenation in the lithium amide-magnesium hydride ($LiNH_2$+$nMgH_2$)(n=0.5-2.0) nanocomposites. International Journal of Hydrogen Energy 2013;38 8313–27.
[75] Varin RA, Mattar DK, Bidabadi AS, Polanski M. Synthesis of amorphous manganese borohydride, its hydrogen generation properties and crystalline transformation during solvent extraction. Journal of Energy Chemistry Article in press.
[76] Varin RA, Li S, Wronski Z, Morozova O, Khomenko T. The effect of sequential and continuous high-energy impact mode on the mechano-chemical synthesis of nanostructured complex hydride Mg2FeH6. Journal of Alloys and Compounds 2005;390:282-96.
[77] Sandrock G, Gross K, Thomas G, Jensen C, Meeker D, Takara S. Engineering considerations in the use of catalyzed sodium alanates for hydrogen storage. Journal of Alloys and Compounds 2002;330–332, 17 696-701.
[78] Varin RA, Parviz R. The effects of the micrometric and nanometric iron (Fe) additives on the mechanical and thermal dehydrogenation of lithium alanate ($LiAlH_4$), its self-discharge at low temperatures and rehydrogenation. International Journal of Hydrogen Energy 2012;37 9088–102.
[79] Williamson GK, Hall WH. X-ray line broadening from filed aluminium and wolfram. Acta Metallurgica 1953;1:22-31.
[80] http://imagej.en.softonic.com
[81] Varin RA, Bidabadi AS. The effect of milling energy input during mechano-chemical activation synthesis (MCAS) of the nanocrystalline manganese borohydride ($Mn(BH_4)_2$) on its thermal dehydrogenation properties. International Journal of Hydrogen Energy 2014;39: 11620–32.
[82] Černý R, Penin N, D'Anna V, Hagemann H, Durand E, Růžička J. $Mg_xMn_{(1-x)}(BH_4)_2$ (x = 0–0.8), a cation solid solution in a bimetallic borohydride. Acta Materialia 2011;59:5171-80.
[83] Severa G, Hagemann H, Longhini M, Kaminski JW, Wesolowski TA, Jensen CM. Thermal Desorption, Vibrational Spectroscopic, and DFT Computational Studies of the Complex Manganese Borohydrides $Mn(BH_4)_2$ and [$Mn(BH_4)$4]2−. The Journal of Physical Chemistry C 2010;114:15516-21.
[84] Varin RA, Zbroniec L. Mechanical and Thermal Dehydrogenation of Lithium Alanate ($LiAlH_4$) and Lithium Amide ($LiNH_2$) Hydride Composites. Crystals 2012;2:159-75.
[85] Soulié J-P, Renaudin G, R Černý KY. Lithium boro-hydride $LiBH_4$ I. Crystal structure. Journal of Alloys and Compounds 2002 346:200–5.

[86] Arnbjerg LM, Ravnsbæk DB, Filinchuk Y, Vang RT, Cerenius Y, Besenbacher F, et al. Structure and Dynamics for LiBH4−LiCl Solid Solutions. Chemistry of Materials 2009;21:5772-82.
[87] Bidabadi AS, Korinek A, Botton GA, Varin RA. High resolution transmission electron microscopy (TEM), energy-dispersive X-ray spectroscopy (EDS) and X-ray diffraction studies of nanocrystalline manganese borohydride (Mn(BH4)2) after mechano-chemical synthesis and thermal dehydrogenation. Acta Materialia 2015;100:392-400.
[88] Swanson HE, Mcmurdie HF, Morris MC, Evans EH. X-ray powder diffraction powder patterns. X-ray powder diffraction powder patterns: National Bureau of Standards Monograph 1970 p. 1-171.
[89] Kril CE, Birringer R. Estimating grain-size distributions in nanocrystalline materials from X-ray diffraction profile analysis. Philosophical Magazine A 1998;77:621-40.
[90] Zhang Z, Zhou F, Lavernia EJ. On the analysis of grain size in bulk nanocrystalline materials via x-ray diffraction. Metallurgical and Materials Transactions A 2003;34:1349-55.
[91] Ungár T. The meaning of size obtained from broadened diffraction peaks. Advanced Engineering Materials 2003;5:323-9.
[92] https://www2.chemistry.msu.edu/faculty/reusch/virttxtjml/spectrpy/infrared/irspec1.htm
[93] http://www.unige.ch/sciences/chifi/?ftirdb.html.
[94] D'Anna V, Spyratou A, Sharma M, Hagemann H. FT-IR spectra of inorganic borohydrides. Spectrochimica Acta Part A: Molecular and Biomolecular Spectroscopy 2014;128:902-6.
[95] http://www.ochemonline.com/Infrared_spectroscopy_absorption_table.
[96] Varin RA, Bidabadi AS. Rapid, ambient temperature hydrogen generation from the solid state Li–B–Fe–H system by mechano-chemical activation synthesis. Journal of Power Sources 2015;284:554–65.
[97] Varin RA, Zbroniec L, Jang M. Mechano-chemical synthesis of nanostructured hydride composites based on Li-Al-N-Mg for solid state hydrogen storage. Engineering Review 2011;31:111-23.
[98] Vincze I, Van Der Woude F, Kemèny T, Schaafsma AS. Magnetic properties of amorphous transition metal alloys. Journal of Magnetism and Magnetic Materials 1980;15:1336-8.
[99] Guan J, Yan G, Wang W, Liu J. External field-assisted solution synthesis and selectively catalytic properties of amorphous iron nanoplatelets. Journal of Materials Chemistry 2012;22:3909-15.
[100] Suslick KS, Choe S-B, Cichowlas AA, Grinstaff MW. Sonochemical synthesis of amorphous iron. Nature 1991;353:414-6.
[101] Au M, Jurgensen A, Zeigler K. Modified Lithium Borohydrides for Reversible Hydrogen Storage (2). The Journal of Physical Chemistry B 2006;110:26482-7.
[102] Jeon E, Cho Y. Mechanochemical synthesis and thermal decomposition of zinc borohydride. Journal of Alloys and Compounds 2006;422:273-5.
[103] http://chemwiki.ucdavis.edu/Physical_Chemistry/Thermodynamics/State_Functions/Enthalpy/Standard_Enthalpy_Of_Formation.

[104] http://www.chemistry-reference.com/Standard%20Thermodynamic%20Values.pdf.

[105] Smith MB, (Jr.) GEB. Chem Eng Data 8 1963: 342-6.

[106] Sandrock G, Gross K, Thomas G. Effect of Ti-catalyst content on the reversible hydrogen storage properties of the sodium alanates. Journal of Alloys and Compounds 2002;339:299-308.

[107] Sandrock G, Gross K, Thomas G, Jensen C, Meeker D, Takara S. Engineering considerations in the use of catalyzed sodium alanates for hydrogen storage. Journal of Alloys and Compounds 2002;330–332:696-701.

[108] Yvon K, Lorenzoni JL. Hydrogen-powered lawn mower: 14 years of operation. International Journal of Hydrogen Energy 2006;31:1763-7.

[109] Bidabadi AS, Varin RA, Polanski M, Stobinski L. Mechano-chemical activation of the (3LiBH4+TiF3) system, its dehydrogenation behavior and the effects of ultrafine filamentary Ni and graphene additives. Journal of RSC Advances. Royal Society of Chemistry. 6: 93245-93258.

[110] Arita M, Shimizu K, Ichinose Y. Thermodynamics of the Ti-H system. Metallurgical Transactions A 1982;13:1329-36.

[111] http://www2.mtec.or.th/th/seminar/msativ/pdf/M10.pdf

[112] http://www.hydrogenfuelnews.com/new-hydrogen-fuel-cell-battery-could-help-power-mobile-devices/8523549/

[113] www.ardica.com

[114] Yang H, Ibikunle A, Goudy AJ. Effects of Ti-Based Additives on the Hydrogen Storage Properties of a / Destabilized System. Advances in Materials Science and Engineering 2010;2010:7.

Appendices

A.1. Solvent extraction of ($2LiBH_4$+$MnCl_2$) nanocomposite ball milled with the milling energy input Q_{TR}=72.8 kJ/g (1h)

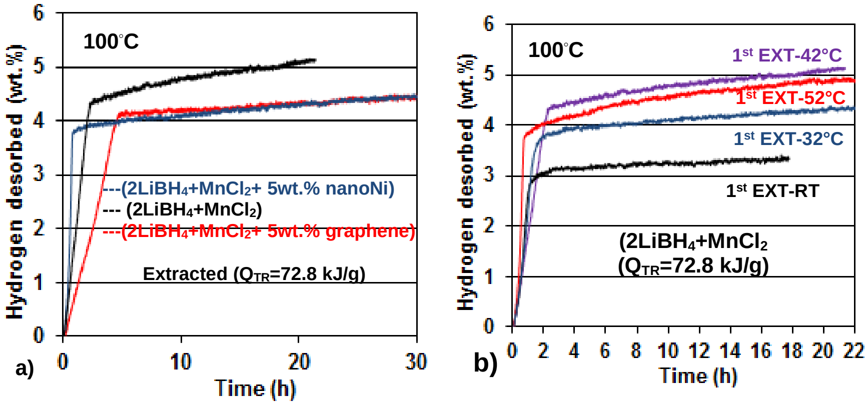

Fig. A.1. a) Dehydrogenation comparison at 100 °C of $2LiBH_4$+$MnCl_2$ extracted at 42°C (black), ($2LiBH_4$+$MnCl_2$) +5 wt.% Ni extracted at 42°C (blue), ($2LiBH_4$+$MnCl_2$) +5 wt.% graphene extracted at 42°C (red) and b) dehydrogenation comparison at 100 °C of ($2LiBH_4$+$MnCl_2$) extracted at RT (black), 32°C (blue), 42°C (purple) and 52°C (red).

Table. A.1 Summary of isothermal dehydrogenation time for the solvent extractions samples

Sample	Time of desorption(h)-wt.% H_2	Time to reach 3wt%H_2 (h)	Time to reach 4wt% H_2 (h)	Time to reach 5wt% H_2 (h)
1h BM and subsequent desorption at 100°C	20.6-4.36	1.4	4.3	---
1h BM and subsequent desorption at 200°C	17.97-4.7	0.07	0.16	---
1st Ext_{RT} and subsequent desorption at 100°C	17.78-3.34	1.43	---	---
1st Ext_{RT} and subsequent desorption at 200°C	8-3.66	0058	---	---
2nd Ext_{RT} and subsequent desorption at 100°C	53-4.62	3.48	9.73	---
2nd Ext_{RT} and subsequent desorption at 200°C	67.94-4.71	0.06	0.45	---
1st $Ext_{32°C}$ and subsequent desorption at 100°C	22.95-4.97	0.63	1.48	----
1st $Ext_{32°C}$ and subsequent desorption at 200°C	72.8-4.9	0.053	1.11	----
2nd $Ext_{32°C}$ and subsequent desorption at 100°C	69.7-5.47	1.9	2.5	14.5
2nd $Ext_{32°C}$ and subsequent desorption at 200°C	43.95-5.34	0.07	0.08	12.7
1st $Ext_{42°C}$ and subsequent desorption at 100°C	21.39-5.14	1.55	2.01	15.75
1st $Ext_{42°C}$ and subsequent desorption at 200°C	69.94-5.72	0.07	0.08	3.77
2nd $Ext_{42°C}$ and subsequent desorption at 100°C	18.4-5.04	0.83	1.01	18.2
2nd $Ext_{42°C}$ and subsequent desorption at 200°C	23-5.41	0.067	0.083	1.25
1st $Ext_{52°C}$ and subsequent desorption at 100°C	25.08-4.42	1.18	4.5	----
1st $Ext_{52°C}$ and subsequent desorption at 200°C	39.58-5.06	0.06	0.083	18
2nd$Ext_{52°C}$ and subsequent desorption at 100°C	23.23-4.82	1.07	1.47	----
2nd $Ext_{52°C}$ and subsequent desorption at 200°C	23.3-5.1	0.054	0.075	17.18

A.2. Nanostructured Li-B-Fe-H system

Table A.2 Summary of XRD analysis of ($2LiBH_4$+$FeCl_2$) nanocomposites after ball milling (BM).

Processing	**Ball milling energy input Q_{TR} (kJ/g)**	**H_2 desorbed after RT and/or during BM (wt.%)**	**Presence of Fe XRD peaks**		**Presence of XRD peaks $FeCl_2$**
			yes	no	
1h keep RT+2 min BM	2.43	0.80	-	X	VS
2 min BM	2.43	0.33	-	X	VS
1h keep RT+5 min BM	6.07	2.19	-	X	S
5 min BM	6.07	0.83-0.87	-	X	S
10 min BM	12.14	2.80	-	X	-
15 min BM	18.20	3.50	-	X	-
30 min BM	36.40	4.02	-	X	-

VS-very strong, S-strong.

Table A.3 DSC data from thermal analysis of the ($2LiBH_4$+$FeCl_2$) mixture.

Milling energy Q_{TR} (kJ/g)/milling time (min)	**H_2 desorbed during processing (wt.%)**	**Phases present after processing**	**Max heating temperature (°C)**	**Peak temp. first endo peak (°C)**	**Peak temp. second exo peak (°C)**
Non BM mixture	-	$FeCl_2$; $LiBH_4$	300	119.7	282.3
Non BM mixture	-	$FeCl_2$; $LiBH_4$	140	118.0	-
(1h RT)+2.43/2	0.80	$FeCl_2$ (large); LiCl (min.); $LiBH_4$ (min.)	300	114.9	216.1-226
(1h RT)+6.07/5	2.19	$FeCl_2$; LiCl (small); a-$LiBH_4$	300	117.2	204.1
(1h RT)+6.07/5	2.19	$FeCl_2$; LiCl (small); a-$LiBH_4$	140	114.8	-
12.14/10	2.80	$FeCl_2$ (min.); LiCl; Fe (min.); a-$LiBH_4$	300	114.9	206.6-209.1

Table A.4 Summary of hydrogen quantities desorbed due to mechanical and thermal dehydrogenation.

Processing	**Ball milling energy Q_{TR} (kJ/g)**	**H_2 desorbed during BM (wt.%)**	**Dehydrogenation time at 100°C or 250°C (h)**	**H_2 desorbed at 100°C/250°C**	**Total H_2 desorbed (wt.%)**	**Presence of Fe XRD peaks after desorption**		**Presence of XRD peaks $FeCl_2$**
						yes	no	
2 min BM	2.43	0.33	100°C /66.3	3.00	3.33	X	-	S
5 min BM	6.07	0.87	100°C /22.6	2.32	3.19	X	-	M
10 min BM	12.14	2.80	100°C /42.4	0.61	3.41	X$^{*)}$	-	-
15 min BM	18.18	3.50	100°C /17.7	0.60	4.10	-	X	-
30 min BM	36.40	4.02	100°C /15.5	0.24	4.26	-	X	-
5 min BM	6.07	0.83	250°C/122	3.68	4.51	X	-	-
Mixture (no BM)	-		250°C/19	3.00	3.00	-	X	M
Mixture (no BM)	-		250°C/67	3.70	3.70	-	X	W
Mixture (no BM)	-		250°C/112	4.00	4.00	-	X	VW
Mixture (no BM)	-		250°C/115	4.30	4.30	-	X	W

$^{*)}$ Diffuse peak at the 100% (110) Fe peak position. VS-very strong, M-medium, W-weak.

Table A.5 XRD estimated grain (crystallite) size of Fe after thermal dehydrogenation at 100 and 250°C.

Processing	**Desorption temperature (°C)**	**Grain (crystallite) size of Fe (nm)**
1h RT+2 min BM	100	46.9±1.9
1h RT+5 min BM	100	27.4±0.7
2 min BM	100	47.2±1.1
5 min BM	100	27.4±0.6
5 min BM	250	32.8±1.5

A.3. List of publications:

Peer reviewed journal articles:

1. **A. Shirani Bidabadi,** R. A. Varin, M. Biglari, M. Polanski, L. Stobinski (2016), The effects of filamentary Ni, graphene and lithium amide on the synthesis of the ($Mn(BH_4)_2$-2LiCl) mixture and its solvent extraction. Ready for submission.
2. R. A. Varin, D. K. Mattar, **A. Shirani Bidabadi,** M. Polanski (2016), Synthesis of amorphous manganese borohydride in the ($NaBH_4$-$MnCl_2$) system, its hydrogen generation properties and crystalline transformation during solvent extraction. Journal of Energy Chemistry (accepted August 30/2016-in press)
3. **A. Shirani Bidabadi,** R. A. Varin, M. Polanski, L. Stobinski (2016), Mechano-chemical activation of the ($3LiBH_4$ +TiF_3) system, its dehydrogenation behavior and the effects of ultrafine filamentary Ni and graphene additives. RSC Advances 6: 93245-93258
4. **A. Shirani Bidabadi**, A. Korinek, G.A. Botton, R. A. Varin, (2015) High resolution transmission electron microscopy (TEM), energy-dispersive X-ray spectroscopy (EDS) and X-ray diffraction studies of nanocrystalline manganese borohydride ($Mn(BH_4)_2$) after mechano-chemical synthesis and thermal dehydrogenation. Acta Materialia, 100: (392-400)
5. R.A. Varin, **A. Shirani Bidabadi**, (2015) Rapid, ambient temperature hydrogen generation from the solid state Li-B-Fe-H system by mechano-chemical activation synthesis, Journal of Power Sources. 284: 554-565
6. R.A. Varin, **A. Shirani Bidabadi**, (2015) Nanostructured, complex hydride systems for irreversible hydrogen generation. AIMS Energy. 3: 121-143
7. R.A. Varin, **A**. **Shirani Bidabadi**, (2014) The effect of milling energy input during mechano-chemical activation synthesis (MCAS) on the microstructure and dehydrogenation properties of nanostructured manganese borohydride ($Mn(BH_4)_2$). International Journal of Hydrogen Energy. 39: 11620-11632
8. **A.R. Shirani Bidabadi,** M.H. Enayati, E. Dastanpoor, R.A. Varin, M. Biglari. (2013) Nanocrystalline intermetallic compounds in the Ni–Al–Cr system synthesized by mechanical alloying and their thermodynamic analysis. Journal of Alloys and Compounds. 581: 91-100
9. **A.R. Shirani Bidabadi**, A. Shokuhfar, M.H. Enayati, M. Biglari. (2011) In-situ Fabrication and Characterization of (NiCr)Al-Al_2O_3 Nanocomposite by Mechanical Alloying. Journal of Nano Research. 16: 21-27
10. **A.R. Shirani Bidabadi**, A. Shokuhfar, M.H. Enayati. (2010) Effect of Mechanical Alloying and Heat Treatment Process on the Phase Transformation of Ni-Cr-Al Powders Mixture. Journal of New Materials, Vol. 1, No. 1: 29-37 (Abstract in English, manuscript in Farsi)
11. M.H. Shirani, A. Saidi, M. Kasiri, **A.R. Shirani Bidabadi**. (2012) The effect of mechanical activation on sintering and mechanical properties of Fe-50Ni-TiC composite. Majlesi Journal of Materials Engineering Vol. 6, No. 1: 57-62 (Abstract in English, manuscript in Farsi)

Conferences:

1. **A. Shirani Bidabadi**, R.A. Varin, M. Polanski, Synthesis of amorphous titanium borohydride [TiBH$_4$)$_3$] and its dehydrogenation behavior. XXI Physical Metallurgy and Materials Science Conference Advanced Materials and Technologies AMT June 2016, Warsaw, Poland (Oral presentation)
2. **A. Shirani Bidabadi** and R.A. Varin, Electron microscopy studies of the manganese borohydride [Mn(BH$_4$)$_2$] and lithium chloride nanocomposite synthesized by mechano-chemical activation. 27th Canadian Materials Science Conference, Halifax (CMSC June 2015) (Oral presentation).
3. D. Mattar, **A. Shirani Bidabadi** and R.A. Varin, Mechano-chemical activation synthesis of disordered manganese borohydride (d-Mn(BH$_4$)$_2$) and its Nanocrystallization after solvent extraction. 27th Canadian Materials Science Conference, Halifax (CMSC June 2015) (Poster presentation).
4. **A.R. Shirani Bidabadi**, A. Shokuhfar, M.H. Enayati, M. Biglari. (June 2011) In-situ Fabrication and Characterization of (NiCr)Al-Al$_2$O$_3$ Nanocomposite by Mechanical Alloying. DSL- 2011, Algarve, Portugal (poster presentation)
5. **A.R. Shirani Bidabadi**, A. Shokuhfar, M.H. Enayati, (Nov 2010) The effect of mechanical alloying and heat treatment on the phase transformation of Ni-Cr-Al powders mixture. 4th conference of metallurgy, Iran University of science and technology, Tehran, Iran (Oral presentation).
6. **A.R. Shirani Bidabadi**, A. Shokuhfar, M.H. Enayati, Study of (Ni,Cr)$_3$Al Nanocrystalline formation by mechanical alloying and detecting its features. (Nov 2010) 4th conference of metallurgy, Iran (poster presentation).